All-Polymer Microfluidic Systems with integrated Nanostructures for Cell Handling

Matschuk, Maria

Publication date:
2011

Document Version
Publisher's PDF, also known as Version of record

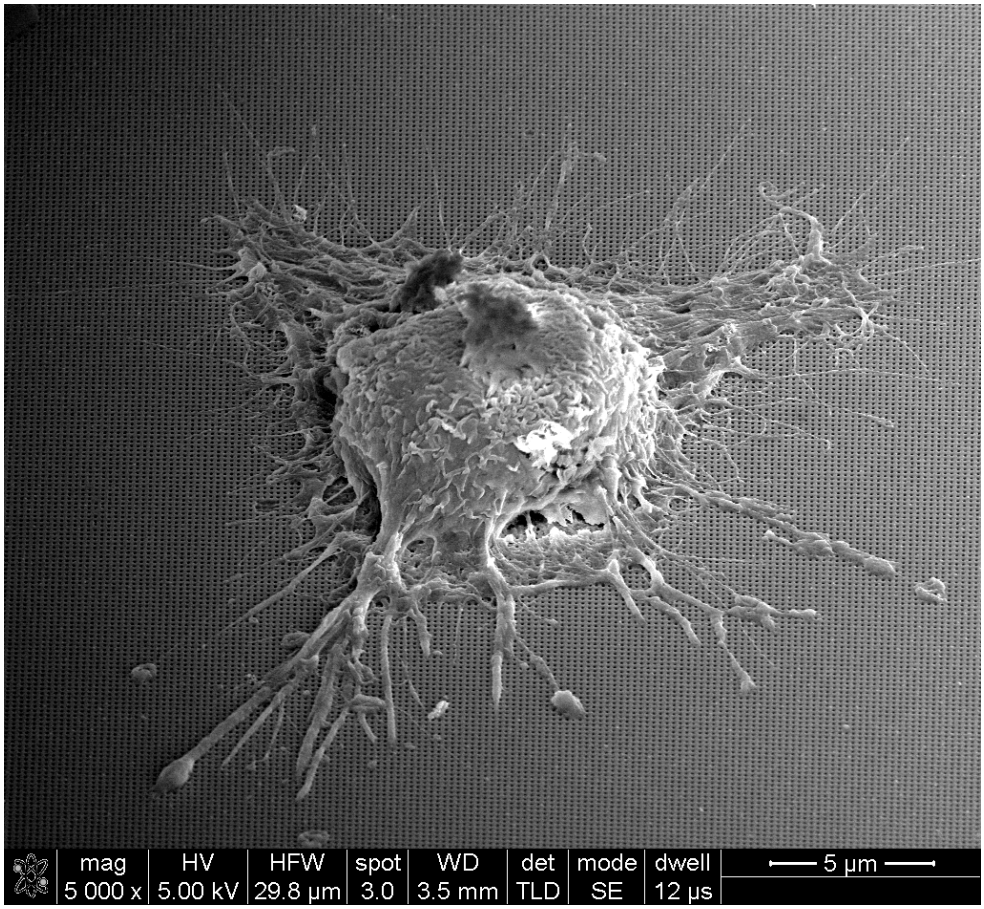

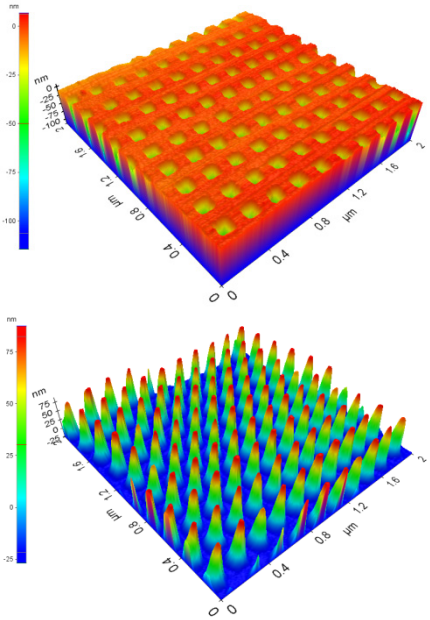

DTU
NANOTECH

ALL-POLYMER MICROFLUIDIC SYSTEM WITH INTEGRATED NANOSTRUCTURES FOR CELL HANDLING

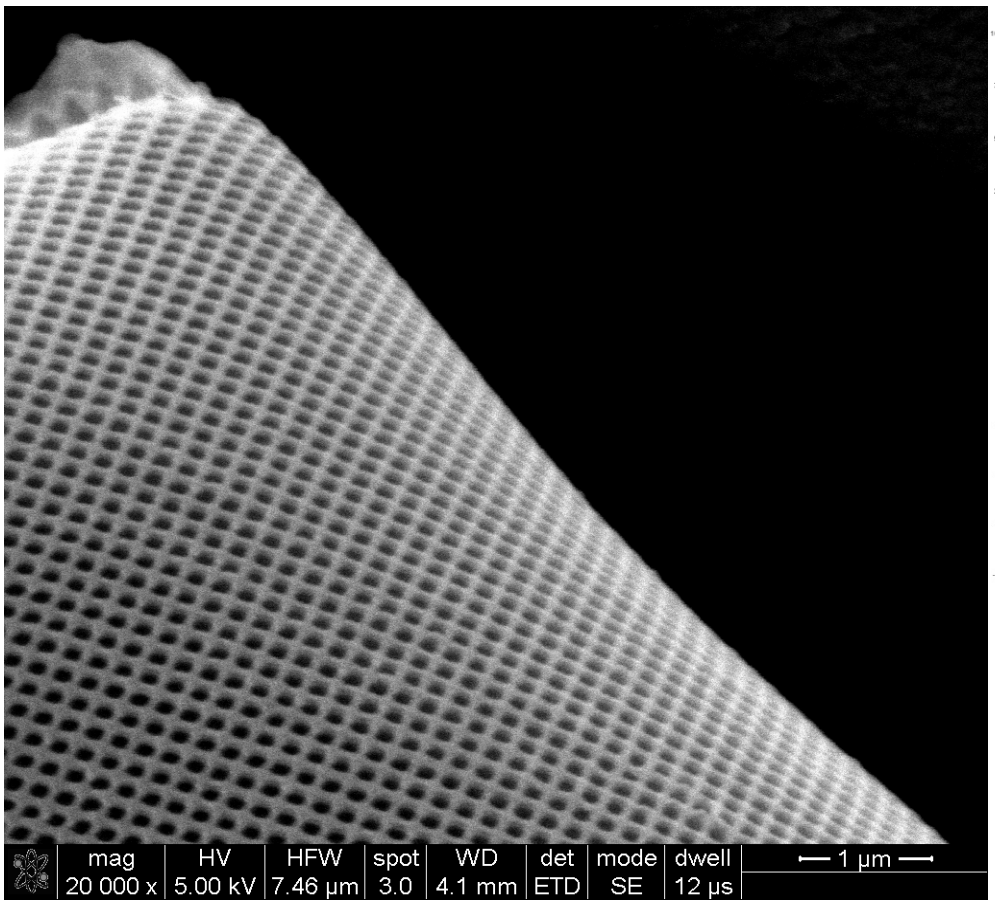

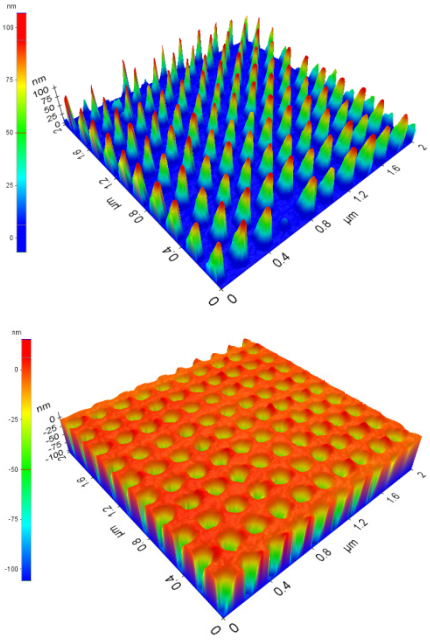

Maria Matschuk

Supervisor:
prof. Niels B. Larsen

All-Polymer Microfluidic Systems with integrated Nanostructures for Cell Handling

DTU Nanotech – Department of Micro- and Nanotechnology

Technical University of Denmark

Cover Images: SEM image of a HeLa cell on 100 nm wide holes (upper left). SEM image of bended layer of nanostructured polymer (lower left). AFM images of 100 nm wide holes (upper right, top) and 100 nm wide pillars (upper right, bottom) replicated in nickel. AFM images of 40 nm wide pillars (lower right, top) and 100 nm wide holes (lower right, bottom) replicated in polymer.

http://www.nanotech.dtu.dk/Research/POLYMIC/POLYCELL

For Jan and my Little Monsters Ria and Finn. And my Parents.

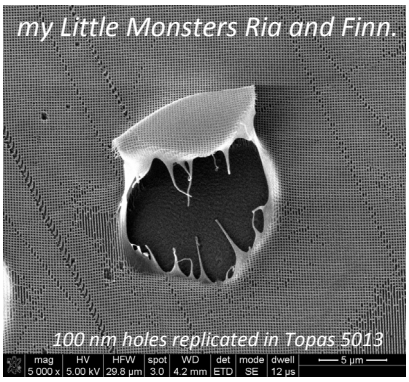

Abstract

There is an increasing need for mass-production of nanostructures with high precision at polymer surfaces, for example to reduce the reflection of light, to reduce the adhesion of smudge, for optical data storage (e.g. Blu-ray discs), and for biological applications. In this project the effects of mold coatings and injection molding conditions on the final nanostructure quality (aspect ratio, shape, uniformity) of nanostructures in the cyclic olefin copolymers Topas 8007 and 5013 were explored. A setup for investigation the behavior of cells on nanostructures was established. Initial cell experiments were performed to investigate the influence of injection molded nanostructured surface topographies on the cell morphology and spreading of different cell types, i.e. mouse fibroblasts (NiH3T3), human epithelial carcinoma cells (HeLa) and immature dentritic cells.

Given sufficient flowability of the polymer melt, interfacial effects like wetting and friction play a major role in injection molding of high aspect ratio nanostructures. The interfacial energy between mold and polymer needs to allow filling as well as demolding which are opposing properties: On the one hand, insufficient wetting of the polymer melt on the mold surface may prevent the polymer melt to fill nanoscale cavities during injection. This will limit the resolution of injection molding. On the other hand, given adequate cavity filling, high frictional forces may cause inability of the solidified polymer to leave the nanoscale cavity during demolding leading to nanostructural failure.

It was found that the mold temperature has a major influence on the replication depth for tested mold coatings while other parameters (melt temperature, injection velocity and pressure, holding pressure and ejection temperature) do not have any significant effect. Nanostructured areas molded on native nickel molds often showed regular nanoscale defects and distortions, and randomly distributed large-scale defects. In contrast, a molecular vapor deposited fluorocarbon based antistiction coating commonly used for silicon molds in nanoimprint lithography was found to improve the replication quality substantially. Large scale defects of the overall patterned surface were fully removed while regular nanoscale defects decreased significantly. Optimized injection molding conditions allowed the replication of highly ordered nanostructures of controlled size. Arrays of pillars of 40 nm in diameter and up to 100 nm in height (height-to-width aspect ratios above unity) were successfully injection molded in Topas 8007 at mold temperatures above glass transition temperature using a fluorocarbonsilane coated nickel mold. Secondly, arrays of holes of 50 and 100 nm in diameter and up to 35 and 100 nm in height, respectively, were injection molded in Topas 8007 and 5013 with high replication quality.

Initial cell experiments of NiH 3T3, HeLa and immature dendritic cells (DC) on oxygen plasma treated Topas 8007 and 5013 showed cell morphologies comparable to cells cultured on commercial tissue culture grade polystyrene. NiH 3T3 and HeLa cells grow visibly slower and often exhibiting elongated shapes and spread less well on native (untreated) Topas of both types. Only HeLa cells showed a clear difference in spreading on different nanostructured surfaces. For example HeLa cells were clearly avoiding patterns of 50 nm wide and 50 nm deep holes while favoring areas containing 350 and 600 nm wide and 250 nm deep holes over flat surfaces. Immature DCs were found to spread less well on native Topas regardless of surface topography forming largely extended lamellopodia and filopodia compared to oxygen plasma treated Topas. No obvious influence on immature DC morphology could be seen for nanostructures on treated or untreated Topas.

Resumé

Behovet er stigende for masseproduktion af nanostrukturer med høj præcision på overfladen af polymer overflader, for eksempel til at reducere reflektion af lys, for at begrænse tilsmudsning, til optisk datalagring med forøget datatæthed, og til biologiske anvendelser. I dette projekt blev effekten af forskellige støbeformsbelægninger og sprøjtestøbningsbetingelser undersøgt i forhold til kvaliteten af den endelige nanostruktur (aspekt ratio, form, ensartethed) i to typer cyklisk olefin copolymer, Topas 8007 og Topas 5013. En forsøgsopstilling til studier af cellers opførsel på nanostrukturer blev etableret. De indledende eksperimenter med celler var rettet mod at undersøge vedhæftning, spredning og morfologi af forskellige cellelinier (NiH3T3, HeLa og umodne dendritceller) på sprøjtestøbte overflader med nanostrukturer.

Befugtning og friktion ved grænseflader spiller en stor rolle ved sprøjtestøbning af nanostrukturer med høj højde-til-bredde ratio, såfremt polymersmelten flyder tilstrækkeligt let. Grænsefladeenergien mellem støbeform og polymer skal både tillade fyldning og udtagning: På den ene side kan utilstrækkelig befugtning forhindre polymersmelten den i at nå hulrum i nanostrukturer under indsprøjtning, hvilket vil begrænse opløsningen af sprøjtestøbningen. På den anden side kan høje friktionskræfter (antaget fyldestgørende fyldning af hulrum) forhindre den størknede polymer i at forlade nano-skala hulrum udtagning, hvilket medfører fejl i nanostrukturen.

Studier har vist at støbetemperaturen har stor indflydelse på replikationsdybden af de undersøgte støbeformsbelægninger, hvorimod andre parametre (smeltetemperatur, indsprøjtningshastighed og -tryk, eftertryk, og formtemperatur ved afformning) ikke har en signifikant effekt. Nanostrukturerede områder støbt i støbeforme af nikkel gav ofte regelmæssige nanodefekter og forvrængninger, samt større defekter tilfældigt fordelt. Replikationskvaliteten blev væsentligt forbedret ved at anvende en belægning af dampfase-deponeret fluorocarbonsilan med lav vedhæftningsevne, der normalt bruges til siliciumforme i ”nanoimprint litografi”. De større defekter på overfladen forsvandt, samtidig med at antallet af regelmæssige nanodefekter blev reduceret betydeligt. De optimerede sprøjtestøbningsbetingelser tillod replikation af mønstrede nanostrukturer af kontrolleret størrelse. Rækker af søjler med en diameter på 40nm og op til 100nm høje (højde-til-bredde forhold over én) kunne sprøjtestøbes i Topas 8007 ved formtemperaturer over polymerens glasovergangstemperatur ved at anvende en fluorocarbonsilan-belagt støbeform i nikkel. Desuden blev rækker af huller med en diameter på 50 og 100nm og højde op til 35 og 100nm sprøjtestøbt i Topas 8007 og Topas 5013 med høj replikationskvalitet.

De indledende forsøg med NiH3T3 celler, HeLa celler og umodne dendritceller (DC) på oxygen plasmabehandlet Topas 8007 og Topas 5013 viste cellemorfologier sammenlignelige med celler i kultur på overflader beregnet til cellekulturer i polystyren. NiH 3T3 og HeLa celler vokser langsommere, spreder sig dårligere, og udviser ofte en langstrakt form på naturligt (ubehandlet) Topas af begge typer. Kun HeLa celler demonstrerede en klar forskel i spredning på forskellige nanostrukturerede overflader: HeLa celler undgik mønstre af 50nm bredde og 50nm dybe huller, og favoriserede områder af 350 og 600nm bredde og 250nm dybe huller i forhold til flade overflader. Umodne DC spredte sig dårligt på ubehandlet Topas uafhængigt af overfladetopografi, og cellerne dannede store forlængede lamellopodia og filopodia sammenlignet med oxygen plasmabehandlet Topas. Der var ikke markant forskel i umoden DC cellemorfologi for nanostrukturer på behandlet eller ubehandlet Topas.

Preface

This thesis is submitted in partial fulfillment of the requirements for obtaining the degree of Doctor of Philosophy (Ph.D.) at the Technical University of Denmark. The work has been carried out at the Department of Micro- and Nanotechnology (DTU Nanotech) and the National Laboratory for Sustainable Energy (Risø DTU), former Risø National Laboratory, at the Technical University of Denmark from January 2007 to April 2011, within the group for Polymer Microsystems for Cell Processing. This work was supported by The Danish Research Council for Technology and Production Sciences, Grant No. 26-04-0074.

The Ph.D. project was supervised by prof. Niels Bent Larsen (main supervisor, DTU Nanotech) and prof. Henrik Bruus (co-supervisor, DTU Nanotech).

First of all, I would like to thank my supervisors, especially Niels B. Larsen for his invaluable support and for many inspiring discussions on injection molding of nanostructures and related fields throughout the entire project.

I would like to express special gratitude to Ina Bloom who was one of the most helpful persons in Risø and after moving to DTU Nanotech. I thank Fredrik Persson and Peixiong Shi for many useful discussions and continuous support with the electron beam lithography, and José Marín for carrying out rheology experiment. Furthermore, I would like to thank the staff at DTU Danchip for their exceptional support, especially Jonas Michael Lindhard for his continues help with SEM imaging. I would like thank all people at DTU Nanotech, Risø DTU, and DTU Danchip in particular current and former members of the Polycell group as well as my former office members Thomas Glasdam Jensen and Pelle Olsen for creating a pleasant and exceptional good atmosphere. I also would like to thank the administration, especially Bente Schlichting (Risø), Jette Rasmussen and Louise Søby Møller (DTU Nanotech) for their extensive help.

I owe huge thanks to Joanna Lopacinska and Maciej Skolimowski for their support with cell culturing and micro milling, but also for moral support and help with the kids.

At last I would like to thank my family and friends, but especially Jan, Ria and Finn for their encouragement, support and tremendous understanding throughout the project, especially during the final weeks.

Maria Matschuk

Department of Micro- and Nanotechnology

Technical University of Denmark

April 2010

Table of Contents

Chapter 1

Introduction

1. Background and Motivation

Nanostructured surfaces enables researchers to handle, culture, and even treat cells in a smart way. Various research groups have shown that cells react to nano- and microstructured surface topographies, often by alignment of the cell body along the structures [Curtis 2001b, Wilkinson 2002, Lehnert 2004, Dalby 2005, Choi 2007] or reduced adhesion sites [Bigss 2007, Cavalcanti-Adam 2007, Arnold 2008]. Especially the adhesion of cells onto surfaces plays a major role in motility, proliferation, and differentiation of most (adherent) cell types and is often required for effective treatment with chemicals or biomolecules.

Cells build up connections to other cells or the extracellular matrix (ECM) using cell adhesion molecules such as selectins, cadherines (cell-cell), or integrins (cell-ECM). The adhesion of a cell to the extracellular matrix, or an artificial surface (*in vitro*), is based on the binding of the transmembrane protein "integrin" to its ligand, for example fibronectin, vitronectin, collagen, or laminin. The ability of integrins to bond to their ligands is largely dependent on three conditions. Firstly, the extracellular part of the integrin (about 15 – 20 nm in activated state) needs to overcome the distance between cell membrane and ligand. Secondly, the cell body must be flexible and follow the surface topography accordingly to limit the distance between integrin and ligand. Thirdly, integrin binding sites must be available down to a certain distance to allow the formation of stable focal adhesions. Information about the structure and properties of integrins and their binding sites are still limited, though they give an idea about important length scales [Carrell 1985, Rivas 1991, Owen 2005, Besser 2006, Vogel 2006]. The research group around J.P. Spatz has shown that the spacing of adhesion sites for cells affect the strength of the cell adhesion, i.e. amount of formed focal adhesions. A spacing of up to 58 nm was sufficient small to allow integrins to bind and form focal adhesion sites while 73 nm and larger resulted in a strongly reduced adhesion [Cavalcanti-Adam 2007, Arnold 2008, Selhuber-Unkel 2010]. Other groups have found varying spacings of integrin binding sites (10 – 140 nm) essential for cell spreading [Humphries 1986, Singer 1987, Danilov 1989, Hughes 1979, Massia 1991]. Massia et al. gives an overview of related results. The deformability of the cell body is non-trivial and very difficult to predict since it depends on many characteristics such as membrane elasticity, cytoplasmic pressure of the cytoplasm, orientation of the cytoskeleton, and proteins incorporated in the membrane [Evans 1983, Bennett 1989, Boal 2002, Wiseman 2004, Safran 2005, Vogel 2006, Kong 2008, Titushkin 2007, Palsson 2008, Schmitz 2008]. A thorough introduction to the mechanisms relevant for cell adhesion to natural (ECM) as well as artificial surfaces (nanostructured polymers) is given in the Appendix I-1.

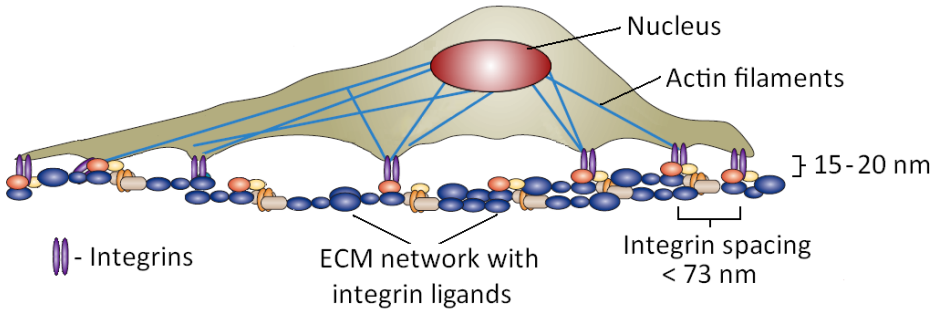

Figure 1: Sketch of a cell spread on a fibronectin network [adapted from Vogel 2006].

Well spread cells often adhere very strongly and are difficult to release for further handling. Commonly cell detachment is supported mechanically e.g. by increased flow rate (shear force over-rule adhesion force), or chemically e.g. by application of calcium ion scavenger or enzymes. Shear force applied by flow exerts stress on the cell and causes mechanical damage of the cell membrane and its proteins. Besides, hydrodynamic resistance in a microfluidic system limits the shear force that can be applied on an adherent cell. The adhesion strength of cells can be controlled by engineering the surface chemistry or by controlling the surface area available for adhesion. Micro- and nanotopography can affect cell behavior directly [Bigss 2007] but can also be employed as a method for patterning homogeneous layers of surface chemistry [Park 2003, Cavalcanti-Adam 2007, Arnold 2008] presented to cells. Employing nanostructured surface topographies, cells could be released without extensive damage of membrane proteins, hence reducing the stress exerted on the cell. Cells could also be captured locally according to their adhesion strength. Ideally, areas could be generated were only one cell type adheres, or at least that specific cell type adheres stronger than others. Non- or low adherent cells would then be flushed out by applying flow.

Previously, it has been demonstrated that mold temperature [Huang 2007, Mönkkönen 2002, Theilade 2007] as well as surface energy [Pranov 2006] plays an important role in the replication depth of micro- and nanostructures above 100 nm lateral dimension. On the one hand, increased mold temperature leads to an improved replication depth. On the other hand, application of a fluorocarbonsilane coating resulted in a strongly reduced replication. However, it has not been investigated thoroughly, whether filling or demolding of nanostructured topographies actually causes limited resolution (lateral dimension and aspect ratio) in injection molded parts. For example, according to Pranov et al., filling is the limiting factor caused by the high surface energy of the mold.

We expected that the filling is strongly influenced by the mold temperature and only to a limited extend influenced by the mold surface energy. In contrast, large frictional forces are exerted on polymeric structures during demolding, possibly causing deformation and fracture. Initial injection molding experiments with low surface energy molds (native nickel) showed that polymer remains on the mold after each cycle, independent of applied mold temperature. Therefore, we expected that decreased adhesion of polymer to the mold would facilitate demolding, hence decrease damage of polymeric nanostructures during demolding, especially of fragile nanostructures. The adhesion of polymer to the mold can be decreased by applying an antistiction coating to increase the surface energy.

1.1. Project Goal

The project was set out to develop new ways of mass-producing polymeric nanostructured topographies. Bonding allowed for their integration into a functional microfluidic device as a first step towards disposable lab-on-a-chip systems, i.e. for studying of cell viability and adhesion on fabricated nanostructured topographies.

We aim to modulate cell adhesion by reducing the surface area available for cells to attach with pattern properties in the dimension of their natural environment (ECM). The remaining adhesion strength is expected to vary between cell types, depending on type and number of specific adhesion molecules. Thus this project had two main objectives. Processes for surface structuring of polymers were developed and optimized to fabricate nano- and microstructures by i.e. injection molding and their integration into a functional microfluidic device. The effects of mold coatings, i.e. fluorocarbons, and injection molding conditions on the final nano- and microstructure quality were explored. Furthermore, interfacial effects (wettability and friction) which are likely to play a role in fabricating of especially nanostructures were investigated. Secondly, fabricated nanostructures were tested on their influence on different cell types, i.e. mouse fibroblasts (NiH 3T3), human epithelial carcinoma cells (HeLa) and immature dentritic cells.

The effect of process conditions and mold surface chemistry on the replication quality of 40 – 600 nm wide structure was explored. Relevant molding parameters like mold temperature, melt temperature, injection velocity and pressure, holding pressure and ejection temperature[1] on the replication quality (aspect ratio, shape, and uniformity) were investigated.

Initial cell experiments of NiH 3T3, HeLa and immature dendritic cells (DC) on oxygen plasma treated Topas 8007 and 5013 showed cell morphologies comparable to cells cultured on commercial tissue culture grade polystyrene. No visible difference in morphology was found for oxygen plasma treated nanostructures in Topas compared to flat surfaces. NiH 3T3 and HeLa cells grow visibly slower and often exhibiting elongated shapes and spread less well on native (untreated) Topas of both types. Only HeLa cells showed a clear difference in spreading on different nanostructured surfaces. For example HeLa cells were clearly avoiding patterns of 50 nm wide and 50 nm deep holes while favoring areas containing 350 and 600 nm wide and 250 nm deep holes over flat surfaces. Immature DCs were found to spread less well on native Topas regardless of surface topography forming largely extended lamellopodia and filopodia compared to oxygen plasma treated Topas. No obvious influence on immature DC morphology could be seen for nanostructures on treated or untreated Topas.

[1] Mold temperature at point of demolding or ejection of the solidified polymer part

1.2. Outline of the Thesis

The thesis is structured according to the different fabrication steps that lead to the mass-production of polymeric nanostructures and their integration into a microfluidic system. Finally, cell culture experiments on fabricated nanostructures are described.

- **Chapter 1** is dedicated to give the reader an introduction to the project with relevant information about background and methods used to improve the understanding of the topic. A short background on cell adhesion is followed by an introduction to cells on polymeric nanostructures. The state of art of the methods used to fabricate polymeric nanostructures is given in the following sections two and tree. Especially these three sections are meant to give the reader a basic understanding on why and how the polymeric nanostructures presented in this thesis could affect the cell. In the last section experimental techniques and methods, including important materials, i.e. polymer and antistiction coatings used in this project, are shortly introduced.

- **Chapter 2 and 3** presents theoretical considerations (design), experimentals and results towards the fabrication of polymeric nanostructures and microfluidic systems (microstructured topographies). The processing steps are similar for nano- and microstructured topographies in terms of fabrication of master (substrate containing nano- or microstructured topographies), mold (inverted metal replica of the master) and injection molding (replication of mold relief leading to inverted polymeric replica). Many aspects in the fabrication of nano- and microstructures vary tremendously so that the separation into structure size rather than process steps was considered to give the reader a better understanding of results and problems related to the specific structure dimension. Similar information with respect to experimental methods, setups or materials will be described extensively in the experimental section of chapter 2 “Fabrication of Polymeric Microfluidic System”. Furthermore, results such as characterization of antistiction coatings applying to both parts will be described in chapter 2, while only differing information will be given in chapter 3 “Fabrication of Polymeric Nanostructures”.

- **Chapter 4** describes the integration of polymeric nanostructures into a microfluidic system by thermal bonding. Pre-treatments as well as bonding process optimization, and related problems will be presented. Lastly, the fabrication of fluidic connectors matching is described.

- **Chapter 5** finally presents initial cell experiments conducted on nanostructured topographies in an open system and integrated in a microfluidic chip.

1.3. Publications during the Ph.D. Project

Papers in peer reviewed journals

1. *Nanostructures for All-Polymer Microfluidic Systems*
M. Matschuk, H. Bruus, N. B. Larsen
Microelectronic Engineering **87** (2010) 1379–1382.

2. *Injection molded chips with integrated conducting polymer electrodes for electroporation of cells*
K. Ø. Andresen, M. Hansen, M. Matschuk, S. T. Jepsen, H. S. Sørensen, P. Utko,T. S. Hansen, N. B. Larsen, N. Rozlosnik, R. Taboryski
J. Micromech.Microeng. **20** (2010) 055010 (9pp).

First author conference contribution

1. *Nanostructures in Polymeric Microfluidic Systems for Cell Adhesion Modulation (Talk)*
M. Matschuk, H. Bruus, N. B. Larsen
Annual Polymer Day, Copenhagen, Denmark, November 2008

2. *Nanostructures in Polymeric Microfluidic Systems for Cell Adhesion Modulation (Poster)*
M. Matschuk, H. Bruus, N. B. Larsen
Nanobio Europe 2009, Grenoble, France, June 2009.

3. *Nanostructures for All-Polymer Microfluidic Systems (Talk)*
M. Matschuk, H. Bruus, N. B. Larsen
Annual Polymer Day, Copenhagen, Denmark, November 2009

4. *Nanostructures for All-Polymer Microfluidic Systems (Poster)*
M. Matschuk, N. B. Larsen
35th International Conference on Micro and Nano Engineering" (MNE), Ghent, Brussels, September 2009.

5. *Fabrication of Polymeric Nanostructures in COC by Injection Molding (Talk)*
M. Matschuk, N. B. Larsen
Annual Polymer Day, Copenhagen, Denmark, November 2010

2. Polymeric Nanostructures

Nanostructured surfaces for application in research and industry gained increasing attention in the last decade. The mass-production of sub-micrometer structures in polymer has been done for e.g. antireflection [Xie 2008, Ting 2008] or antistiction coatings [Koponen 2007], optical data storage (e.g. DVD and Blue-ray disk) and for biomaterial applications [Biggs 2007, Dalby 2007, Gadegaard 2006].

Originally it was expected that the size of nanostructures in polymer will be limited when approaching the "size" of a single polymer chain (radius of gyration). Mesoscopic effects like memory effect or internal stress caused by the attractive and repulsive forces in the polymer chains were expected to inhibit structures smaller than the radius of gyration[2] (several nanometer) [Schift 2000, Schift 2007]. The origin of deformation lies in the capability of the polymer to adjust their chain configuration on a molecular level by rotation around single covalent bonds in the main chain. This freedom of rotation is controlled by intra-molecular (chain stiffness) and inter-molecular interactions [Klompen 2005]. So far no resolution limit was found proving this assumption, and even structures below 10 nm were already hot embossed. Various research groups proved that nanostructures can be replicated into polymer with high-precision by nanoimprint lithography [Chou 1997, Heyderman 2001, Schift 2008] or by injection molding [Macintyre 1998, Schift 2000, Mönkkönen 2002, Liou 2006, Huang 2007, Chen 2007], though injection molding is the industrially preferred technology platform for low cost fabrication of polymer items in large numbers. Examples of nanostructures fabricated by injection molding are shown in Figure 3. The highest aspect ratio achieved by injection molding so far was demonstrated by the replication of 25 nm wide and 40 nm deep holes in polycarbonate, though the replication uniformity was sub-optimal even over a small area (< 4 μm^2) (Figure 3a) [Schift 2000].

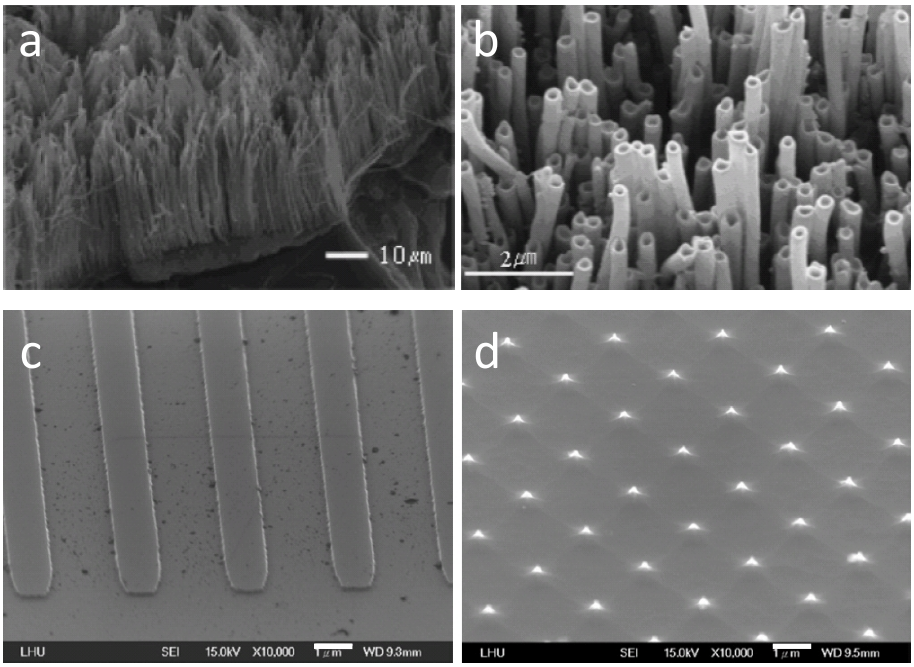

Figure 2: SEM images of injection molded nanostructured topographies fabricated by [Yoo 2009] (a, b) and [Huang 2007] (c, d). Scale bars: 10 µm (a), 2 µm (b), and 1 µm (c, d).

[2] Radius of gyration: Root mean square distance from the center of the gravity to a chain segment.

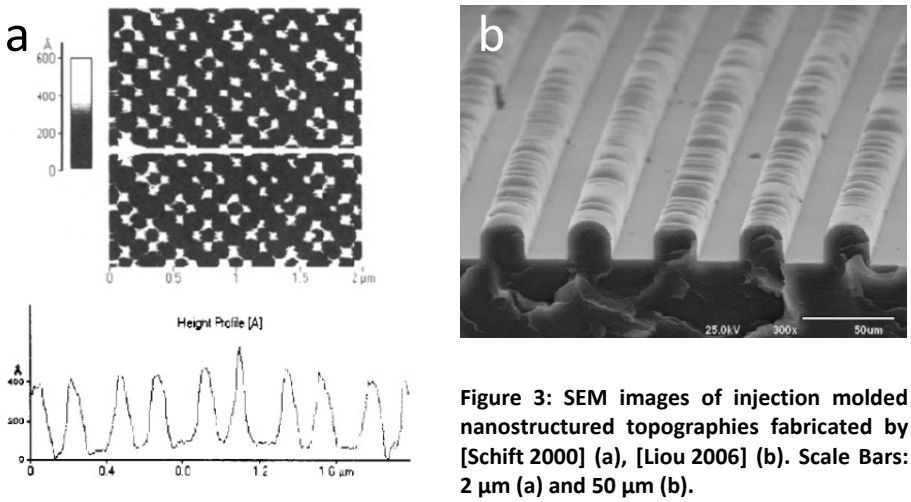

Figure 3: SEM images of injection molded nanostructured topographies fabricated by [Schift 2000] (a), [Liou 2006] (b). Scale Bars: 2 µm (a) and 50 µm (b).

It turned out that injection molding of nanostructured patterns over a large area (4" wafer scale) is more difficult than in nanoimprint lithography. Injection molding of nanostructures with large height-to-width aspect ratio is still very limited, especially in increasingly used cyclic olefin co-polymer (COC). In fact, COC has been shown to replicate sub-micrometer structures worse than materials commonly used for injection molding, like polycarbonate or polymethmethylacrylate [Mönkkönen 2002]. Cyclic olefin copolymers, like Topas from Topas Advanced Polymers, possess excellent physical (optical, mechanical, electrical, thermal) and chemical resistance which are superior most other commonly used polymers like polycarbonate or polystyrene. Their ultra-low moisture absorption (< 0.01 %) coupled with excellent flow properties (melt flow index of up to 3.2 $cm^3\ min^{-1}$) and dimensional stability (low shrinkage, high stiffness) enables high precision molding. Although Mönkkönen et al. pointed out that nanostructures in COC might exhibit worse replication fidelity that other injection molding grade polymers, properties of COC indicate excellent flow behavior and reduced appearance of molding defects, like warpage[3] [Topas Advanced Polymers, Nunes 2010].

[3] Warpage (or warping) relates to part distortion when the part is bowed, bent, twisted or stretched beyond intended specification.

3. Cells on Polymeric Nanostructures

Polymers are increasingly used for cell culture; especially microfluidic cell handling systems due to a variety of adjustable properties (e.g. biocompatibility, chemical resistance, mechanical stability, biodegradability) and applicable processing methods (e.g. hot embossing, injection molding, laser machining, milling) and economical considerations compared to silicon based technology.

However, two factors aggravated the directed research towards understanding the fundamental mechanisms that controls the reaction of cells towards different surfaces. Firstly, it was shown that the cell reaction on a specific substrate depends on its topography [Curtis 1997, Curtis 2001a, Curtis 2001b, Wilkinson 2002, Gallagher 2002, Lehnert 2004, Dalby 2004, Sniadecki 2006, Choi 2006, Gadegaard 2006, Dalby 2007, Biggs 2007, Cretel 2008, Ghibaudo 2009,], and chemical composition [Cretel 2008, Mitchell 2005, Curtis 2001a] and varies for different cell types. Martinez et al. gives a summary of some research done in that area, showing the effects of micro- and nanostructured surfaces on cell orientation and adhesion [Martinez 2008].

Effect of topographical or chemical cues on cells properties

(1) Adhesion
(2) Alignment and orientation of cell body
(3) Cell morphology
(4) Cytoskeletal orientation
(5) Physiology

For example, Choi et al. showed that cells align to nanostructures (Figure 4Figure 4) [Choi 2006]. Biggs et al. showed that nanostructured topologies reduce the adhesion sites of human osteoblasts [Bigss 2007]. Dalby et al. showed that osteoprognitors and human stem cells react to nanoscaled topologies by modified expression of bone-specific extracellular matrix proteins (osteopontin and osteocalcin) (Figure 5) [Dalby 2007].

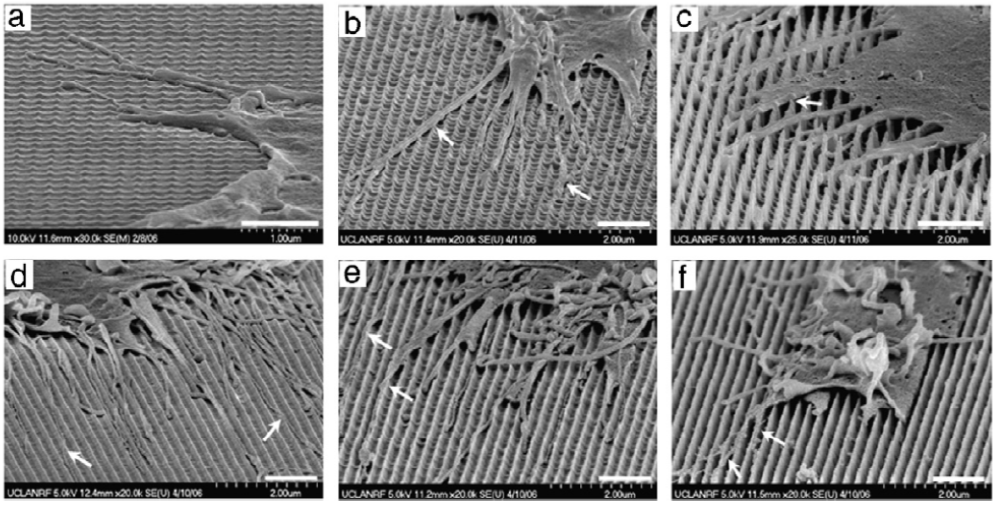

Figure 4: Alignment and filopodial interactions of fibroblasts with 3D sharp-tip nanotopography. The SEM images of cells' filopodia were taken at the culture periods of 3 days for nanopost (a: low, b: mid, c: high) and nanograte (d: low, e: mid, f: high) samples. Scale bar: 1 µm [Choi 2006].

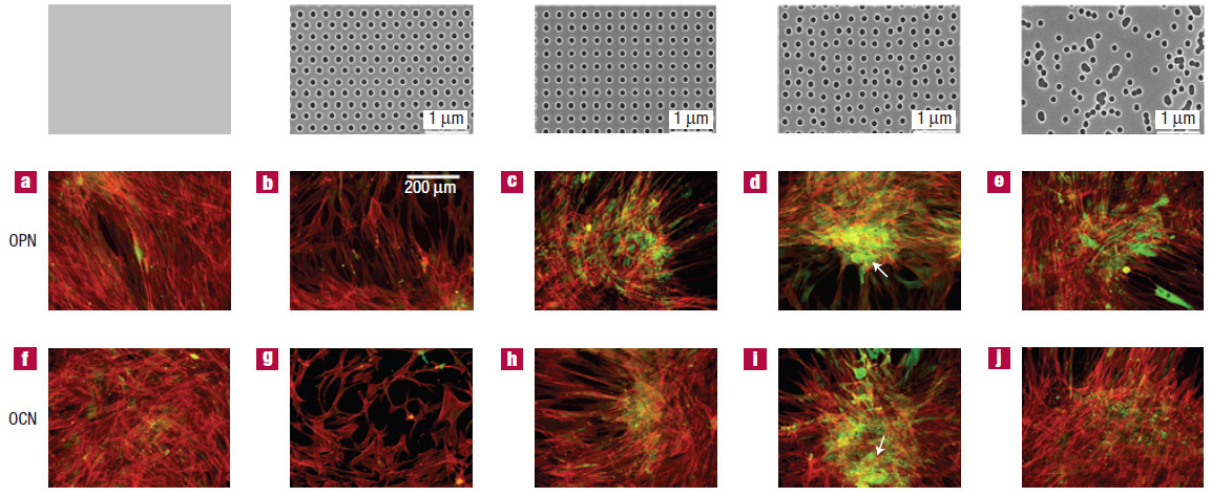

Figure 5: Reaction of osteoprognitors to nanoscaled topologies by modified expression of bone-specific extracellular matrix proteins (osteopontin (OPN) and osteocalcin (OCN)). The top row shows SEM images of nanotopographies fabricated by EBL (120 nm wide and 100 nm in deep pits) (scale bar: 1 µm), the lower two rows showing osteoprogenitors labeled for actin (red) and OPN/OCN (green) (scale bar: 200 µm). Osteoprogenitors cultured on the control (flat surface) lacking OPN and OCN expression (a, f); the hexagonal pattern causing loss of cell adhesion (b, g); the squared pattern with a reduced number of cells but some OPN and OCN positive cells (c, h); DSQ50 pattern with bone nodule formation (arrows) (d, i); random pattern with good cell populations with cells expressing OPN and OCN (e, j). Actin=red, OPN/OCN=green [adapted from Dalby 2007].

Secondly, there is an excessive amount of materials available, and especially polymers can be synthesized with manifold properties. Unfortunately, despite the increasing research activities in that field no consistent results have been presented so far, explaining fundamental mechanisms behind reaction of cells to nanotopographies, or simply showing that cells react in a certain way to certain patterns. Results of different research groups are difficult to compare since most groups have fabricated their own pattern and often on materials (e.g. glass, silicon, gold, PMMA, PS, TCPS) different from others. In addition, nanostructures are coated with biomolecules or treated chemically with e.g. oxygen plasma to change surface properties and improve the biocompatibility.

Literature study of various papers about cell adhesion on nano- and microstructures leads to a major question: what actually affects the cell adhesion - the area fraction that is presented to the cell or the actual properties (size, height or depth, etc.) of single structures? Unfortunately none of the mentioned research groups state their intention or fundamental idea about how and why the structure sizes or materials they employed should affect cells in a certain way. For instance, if the cell could only form focal adhesion points every 70 nm on any kind of structure presenting the right ligand motif, irrespective of shape or pattern, the adhesion strength could be reduced by creating nanostructured patterns with spacing larger than that (Figure 6). As already described, the effect of spacing between integrin binding sites has been extensively studied by a research group around J. P. Spatz. On the other hand, single integrins do not form a strong bond between cell and substrate, thus it is very likely that the area fraction presented to a cell is important as well. The area fraction is determined by a variety of factors such as structure shape, size and pitch (center-to-center distance). For example regular holes of a certain width and a pitch of double the width would result in a 75% area fraction.

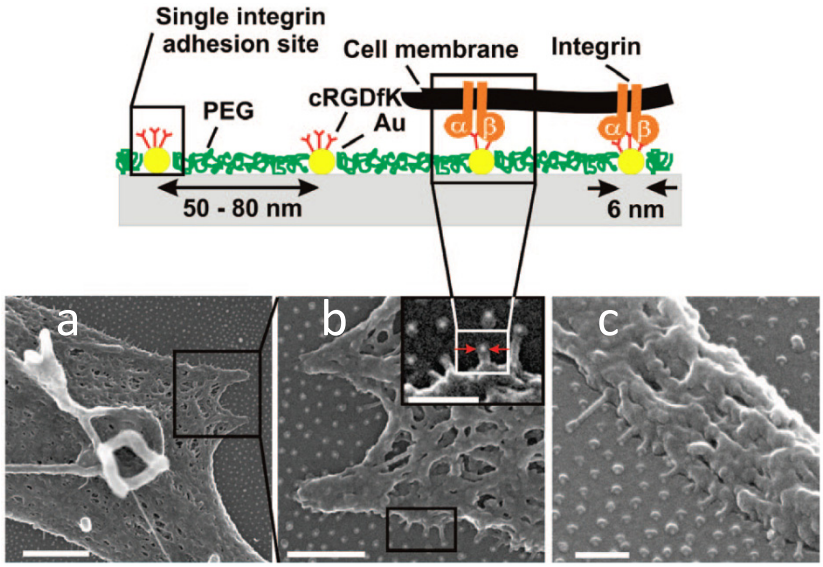

Figure 6: MC3T3 osteoblasts plated on a biofunctionalized substrate (8 nm wide gold dots coated with a RGD presenting peptide, spacing about 60 nm): Scheme of substrate (top), and Scanning electron micrographs show parts of critical point-dried MC3T3 osteoblasts. The inset in shows a close-up of ultra small cellular protrusions with a diameter of 10 to20 nm and a length of 30 to 50 nm interacting selectively with the RGD-motif on the gold dots. Scale bars: 500 nm (a), 200 nm (b), 100 nm (inset in b, c) [Arnold 2008].

In contrast, if the cell could form focal adhesion points at every position but is dependent on a certain area of a single structure, the size would play a major role. A list of possible factors is given in Table 1. Investigating all factors is not possible in the given time schedule for this project. The adhesion of cells to nanostructured topographies in Topas 8007 and 5013 with low (hydrophilic) and high surface energy (hydrophobic) is studied, varying area fraction, aspect ratio and pitch of the nanostructured pattern.

Table 1: List of topological and chemical factors relevant for adhesion of cells on nanostructured surfaces

Topology:	▪ Area fraction ▪ Pattern: honeycomb-like, hexagonal, squared, triangular … ▪ Regularity: regular, irregular, random ▪ Shape: circular, rectangular, hexagonal … ▪ Aspect ratio: width, depth or height ▪ Pitch
Chemical Composition:	▪ Bulk: polymer, glass, silicon, metal … ▪ Surface modification: oxygen plasma treatment, plasma polymerization, grafting … ▪ Biological modification: coating with albumin, collagen, fibronectin …
Medium:	▪ Composition ▪ Temperature ▪ pH

4. Experimental Techniques and Materials

In this section general information about methods and techniques used to fabricate and characterize polymeric nanostructures and microfluidics system will be described.

Processing methods are presented in the first sub-section, leading from the fabrication of resist or silicon based masters over injection molding of nano- and microstructured polymer parts to bonding into functional microfluidic chip. Following techniques and methods are covered: UV lithography was used to fabricate microstructured masters while laser and electron beam lithography were tested on their capabilities to produce nanostructured masters with feature sizes from 40 – 600 nm. Mold inserts were fabricated by means of galvanic plating of nickel. Based on the structured mold inserts, polymeric parts containing the nano- or microstructured surface reliefs were injection molded. Finally micro- and nanostructured parts were thermally bonded to a functional device.

General process steps

a. Design of microfluidics and nanostructured patterns
b. Fabrication of a structured master by lithography
c. Replication into nickel by galvanic plating
d. Replication into polymer by injection molding
e. Bonding to a functional microfluidics device
f. Investigation of the effect of nanostructured surface on different cells types

In the second sub-section techniques used to characterize nanostructured topologies in resist, nickel and polymer, like atomic force or scanning electron microscopy are shortly described. The surface chemistry of native and coated nickel mold inserts were characterized by means of contact angle measurements and x-ray photon and energy dispersive spectroscopy. Combined with results from a lateral ball shear test the adhesion of polymer on the different nickel mold surfaces was evaluated.

In the last sub-section, materials relevant for successful injection molding of polymeric nano- and microstructures, i.e. polymer of choice, Topas 8007 and Topas 5013, and chemicals used for antistiction coatings, Fluoroform (CHF3), Perfluorodecyltrichlorosilane (FDTS), Perfluordecanethiol (PFDT), are described.

4.1. Processing Methods

4.1.1. UV Lithography (UVL)

UV lithography is based on the principle that a photoactive polymer (resist) is chemically modified by means of photon energy from a UV light source (300 - 400 nm). Commercial photo resists are often optimized for exposure using a mercury lamp (10 mW/cm^2) at 365 nm (i-line). Photo resists is usually composed of monomers or pre-polymers (negative resist) or polymers (positive resist) dissolved in a solvent, e.g. anisol and probably some additives to modify certain properties of the final resist, e.g. increased etch resistance. The solvent enable spinning of the resist on a substrate, e.g. silicon or glass wafer followed by a baking step to evaporate the solvent. UV light is shined through a patterned photo mask which partially reflects and transmits light so that only certain areas of the underlying resist are exposed to the UV light (Figure 7). Thereby, patterns can be created with feature sizes from some micrometers to millimeters. The resolution is limited by the wavelength of the light source and the optics applied. Commonly structures are well reproduced above 10 µm, though smaller structures can be made but require optimized process parameters. The patterned resist can be directly used for further processing, e.g. fabrication of an inverted replica by means of galvanic plating. More likely the resist is used as mask for dry or wet etching of e.g. silicon, or for local deposition of material, e.g. gold for metal lift-off.

There are two types of photo resists, positive and negative. A positive photo resist consists of long chain polymer molecules which are hardly soluble in specific developer. Upon exposure with UV light chain scission is initiated by photon energy creating polymers with smaller chain lengths. The decreased chain length makes these polymer molecules more soluble in the specific developer. In contrast, a negative photo resist consists of monomers or pre-polymers. Upon exposure with UV light, photon energy initiates cross-linking into polymer. The exposed, cross-linked polymer is less soluble in specific developer than the unexposed resist.

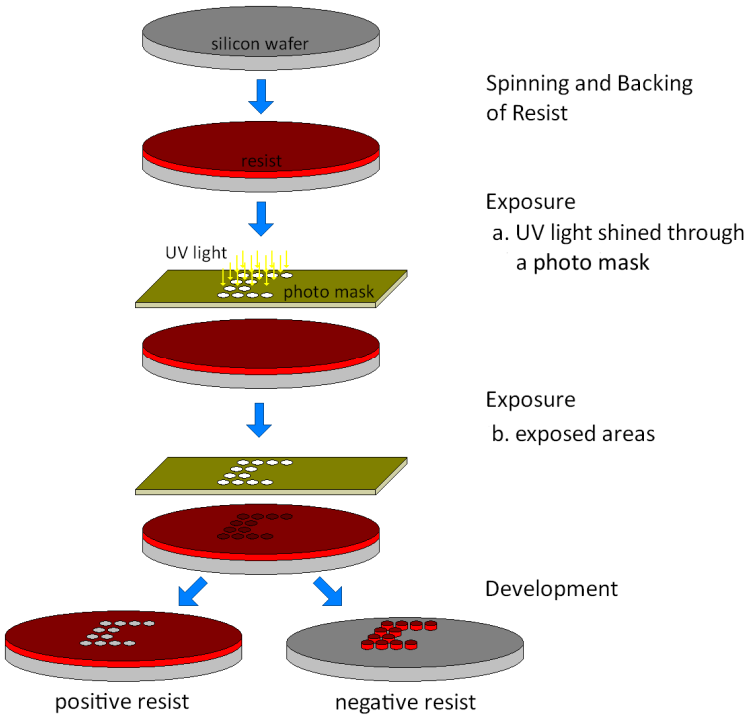

Figure 7: Schema of UV lithography: Positive or negative resist is exposed by UV light, creating patterned film after development.

4.1.2. Laser Lithography

Laser lithography is based on the same principle as UV lithography, initiating chain scission or cross-linking of photo sensitive resist by photon energy. In contrast to UV lithography where a broad UV light source exposes the resist through a patterned photo mask, laser lithography is directly exposing the resist in the area of interest by a focused laser beam.

The substrate (commonly silicon or quartz) covered with positive or negative photo resist is placed on a high precision stage that can resolve several nanometers. A system of lenses, mirrors, deflectors and shutters control the laser intensity, beam spot size, focus, exposure time, and x-y movement. The laser scans the substrate locally and induces chain scission or cross-linking in the resist. After development the patterned resist can be directly used for further processing, or as etch mask, e.g. for subsequent chrome etch to create a patterned photo mask for UV lithography. Laser lithography is one of the few optical systems that allow for sub-micron resolution, down to 0.6 µm.

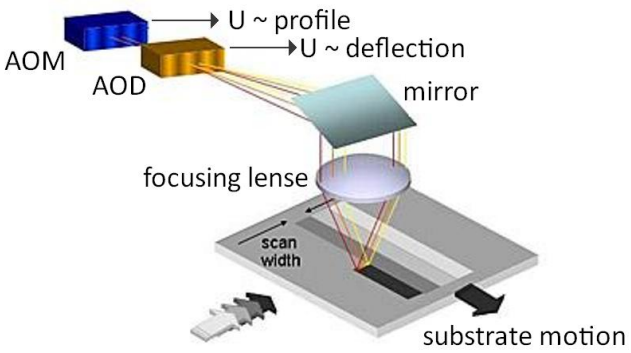

Figure 8: Working Principle of a laser writer exemplified for the DWL66 (Heidelberg Instruments). The acousto-optic modulators (AOM) and deflector (ADM) control the laser beam intensity and scan direction [HIMT 2011].

A variety of lasers can be used for laser lithography, enabling the user to expose most commercial photo resists. For example, a helium-cadmium laser can be used with a wavelength of 442 nm. Although the wavelength does not quite superimpose with the wavelength used to expose most photo resists, the small beam spot size and high energy of the laser beam enables high precision exposure of standard photo resist.

4.1.3. Electron Beam Lithography (EBL)

Electron beam lithography is the preferred technology for patterning of electron sensitive polymers on nanoscale for direct use or as mask for subsequent etching of underlying material or material deposition. Electron beam lithography is a maskless, serial writing process with very low throughput. Furthermore, electron beam writing is rather expensive (about 1000 €/h at DTU Danchip (Technical University of Denmark). The fabrication of sub-100nm structures is very sensitive to for example wearing of electron gun which complicates optimization towards high precision writing.

The setup and working principle of an electron beam writer (Figure 9) is similar to that of a scanning electron microscope (SEM) though the spot size is larger and energy of the electrons is usually lower in SEM imaging to avoid sample damage. A focused high energy electron beam (up to 100 keV) is pulsed with high frequency rate (up to 25 MHz) scanning over the surface and exposing the electron sensitive resist to electrons and thereby inducing chain scission (positive resist) or polymerization by cross-linking (negative resist). Unexposed and exposed areas, respectively, are dissolved in the following development step.

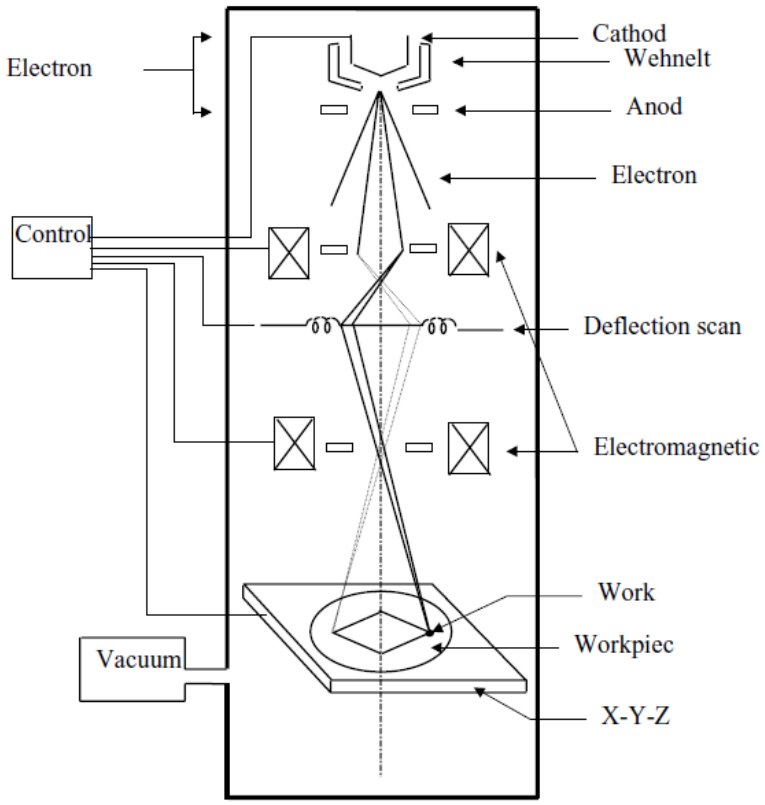

Figure 9: Sketch of the electron beam writer column [Zhou 2005].

PROXIMITY EFFECT. Electron beam lithography exhibits very high resolution which is compromised by electron scattering events which result in the so-called “proximity effect”. The proximity effect is a phenomenon caused by exposure dose distribution. It exposes areas outside the electron beam spot as well though with smaller dose. Since the contribution of each exposed spot to the final dose per spot is larger in the center than at the corner, features gradually enlarge from the corner towards the center (Figure 11). The dose distribution is caused by the interaction of the primary electrons from the beam with electrons in the resist and substrate, resulting in forward and backward scattering. Primary electrons posses high energy and penetrate deep into the substrate, up to several tens of micrometers, depending on the substrate properties (Figure 10). Forward scattering is caused by electron-electron interaction. Primary electrons knock secondary electrons out of the substrate which usually have a short range (about 10 nm) and scatter with small angle. Secondary electrons penetrate into the substrate and contribute to the exposure by scattering back into the resist. Secondary electrons contribute in a rather small extent to the proximity effect due to their short range. Backscattering originates from collision of primary electrons with substrate nuclei by coulomb interaction giving rise to large angle scattering. Thus, primary electrons are scattered back to the surface, contributing to the exposure of the resist. The area outside the beam spot is exposed (up to several tens of micrometers) though the effective dose is lower than inside the incident electron beam. The radius of the exposed area, i.e. radius of back scattering is increasing with increasing density of the substrate and nuclear charge. The proximity effect can be corrected using specialized software which calculates the dose distribution according to pattern and material characteristics. It can also be corrected applying a “poor-man approach” where auxiliary structures are added close to the corners to increase the dose locally.

The effect of forward and backward scattering can be modeled using Monte Carlo simulation. The Monte Carlo simulation calculates the theoretical dose distribution from an incident electron beam influenced by back- and forward scattering in a given substrate composition.

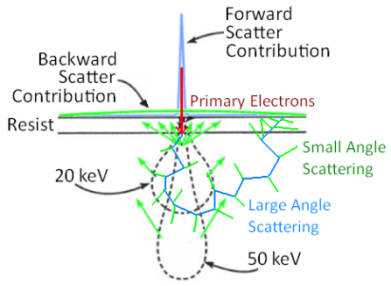

Figure 10: Sketch visualizing electron scattering and exposure dose distribution cause by scattering effects [adapted from Henderson 2011].

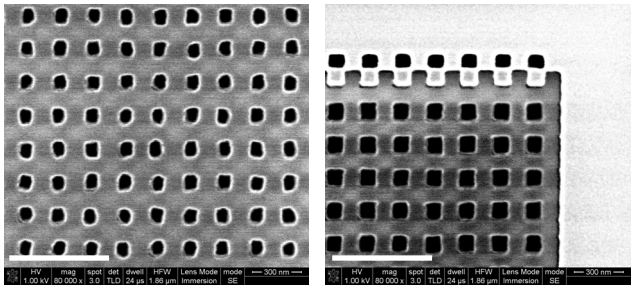

Figure 11: Scanning electron image exemplifying the proximity effect in arrays of 100 nm wide pillars: structures at the center (left) are exposed with higher dose than at the corner (right) resulting in smaller pillars. Scale bar: 600 nm.

4.1.4. Deep Reactive Ion Etching (DRIE)

Deep reactive ion etching, also known as “advanced silicon etching” (ASE) is an anisotropic dry etch process. It employs deep reactive ion etching to achieve high height-to-width aspect ratio structures with (near) vertical sidewalls in silicon. DRIE is based on the alternating nearly anisotropic silicon etching step and deposition of a chemically inert passivation layer to achieve almost vertical sidewall profiles, also called “Bosch process”.

Silicon is etched using sulfur hexafluoride (SF_6). Two electrodes create an electrical field that accelerates reactive ions ($F^- + SF_5^+$) from plasma towards the target surface. The ions react chemically with the surface (etching) and “kick out” (sputtering) some material. The etching is followed by a passivation of the sidewalls by depositing a polymer with lower etch rate than silicon, for example plasma-polymerizing a Teflon-like polymer ($[CF_2]_n$) from octafluorocyclobutane (C_4F_8). Although this passivation layer protects the whole surface from further etching, the passivation does allow for etching in the vertical direction. The polymerized C_4F_8 is etched as well in hexafluoride plasma (like silicon) but with a lower etch rate. Similar to silicon, the etch rate is fastest in the absolute vertical direction while exhibiting the lowest etch rate in absolute horizontal direction. Thereby, sidewalls are protected while the bottom is etched further down. Also true vertical sidewalls (α = 90°) can be achieved, but often the walls are slightly tapered, e.g. 88° or 92° ("retrograde"). Dependent on the duration of etch and passivation step, the etching undercuts the silicon creating scalloped or undulated sidewalls (Figure 12, no. 8; Figure 13) [WIKI 2011-RIE, WIKI 2011-DRIE].

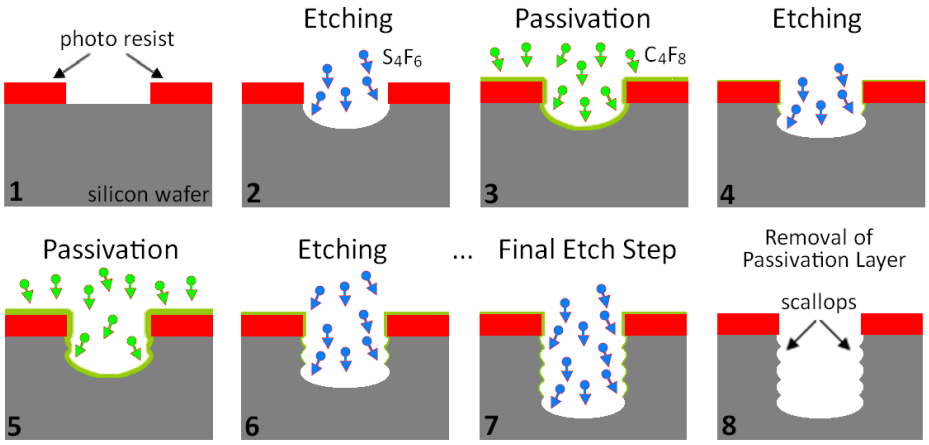

Figure 12: Schema of Bosch process etching silicon anisotropic showing scalloping created by alternating etch and passivation steps [adapted from WIKI 2011-DRIE and Maluf 2004].

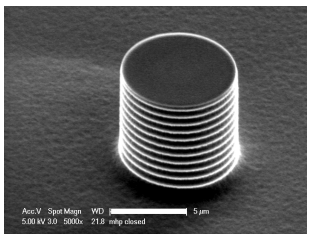

Figure 13: SEM image of a silicon pillar fabricated by deep reactive-ion etching (Bosch process) [WIKI 2011-DRIE]. Scale bar: 5 µm.

4.1.5. Galvanic Plating

Galvanic plating, also known as electroplating or electroforming is a replication process that transfers patterns from a so-called “master” into an inverted metallic copy by electrodeposition of metal on a conductive surface. In electrodeposition metal ions, e.g. nickel or copper ions in solution are deposited on a target material, the master, by an applied electrical field. Various materials can be used as master substrate, like polymer or compatible metals, but often structures in photo resist are used as masters. Such masters can be fabricated by patterning resist by means of UV or electron beam lithography, or e.g. from etched silicon or milled metallic substrates. A commercial galvanic process is employed in the fabrication of a metal mold for injection molding of CDs or DVD. A DVD or CD is replicated from a master that is written into photoresist from a bitmap image by laser lithography. CDs or DVDs contain structures on the nanometer scale, 830 nm and 400 nm minimum pitch length, respectively.

Electrodeposition requires a galvanic bath containing dissolved metal ions (electrolyte) and an electrical current formed between two electrodes (anode and cathode) immersed in the galvanic bath. A schematic drawing of a nickel-electroplating cell is shown in Figure 14. A potential is applied between the master cathode and the metal to be plated (anode) resulting in a direct current from anode to cathode. The applied potential oxidizes the anode, dissolving metal cations. The metal cations are flowing according to the electrical field from anode to cathode. They are reduced at the interface between solution and cathode and deposited onto the cathode (master surface). The deposition rate is equally to the rate at which the anode is dissolved. The final thickness can be controlled to a high degree of precision through timing and current density. Only conductive areas of the cathode surface result in a deposition of metal. To achieve uniform metal growth, an overall electrical conductive surface is required. In some cases a patterned conductive surfaces can be favorable to reduce stress in the electroplated replica [Winter 2009]. Since the master is usually made of insulating materials (e.g. polymer) a thin metal layer of a few hundred nanometers is sputtered onto the structured surface.

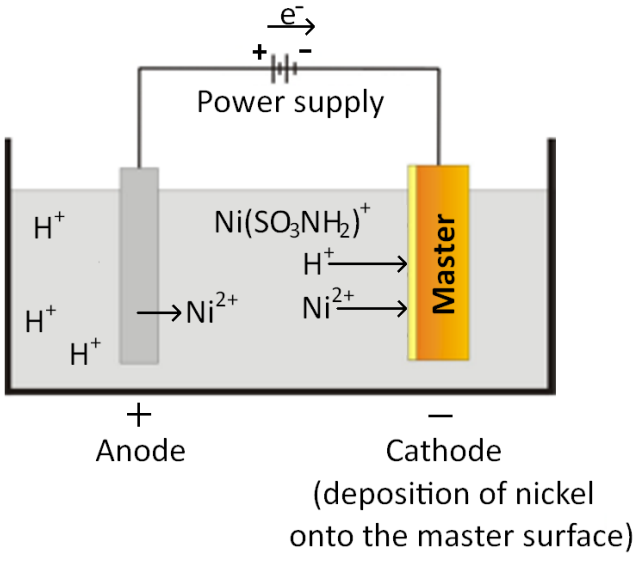

Figure 14: Scheme of the electroplating of nickel. Nickel ions are dissolved from the anode and deposited onto the master surface by applying a potential [adapted from UT 2011].

In principle, the master can be replicated into metal only by employing sputtering. However, sputtering is a fairly slow process compared to galvanization. The deposition rates for sputtering and electroforming is some Ångströms per second (≈ 10 Å s^{-1}) and several hundreds of Ångströms per second (≈ 800 *Å* s^{-1}), respectively. The minimum as well as maximum resolution of electroplated features is limited by the sputter process (adequate conductivity required for electroplating) and therefore dependent on the feature size, pitch and aspect ratio.

INTERNAL STRESS. The sputtering but especially the electroplating process can create/build up stress inside the metal causing deformation of the metallic replica. The stress can be reduced by carefully optimizing electroplating parameters like current density, pH, and temperature. An appropriate choice of electrolyte composition is also important (described below). Furthermore, commercial stress reducer, e.g. JB-100 from Techniques, can be added to reduce stress. Internal stress, varying chemical compositions or differing grain structures in sputtered and electroplated metal can cause delamination of the sputtered layer from the electroplated bulk. The sputtered seed layer is unimportant for the replication of microstructures, possibly wanted, but essential for nanostructures, since they are mostly formed by the sputtered material. Due to the small grain size of the material it is possible to replicate structures down to sub-50nm.

ELECTROLYTE COMPOSITION. The material properties such as tensile modulus and tensile strength of the nickel replica are strongly dependent on the process parameters and the electrolyte composition. For example nickel electroplated from Watts solution containing nickel sulphate, nickel chloride and boric acid results in a tensile strength of 345 – 485 MPa with internal stress of 125 – 185 MPa. The lowest stress (0 – 55 MPa) and highest tensile strength are produced by nickel sulphamate solutions consisting of nickel sulphamate, nickel chloride and boric acid [Kopeliovich 2011].

MOTHER AND SONS. It is possible to invert the first nickel replica, called “father” to create an inverted replica, called “mother”, with the same topography as the original master by a second galvanization process. In order to be able to separate father and mother replica after galvanization, the father is immersed in an electro-chemical passivation bath to form a non-reactive film on the surface of the mold. Additional replicas can be made from the mother, called “sons”.

SEPARATION OF MASTER FROM METAL REPLICA. After electroplating, master and replica need to be separated and cut to fit into the molding setup, i.e. injection mold cavity or hot embossing setup. In case of employing photo resist as master, the master and inverted metal replica can be easily separated. The metal replica is subsequently cleaned in e.g. acetone and ready for use. In some cases separation of master and metal replica can be quite an issue as will be discussed in Section 2-3.

4.1.6. Injection Molding

Injection molding is a commercial process for mass-fabrication of structured polymer parts. Commonly, heat and pressure are applied to fill a structured cavity with thermoplastic or thermosetting polymer. An injection molder is composed of three parts: injection unit, mold and clamping unit (Figure 15). The injection unit consist of the hopper to feed the raw polymer granulate, the barrel with heaters, and the reciprocating screw to melt and homogenize granulate into low viscose polymer melt and transport it to the nozzle. The nozzle forms the entrance to the mold cavity. The mold assembly contains the mold cavity presenting a surface relief, heating and cooling

system of the mold, and ejector pins necessary to eject cooled, solidified parts. The third part, the clamping, enables closing and opening of the mold assembly and movement of ejector pins.

An injection molding process can be divided into four steps:

(1) Melting of raw polymer
(2) Injection of polymer melt into the mold
(3) Cooling (and packing)
(4) Ejection of molded part

In the first phase (melting), polymer pellets are fed through the hopper into the barrel where they are melted and homogenized by the application of heat (heaters) and shear (reciprocating screw). The low viscose polymer melt is transported to the nozzle and injected into the mold cavity by the reciprocating screw until a specified injection pressure is achieved (injection). Under optimal conditions the mold cavity should be filled completely. However, too low injection velocity at too low mold temperature can cause so called “short shots” which results in only partial filling. Subsequently, the filled mold is cooled until the polymer is sufficiently solidified (cooling). During cooling, pressure (holding/back/after pressure) is applied to “pack” even more polymer material into the cavity to compensate for shrinkage of the polymer during cooling and solidification. After solidification, the polymer part carrying the replicated relief structure is ejected aided by ejector pins (ejection). In case of thermoplastics applied heat lowers the viscosity of the polymer and makes it deformable. Upon cooling the thermoplastic solidifies and keeps the shape. Thermosetting polymers consist of pre-polymer molecules, which cross-link upon applied heat. Once they have cooled and solidified they remain the shape even upon application of heat. In contrast, thermoplastics deform again if heat is applied.

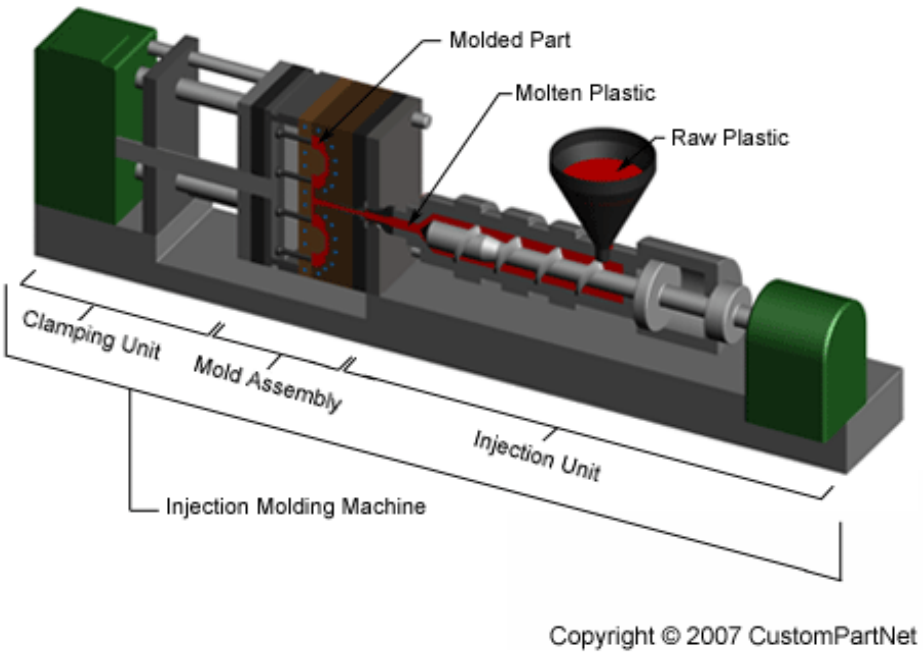

Figure 15: General layout of an injection molding machine consisting of injection unit for melting and homogenizing of the raw polymer and injection into the mold assembly which is open and closed by the clamping unit [CPN 2011].

MOLDING CONDITIONS. Injection molding is based on the principle that the polymer melt can flow into or at least deform into the mold cavities. Under optimized conditions the cooled and solidified polymer part contains the perfect inverted replica of the metal mold. Different research groups have shown that especially for micro- and nanostructures, following process parameters are important for the replication quality [Liou 2006, Theilade 2007, Mönkkönen 2002, Pranov 2006].

Important process parameters

(1) Mold temperature
(2) Melt temperature
(3) Injection velocity
(4) Injection pressure
(5) Holding pressure
(6) Ejection temperature

These six parameters influence either the viscosity of the polymer melt during the different process steps or the force applied on the polymer chains to deform into a certain shape. In principle, structures in the mold can be perfectly replicated if following requirements are full-filled: first and mainly, the viscosity should be low enough so that the melt can flow into the mold cavities. Secondly, the pressure applied can deform the polymer melt into the structures. The polymer does not need to be in a fluid-state but still deformable. Thirdly, a sufficient wetting of the mold surface is required, especially for submicron structures to allow for filling of structures.

Interfacial flow and cooling at the melt/mold interface occurs both within few nanoseconds [Pranov 2006, Biancardo 2008]. Based on their model a nanometer thick skin layer of polymer bulk at 270 °C brought into contact with a nickel mold at 30 °C is cooled down to 70 °C in about 10 ns and further down to 50 °C within 100 s [Biancardo 2008]. Although injection and later-on holding pressure is applied on the melt, the initial filling of structures occurs under zero pressure condition. Thereby, it is easy to understand that the mold temperature is one of the most important parameter. The mold temperature widely defines the actual melt temperature and hence the viscosity of the melt at the melt/mold interface. The viscosity of the bulk polymer needs to be low enough that a certain flow is given. An increased mold temperature can reduce the “cooling effect” once the polymer melt touches the mold surface. However, the mold temperature is not capable of “heating up” the polymer bulk, hence decreasing its viscosity. Besides, economic considerations require a compromise between high mold temperature for low melt viscosity and low mold temperature for faster cooling to reduce the cycle time. Industrial injection molding, e.g. for CD or DVD production requires fast molding cycles (< 10 s) and is done at mold temperatures well below the so-called “glass transition temperature” whereby no or minor cooling required. The glass transition temperature is s specific temperature for thermoplastics above which they start to soften. Increase of the temperature leads to a decrease in melt viscosity. However, if thermoplastics are kept at too high temperatures for too long, they start to degrade (“yellowing”), usually caused by oxidation of the polymer chains. Therefore the melt temperature in the barrel needs to be kept as low as possible to avoid degradation while maintaining the required viscosity of the melt.

INJECTION MOLDING OF NANOSTRUCTURES. The fabrication of nanostructures by injection molding requires certain conditions to be fulfilled. Firstly and mainly, as already discussed the polymer needs to be sufficient low viscous and it needs adequate time to flow into nanoscaled cavities.

In industrial injection molding of e.g. CDs or DVDs, the hot low viscose polymer melt is commonly injected onto a cold mold reducing the time spend for heating and cooling of the mold. The polymer is injected very fast and pressure applied enables the polymer to fill the nanoscaled surface structures. Molded parts can often readily be ejected. Nanostructures on e.g. CDs or DVDs have a low height-to-width aspect ratio (1:2 – 1:4) and can be filled fast enough even applying a cold mold. For larger aspect ratios, the polymer melt may not reach the bottom if mold temperatures below the glass transition temperature of the polymer are applied.

Secondly, due to the increase in surface-to-volume ratio for decreasing dimensions interfacial effects such as wettability and friction gain importance. The interfacial energy (and pressure applied) between mold and polymer needs to favor filling (low surface energy) as well as demolding (high surface energy) which supports either way. Inability of the polymer melt to fill nanoscale cavities during injection will limit the resolution of injection molding. This may be caused by insufficient wetting of the mold surface by the polymer melt (Figure 16, left and center). Given adequate cavity filling, inability of the solidified polymer to leave the nanoscale cavity during demolding may lead to structural failure of the polymeric nanostructures (Figure 16, right).

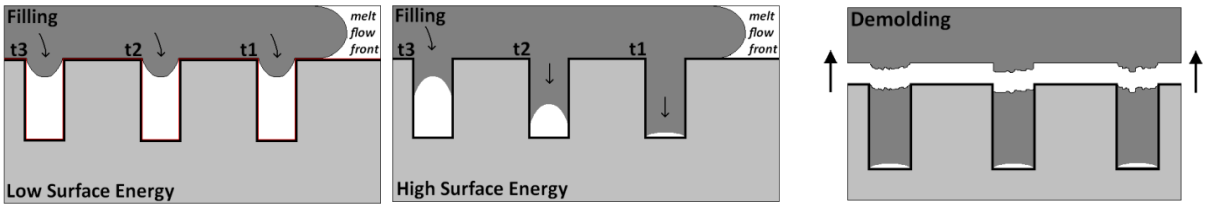

Figure 16: Filling of nanostructured cavities on mold surfaces with low (left) and high surface energy (center), and fracturing of nanostructures during demolding from molds with low surface energy (right).

Demolding exposes the molded polymer nanostructures to high frictional forces compared to their relatively low mechanical stability (tensile strength TS_{T5013} = 46 MPa [4], TS_{T8007} = 63 MPa [5]) which may lead to their break-off from the bulk of the molded polymer. Pranov et al. showed that the mold surface energy is highly important for the replication of sub-micrometer structures (lateral dimensions ≥ 100 nm) [Pranov 2006]. They described that rather the filling of nanoscaled cavities is problematic and limited by the surface energy than the final demolding step. Structures replicated with a low compression molding setup were replicated up to a depth of 350 nm (melt temperature of 320 °C, mold temperature of 60 °C, molding pressure of about zero bars) which corresponds to incomplete filling (nominal mold depth: 450 nm). The filling decreased strongly below 10 nm (same molding conditions) after application of a fluorocarbonsilane.

[4] Ultimate tensile strength: tensile stress before break (at 5 *mm min*$^{-1}$), tensile strain at break: 1.7 % (Topas Advanced Polymers)

[5] Yield Strength: Tensile stress at yield point (point in the stress-strain curve at which plastic deformation begins to occur) (50 *mm min*$^{-1}$), tensile strain at yield: 4.5 % (Topas Advanced Polymers)

The application of antistiction coatings like fluorocarbonsilanes [Schift 2007], fluorocarbons [Guo 2007] or self-assembled monolayers [Lee 2006] on the mold have been shown to improve the replication fidelity of nanoimprinted or hot-embossed features. In nanoimprint lithography and hot embossing the polymer melt is actively forced into the mold cavities by the applied pressure. In contrast, the pressure on the polymer melt at the time of its initial contact with the mold surface is very low in injection molding. This implies that filling of nanostructures may be strongly dependent on the interfacial energy of the mold and the polymer melt. Thus, a low surface energy antistiction coating could limit the filling of nanoscale cavities in the mold due to insufficient wetting of the coating by the polymer melt.

4.1.7. Bonding Techniques

Sealed microfluidic systems can be fabricated by bonding two polymeric parts carrying lid and microfluidic structures together. Different techniques, like thermal bonding, laser welding (laser transmission bonding), or ultrasonic bonding can be employed to bond two thermoplastic parts.

In thermal bonding two thermoplastic parts are bonded together by applying heat and pressure simultaneously. Polymer parts are placed between two hot plates and pressed together. The applied heat increases the mobility of polymer molecules, while pressure forces polymer chains at the interface to move and interact with molecules of the opposite surface. Upon cooling, the mobility of the polymer molecules is reduced again and forming stable mechanical bond between the two parts (Figure 17, left). The bonding temperature is kept below the glass transition temperature of the polymer to avoid extensive softening and polymer flow. Thermal bonding is a compromise between softening and deformation of the structured parts and the necessity to have sufficient mobility of the polymer chains.

Oxygen plasma treatment is often used to improve the bonding strength of thermal or laser bonds while simultaneously achieving appropriate biocompatibility. The plasma pre-treatment decays polymer chains at the surface and thereby locally lowers the glass transition temperature and increases the hydrophilicity. Smaller molecule chains result in lower viscosity and thereby increased movement of the molecules at the bond interface forming stronger bonds (at lower bonding temperatures). However, extensive treatment (”over treatment”) with low pressure oxygen plasma (< 1.0 mbar) can lead to the formation of low molecular weight oxidized COC which can result in a weaker bond interface [Nikolova 2004].

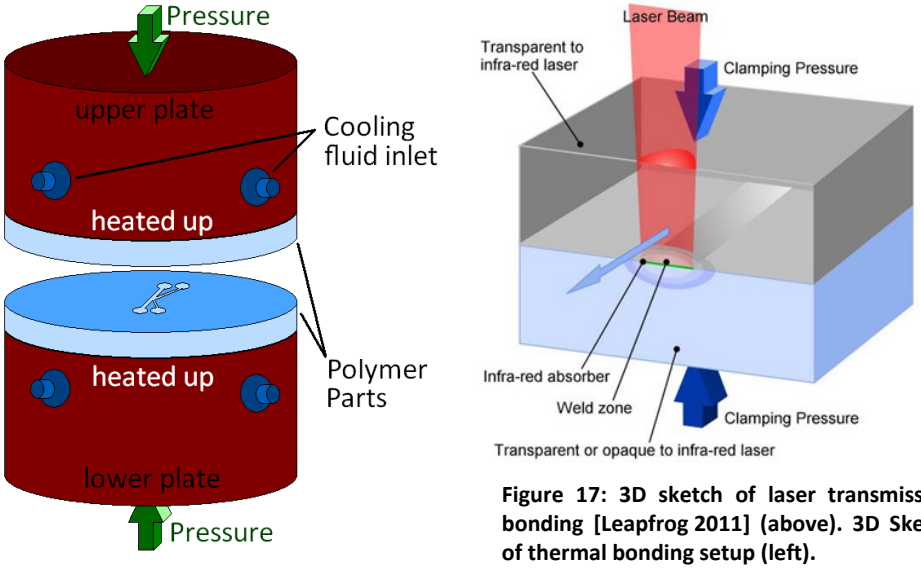

Figure 17: 3D sketch of laser transmission bonding [Leapfrog 2011] (above). 3D Sketch of thermal bonding setup (left).

Besides, two thermoplastics can be bonded by are laser welding or ultrasonic bonding. Both techniques are basically based on the same principle. Laser welding employs infrared light absorbed in the vicinity of a special absorption layer, e.g. carbon black or ClearWeld^{TM}, to locally heat the thermoplastic. Infrared light is not absorbed by common thermoplastics like PMMA, PC, or COC. Ultrasonic bonding uses high frequency low amplitude vibration to create heat by means of friction between the two polymer parts.

The major problem in thermal bonding is the over-all softening of the polymer parts. Micro- and nanostructures can easily deform. Bending of channel lid or bottom and the deformation of single features can reach an inacceptable degree, e.g. clogging of microfluidic channels, collapse of nanopillars. The advantage of laser welding and ultrasonic bonding is clearly that the heating can be induced locally targeting mating interfaces. By optimizing process parameters, cavities between the two parts can be kept undamaged.

BONDING OF CELL HANDLING SYSTEMS. Microfluidic systems used for cell experiments require compatibility of the bonding technique with cell culturing prerequisites, e.g. biocompatibility. Furthermore, cell culture materials should retain their original surface chemistry to allow for comparison between different experimental setups. Thermal bonding is one of the cleanest, simplest and cheapest bonding techniques. Thermal bonding does not change the surface chemistry nor leaves any kind of hazardous residuals or requires additional layers. In contrast, laser welding requires an additional absorption layer (e.g. Clearweld^{TM} or carbon black) and more expensive equipment (transmission laser). Ultrasonic bonding is equally well suited as thermal bonding. Although adhesives or solvents also can be used to stably bond two polymer parts, solvents can diffuse into the cell culture medium inside the microfluidic channels and cause alteration in the cell physiology.

4.2. Characterization Techniques

4.2.1. Scanning Electron Microscopy

In scanning electron microscopy, a focused beam of high-energy electrons is used to examine a surface. When the electron beam hits the sample surface, interaction of the incident electrons with the sample generate free electrons, e.g. secondary electrons and back scatter electrons, as well as photon signals (cathodoluminescence) (Figure 18). The various signals reveal information about the surface topography, chemical composition, crystalline structure, electrical conductivity and other properties.

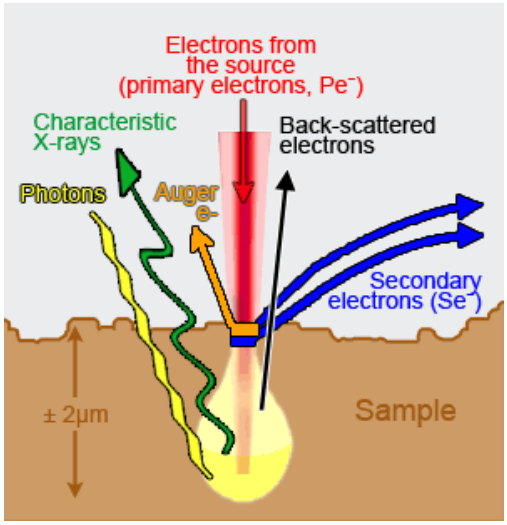

Figure 18: Types of electron and photon signals produced by the primary electron beam [VCB 2011].

A scanning electron microscope consists mainly of an electron gun, condenser lenses, deflectors and several detectors each specific for a certain emitted signal. A high energy electron beam (0.5 to 40 keV) is emitted from an electron gun (cold field, thermionic or thermal field emitter), accelerated by an anode and focused by a set of electromagnets (condenser lenses) to a spot of about 0.4 to 5 nm in diameter. An aperture placed after the lenses is usually used to exclude peripheral electrons and decrease the final spot size of the electron beam. Finally, pairs of scanning coils or deflector plates are used to deflect the beam in x- and y-direction over the sample, scanning the surface line by line. Dedicated detectors collect specific signals (e.g. secondary and backscatter electrons by Everhart Thornley detector) and generate a 2-dimensional image of the sample surface. The large field depth of the scanning electron microscope allows focusing of rather large areas (half field width: 1 µm up to 1 cm). The electromagnetic lenses facilitate very precise control of the degree of magnification (10 – 500.000fold) with a spatial resolution of about 10 nm [Ardenne 1937, WIKI 2011-SEM, GEA 2011-SEM].

Primary electrons from the incident electron beam can be collected and build up negative charge at the surface if the sample is insulating. These charging effects heavily disturb proper imaging and can finally lead to a degradation of sensitive samples, like polymer (e.g. resists, COC) or biological samples (e.g. dried cells). Therefore such insulating materials are commonly sputter-coated with a thin conductive layer, like 5-10 nm gold (or titanium) which reduces charging effects.

ASTIGMATISM. Astigmatism is one of the major problems in scanning electron imaging and refers to the geometry of the electron beam. The beam exhibits an elliptical shape with different foci in x- and y-direction whereby images appear stretched. The astigmatism can cause periodical oriented features to look different from the actual shape, i.e. ordered lines instead of pillars (Figure 19). Tilted images can even appear very realistic in a wrong pattern, e.g. riffled lines instead of pillars (Figure 20).

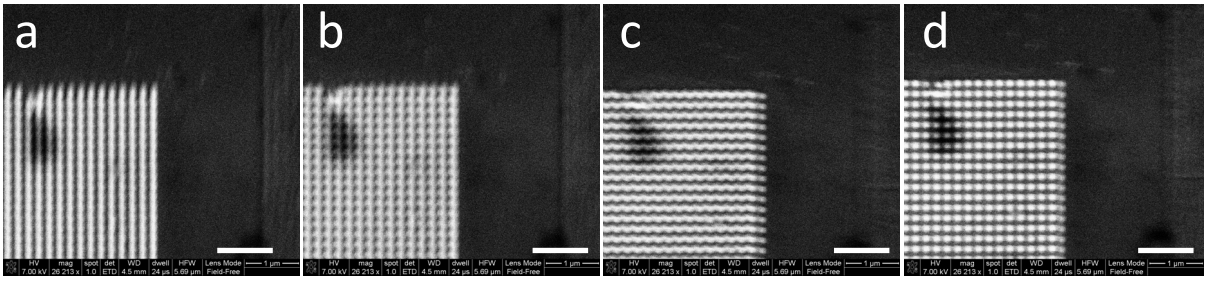

Figure 19: SEM images of 100 nm wide and high pillars in nickel with uncorrected (a-c) and corrected astigmatism (d). Scale bar: 1 µm.

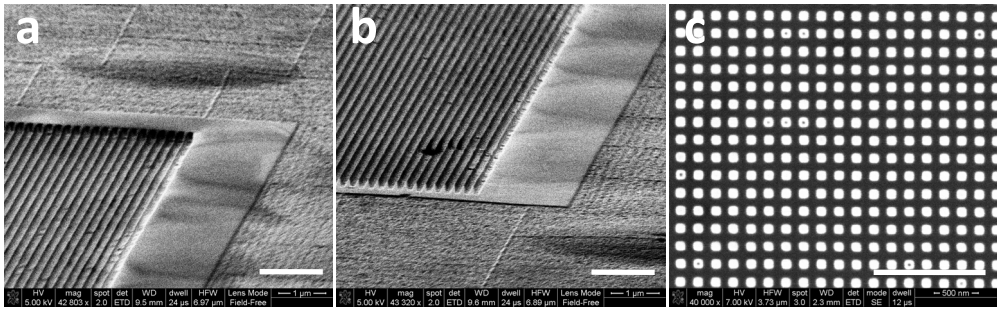

Figure 20: SEM images of 100 nm wide and 200 nm high pillars in nickel with uncorrected (a and b, 25° tilted) and corrected astigmatism (c, 0° tilted). Scale bar: 1 µm.

4.2.2. Atomic Force Microscopy

Atomic force imaging is based on the interaction of the cantilever with repulsive and attractive forces exerted by the substrate. A cantilever scans a sample surface and reacts to the substrates' topology. As the cantilever tip approaches the surface attractive forces (van der Waals forces) between tip and surface causes the cantilever to bend towards the surface. Further approach of the cantilever increasingly repulsive forces (coulomb interactions) deflect the tip away from the surface. A laser beam is used to detect the vertical movement. The laser is reflected from the backside of the cantilever onto a position sensitive photodiode. Any deflection of the cantilever results in a change of the reflection angle and is recognized by a shift of the position of the reflected beam on the photodiode. The topographical image is calculated based on a feedback loop that keeps the height of the tip above the surface constant, thereby maintaining a constant laser position. Two parameters are important for the standard user to optimize the image quality, set point and (Z servo) gain. The set point determines the distance between AFM tip and sample surface. The gain controls how fast the tip reacts towards changes in the topography.

RESOLUTION LIMITATIONS. Although AFM can be used to measure materials on atomic scale the resolution, especially in the vertical direction, is very dependent on the tip shape. The resulting image will always be a product of the forces exerted on the cantilever and its tip convolution, e.g. rounded or squared features for conical or pyramidal tip (Figure 21), respectively. Real slopes of the sidewalls, especially for features with large height-to-width aspect ratios are difficult to determine without proper knowledge of the actual tip shape.

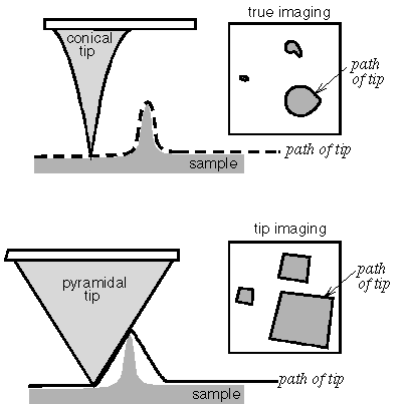

Figure 21: Sketch of the resulting image for different tip shapes [Howland 2011].

The tip shape does not only cause problems in exact rendering of the surface topography (artefacts) but also limits the vertical resolution. In case of high aspect ratio nanostructures, especially for holes a very sharp tip is necessary to image the surface topology properly. Various factors are likely to contribute in the effective resolution of an AFM tip (Figure 22):

(1) Insufficient tip properties (too large tip radius of curvature and half cone angle),
(2) Contamination of the sample surface increase the tip radius of curvature during scanning
(3) Suboptimal imaging parameters, like too low set point (hard contact of the tip on the sample) and too high gain (strong oscillation of the tip), can damage the tip and lead to an increase in the radius of curvature of the tip.

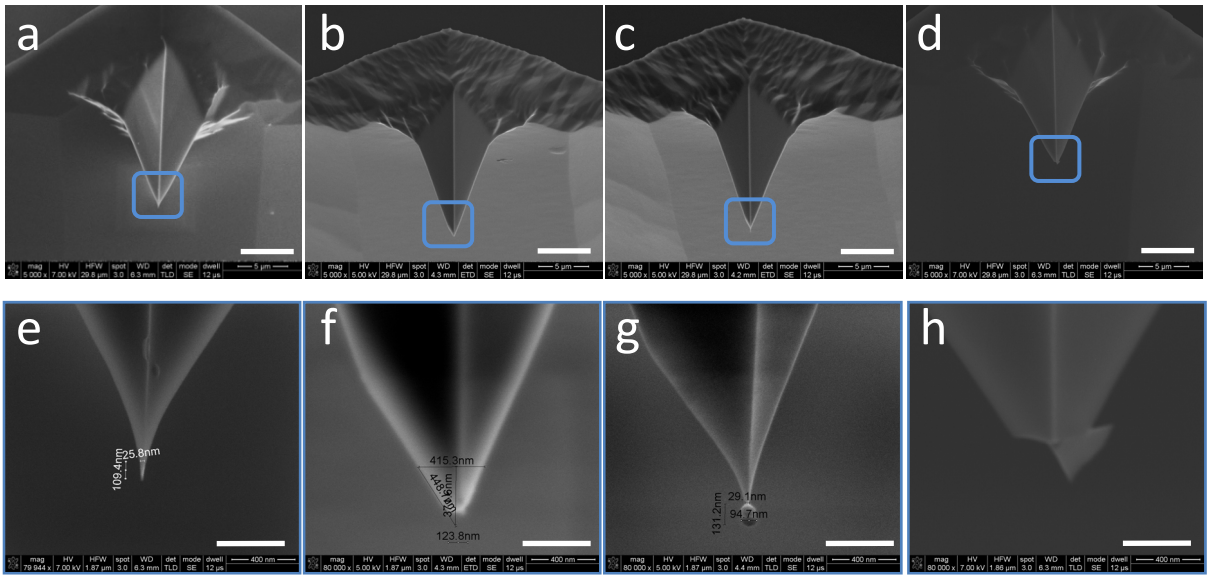

Figure 22: Super sharp tips used for AFM measurements (new (a, e), degraded (b, f), contaminated (c, g), and fractured (d, h)). Scale bars: 5 µm (a-d), 400 nm (e-h).

4.2.3. Ball Shear Test

A ball shear tests applies lateral shear force to features until mechanical failure (fracture) occurs. The sample is placed and vacuum is applied to fix the sample on the table. The load tool, a sharp resilient knife is positioned close to the test feature (here: Topas drop). After positioning, the knife is automatically lowered to the surface and a lateral shear force is applied onto the drop until mechanical failure (fracture or detachment) occurs or maximum load is achieved (Figure 23). The lateral position of the knife related to the applied pressure is monitored

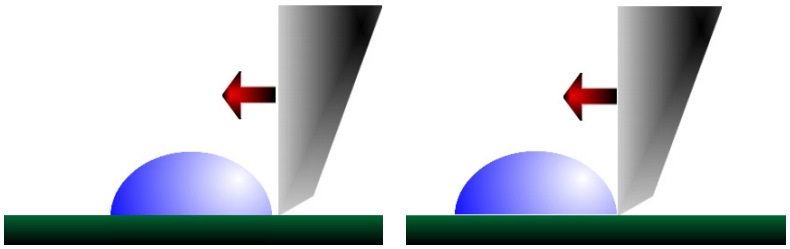

Figure 23: Sketch of the ball shear test applying lateral shear force to determine the bonding strength. Under optimal conditions the drop detaches fully, leaving no residuals on the surface.

The ball shear test was originally developed to measure the bonding strength of soldered ball point wire bonds and is therefore not perfectly applicable for measuring the adhesion strength of solidified Topas drops. Unfortunately, various problems can lead to rather unreliable results: Fracture of polymer drop instead of detachment (Figure 24a) or rolling (Figure 24b). Furthermore, the absolute area of the drop adhering to the nickel surface plays a major role. To minimize at least errors arising from deviant areas, the lateral force was normalized to the area, resulting in a pressure.

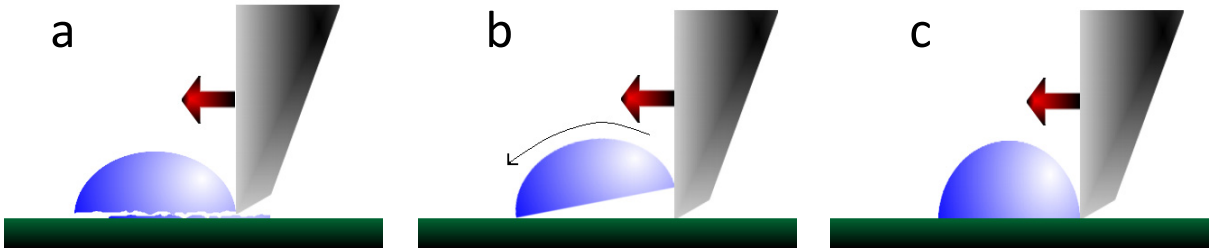

Figure 24: Sketches of different possibilities to remove a polymer drop from a solid surface leading to false results: fracture (a), and rolling of the drop (b), or deformation (c).

4.2.4. Contact Angle Measurements

Contact Angle Measurements are useful tools to study physical properties of the interaction between solid (i.e. nickel shim) and liquid phase (i.e. water, hexadecane, and Topas), like wettability, affinity, adhesiveness and repellency (Figure 25). The goniometer, device for measuring contact angles, usually consists of an optical system to captures the profile of a drop of liquid on a solid substrate computer-assisted, and software that calculates the contact angle based on different approaches. The contact angle θ can take values between 0° and 180°. A contact angle between 0° and 90° indicates that the liquid spreads well on the surface (good wetting) while a contact angle between 90° and 180° displays a poor wetting (Figure 25 a). In the former case adhesive forces between liquid

and surface molecules over-rule the cohesive forces inside the liquid. However, 0° and 180° are impossible to achieve. A contact angle of 0° implies that the liquid spreads out to a monolayer and 180° implies that the liquid does not touch the surface at all. [Attension 2011, Ramehart 2011].

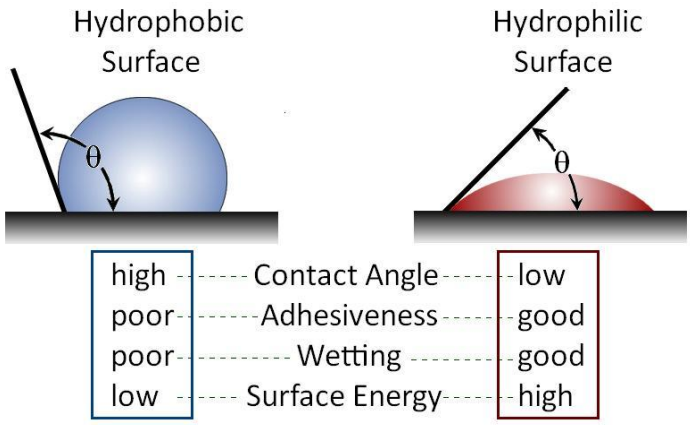

Figure 25: Static contact angle of a water drop on hydrophobic (low surface energy) and hydrophilic (high surface energy) surface [adapted from Ramehart 2011].

4.2.5. X-ray photoelectron Spectroscopy (XPS)

X-ray photoelectron spectroscopy allows for qualitative and quantitative analysis of elemental composition and electronic state of a given material. Electron emission spectra resulting from irradiation with X-rays are recorded.

The sample is irradiated with low energy X-rays (≈ 1.5 keV) which can penetrate about 2 µm into the sample depending on the density of the sample. Single electrons are excited by the photon energy (excitation energy $h \cdot \nu$). These electrons leave the sample with a given kinetic energy which equals the excitation energy reduced by the specific binding energy of the electron. This effect is called photoemission. However, only electrons from the first 1 – 10 nm escape without scattering, hence maintain their full kinetic energy which gives XPS its surface sensitivity. Scattered electrons contribute to the background signal leading to tails in between actual signals for each binding energy. The kinetic energy and number of electrons that escape from the sample are detected and analyzed (Figure 26). Electrons have a specific binding energy that is unique for each chemical element. The elemental composition can be mapped by assigning binding energy of emitted electrons to their specific elements. A table of elements and their specific binding energies is given by the National Institute of Standards and Technology [NIST 2011]. The concentration of elemental composition can be measured with accuracy of about 0.5 at.%. The lateral resolution reaches down to a few micrometers depending on the beam spot size [Zemlyanov 2007].

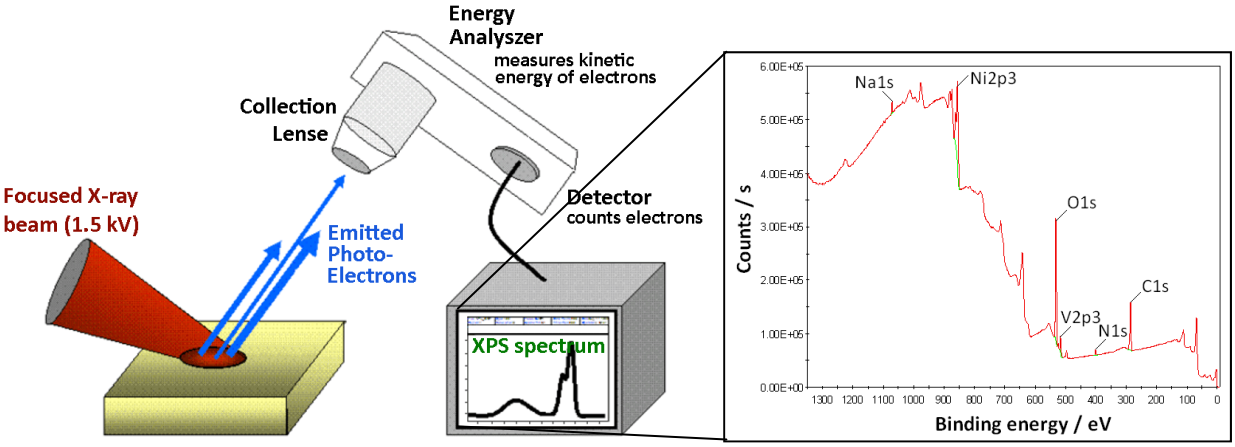

Figure 26: Basic components of a monochromatic XPS system (left) [adapted from WIKI 2011-XPS] and XPS spectrum for native nickel mold surface (right).

4.3. Materials

4.3.1. Polymers of Choice: Topas 8007S-04 and 5013L-10

Topas is a cyclic olefin copolymer (COC) from Topas Advanced Polymers. COCs possess superior material properties which make them suitable for fabrication of lab-on-chip applications for cell handling [Nunes 2010, Larsen 2008]. Possible applications in commercial CD and DVD production were investigated [Khanarian 2001].

SYNTHESIS. COCs can be synthesized either by ring-opening methasis polymerization or chain polymerization. In this thesis, cyclic olefin copolymers purchase from Topas Advanced Material, i.e. Topas 5013L-10 and Topas 8007S-04, were used and its possible application in mass-fabrication of nanostructures for cell handling systems was investigated. Topas is a random copolymer synthesized by chain polymerization of norbornene and ethylene. Ethen and cyclopentadiene react to form 2-norborne (cyclic olefin). The chain polymerization of cyclic olefin with ethylene is catalyzed by metallocenes resulting in a cyclic olefin copolymer (Figure 27). The norbornene content in COC determines its stiffness and glass transition temperature (T_g). The higher the norbornene content in the chain, the higher the stiffness and T_g (70 - 180°C).

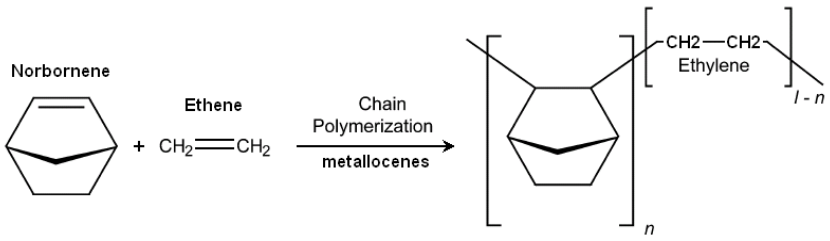

Figure 27: Chemical structure of Topas® COC [adapted from Khanarian 2001 and Shin 2005].

PROPERTIES. COCs posses excellent physical (optical, mechanical, electrical, thermal) and chemical resistance, which are superior to most other commonly used polymers like poly(methylmethacrylate) (PMMA), polycarbonate (PC) or polystyrene (PS). COCs ultra-low moisture absorption (< 0.01 %) coupled with excellent flow properties (1.5 - 48 ml/10 min at 2.16 kg and 260°C) and dimensional stability (low shrinkage, high stiffness (tensile strength = 66 N mm^{-2} and elastic modulus = 2.6 - 3.2 kN mm^{-2})) enable high precision molding of micro- and nanostructures by e.g. hot embossing or injection molding. Its excellent chemical resistance towards water-soluble chemicals, acids, alkalis, and polar solvents combined with its high thermal stability makes COC compatible with various sterilization processes. Furthermore, COC displays a high water-vapor barrier (0.02 – 0.04 g mm m^{-2} day) and low oxygen permeability (100 - 300 cm^3 mm m^{-2} d^{-1} bar^{-1}), making it well suitable for cell handling systems. Detailed descriptions of the properties of COCs were described by different research group [Nunes 2010, Khanarian 2001, Shin 2005]. Nunes et al. gives a summary of properties and applications of COPs for lab-on-chip devices. Properties relevant for injection molding of nano- and microstructures are listed in Table 2.

Table 2: List of relevant physical properties of different Topas grades for injection molding [Topas Advanced Polymers]

Property	unit	8007	5013	6017	6015	6013
Glass transition temperature	°C	78	134	178	158	138
Heat deflection temperature	°C	75	130	170	150	130
Melt flow index (2.16 kg, 260 °C)	ml 10^{-1} min^{-1}	32	48	1.5	4	14
Melt flow index (MVI) (2.16 kg, HDT + 115 °C)	ml 10^{-1} min^{-1}	2	24	5	5	6
Tensile strength (5 mm min^{-1})	MPa	63 [6]	46 [7]	58	60	63
Elongation at break (5 mm min^{-1})	%	4.5	1.7	2.4	2.5	2.7
Tensile modulus (1 mm min^{-1})	GPa	2.6	3.2	3.0	3.0	2.9
Coefficient of linear thermal expansion	K^{-1}	$7 \cdot 10^{-5}$	$6 \cdot 10^{-5}$	$6 \cdot 10^{-5}$	$6 \cdot 10^{-5}$	$6 \cdot 10^{-5}$
Mold shrinkage	%	0.4 - 0.7	0.4 - 0.7	0.4 - 0.7	0.4 - 0.7	0.4 - 0.7
Water absorption (24h in water at 23°C)	%	< 0.01	< 0.01	< 0.01	< 0.01	< 0.01
Water permeability (85 % humidity at 23°C)	g mm m^{-2} d^{-1}	0.023	0.030	0.045	0.035	0.035
Oxygen permeability (50 % humidity at 23°C)	cm^3 mm m^{-2} d^{-1} bar^{-1}	0.0023	0.0030	0.0045	0.0035	0.0035

EXPERIMENTALLY DETERMINED PROPERTIES. Glass transition temperature and thermal degradation are important properties in injection molding. They were therefore experimentally determined. The actual glass transition temperature was measured by differential scanning calorimetry. The actual glass transition temperature was found to differ minimal from the values stated by the manufacturer. Topas 8007 and 5013 have a glass transition temperature of 83 and 137 °C, respectively. Degradation of most polymers occurs at elevated temperatures as required for injection molding. Especially in the setup used for this project cycles times of 5 - 10 min are common. The degradation of polymer was measured by means of thermogravimetric analysis. No degradation was observed for temperatures of up to 300 °C in oxygen-free atmosphere. All measurements were conducted by José Manuel Román Marín (Danish Polymer Center, Technical University of Denmark).

[6] Yield Strength: Tensile stress at yield point (point in the stress-strain curve at which plastic deformation begins to occur) (50 *mm* min^{-1}), tensile strain at yield: 4.5 % (Topas Advanced Polymers)

[7] Ultimate tensile strength: tensile stress before break (at 5 *mm* min^{-1}), tensile strain at break: 1.7 % (Topas Advanced Polymers)

4.3.2. Antistiction Coatings for Injection Molding

4.3.2.1. Fluoroform (CHF_3)

Fluoroform is a fluorinated carbohydrate that can be plasma-polymerized on a substrate such as nickel from a gas phase creating an antistiction coating. Radicals of CHF_3 monomers are created by a reactive ion etching and form random oriented multilayers on the exposed surfaces with a CF_2-termination. The orientation of the fluorocarbon polymer is not controllable. Due to CF_2 termination and co-deposition of contaminants from the gas phase, contact angles of water are commonly lower than achievable for molecular vapor deposited anti-adhesive coatings based on Perfluorodecyltrichlorosilane (FDTS).

DEPOSITION AND REMOVAL. Fluorocarbon based antistiction coatings is plasma-polymerized from radicals formed from monomers in gas phase by a reactive ion etcher Plasmatherm 740 RIE system (Unaxis, St. Petersburg, FL). CHF_3 is deposited with a rate of about 10 nm min^{-1} (Figure 28) and can be etched in oxygen plasma with a rate of 5 – 10 nm s^{-1} (90W, 100 mTorr, 25 sccm) depending on the power, pressure and gas flow. Thermal and mechanical stability of the deposited CHF_3 during injection molding was investigated.

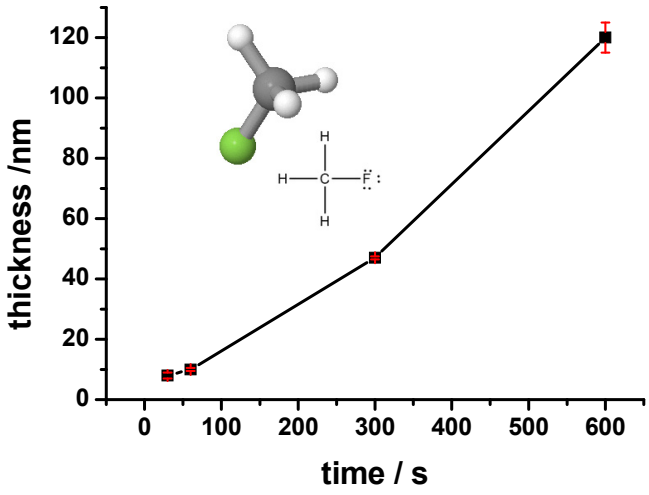

Figure 28: Deposition of plasma-polymerized fluorocarbon polymer. Insert: Chemical structure of fluoroform.

4.3.2.2. Perfluorodecyltrichlorosilane (FDTS)

Perfluorodecyltrichlorosilane (CAS Number: 78560-44-8) is a fluorocarbonsilane with 17 fluorine atoms. Self-assembled monolayers can be formed using molecular vapor deposition. Surfaces containing hydroxyl groups like silicon oxide, titanium oxide, or nickel oxide can be silanized. FDTS achieves a contact angle of water to silicon of about 110°.

HYDROLYTIC DEPOSITION OF SILANES. Silane molecules such as FDTS are hydrolyzed under presence of water forming reactive hydroxyl groups by eliminating hydrogen chloride. Hydrolyzed silane molecules diffuse and adsorb to the nickel surface containing hydroxyl groups and form loose hydrogen bonds. At elevated temperature hydroxyl groups condensate forming covalent bonds between hydroxyl groups of either different silane molecules or silane and nickel surface by eliminating water. Subsequent silane molecules align with already bonded molecules, forming covalent bonds with the surface and with other silane molecules (Figure 29, left). The presence of a reductant, like vanadium in nickel might decrease the amount of available hydroxyl groups at the surface and thereby reduce the load of covalent bound silane. As stated by Gelest Inc., a manufacturer for silanes, silanes couple less good to silicon and especially nickel surfaces than they do for silica (Figure 29, right).

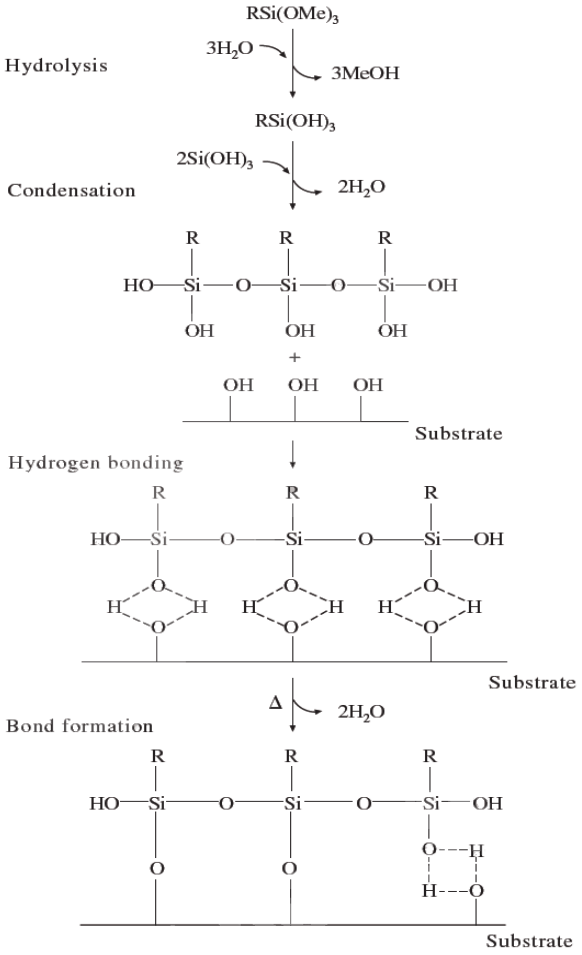

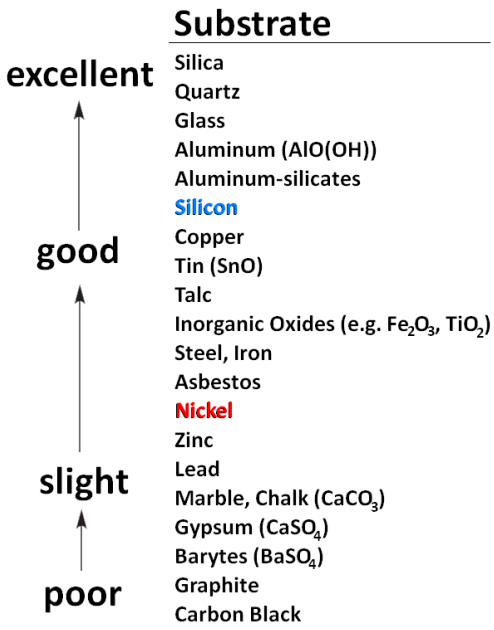

Figure 29: Hydrolytic deposition of silanes on silicon (left). Silane effectiveness on Inorganic substrates (right). Nickel has a lower reactivity towards silanes than silicon [Gelest 2011].

MECHANICAL STABILITY. Experiments were conducted by different research groups employing ultra-thin Teflon-like antistiction films on nickel stamps for hot embossing and low compression molding. Their results suggest low adhesion strength of the antistiction coatings to the nickel mold [Jaszewski 1999, Pranov 2006]. Jaszewski et al. showed that the fluorine content on the nickel stamp surface decreased with each embossing cycle at embossing temperature of 205°C. Transfer of fluorine atoms to the polymer replica was proven. Pranov et. al states that the silane layer delaminated completely during the first compression molding cycle and is therefore usable for injection molding.

THERMAL STABILITY. Devaprakasam et al. report that the molecular order of self-assembled monolayers of FDTS undergoes several states. The molecular order increases for temperatures up to 152 °C leading to higher contact angles of water on FDTS coated surfaces. For further increase in temperature the molecular order ceases whereby the order can be re-established by reversal thermal treatment. The disorder increases at temperatures above 302 °C and becomes irreversible at about 327 °C [Devaprakasam 2004]. These results suggest that the self-assembled monolayers of FDTS are thermally stable to survive temperatures applied during injection molding. It even indicates that annealing of deposited FDTS at temperatures of about 150 °C improves layer uniformity and possibly mechanical stability.

DEPOSITION AND REMOVAL. FDTS is deposited by forming self-assembled monolayers using a molecular vapor deposition system (MVD 100 System, Applied Microstructures Incorporation). The process chamber is cleaned and conditioned using another standard recipe *dual layer* COLDPREP (duration: 15 minutes). Subsequently, FDTS is deposited on nickel and silicon substrates using the standard recipe *multilayer* STAMP (duration: 1:15 hours). Process parameters are given in the appendix 3-1., Table 29. FDTS can only be removed from a nickel surface by oxygen plasma to a limited extent, because not all fluorine atoms are likely to be removed. Besides, Ni-O-Si bonds cannot be broken by oxygen plasma thus silicon is remaining on the surface.

4.3.2.3. Perfluordecanethiol (PFDT)

Perfluordecanethiol (CAS Number: 34143-74-3) is a perfluorianated thiol presenting the 17 fluorine atoms, like FDTS. PFDT immersed in absolute ethanol spontaneously adsorb on gold surfaces forming a self-assembled monolayer.

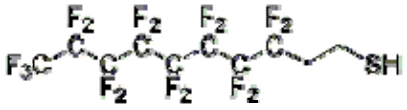

Figure 30: Chemical Structure of Perfluordecanethiol (PFDT).

DEPOSITION AND REMOVAL. Gold covered nickel samples were coated according to a protocol adapted from Grampel et al. Samples were immersed in thiol solution containing 1 - 100 mM PFDT diluted in ethanol for at least three hours. Subsequently, samples were rinsed three times in absolute ethanol and blow dried with nitrogen [Grampel 2002]. Thiols can be removed from gold surface applying various methods: Plasma cleaning [Kang 1998, Raiber 2005], thermal desorption [Tate 2000], UV photooxidation [Hutt 1996], piranha solution [Guo 1994], ammonium hydroxid solution [Kim 2008].

Chapter 2

Fabrication of Polymeric Microfluidic System

The fabrication of a polymeric device containing micro- (microfluidics) and nanostructures (functionalized areas) can be done in different ways either by combining both structure dimensions on one part while using a flat lid (Figure 31, left) or by separate fabrication of microstructures on one part and nanostructures on another (Figure 31, right).

It might be possible and for commercial purpose desirable to fabricate nano- and microstructures combined in one injection molding cycle. In this way, alignment would not play any role since the structured microfluidic system could be sealed with a flat lid. Different reasons account for developing nano- and microstructures independently, especially during system development phase. Firstly, separate fabrication maintains certain flexibility in respect to exchange of microfluidics or nanostructures independently. Secondly, the fabrication of the nanostructures is more expensive and time-consuming compared to the fabrication of microstructures. Thirdly, the microfluidic structures are probably exchanged frequently in order to modify flow properties to study cell properties like adhesion or release behavior. Finally, separated fabrication of nanostructures promotes accessibility and thereby facilitates a possible local functionalization of nanostructured patterns, e.g. by modification with biomolecules or plasma-polymerization. For optimization purpose it is in any case reasonable to fabricate both parts separately (Figure 31, right).

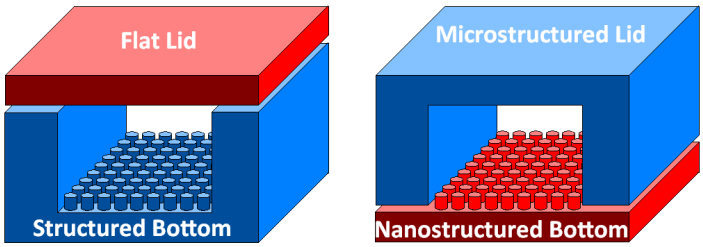

Figure 31: 3D sketch of the molded part containing microfluidic and nanostructures by combined (left) and separated fabrication (right) of both structure types.

Fluidic connection can be integrated during polymer processing by using a mold with respective cavities. A custom made luer steel mold containing twelve female luer fittings was used for injection molding of microstructures aiming at simple fluidic connection of the assembled polymer chip. Nanostructures were fabricated using a custom made “flat” steel mold matching the dimensions of the “luer” mold (Figure 32).

1. Design: Microfluidic System

For initial cell experiments including cell adhesion and cell viability a simple microfluidics system was developed. The design consisted of one main channel and one side channel to clean and fill the bonded chip with cell culture medium and inject suspended cells, respectively. The main channel holds nanostructured patterns (Figure 32). In this way all patterns can be tested under close to equal conditions (cell viability, system temperature, medium properties). Detailed description of the setup for investigating cells on nanostructures will be given in chapter 5.

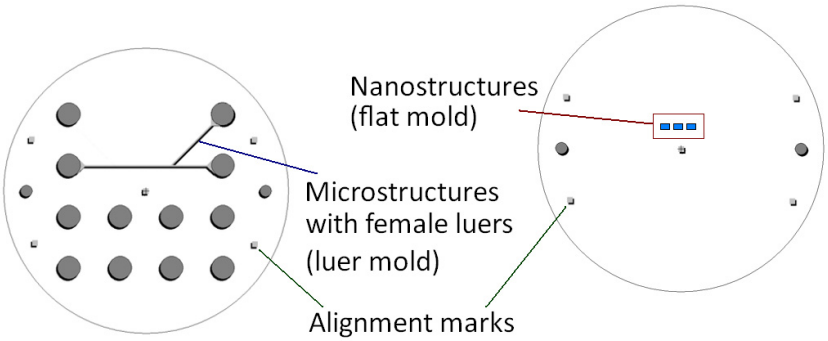

Figure 32: 2D sketch of polymer parts containing microfluidic (left) and nanostructures (right) separately. Microstructures are molded from the luer steel mold additionally containing cavities for female luer connectors and nanostructures are molded from the flat mold. Alignment marks help to align micro- and nanostructures for thermal bonding.

2. Experimentals

2.1. Fabrication of Microstructured Topographies

Injection molding of microstructures was performed from nickel molds replicated from microstructured masters. Two different fabrication schemes were tested. Either photoresist was patterned on a silicon wafer by UV lithography directly followed by electroplating of nickel, or photoresist was used as etch mask to introduce microstructures into the silicon wafer. Subsequently, a nickel replica was formed by electroplating using the etched silicon wafer. After separation from the master and cutting into the right dimension, the nickel shim was used as insert for injection molding. Samples were investigated using a Nova 600 NanoSEM (FEI company) in low vacuum mode which enables imaging of polymer samples by introducing water vapor to reduce charging effects.

Figure 33: Cross-sectional sketch of the fabrication scheme used to fabricate master based on structured resist on silicon (upper left) and structured silicon (upper right). Separation and cutting of the resulting nickel shim follows the same scheme (left).

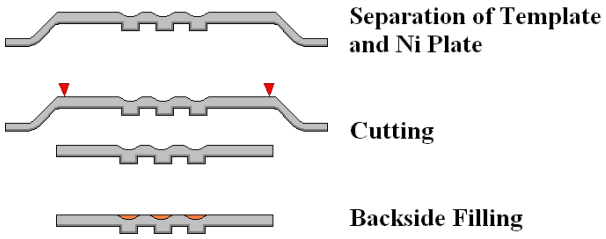

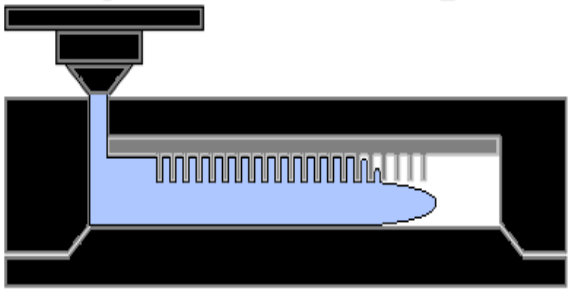

Figure 34: Sketch of polymer replication by injection molding. The nickel shim is fixed into the holder located in the (stationary) steel mold. The temperature of the mold (stationary and movable part including nickel shim is heated up and polymer melt is injected until the cavity is filled. The mold is cooled down and the solidified polymer part containing the inverted surface relief of the nickel shim is ejected.

2.1.1. UV Lithography of SU-8

SU-8 is a negative photo resist exhibiting and allows fabrication of high aspect ratio structures with near vertical sidewalls. Film thickness of 0.5 – 200 µm can be achieved in a single coating. SU-8 consists of eight reactive epoxy groups per molecule (Figure 35) which cross-link upon excitation with UV light to a chemically and thermally stable image (T_g > 200 °C). The high degree of cross-linking makes SU-8 especially suitable for permanent applications. The fabrication of microstructures in SU-8 is a widely used and well-established cleanroom process. It requires little optimization on process steps like baking, exposing and developing. A wide range of parameter sets can be applied while maintaining an adequate accuracy.

PROCESSING. The layer thickness of SU-8 determines the final depth of structures in COC since SU-8 is directly used for electroplating. Spinning curves of SU-8 2075 from MicroChem were obtained for different spin speeds and spin durations using a CEE 100 spinner/hot plate (Brewer Science Inc.). Commonly a layer thickness of about 50 µm was applied to fabricate 200 µm wide and 50 µm deep channel structures in polymer. SU-8 2075 was poured directly from the bottle onto clean silicon wafers or nickel inserts. Wafers were spun at 5000 – 6000 rpm for 30 s with an initial acceleration of 500 rpm/s. Subsequently, samples were pre-baked at 90 °C for 5 min. SU-8 was exposed through a structured photo mask for 50 – 70 s aiming at 190 - 270 mJ/cm2 using a MA4 mask aligner (Karl Süss MicroTec). Exposed samples were post-baked at 90°C for about 5 min. Subsequently they were immersed in developer mr-Dev600 from Micro Resist Technology GmbH for 4 - 6 min, rinsed with isopropanol and blow dried with nitrogen. Hard-baking is usually applied to reduce stress and thereby cracking, and harden the cross-linked SU-8. Samples were hard-baked at 163°C for 10 min.

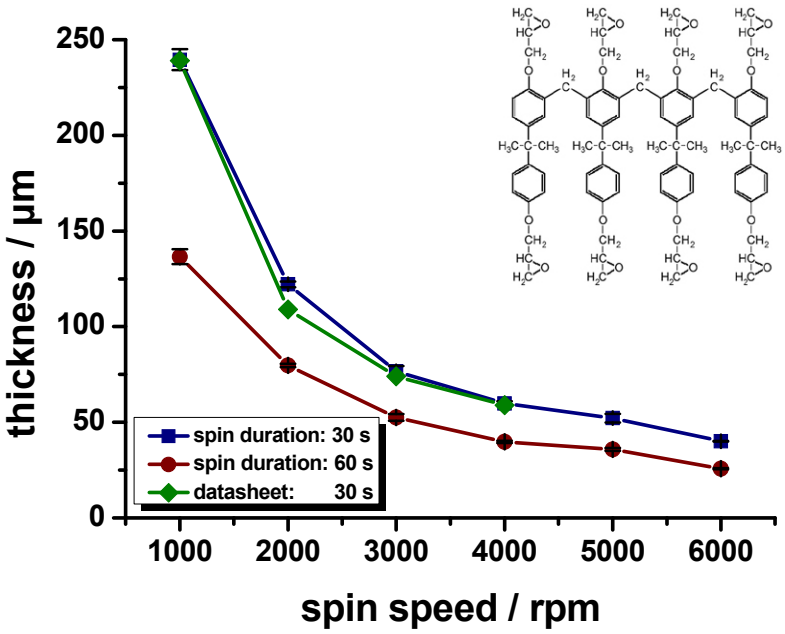

Figure 35: Spinning curve for spin durations of SU-8 2075; Insert: chemical structure of SU-8 [LaBianca 1995].

2.1.2. Anisotropic Etching of Silicon

Silicon wafers were etched employing the Bosch process by using an Advanced Silicon Etcher (STS MESC Multiplex IC). Microstructures of 200 µm width were etched to varying depth into silicon by a standard recipe *shallolr* available at Danchip with an etch rate of about 122 – 128 nm s^{-1} for the specific microstructure design (Figure 32). Detailed specifications of the etch recipes can be found in the Appendix I-3. Etching of silicon is done by sulfur hexafluoride (S_4F_6) for 6.5 s with 260 sccm S_4F_6 and 26 sccm O_2 with coil power of 2800 W and platen power of 16 W. Passivation of sidewalls is achieved by depositing octafluorocyclobutane (C_4F_8) for 5 s with 120 sccm C_4F_8 with coil power of 1000 W and platen power of 0 W.

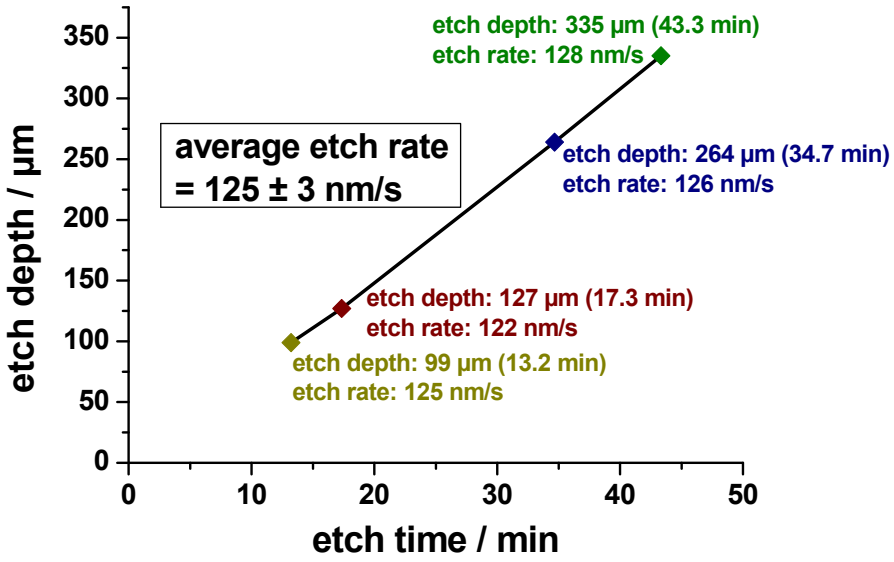

Figure 36: Specific etch rate of silicon for the described design of 200 µm wide channel (one main and one side channel) (Figure 32).

The anisotropic etching of microstructures into silicon was done based on structured resist. Silicon wafers were cleaned in hydrofluoric acid for 1 min, rinsed in water and spin dried. Subsequently, wafers were coated with standard photoresist, AZ5214E, using a standard recipe, *PR_1_5,* available at DTU Danchip. Wafers were automatically spun using SSI system 150 track (Semiconductor Systems Inc.) at 4500 rpm for about 90 s at 115 °C to achieve a uniform film thickness of 1.5 µm. The resist was exposed by UV light (λ = 365 nm) for 11 s through a photo mask in vacuum contact using the mask aligner MA6 (Karl Süss MicroTec). The exposed resist was developed in AZ351B for 60 s, washed in ultrapure water and spin dried.

On some samples, silicon oxide was deposited and etched to reduce sidewall roughness. Silicon oxide was deposited in the anneal-oxide (C2) furnace (Tempress Systems) for 3 h at 1100 °C using a standard recipe *wet1100C* available at Danchip with a deposition rate of about 200 nm h^{-1}. Subsequently silicon oxide was removed by hydrofluoric acid for 15 min, followed by rinsing in water, and spin drying.

2.1.3. Galvanic Plating

Mold inserts were fabricated as a replica relief by galvanic plating of nickel on a silicon wafer based master structure. All nickel mold inserts were produced by DVD Norden A/S, which commercial injection molds DVDs and CDs.

The master, i.e. structured resist or structured silicon wafer, was sputter-coated with 50 – 100 nm nickel-vanadium alloy (7 wt% vanadium) with a rate of 5 – 10 Å s^{-1} [8] by a Mastering ODME AM-100, an automatic mask aligner for spinning, baking, and exposure of photoresist and subsequent sputtering of a conductive seed layer.

The electroplating is done in a Toolex Alpha P250 galvanic nickel bath at 50°C. According to Toolex Alpha, a manufacturer for electroplating bathes, stamps fabricated in a nickel sulfamate bath exhibiting lower stress than possible for sulphate or all-chloride galvanic bathes. A potential of 18 V and a peak-current of 50 A result in a current density of 20 – 23 A/dm^{-2} and create a deposition rate of about 830 Å s^{-1}. After approximately one hour a 275 – 300 µm thick nickel layer is achieved. The resulting nickel shim presented an inverted replica relief of the original master relief. Recipe for the sulfamate bath are described in detail in the appendix.

The nickel molds insert were cleaned from residual SU-8, silicon, or other contaminants. Finally, nickel plates containing (nano- or) microscaled patterns are cut into circular shape with radius of 85 mm and two straight cuts of varying sizes (Figure 37) to comply with the dimensions of the insert holder of the injection molder. The two straight cuts allow for precise positioning in the insert holder. The cutting was either done employing laser cutting by COVI Gravur (Herlev, Denmark) or by mechanically punching the shims using a custom made punching tool.

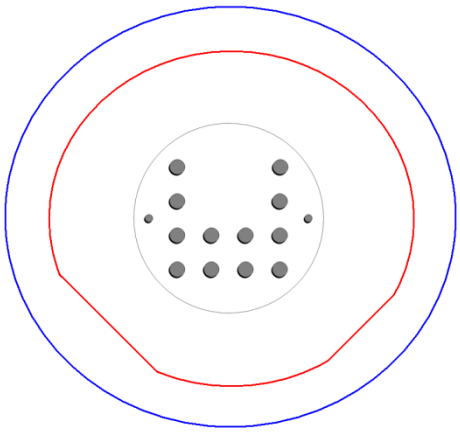

Figure 37: Sketch of the outlines original silicon based master (blue), nickel sim (red), and final polymer part (light grey) with female luer connectors and alignment holes (dark grey).

From the first nickel replica, called “father” further inverted copies can be made by subsequent galvanic plating. In order to be able to separate the *father* (1st order replica) from following nickel replicas, called “mother” (2nd order replica) or “son” (3rd order replica) the *father* (or *mother*) needs to be passivated. Electrochemical passivation is done by immersing the *father* in a special passivation bath. A negative current of 20 A at a potential of 14 V is applied, followed by 2 A at 8 volts. Recipe for the passivation bath are described in detail in the appendix.

[8] The actual sputter rate as well as thickness of the sputtered nickel-vanadium layer is unknown. DVD Norden does not measure the thickness but the reflectance of the surface to evaluate the thickness. Measurements based on delaminated nickel-vandium layers resulted in a thickness of 60 – 80 nm (measured by AFM).

There are different aspects determining the resolution limit. On the one hand, the resolution is determined by the resolution limit of the master fabrication process. It has been shown that sub100 nm structures can be replicated with high fidelity. On the other hand, the electroplating process commonly requires a homogenous conductive surface provided by the sputter coating with e.g. nickel-vanadium or gold prior to electroplating. The possibility of coating the whole surface of a structured surface determines a second aspect for limited resolution. In case of very high aspect ratios limited coating might cause problems. However, microstructures with aspect ratios of 3:1 [Song 2007], 4:1 [Heyderman 2000], 7:1 [Becker 1999], and even 21:1 [Kim 2006] have been replicated successfully by electroplating. Microstructures of about 10 – 100 µm depth with aspect ratios of up to 1:2 used in this project were replicated without problems.

FILLING OF CAVITIES ON THE MOLD BACKSIDE. Different materials were used to fill the cavities on the backside of microstructured nickel shims: *CW2400* from ITW ChemTronics, commercial *tin/lead alloy*, *Art Clay Silver 650 paste* from Art Clay World USA Inc., and *Super Spackel Elastic* from LOCTITE Technology. The conductive epoxy *CW2400* was prepared according to the manufacturer's instructions and applied using a spatula. Subsequently, sampled were cured at 60°C in a common oven for 1 h. Excess material was polished off with abrasives. The epoxy is thermally stable for operation temperatures of up to 100°C. Commercial *tin/lead alloy* was soldered at 250 – 300 °C aided by solder flux on a native and gold covered nickel shim backside. After solidification at room temperature, excess material was polished off with abrasives. The Tin/lead alloy has a melting point of about 180°C and is assumed to be stable at least up to 150 °C. *Art Clay Silver 650 paste* is a special paste used for fabrication of silver jewelry. It consists of pure silver mixed with an organic solvent and some additives. It is a low viscous paste and easy to apply using a spatula. The paste is cured by applying temperatures of 650 – 800 °C. In this temperature range, organic components evaporate and pure silver remains. Excess material was polished off with abrasives. The maximum operation temperature is unknown. But considering the melting point of pure silver (about 1000 °C), the maximum operation is assumed to lie well above temperatures applied for injection molding of COC. *Super Spackel Elastic* is metal glue designed to fill dents or holes in metals. It offers higher thermal stability than *CW2400* with operation temperature of up to 160 °C and up to 230 °C for < 10 min. It is applied by a spackel and cures at room temperature within 20 min. After curing it can be processed similar to metal, i.e. excess material was polished off by abrasives.

To probe for mechanical and thermal stability, nickel shims filled with the particular filler were after used for several injection molding cycles. A cross-sectional profile of the channel was recorded by a mechanical profilometer, Dektak 8 (Veeco Instruments Inc.). The channel bending was measured by subtracting the minimum height at the channel center from the maximum height at the sidewall.

2.1.4. Injection Molding

Microstructured surface topographies were replicated in cyclic olefin copolymer, Topas 8007S-04 and Topas 5013L-10 (TOPAS Advanced Polymers), by means of injection molding using a commercial injection molder, ENGEL CC200 Victory 80/45 with a screw diameter of 18 mm (ENGEL Austria) (Figure 38a).

After installation of the electroplated nickel mold insert, the mold consists of a disc-like cavity with a diameter of 50 mm and a thickness of 2 mm. One side is polished to mirror-like finish but also holding the mold for twelve luer connectors (movable mold) while the other holds the microstructured nickel insert (stationary part) (Figure 38b) [Andresen 2010]. The *luer* or *flat* steel molds (movable mold part) were treated with an antistiction coating by the mold manufacturer (Center Tools A/S). Most nickel inserts contain alignment marks, counterparts to alignment marks on the nanostructured nickel shim: One in the absolute center and four close to the edge, above and below the alignment holes. The alignment marks facilitate visual alignment of nano- and microstructures for bonding purpose. Nickel shims were partially coated with a fluorocarbonsilane based antistiction coating (FDTS).

Figure 38: ENGEL CC200 Victory 80/45 used in this project (a), and a close view of the mold (b). The movable mold (left part) moves towards the stationary mold (right part). The nickel shim is inserted in the dedicated holder in the stationary mold part (red circle).

Injection molding parameters were optimized for microstructures, though not extensively studied as for nanostructures to achieve a fair replica with acceptable surface finish. Final microstructures were molded using the following parameter sets (Table 3).

Table 3: Optimized process parameter used to injection mold microstructures in Topas 8007 and 5013

	Topas 8007	**Topas 5013**
Mold temperature T_{mold}	80 °C	135 °C
Melt temperature T_{melt}	250 °C	280 °C
Injection pressure P_{inject}	750 ± 25 bars	750 ± 25 bars
Injection velocity v_{inject}	100 mm s^{-1} [9] ($10\ cm^3\ s^{-1}$)	100 mm s^{-1} [9] ($10\ cm^3\ s^{-1}$)
Holding pressure P_{hold}	800 ± 25 bars for 10 s	800 ± 25 bars for 10 s
Ejection temperature T_{eject}	40 ± 3 °C	55 ± 3 °C

[9] Maximum speed at maximum width of 50 mm of the 2 mm thick circular mold.

2.2. Characterization of Mold Surface Modifications

Various techniques were simultaneously used to characterize mold surfaces of different chemistry. All surfaces were based on nickel molds presenting a 50 – 100 nm thick layer of nickel-vanadium alloy (7% wt vanadium). Firstly, the surface energy was evaluated by means of contact angle measurements of ultrapure water, hexadecane and Topas 8007 and 5013. Secondly, the adhesion strength of Topas 8007 and 5013 was qualitatively measured by employing a lateral ball shear test on solidified Topas drops. Thirdly, the chemical composition of the test surfaces was analyzed by means of X-ray photoelectron spectroscopy. All experiments were conducted on flat, structureless nickel inserts. Antistiction layers for silicon stamps to reduce friction applied on the polymer during demolding are well-established in nanoimprint lithography. Therefore silicon wafers with equal surface treatments were analyzed to verify coatings on nickel compared to silicon. All samples were treated simultaneously to assure similarity of the chemical composition.

Analyzed nickel or silicon surfaces

(1) Native nickel and silicon
    a. Native
    b. oxygen plasma cleaned
(2) CHF_3 coated nickel
    a. CHF_3 coated
    b. oxygen plasma cleaned
(3) FDTS coated nickel and silicon
    a. FDTS coated
    b. oxygen plasma cleaned

SURFACE TREATMENTS. Native nickel shims were directly used from the manufacturer (DVD Norden) without any pre-treatment. Oxygen plasma treatments were performed using a Plasma Asher model 300 Semi Auto Plasma Processor (PVA TePla) with commonly 240 Sccm oxygen and 70 Sccm nitrogen at 0.8mbar and 300W for 5 - 10 min. A temperature of about 70°C was reached during the plasma treatment. Antistiction coated nickel shims were treated with oxygen plasma prior to coating. A set of nickel shims were coated with 10 nm randomly oriented fluorocarbon polymer by plasma-polymerization of CHF_3 monomer using a Plasmatherm 740 RIE system (Unaxis, St. Petersburg, FL). On a second set of nickel shims, a monolayer perflourodecyltrichlorosilane (FDTS, CAS No. 78560-44-8) was applied by molecular vapor deposited using an MVD 100 Molecular Vapor Deposition System (Applied Micro Structures Inc.).

CONTACT ANGLE MEASUREMENTS. Contact angle measurements of water and hexadecane were used to study changes in surface energy on mold surfaces with different surface chemistry present polymer processing. Uniformity and long-term stability in terms of thermal and mechanical stability during injection molding, especially of molds with antistiction coating was characterized based on changes in the contact angle. Simultaneous contact angle measurements of Topas 8007 and 5013 on equally treated surfaces were conducted to gaining qualitative information about the behavior of Topas before and after applying an antistiction coating.

Contact angle measurements were performed on a contact angle system DCA from dataphysics consisting of an optical system that captures the profile of a liquid drop on a solid substrate, and software that calculates the contact angle. Contact angles of water, hexadecane and solidified Topas 8007 and 5013 drops were measured at room temperature.

CONTACT ANGLE OF N-HEXADECANE AND WATER. Ultra pure water (18.2MOhm cm) water and n-hexadecane (CAS nr. 544-76-3) were used to evaluate hydrophilic and oleophobic behavior of the different nickel and silicon surfaces, respectively. Hexadecane was chosen due to its olephobic character and was assumed to mimic the behavior of the Topas melt on a given surface best[10]. Contact angles were determined by the static sessile drop method. A continuous evaluation of the surface chemistry requires rather fast and simple results to follow changes caused by injection molding process. The reproducibility of the static sessile drop methods was tested and resulted in an absolute deviation of ±5°. Based on all experiments conducted, a deviation of 5° is considered to be within measurement accuracy. For each measurement, at least three drops were measured and the average of all six contact angles (both sides of a drop) was noted.

CONTACT ANGLE OF TOPAS 8007 AND 5013. Initially an automatically heated goniometer (atmosphere: air) was tested but failed to provide successful low viscosity to form usable polymer drops. The Contact Angle System DCA from Dataphysics is able to apply heat in a metal syringe and heating the table. In that way, the contact angle of thermoplastics can be measured. Unfortunately, it was not possible to produce a measurable drop of molten Topas, at least for Topas 8007. A temperature of 300°C results in too high viscosity of Topas 8007 to eject an appropriate polymer drop (Figure 39). Furthermore, Topas 8007 started oxidizing above 230°C. Therefore another setup employing a hotplate was used.

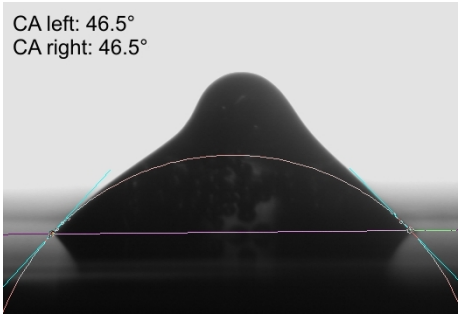

Figure 39: Photo of a molten Topas 8007 drop created by a goniometer with heated syringe and table at 300°C.

[10] Hexadecane is the hydrocarbon with the longest chain that is still liquid and therefore useful for mimicing behaviour of polymers like Topas 8007 and 5013.

Topas drops were successfully melted from granulate on common hotplate, RCT Basic from IKA WORKS. At a plate temperature of 300°C a measurable drop shape was obtained after 2 min. Nitrogen atmosphere prevented oxidation of Topas above 230°C. The substrate (glass, nickel or silicon) was left on the hotplate for about 5 minute to stabilize temperature and atmosphere. After a drop was formed the substrate was removed and left in air to cool down. The contact angle was measured on the cooled, solidified polymer drop. The melting time was experimentally determined, choosing a time span that melts the Topas granulate and forms a usable drop shape while keeping the melting period as short as possible. Thermal degradation should not occur at 300 °C based on TGA measurements (Section I-4.3.1.). To verify that the contact angle of Topas on nickel does not vary for longer melting times polymer drops were formed and measured after 1.5, 2.5 and 4 minutes. The resulting contact angles of Topas 8007 were 88.8± 1.3°, 84.4 ± 1.3°, and 90.5± 1.7°, respectively. At a melting time of 1.5 min Topas 8007 drops often exhibited a non-circular shape (Figure 40). Though the deviation is slightly above 5° it is still considered to be within measurement accuracy.

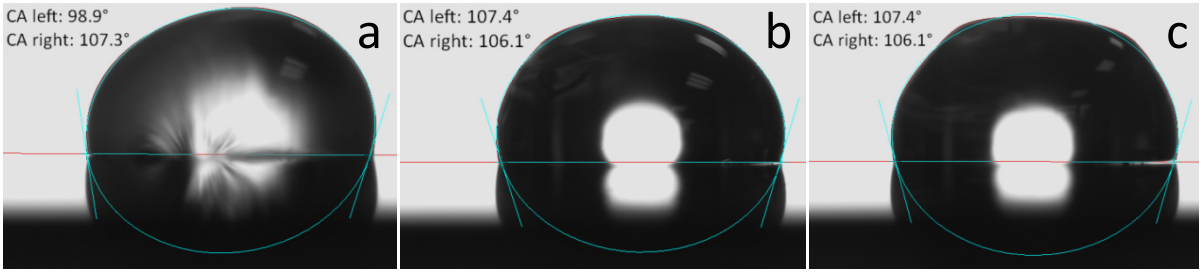

Figure 40: Contact angles of Topas8007 on a FDTS coated nickel surface at molten at suboptimal temperatures.

A melting temperature of 250°C resulted in only partial melting, even after 10 min while 300°C successfully created drops already after 2 minutes. Placing the cylindrical granulate in a laying position resulted in more homogenous contact angles (absolute deviation < 5°). Topas of both grades could not be melted in air without visible degradation (“yellowing”). A tight polycarbonate chamber was used to create an oxygen-free atmosphere by constantly flushing with nitrogen, which successfully prevented oxidation of Topas pellets. Typically, nice drop shapes were formed though Topas 5013 drops contained air bubbles (already entrapped in granulate). Even though oxidation was prevented, sometimes deformed Topas 8007 drops were generated (Figure 41 c), possibly caused by degradation of polymer. This method gives a fair estimation for the behavior of molten and solidified Topas on different nickel surface. For each material, two experiments with each three drops were measured and in each case both contact angles (left and right) were used to determine the average contact angle.

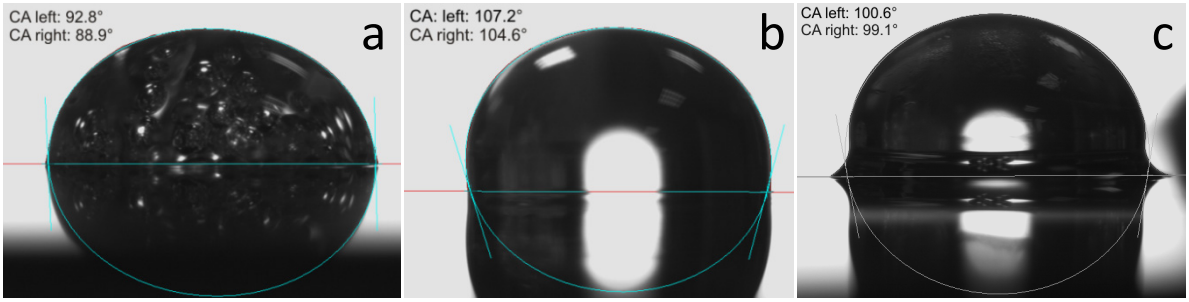

Figure 41: Contact angles of Topas 5013 (a) and 8007 (b, c) on a FDTS coated nickel surface. Partially creeping Topas8007 was observed on the edges of a "drop".

BALL SHEAR TEST. Lateral shear force experiments were conducted to investigate the adhesion force of Topas 8007 and 5013 on surfaces with varying surface energy. Samples with Topas drops were melted on nickel shims of different surface chemistry. The adhesion strength was measured by a Dage 4000 (Dage Deutschland GmbH) with a BS 5kg cartridge. Thereby, lateral forces of up to 50 N can be applied.

X-ray photoelectron spectroscopy (XPS). XPS experiments were conducted on nickel samples of different surface chemistry and on injection molded COC parts using a Thermo Fisher Scientific K Alpha (East Grinstead, U.K.). A 400 µm spot on each sample was irradiated using monochromatized aluminum Kalpha radiation, and survey (pass energy: 200 eV) and high resolution spectra (pass energy: 25 eV) of relevant elements were acquired. Flood-gun charge compensation was used for all samples. Data analyses of the XPS spectra were performed using the Avantage software package supplied by the manufacturer.

3. Master and Mold Fabrication

The fabrication process for microstructured surfaces is a well established cleanroom process and requires only small optimization. The master is structured by UV lithography through a structured photomask of either a thick layer SU-8 for direct application or a thin layer AZ5214E with subsequent anisotropic etching into silicon. The final height of the structures (in the mold) is defined by the initial resist thickness of SU-8 or the etch depth in silicon. The mold fabrication follows the same procedure as described for nanostructured nickel shims.

3.1. UV Lithography of SU-8

Very homogenous layers of SU-8 2075 were obtained by pouring directly from the bottle and applying appropriate baking times. Channel structures of 190 – 200 µm width and 40 – 50 µm depth were fabricated depending on process parameters (spin speed, spin duration, exposure dose). Although process parameters were optimized in terms of exposure dose and baking duration, the final structures showed partially re-entrant sidewalls of 1-2° (Figure 43). The resist thickness of SU-8 varied about up to 5 µm for equal process parameters. For example, SU-8 2075 spun at 5000 rpm resulted in a thickness of 49 ± 2 µm (Figure 44). Furthermore, the SU-8 exhibited a second “undercut” at the SU-8/silicon interface (Figure 46b).

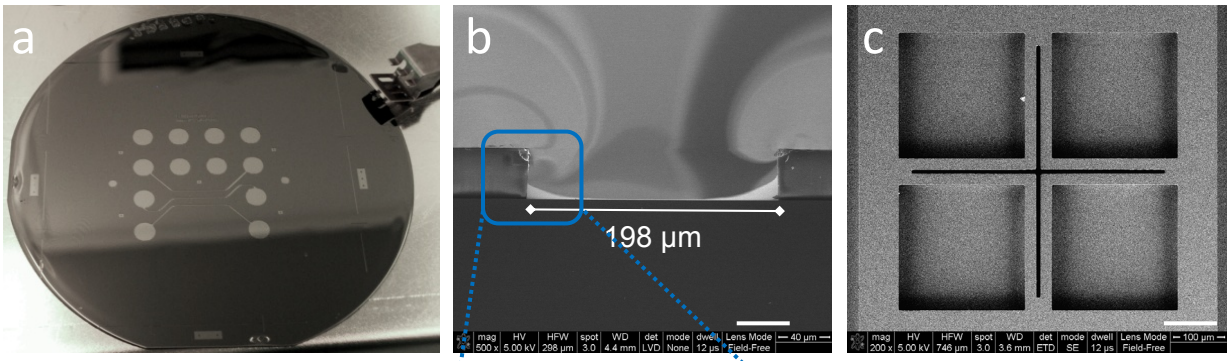

Figure 42: Microstructures exposed in SU-8. Photo of patterned SU-8 on a 4” silicon wafer (a) and SEM images of the cross-section of a channel (b) and top view of an alignment mark (c). Scale bars: 40 mm (b) and 100 mm (c).

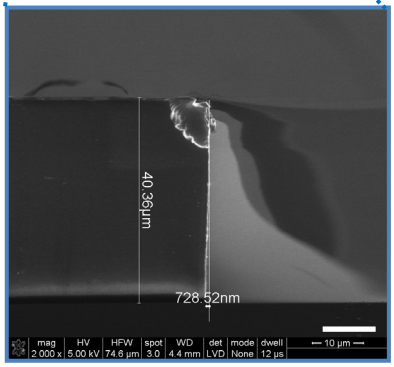

Figure 43: SEM images of the channel cross-section (Figure 42 b) showing re-entrant sidewall profile of 1 – 2 °C. Scale bar: 10 µm.

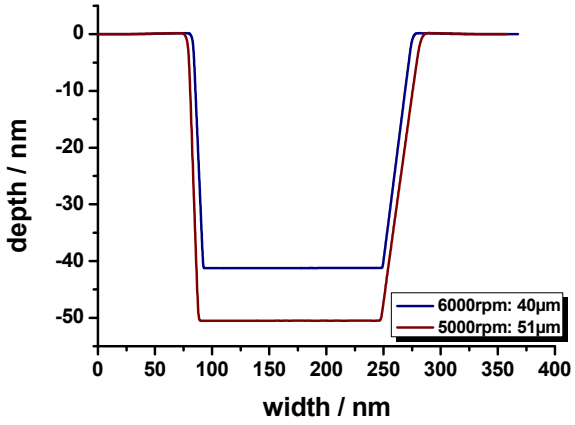

Figure 44: Cross-sectional profile of about 200 µm wide and 40 - 50 µm deep channel structures. SU-8 thickness varies up to 5 µm for similar spinning parameters. The width shown in the graph is smaller than the actual width due to the 5 µm stylus used to measure the channel[11].

ELECTROPLATING. Microstructures written into SU-8 were replicated into nickel with high fidelity (Figure 46). Cross-sectional profiles taken by a mechanical profilometer and SEM images showed good reproducibility. Even the "small undercut" at the SU-8/silicon interface (Figure 46b) was replicated well resulting in a nickel replica with a "rim" on the top of the microstructures (Figure 46d). Microstructured cavities were visible on the backside of the nickel shim complying with protruding structures on the front side (Figure 45). The filling of these cavities will be described later.

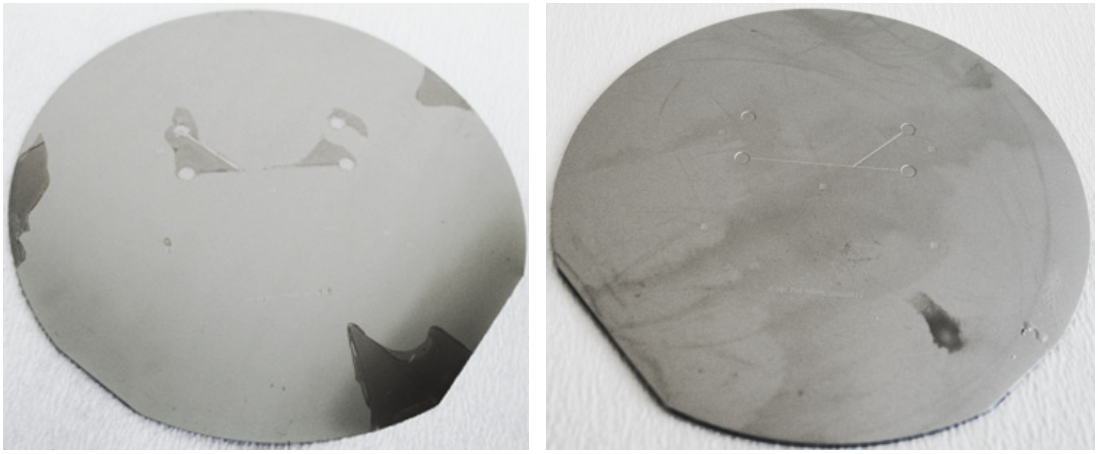

Figure 45: Photos of front (left) and backside (right) of a nickel shim replicated from a SU-8 based master. SU-8 remains partially on the nickel surface, especially in vicinity of microstructures (dark areas on the left image).

[11] Cross-sectional profiles were recorded using a Dektak 8 from Veeco Instruments Inc.

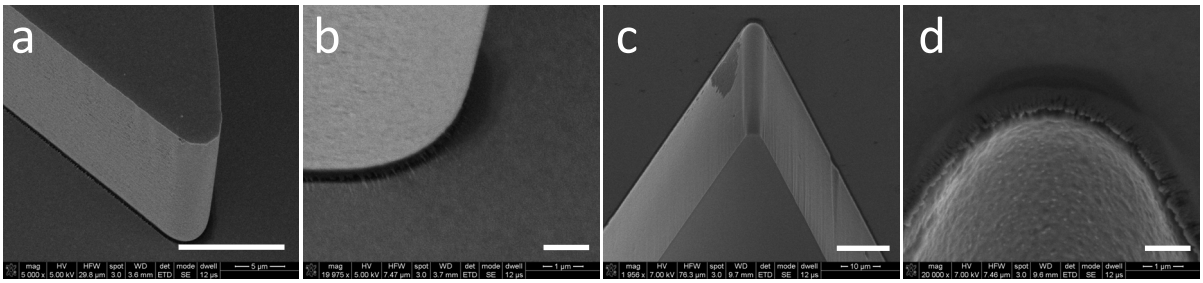

Figure 46: SEM of 25° tilted microstructures in SU-8 (a, b) and the nickel replica thereof (c, d). The high magnification SEM images (b, and d) show that the "small undercut" at the SU-8/silicon interface was replicated with high fidelity. Scale bar: 10 µm (a, c), 1 µm (b, d).

SU-8 and nickel exhibit approximately the same surface roughness as observed by SEM. Master and nickel mold were commonly extremely difficult to separate. SU-8 adheres very strong to the nickel shim and commonly delaminates rather from the silicon substrate. The adhesion strength of SU-8 to nickel can be even strong enough to break a silicon wafer in plane (not along the crystal line) (Figure 47). The microstructures formed in SU-8 (not etched into silicon) were visible inside the silicon wafer, on both parts. Even shapes of alignment marks were visible although not in detail. This was possibly caused by stress applied on silicon during SU-8 processing or electroplating. The same phenomenon was observed for further nickel plates though not as precisely. Different methods were tested to either reduce adhesion of SU-8 to nickel by applying antistiction or sacrificial layers, or to remove SU-8 from the nickel surface.

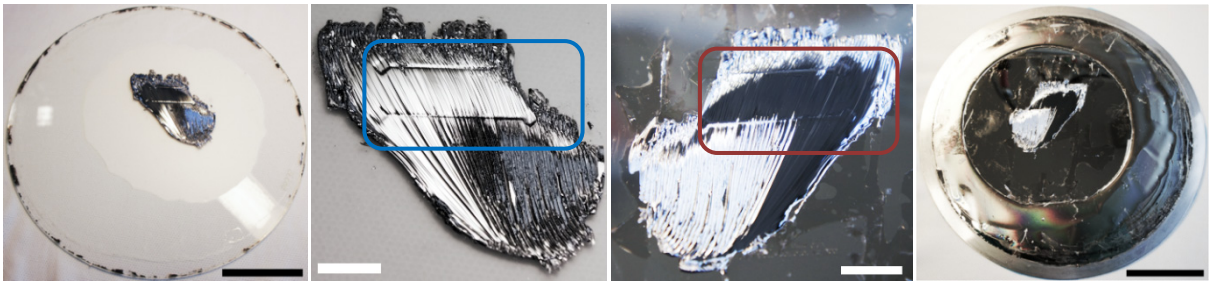

Figure 47: Photos of separated glass carrier and nickel plate after electroplating. Full view of glass (a) and nickel plate (d), and close view of silicon halves on the glass (b) and nickel plate (c). Microstructures were visible inside the silicon wafer, recessed on the part adhering to the glass (blue square) and elevated on the part adhering to the nickel (red square). Scale bars: about 10 mm (white) and about 40 mm (black).

REMOVAL OF SU-8. Cross-linked SU-8 is difficult to remove compared to photoresists like S1805 or AZ5214E which are dissolvable in solvents of intermediate polarity such as acetone. According to Hong et al., SU-8 can be etched with a rate of 1.5 – 2.0 µm min^{-1} by application of a mixture of oxygen and plasma sulfur hexafluoride plasma (60 Sccm O_2, 4 Sccm SF_6). The development is done by ferric chloride solution ($FeCl_3$) [Hong 2004]. A test using these chemicals to remove SU-8 from the nickel shim produced a white film comparable to simple oxygen plasma treatment of SU-8. Subsequent development of exposed SU-8 (white film) with $FeCl_3$ solution etched not only the treated SU-8 but most importantly it corroded the nickel surface visibly. Impressively, Hong et al. used nickel as mask material but no corrosion of nickel was mentioned.

Another approach employed common Magic™ Tape from Scotch® Brand (3M) to remove SU-8. The tape was applied on top of the SU-8 and nickel and carefully removed. SU-8 remained partially on the tape, but also on the nickel shim. After few applications the major amount of SU-8 was removed though small parts remained on the nickel surface, especially attached to the microstructures. The major advantage of Magic™ Tape towards common tape is that no residuals of adhesives are left on the nickel surface.

Other research groups have been shown that cross-linked SU-8 can be removed from a nickel surface after electroplating [Kim 2008, Shim 2010]. In both cases, SU-8 was structured on nickel substrates and used as mask for electroplating directly on nickel. However, their major problem was the actual low adhesion of SU-8 on nickel and not the removal caused by high adhesion. After electroplating, SU-8 was removed from the nickel substrate applying commercial remover such as Remover PG from MicroChem. Own experiments conducted to remove SU-8 from electroplated nickel did not result in complete removal. Following experiments concentrated on reducing the adhesion of SU-8 to nickel (or vice versa) by applying an antistiction coating or by introducing a sacrificial layer such as gold prior to electroplating. For example, gold can be easily etched without damaging the nickel surface and thereby enable separation.

FLUOROCARBON BASED ANTISTICTION LAYERS. Two types of fluorocarbon based antistiction were employed, 10 nm of plasma-polymerized CHF_3 and a monolayer of molecular vapor deposited FDTS. The CHF3 did not show any significant improvement towards uncoated masters. No difference in adhesion strength was observed seen during separation of master and nickel plate though removal of SU-8 by manual application of Magic™ Tape appeared to be improved. FDTS facilitated the separation between master and nickel replica significantly. The amount of SU-8 was substantially reduced though small amounts remained in the vicinity of microstructures such as labels, alignment marks, or channel bifurcations. However, residuals of SU-8 were completely removed by applying Magic™ Tape as previously described.

SACRIFICIAL LAYERS. Though common antistiction coatings improved the separation the result was suboptimal. Therefore, gold and silver as sacrificial layers were tested. Silver was deposited by sputter-coating to a thickness of about 50 – 100 nm using a Sputter System from Kurt J. Lesker Company. Gold was electron beam evaporated to a thickness of 200 nm using SCM600 from Alcatel Vacuum Technology. The SU-8 delaminated almost perfectly in both cases though small amounts of SU-8 remained on the nickel shim in case of the silver coated master. The remaining SU-8 was easily removed by applying and removing Magic™ Tape. It is to note that neither gold nor silver delaminated from the nickel plate but the metal layer was perfectly transferred to the nickel surface. Injection molding experiments showed that the gold is mechanical stable and survived over 500 molding cycles without visible damage. The silver was not adhering as well and delaminated completely during the first injection molding cycle. However, microstructures were not damaged and, though not expected, the delamination of silver provided the original nickel (or nickel-vanadium) surface.

FILLING OF BACKSIDE CAVITIES. Cavities on the mold backside originating from the electroplating process need to be filled with a hard, resilient and heat-conductive material to avoid deformation during injection molding. Different experiments were conducted to optimize the backside filling. The conductive epoxy *CW2400* and *Super Spackel Elastic* were easy to apply using a spatula without producing large excess of material. The backside was easily polished using abrasives. *Tin/lead* alloy was difficult to apply and produced a large amount of excess material. It was successfully soldered on a nickel shim backside coated with 200 nm gold. It was not possible to achieve a stable bond between *tin/lead alloy* and untreated nickel shim backside even if aided by solder flux. The large amount of excess material was polished using abrasives. However, since it was more difficult to obtain a smooth polished surface, soldering of *tin/lead alloys* was not further applied. *Art Clay Silver 650 paste* was easy to apply using a paint-brush producing almost negligible amount of excess material. Samples fired in air resulted in a strong color-change of the nickel surface to dark greenish and the shims became extremely soft, comparable to lead. Samples with *Art Clay silver 650* were successfully cured in a furnace containing a mixture of argon and nitrogen (composition unknown). However, these nickel shims as well became soft like lead.

Nickel shims prepared with the different backside fillers (except for *tin/lead alloy*) were tested in injection molding to probe for their thermal and mechanical stability, i.e. deformation of the microstructures. *CW2400* was stable for injection molding of Topas 8007 (T_{mold} = 80°C) but it disintegrated and finally delaminated from shims used for molding of Topas 5013 (T_{mold} = 125 °C). A bending the channel of 500 – 600 nm [12] was observed after injection molding. No delamination was observed for nickel shims filled with *Super Spackel Elastic*. Bending of 100 - 200 nm [12] was observed after injection molding. As described before shims prepared with *Art Clay Silver 650* softened during curing of the paste. Injection molding tests resulted in a deformation of the shim on small scale. The shim surface displayed a rough grainy surface. COC parts molded from that shim could not be used.

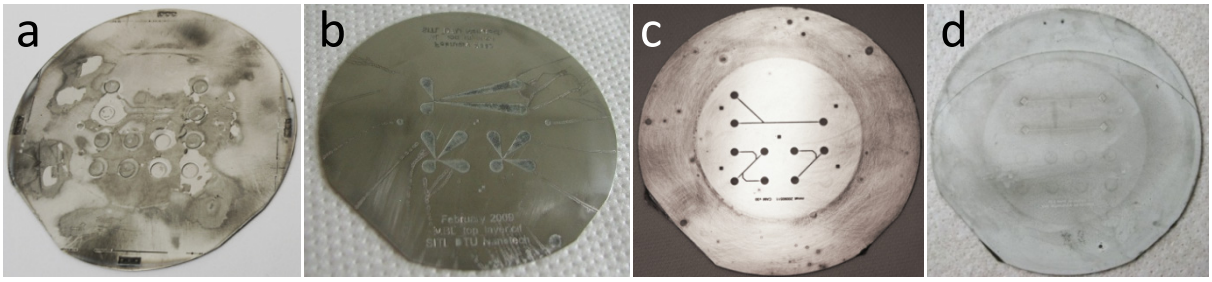

Figure 48: Photos of nickel shim backsides filled with different materials after injection molding: *CW2400* at 125 °C (a) and 80 °C (b); *Super Spackel Elastic* at 125 °C (c), *Art Clay Silver 650* at 125 °C (d). *CW2400* delaminated from the nickel shim during injection molding at 125°C. The nickel shim filled with *Art Clay silver 650* exhibited a very rough surface after injection molding at 125 °C (shim softened during baking of paste). Shim diameter: 85 mm.

[12] Nickel shims with the particular filler were measured after utilized for injection molding. A cross-sectional profile of the channel was recorded. The channel bending was measured by subtracting the minimum height at the channel center from the maximum height at the sidewall.

DISCUSSION. Microfluidic structures were successfully written into SU-8 without major problems. The decrease of the intended 200 µm wide channel of about 10 – 20 µm is of minor importance for first evaluation of nanostructured patterns. A deviation in depth as well is of minor importance as long as a microfluidic channel system of appropriate height can be assembled allowing transportation of cell suspension and preventing clogging.

Structures written in SU-8 were replicated with high fidelity. Nickel shims replicated even the smallest defects of the master (Figure 46b, d). The separation of SU-8 and nickel shim was problematic. The SU-8 delaminated rather from the master substrate (silicon wafer) than from the nickel mold. According to the manufacturer of SU-8 (MicroChem) and other research groups [e.g. Kim 2008], SU-8 adheres poorly to nickel. It is possible that the re-entrant sidewall profile of 1 – 2 ° and the "small undercut" mentioned before prevented smooth demolding. This assumption is supported by the fact that SU-8 tended to adhere especially strong to microstructures. Experiments were conducted either to remove SU-8 from the nickel shim or to reduce the adhesion of SU-8 to nickel and facilitate complete separation of both. Fluorocarbon based antistiction coatings reduced the adhesion of SU-8 to nickel though perfect separation was not achieved. The deposited antistiction coatings were not tested by for example contact angle measurements. It is possible that the antistiction coating was not uniformly deposited and thereby not sufficient to allow for complete separation. Gold and silver acting as "antistiction" improved the separation substantially, although gold was deposited by electron beam evaporation which is known to cover sidewalls badly. The metal layer was in both cases perfectly transferred to the nickel shim. The adhesion of silver to the sputtered seed layer of nickel-vanadium alloy was slightly better than to SU-8. The silver delaminated during the first injection molding cycle most probably perfectly, leaving the microstructured undamaged. In contrast, gold adheres very well to the nickel shim remaining undamaged even after 500 injection molding cycles.

The replication of the microstructured master by electroplating implies the formation of cavities on the backside of nickel plates complying with protrusion on the front side. The depth of cavities on the backside decreases with decreasing structure size and aspect ratio of features. In case of 200 µm wide and 50 µm deep structures, the cavities are too large and the growth of nickel in vertical direction to small to fully cover and flatten the backside cavities. The major problem of these "hollow" protrusions is that they are very likely to be compressed by the high pressures applied during injection molding. Different materials were tested as fillers but only Super Spackel Elastic and CW2400 showed acceptable results. Both epoxies were easy to apply and process by abrasives. Though still small deformation of microstructures was visible, the filling prevented significant collapse. Due to its higher thermal stability, Super Spackel Elastic has been used for future shims.

3.2. Anisotropic Etching of Silicon

Microstructures of 200 µm width were successfully exposed into positive resist AZ5214E and further etched into silicon with an etch rate of 126 ± 5 nm s^{-1} with almost vertical sidewalls. 200 - 215 µm wide channel structures up to a depth of 100 µm were successfully etched with sidewall scalloping occurring as typical for the Bosch process. Deeper structures showed increasingly defects (Figure 50a). A test was performed to lower the sidewall roughness by growth of 600 nm silicon oxide and its removal by hydrofluoric acid. No significant change in sidewall roughness was observed (Figure 50, b and c). Final microfluidic structures were etched for about 6.6 min to achieve a depth of about 53 µm.

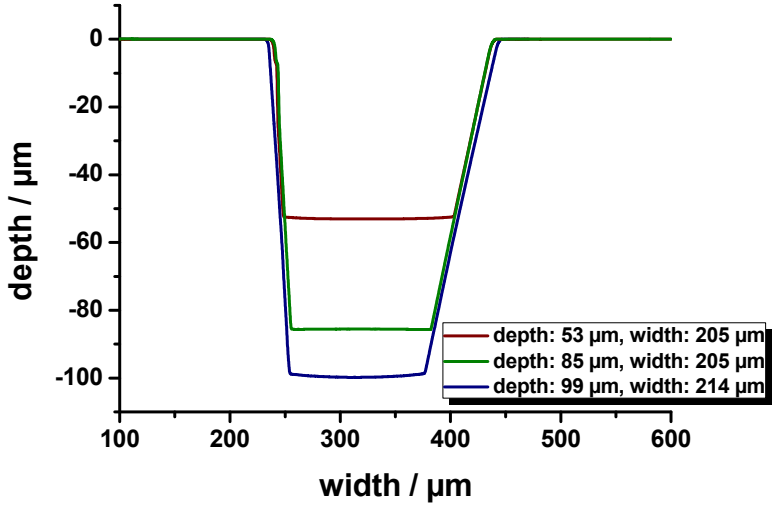

Figure 49: Cross-sectional profiles of about 200 µm wide channels etched into silicon with different depth.

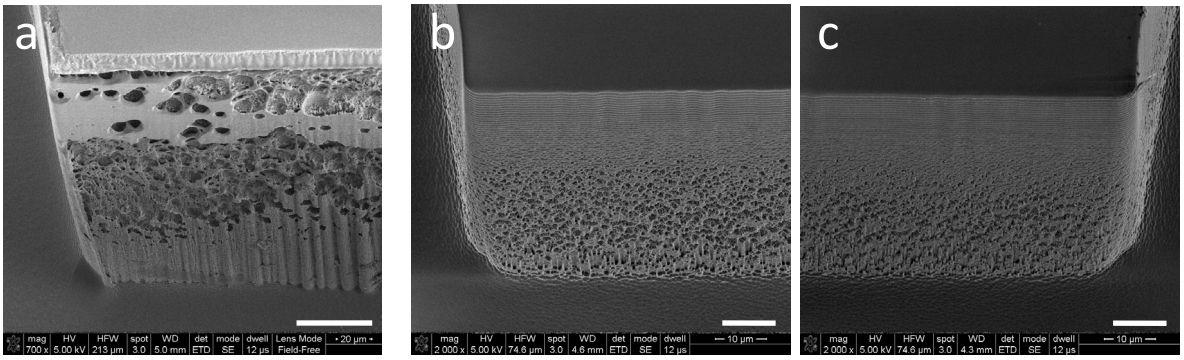

Figure 50: SEM of 30° tilted microstructures in silicon etched down to 335 µm (a) and 85 µm before (b) and after growth and removal of 600 nm silicon oxide (c). Scale bars: 40 µm (a), 10 µm (b, c).

ELECTROPLATING. Microstructures were replicated into nickel with excellent quality. Even the scalloped sidewalls of structures produced during etching were replicated with high fidelity. Similar to SU-8, silicon adheres strong to the microstructured nickel surface, especially in cavities and at edges leaving large parts of silicon on the nickel plate (Figure 51, Figure 52). From SEM images the scalloped sidewalls of microstructures in nickel appeared "smeared" (Figure 51b and c).

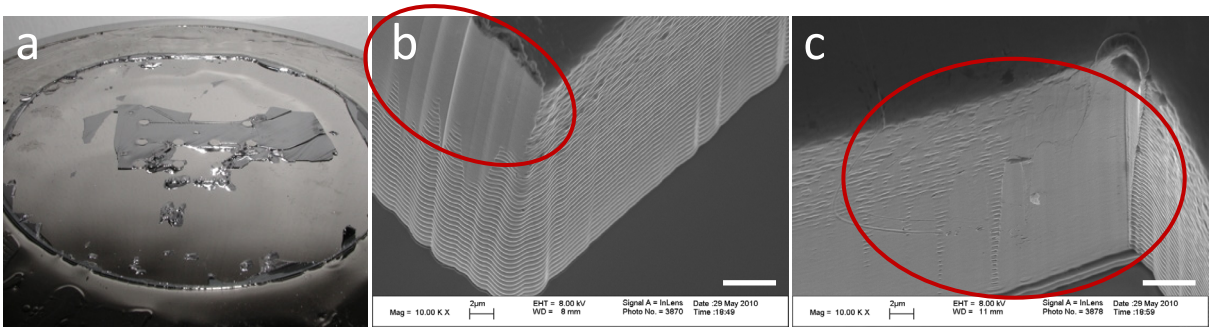

Figure 51: Photo of a nickel shim after separation with large amount of silicon remaining on its surface (a). High magnification SEM images exemplifying the partially "smeared" scalloped sidewall (b, c) high lightened by the red rectangle. Scale bar: 4 µm.

FLUOROCARBON BASED ANTISTICTION AND SACRIFICIAL LAYERS. Strong adhesion of silicon to the final nickel plate led to tests to decrease the adhesion of silicon and nickel. Structured silicon wafers were coated with FDTS and silver prior to electroplating similar to SU-8 based masters. Firstly, silicon wafers were coated with a monolayer of molecular vapor deposited FDTS. Secondly, silicon wafers were sputter-coated with 50 – 100 nm silver or gold. The results are very similar to those obtained with structured SU-8 masters. The adhesion between silicon and nickel was significantly reduced by application of either FDTS or silver though separation was imperfect. Small residues of silicon remained on the surface attached to microstructures. The silver was completely transferred to the nickel shim. In case of gold coated silicon master, the gold delaminated perfectly from the silicon enabling easy separation. The gold adhered well to the nickel shim remaining intact during injection molding experiments.

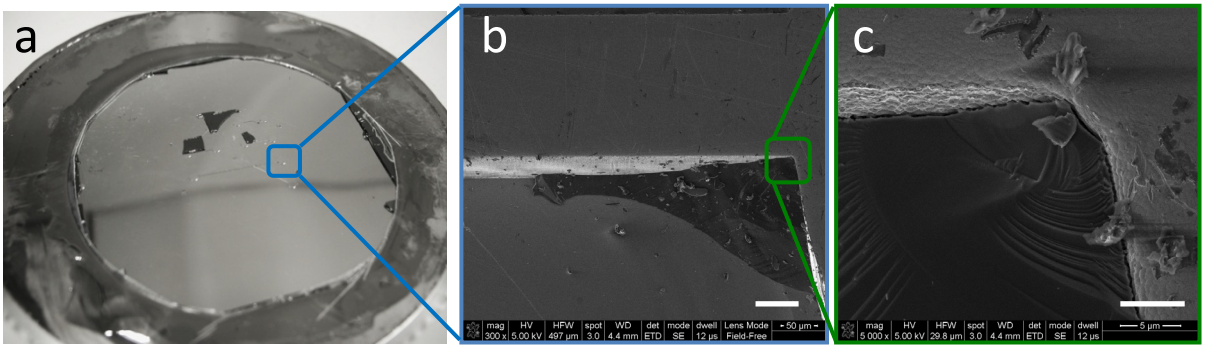

Figure 52: Photo of a nickel shim replicated from a silicon based master coated with silver prior to electroplating. Residual silicon can be observed on the surface (a). SEM images magnify areas of silicon adhering to an inlet (b, c; 25° tilted). Scale bar: 50µm (b), 5 µm (c).

REMOVAL OF SILICON. Silicon can be etched by either dry or wet etch processes. Both methods have been tested on their compatibility with the process described here. The removal of silicon by wet etching applying 30 % potassium hydroxide for 1 h showed only minor improvement but corrosion of the nickel surface as also described for nanostructured nickel shims (Section III-3.2.).

The dry etching of silicon was performed using the same recipe as used for etching microstructures into a silicon wafer (described above). The dry etching showed better results than achieved for the wet etching. Silicon was removed to a large extent (Figure 53) though some etch residuals ("black dust") were visible deposited on the nickel surface. Etch residuals were washed off with acetone, isopropanol and water. In case of silver coated nickel shims, the silver was attacked by the SF_6/O_2 plasma leaving an "opaque" film on the nickel surface. The film was completely transferred to the polymer part during the first injection molding cycle. Microstructures remained intact and the shim was used for further replication cycles. As described earlier, the sputtered silver layer was about 50 – 100 nm thick. Compared to the microchannel dimensions of 200 µm in width and 50 – 100 µm in depth with variations of up to 15 µm the absence of a 100 nm thick layer of silver is negligible and will not do any damage.

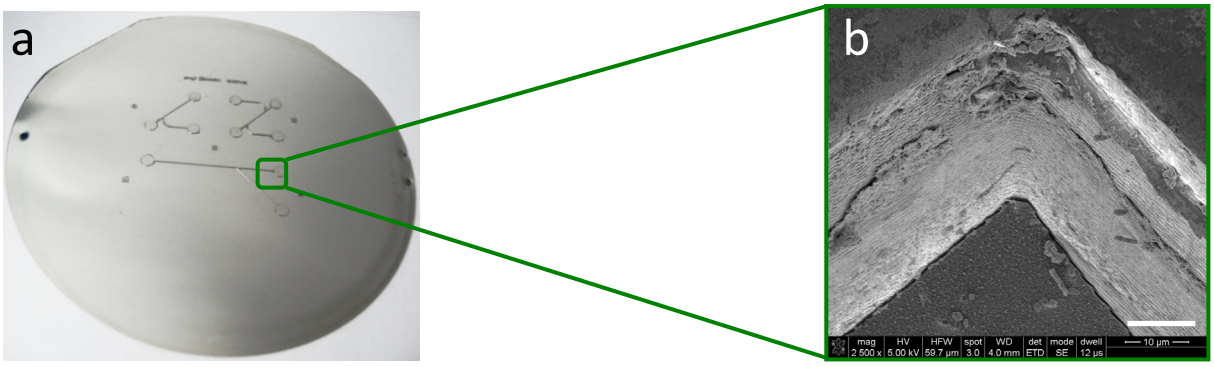

Figure 53: Photo of the nickel shim (silver coated master) after etching of silicon by reactive ion etching (a). SEM images magnify the same areas as shown in Figure 52c. Silicon was widely removed though small amounts are still visible. Scale bar: 10 µm (b).

DISCUSSION. Microfluidic structures were successfully written into photosensitive resist and further etched into silicon. Standard parameters for exposure dose and etching resulted in well defined nickel mold for replication of microfluidic channel systems into COC. As already discussed a small deviation in depth and width as measured for structures etched into silicon are of minor importance as long as thermal bonding results in appropriate channel height. Similar to the SU-8 based master, large amounts of silicon fractured and remained on the nickel shim making complete separation impossible. The sidewall scalloping created a large surface-to-volume ratio and simultaneously undercuts which prevented demolding. The adhesion strength between silicon and nickel together with the increased surface roughness cause silicon to fracture from the bulk silicon rather than to detach from the nickel surface. Partially "smearing" of the scalloped sidewalls in nickel appeared. This most probably happened during the separation of the silicon master and the nickel replica when the two scalloped sidewalls slid along each other. The harder silicon scallops deformed the nickel

plastically giving it this “smeared” appearance. This effect is even stronger in regions were the silicon etching form a porous area (lower region of the sidewall, Figure 50 a and b).

Although residual silicon can successfully be etched away employing reactive ion etching, anti-adhesion layers based on fluorocarbonsilane (FDTS), gold or silver improve the separation tremendously. Finally a clean nickel shim containing the inverted microfluidic system (protruding channels) was produced.

4. Polymer Replication by Injection Molding

Microstructures forming the microfluidic system were injection molded together with twelve female luer fittings to provide easy fluidic connection [Andresen 2010]. The injection molding of microstructures above 10 µm is well established and requires only small process optimization. A wide range of parameter settings can be used to gain sufficient surface finish as will be explained later.

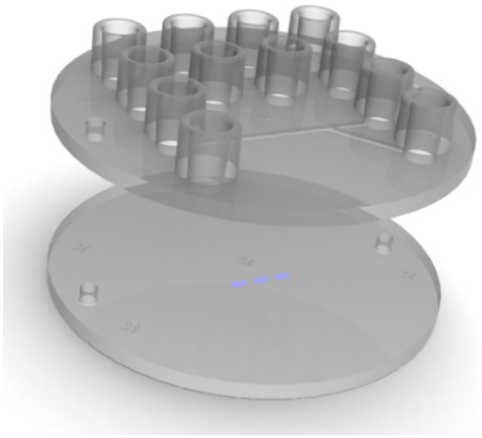

Figure 54: 3D sketch of injection molded assembly of parts containing microstructures with female luer connectors (top) and nanostructured pattern (bottom, nanostructures blue rendered).

4.1. Heating and Cooling System

The heating and cooling ability of an injection molding machine plays an important role since it heavily influences the cycle time. Based on the special mold design used in this project, flat chips (without luer connectors) made of Topas 5013 and 8007 need to cool down below at least 70 and 40°C, respectively, to avoid polymer deformation during release. In case of injection molded chips with luer connectors the polymer need to be cooled even further about additional 5 – 10°C to facilitate demolding.

The steel mold of the Victory 80/45 Tech is electrically heated by resistive heating and cooled using an external water supply. The mold temperature is controlled via a feedback loop from one thermistor and two heating elements located in each mold part. The heating elements are software controlled and activated or deactivated depending on the measured temperature. The resistive heating is in principle very efficient but its heating capacity is limited based on the installed heating elements. Active cooling of the each mold part can be achieved by feeding cold water (10 – 40 °C) into the mold. The cooling is controlled separately and can only be activated during the cooling phase but not for active adjustment of the mold temperature during heating or injection phase.

COOLING SYSTEM. The cooling system has changed over the period of this project. Initially, the cooling was supported by a thermostat which was fed by 10°C tap water (setup 1: thermostat). The actual water temperature fed into the mold was adjusted on the thermostat, but minimum temperature possible was about 17 °C. The cooling water was constantly running through the mold, even during heating cycles. Later-on two valves were installed to prevent the flow of cooling water during the heating cycle (setup2: thermostat with valves). The valves were cutting off the water inside the mold from the circulating cooling water. At last, the thermostat broke down (February 2010). The 10°C

cold tap water was now directly fed into the mold connected via two valves to prevent the flow of cooling water during the heating cycle (setup 3: valves).

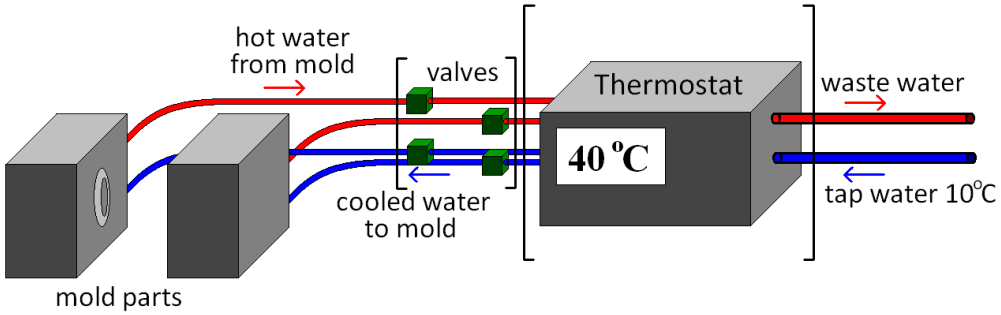

Figure 55: Schematic of the cooling system (setup 2) of the Victory 80/45 Tech used in this project. Both mold parts are connected via tubings to the valves and a thermostat. The thermostat is fed by tap water of 10°C but regulate the actual cooling to the value set by the user.

There are two main problems connected with the different cooling systems. On the one hand, the cooler the cooling water the faster the cooling rate but also the lower the heating, at least for setup 1 (thermostat). The heating was improved by cutting off the cooling water inlet as done by installing the valves. The valves prevented water circulation inside the mold. Problematically, the water inside the mold is heated up together with mold reaching temperatures above 100°C. The pressure inside the mold increases and can finally cause collapse of the valve system or damage the mold. Nevertheless, injection molding tests have been made using setup 2 (thermostat with valves) reaching mold temperatures of up to 165°C without visible problems. The installation of the valves should facilitate fast heating and cooling. However, it was not possible to heat up the mold to above 130 °C in durable time (<10 min) if the cooling water was kept at a temperature of 10 - 20°C. The system was checked thoroughly but the reason could not be found so far. The functionality of the two valves was checked by installing flow meters to check if water keeps on running although valves are activated. This was not the case. Furthermore, the flow meter allowed evaluation of the cooling rate. It was found that the flow rate of the cooling water has a varying speed of 3 – 4 l/min leading to small changes in the cooling rate resulting in a difference of up to 5 °C for a target temperature of about 40 °C.

MOLD TEMPERATURE. The mold temperature of the stationary mold part was measured since this part holds the nanostructured nickel shims. Precise knowledge of the actual mold temperature in the vicinity of nanostructures might be valuable knowledge to evaluate the replication quality and causes for molding defects. The actual mold temperature was measured by placing a thermoelement (K-type) in the center behind the nickel shim. The cooling water was "running" (valves closed) and injection molding parameters were set to the standard parameters for molding of Topas 8007 (Section III-2.1.4.). The mold temperature was set to a specific value and measured after a visible stabilisation occurred[13]. The measured mold temperature was constantly higher than the setpoint with increasing difference (Figure 56). The difference increased from 4 °C (setpoint: 15 °C) to 13 – 14 °C (setpoint: 100 – 140 °C). The heating of the mold is with about 10 min considerable slow for mold temperature above 120 °C. In case of an temperature increase from 130 °C to 140 °C the setpoint was not reached within 10 min.

[13] The mold temperature is considered as stable as soon as the software of the injection molding machine displays the setpoint with less than 1 °C absolut variation.

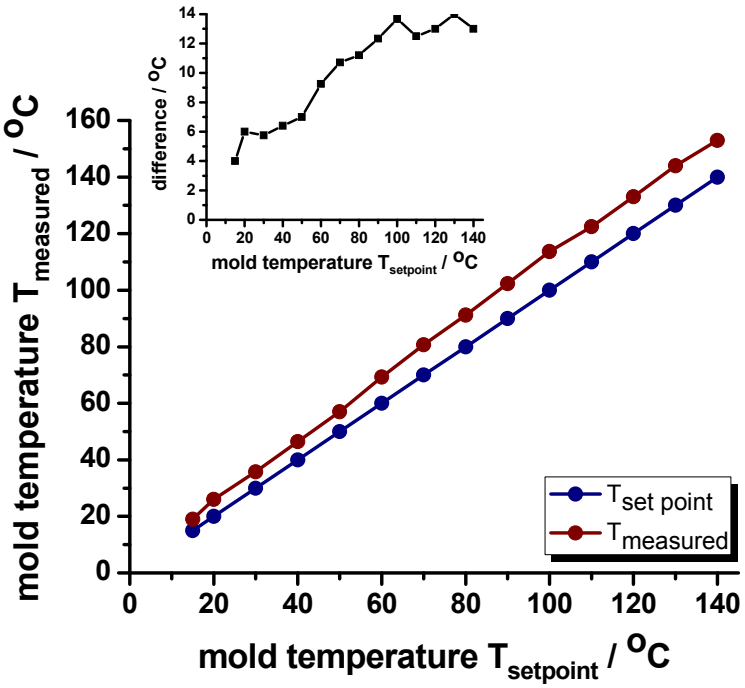

Figure 56: Comparison of mold temperature set point and actual measured value (stationary mold). The standard deviation is below 0.5 °C for all measurements and was left out to facilitate visibility.

MELT TEMPERATURE. The melt temperature determines the viscosity and might thereby influence the replication quality. The actual melt temperature between 240 and 280 °C was measured. The maximum volume of molten polymer (about 30 cm^3) was ejected at maximum speed through the open nozzle and the temperature in the center of the bulk was immediately measured.

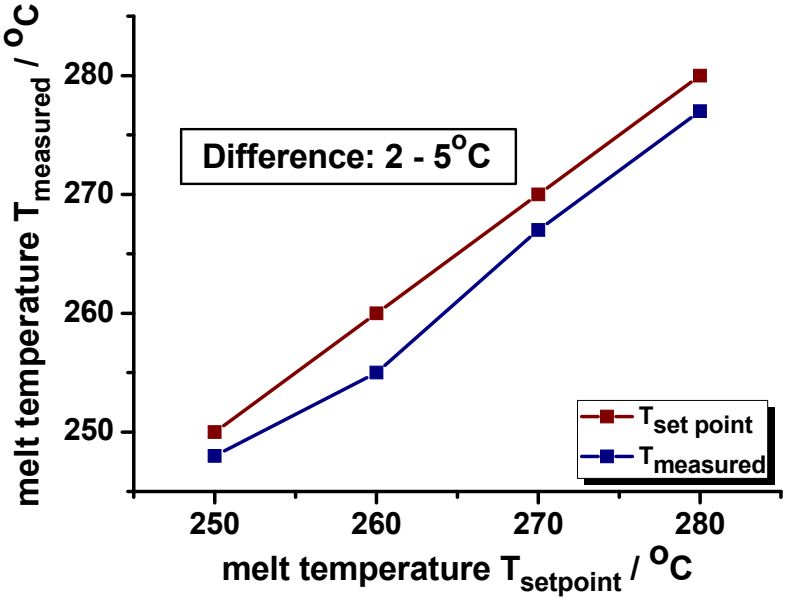

Figure 57: Comparison of melt temperature set point and actual measured value.

4.2. Characterization of Nickel Mold Surfaces

Reliable results for injection molding on native and antistiction coated nickel surfaces as well as identification of problems and defects related can only be obtained if the surface chemistry of the utilized nickel shims can be accurately determined. The strong adhesion of Topas 8007 and 5013 to native nickel molds was assumed to be a major problem, especially for fabrication of high aspect ratio nanostructures. Frictional force applied during demolding of solidified polymer can cause deformation and finally fracture of especially nanopillars. Antistiction coatings increase the surface energy of nickel molds and thereby reduce the adhesion strength between polymer and mold. The application of an antistiction coating should thereby facilitate demolding and decrease polymer deformation. Pranov et al. have been shown that antistiction coatings limit the filling of nanoscaled cavities reducing the replication depth tremendously [Pranov 2006].

Fluorocarbonsilane based antistiction layers are commonly applied on silicon molds for nano imprint lithography. Silanes are described to bind less good to nickel than to silicon or even silica or quartz as stated by Gelest Inc. [Gelest 2011]. Therefore mechanical and thermal stability of fluorocarbonsilane coatings and long-term stability during injection molding were investigated. Moreover, commercial electroplating of nickel molds is sometimes done using few nanometers of gold instead of nickel-vanadium as conductive seed layer for the plating process. Final nickel shims presents gold on the surface. Since silanes do not adhere to gold, a fluorocarbonthiol with similar chemical structure to the fluorocarbonsilane was investigated. The application of a gold layer on nickel molds allows modifying nickel mold surfaces with a large variety of chemicals based on thiol/gold chemistry.

Three different chemicals and methods were used to employ fluorocarbon-based antistiction coating on nickel mold surfaces. Firstly, a multilayer of fluorocarbon polymer was plasma-polymerized on native nickel molds from Fluoroform monomers (CHF_3). Commonly a layer thickness of 10 nm was deposited. Secondly, a monolayer of Perfluorodecyltrichlorosilane (FDTS) was deposited on native nickel molds by molecular vapor deposition. Thirdly, a monolayer of Perfluordecanethiol (PFDT) was adsorbed on gold coated nickel molds by self-assembly of the PFDT molecules. PFDT and FDTS have the same structure except for their termination, forming either a thiol or a silane, respectively. Deposition and removal of the antistiction coatings are described in Section I-4.3.2.

The surface energy of native and coated nickel molds was analyzed by contact angle measurements of ultrapure water, hexadecane, Topas 8007, and Topas 5013. The adhesion strength of Topas 8007 and 5013 was qualitatively measured by employing a lateral ball shear test on solidified Topas drops. The chemical composition of the native and coated nickel surfaces and injection molded Topas parts was analyzed by X-ray photoelectron spectroscopy. Especially the fluorine concentration allows verification and comparison the different antistiction coatings including possible transfer of fluorine atoms from nickel shims to Topas replicas. Since antistiction coatings on silicon are well-established in nanoimprint lithography, silicon wafers with equal surface treatments were analyzed to verify coatings on nickel. The applicability of PFDT as antistiction coating was evaluated by contact angle measurements of water and hexadecane at a temperature range similar to mold temperatures applied during injection molding. Moreover, contact angles of water and hexadecane were recorded to verify applicability as antistiction layer.

4.2.1. Topas 8007 and 5013 on Nickel Shims: Wetting and Adhesion

The contact angles of water and hexadecane were recorded to investigate the change in surface energy for different surface treatments that nickel shims undergo during injection molding. Subsequently, droplets of solidified Topas 8007 and 5013 were measured to determine wetting behavior of Topas on different (nickel) mold surfaces.

Nickel shims were heated up to 300 °C required to form measurable droplets of Topas 8007 and 5013. To monitor the surface energy during the droplet formation, later referred to as "thermal treatment", contact angles of water and hexadecane were taken before and after the thermal treatment. A set of nickel samples was prepared mimicking the nickel shim surfaces as present during injection molding (described in Section II-2.2.). Surfaces were investigated presenting native nickel, oxygen plasma cleaned nickel, FDTS, PFDT, and CHF_3 coated; and FDTS coated followed by oxygen plasma cleaning. It is to note that the "native nickel" surface is in fact a nickel-vanadium alloy surface (7 wt.% vanadium). For better clarity and since all investigated nickel shims present the same surface chemistry, i.e. nickel-vanadium, samples will be referred to as "native nickel". A second set of nickel samples was simultaneously treated and used to analyze the chemical composition by XPS. The only exception was CHF_3. CHF_3 coated nickel samples used for XPS analysis[14] were not coated together with samples used for contact angle measurements and lateral ball shear test.

WATER AND HEXADECANE ON NICKEL. Water achieved contact angles of 62 ± 4 nm for native nickel shims and 12 ± 3 nm for oxygen plasma cleaned indicating a good wetting on nickel. The contact angle increased strongly for antistiction coated nickel surfaces resulting in 99 ± 2 and 106 ± 1 ° for CHF_3 and FDTS coated shims, respectively. Hexadecane exhibited very good wetting for native and oxygen plasma treated surfaces leading to immeasurable contact angles. CHF_3 and FDTS modification of nickel resulted in contact angles for hexadecane of 31 ± 2 and 70 ± 1 °, respectively.

After thermal treatment, contact angles of water equilibrates for native and oxygen plasma cleaned shims to about 35 – 40 °. The contact angle of water on antistiction coated nickel was reduced from 70 ± 1 to 47 ± 4 ° for FDTS and from 31 ± 2 to 25 ± 4 for CHF_3. The contact angle of hexadecane is only measurable for FDTS coated shims displaying a value of 47 ± 4 °. The contact angles of water and hexadecane on PFDT coated nickel were similar to FDTS coated shims. The contact angles for water and hexadecane decreased to 84 ± 5 and 25 ± 4 °C, respectively, for a thermal treatment of 80 °C. No further decrease was observed for an increase in temperature up to 150 °C.

[14] It is to note that these samples were not thermally treated.

Table 4: Contact angle of water and hexadecane on different nickel surfaces before and after thermal treatment of nickel shims (T = 300 °C)[15].

Surface treatment	Water / °	Hexadecane / °	Water after 300 °C / °	Hexadecane after 300 °C / °
Native	62 ± 4	< 5	34 ± 2	< 5
Oxygen plasma	12 ± 3	< 5	39 ± 2	< 5
Oxygen plasma → FDTS	106 ± 1	70 ± 1	89 ± 2	47 ± 4
Oxygen plasma → FDTS → Oxygen plasma	-	-	30 ± 4	< 5
Oxygen plasma → CHF_3	99 ± 2	31 ± 2	76.7 ± 2	< 5
PFDT[16]	106 ± 5	63 ± 2	84 ± 5	25 ± 4

DISCUSSION. The difference in contact angles of water on native and oxygen plasma cleaned nickel shows that firstly, organic contaminants were present on the nickel shim. The nickel shims are commonly coated with a lacquer to protect the surface. Nickel shims used for surface characterization and analysis of the adhesion strength of Topas were produced from a cleaned glass plate directly sputter coated with nickel. Therefore organic contaminations on the nickel shim can only originate from the lacquer or from the atmosphere. Secondly, it suggests that reproducible results for the replication of nanostructures using "native" nickel shims are only possible if nickel shims are initially and repeatedly cleaned with oxygen plasma. Moreover, change in contact angle of water and hexadecane need to be monitored during injection molding cycles to assure reproducibility. With respect to the data volume necessary to analyze each surface condition during injection molding only CHF_3 and FDTS coated shims were frequently monitored as will be described in the following sub-section.

The similar contact angle achieved for water on native and oxygen plasma cleaned shims after thermal treatments might be caused by two effects. Firstly, organic components were burned off from the native shim leading to lower contact angles. Secondly, contaminants from the air were deposited on the previously oxygen plasma cleaned shim in between thermal treatment and measurements leading to increased contact angle.

The decrease of the contact angles of water and hexadecane indicate that both coatings degrade if temperatures of 300 °C are applied. The degradation of CHF_3 resulted in a decrease of the contact angle of hexadecane from 99 ± 2 ° to 76.7 ± 2 ° and 31 ± 2 ° to < 5 ° for water and hexadecane, respectively, on CHF3 coated nickel. The contact angle for water and hexadecane on FDTS coated nickel decreased from 106 ± 1 ° to 89 ± 2 ° and 70 ± 1 ° to 47 ± 4 °, respectively. The stronger decrease of the contact angle of hexadecane on CHF_3 give rise to the assumption that FDTS might degrade less. Even after the thermal treatment of 300 °C, the contact angle of hexadecane and water are higher on FDTS coated nickel than on freshly CHF_3 coated nickel.

[15] Contact angles below 5 ° were not measurable.

[16] PFDT on gold coated nickel was heated up to 80 and subsequently 150 °C to simulate temperatures applied during injection molding of Topas 8007 and 5013. No contact angles of Topas 8007 and 5013 were measured, hence samples were not heated up to 300 °C.

The contact angles of water and hexadecane were not measured for FDTS/oxygen plasma cleaned nickel shims. However, it is very likely that the contact angles after oxygen plasma cleaning decreases to similar values as obtained for native/oxygen plasma cleaned shims, similar to contact angles observed for thermal treated shims. The strong decrease in the contact angles of water and hexadecane after thermal treatment indicate complete removal of FDTS from the nickel surfaces. However, oxygen plasma is known to remove only organic components. The silicon should therefore remain on the nickel surface, as will be discussed later.

PFDT obtains contact angles similar to FDTS complying well with their similar structure. According to the contact angles the coating seems to have similar uniformity as achieved for FDTS. However, the strong decrease in contact angle, especially for hexadecane already at temperatures of 80 °C suggests low thermal stability. It is therefore very likely that the coating is useless as antistiction coating for injection molding of both grades. Nevertheless, contact angles of hexadecane and water on nickel samples were measured after again injection molding to demonstrate possible applicability as antistiction coating (described in the following sub-section).

TOPAS 8007 AND 5013 ON NICKEL. Topas 8007 displayed higher contact angles than obtained for Topas 5013 regardless of treatment (Table 5). Contact angles of 79 ± 2 ° and 75 ± 1 ° for Topas 8007 and 52 ± 1 ° and 53 ± 1 ° for Topas 5013 on oxygen plasma cleaned nickel surface were measured, regardless of previous surface (native of FDTS coated). Oxygen plasma treated samples, regardless of the prior surface chemistry, resulted in a contact angle of about 75 – 80 ° and 50 – 55 °C for Topa s8007 and 5013, respectively. CHF_3 covered samples showed an increase of the contact angle on Topas 8007 (60 ± 4 ° to 75 ± 1 °) and 5013 (48 ± 2 ° to 88 ± 2 °). The contact angle of both Topas grades increased tremendously for FDTS coated nickel of about 40° compared to native nickel. Topas 8007 and 5013 achieved contact angles of 97 ± 3 ° and 88 ± 2 °, respectively.

Table 5: Contact angles of Topas 8007 and 5013 on nickel of different surface treatments[17].

Surface treatment	T8007	T5013
Native	60 ± 4 °	48 ± 2 °
Oxygen plasma	79 ± 2 °	52 ± 1 °
Oxygen plasma → FDTS	97 ± 3 °	88 ± 2 °
Oxygen plasma → FDTS → Oxygen plasma	75 ± 1 °	53 ± 1 °
Oxygen plasma → CHF_3	86 ± 2 °	63 ± 2 °

[17] Surface treatments. Native: nickel without treatment; O2 plasma/oxygen plasma: oxygen plasma cleaned nickel; FDTS: oxygen plasma cleaned nickel followed by coating with FDTS; FDTS/O2pl: oxygen plasma cleaned nickel followed by coating with FDTS followed by a 2nd oxygen plasma cleaning; CHF3: oxygen plasma cleaned nickel followed by coating with CHF_3.

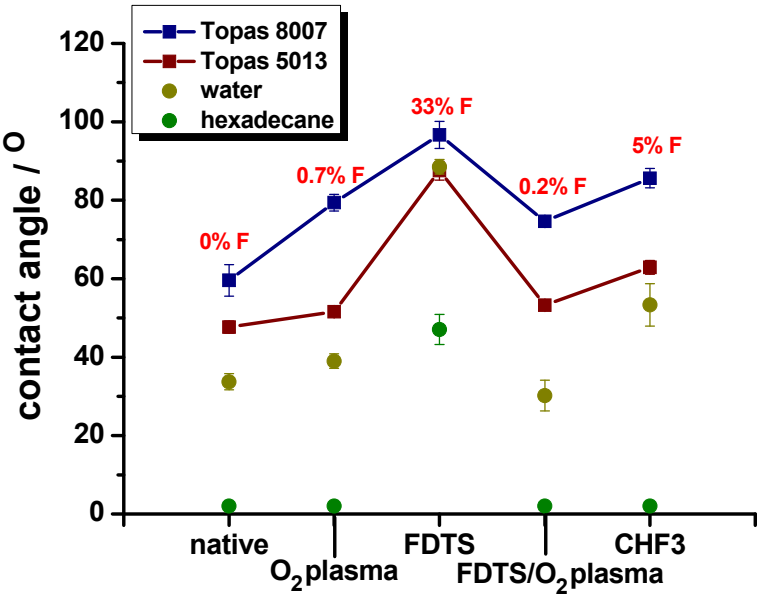

Figure 58: Contact angles of water, hexadecane[18], and Topas 8007 and 5013 on nickel of different surface treatments[18]. The numbers in red reflecting the fluorine content on the specific nickel shims measured by XPS[19].

XPS measurements (Table 6) showed a huge increase of fluorine atoms for FDTS coated shims (33 at.%) compared to native and oxygen plasma cleaned shims (up to 0.7 at.%). The amount of fluorine on CHF_3 coated nickel was with about 5 at.% considerably lower. The oxygen plasma cleaning of FDTS coated shims resulted in a strong decrease of the fluorine content down to 0.2 at.% while silicon (1.68 at.%) remained on the surface. CHF_3 covered shims exhibit a comparably higher content of silicon (8 at.%). None of nickel shims, except for CHF_3 coated samples (1.18 at.%) contained a measurable amount of vanadium. Approximately 20 – 25 at.% of carbon can be found on all samples, except on native nickel. Only native nickel shims exhibited a visible higher content of about 40 at.%. The oxygen content of native nickel is about 40 at.% and increases about 5 at.% for oxygen plasma cleaned surfaces. FDTS coated nickel showed the least (22 at.%) while CHF_3 contains with 51 at.% the largest amount of oxygen. A low amount of silicon can be found on FDTS treated (1.26 at.%) and subsequently oxygen plasma cleaned (1.68 at.%) nickel shims and CHF_3 coated samples.

[18] Contact angles of water and hexadecane were measured after forming Topas droplets (heated up to 300 °C and cooled down before CA measurement).
[19] XPS was measured on simultaneously treated shims but did not undergo the thermal treatment of 300°C.

Table 6: Elemental composition of the differently treated nickel surfaces measured by XPS (in atomic percentage (at.%)).

Element	Native	Oxygen plasma	Oxygen plasma → FDTS	Oxygen plasma → FDTS → Oxygen plasma	Oxygen plasma → CHF_3
Si2p	0	0	1.26	1.68	7.86
C1s	40.60	26.49	22.39	24.96	18.99
V2p3	0	0	0	0	1.18
O1s	39.06	44.17	27.53	46.92	51.11
F1s	0	0.70	33.03	0.22	4.99
Ni2p3	13.72	26.42	13.10	23.04	14.02

DISCUSSION. The constantly higher contact angles of Topas 8007 compared to 5013 suggest a better wetting of Topas 5013 regardless of the surface treatment. Contact angles of below 90 ° for all surfaces except for FDTS coated samples lead to the assumption that both Topas grades wet these surfaces. In contrast, the strong increase in contact angle for FDTS coated nickel implies a decreased wetting while even repelling Topas 8007. It might be possible that especially for Topas 8007 with contact angles up to 97 ± 3 °, the decreased wetting interferes with injection molding of especially nanostructures. The low repelling character of FTDS can obstruct or even prevent the molten polymer from flowing into nano- or microstructured cavities. The lower contact angle of CHF_3 compared to FDTS indicates that FDTS is the superior antistiction coating. The decreasing contact angle for oxygen plasma cleaned previously FTDS coated samples support the assumption that FDTS coated nickel can be cleaned by applying oxygen plasma. Furthermore, according to contact angle measurements conducted for water and hexadecane, Topas of both grades behave rather like water than like hexadecane, except for oxygen plasma cleaned nickel. This behavior is difficult to explain since the hexadecane should be a superior model compared to water due to its chemical structure.

XPS was measured on shims treated simultaneously with samples used for contact angle measurements but did not undergo the thermal treatment of 300°C. The actual fluorine content of at least on FDTS and CHF_3 coated nickel shims used for contact angle measurements and lateral ball shear test could vary caused by possible degradation during thermal treatment as explained above. The amount of fluorine atom correlates well with the change of contact angle for different surfaces. The higher the fluorine concentration, the higher is the resulting contact angle. Native and oxygen plasma cleaned nickel contained a negligible amount of fluorine and therefore low contact angles for both polymers, water and especially hexadecane. An increase of the fluorine atom concentration to 33 at.% lead to a noticeable increase in the contact angle, and finally in a measurable contact angle for hexadecane. The low content of fluorine atoms for CHF_3 coated surfaces explains the visibly lower contact angles achieved for CHF_3 coated compared to FDTS coated samples. However, although plasma-polymerized mulitlayers of CHF_3 result only in a CF_2-termination (compared to CF_3-termination of FDTS) the content of fluorine was expected to achieve higher values. Technical problems that randomly occurred with the reactive ion etcher used to deposit CHF_3 could have caused insufficient deposition of CHF_3 for the tested samples. This is also supported by the fact that the oxygen concentration in CHF_3 coated nickel was even higher than for oxygen plasma cleaned surfaces. The fluorine content present on the oxygen plasma treated shim (without prior FDTS coating) is most likely caused by fluorine residuals in the plasma asher. The plasma asher can be used

for deposition of CF_4. Most probably, the chamber has not been cleaned sufficiently prior to oxygen plasma treatment.

The significant difference in contact angles of water for oxygen plasma cleaned compared to native nickel is most probably caused by the different amounts of carbonhydrate contamination found on the nickel. Oxygen plasma removed a large amount of organic contaminations leading to a decreased contact of water and hexadecane. This supports the assumption that FDTS covered shims can be widely cleaned off from fluorine atoms. Interestingly, the contact angle of Topas increased on the surfaces though a decrease would have been more likely according the surface energy presented by these samples. The reason for the increase has not been investigated in further detail. The concentration of silicon on nickel shims after coating with FDTS and after oxygen plasma cleaning is about the same supporting the second assumption that silicon atoms from the FDTS molecule cannot be removed. The silicon content found in CHF_3 coated shims could originate from the 10" silicon wafer working as carrier during plasma-polymerization of CHF_3.

The nickel shims are electroplated based on a nickel-vanadium alloy containing 7 wt.% vanadium. Only CHF_3 coated shims exhibited a measurable concentration of vanadium. Since no delamination or other kind of degradation was observed for the metal surface it is unknown why the other shims did not contain any vanadium. Contaminations from carbohydrates should not be able to mask the vanadium content.

LATERAL BALL SHEAR TEST. Lateral shear test was employed to obtain a qualitative measure of the adhesion strength of Topas droplets on different nickel surfaces. For better comparison of the actual adhesion strength, the forces applied to detach a Topas droplet were normalized to the drop area resulting in a pressure. The maximal pressure commonly achieved by indestructibly drops, i.e. drops that could not be removed from the sample surface, ranged at about 3 N mm^{-2}. The calculation takes the 50 kg maximum load and the drop area (typically: 10 - 17 mm^2) into account. Droplets that could not be removed were presented with 5 N mm^{-2} (Figure 59).

It was not possible to remove Topas 8007 from any of the nickel surfaces including FDTS coated nickel. In contrast, Topas 5013 was removed from native and antistiction coated surfaces by applying 0.3 and 2.7 N mm^{-2}, respectively. Moreover, Topas 5013 could be removed from the native nickel surface, though higher forces were required.

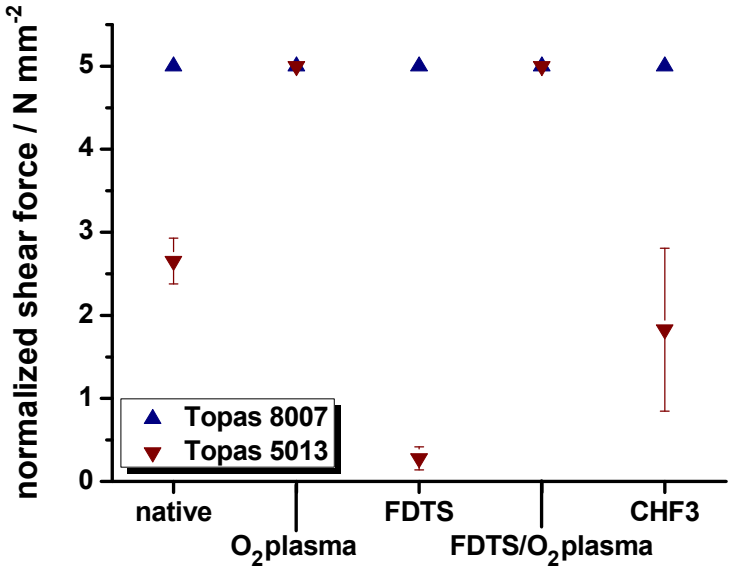

Figure 59: Normalized shear force (pressure) applied to remove droplets of Topas 8007 or 5013 from different nickel surfaces.

DISCUSSION. To date it is impossible to obtain quantitative values for the adhesion strength. Too many variables interfere with the obtaining reliable measurement of the adhesion strength related to the lateral applied shear force. For example, the surface of nickel has been shown to change its properties at elevated temperatures (300 °C). The actual degree of degradation and its influence on the adhesion strength was not investigated. Furthermore, the drop might fracture or deform leading to false results (Section I-4.2.3.). However, the obtained measurements allow for good differentiation between the Topas grades and for the different surfaces.

Results from the lateral shear test show that firstly, Topas 5013 exhibits lower adhesion strength for most of the surfaces compared to Topas 8007. Secondly, it proves that antistiction coatings decrease the adhesion of at least Topas 5013 to nickel. This agrees well with the results obtained from the XPS measurements. The adhesion strength decreases with increasing amount of fluorine atoms on the surface of the nickel shims. Thirdly, a self-assembled monolayer FDTS seems to be the superior antistiction coating over randomly oriented multilayers of CHF_3 with respect to reducing the adhesion strength of Topas (5013).

The adhesion of Topas 8007 was for all surfaces, FDTS coated as well, too strong to detach the drop from nickel. Considering the contact angles measured for these Topas 8007 and 5013 droplets, the outcome of the lateral shear test is surprisingly. Topas 8007 showed higher contact angles for all surfaces implying a lower wetting and thereby lower adhesion. Nevertheless, it was Topas 5013 that could be removed while 8007 remained on the surface. There are two possible causes for that. Firstly, Topas 5013 contains an unknown lubricant that is added by Topas Advanced Polymers GmbH to increase the flowability during injection molding. This lubricant caused the lower adhesion. Topas 8007 is a “standard”[20] grade without any additives. However, more likely is the assumption that air

[20] Topas 8007S-04 is a ”standard” Topas grade as stated by Topas Advanced Polymer GmbH. No further explanation of that term was given.

visibly entrapped in Topas 5013 droplets actively decreased the adhesion strength measured for Topas 5013. Granulate as well as molten and solidified droplets of Topas 5013 have a large amount of air entrapped (Figure 60, right). In contrast, Topas 8007 does not visibly contain voids (Figure 60, left). If the air entrapped in Topas 5013 is located at the polymer/nickel interface the effective interfacial area covered by Topas 5013 is reduced by the area of air/nickel interface. Thereby, the interfacial area of polymer/nickel is lower for Topas 5013 than for 8007 even if the droplets have equal dimensions. The measured adhesion strength of the Topas 5013 droplet takes a smaller value though the actual adhesion of both grades for equal interfacial area is equal or, as indicated by the contact angle measurements, even higher for Topas 5013.

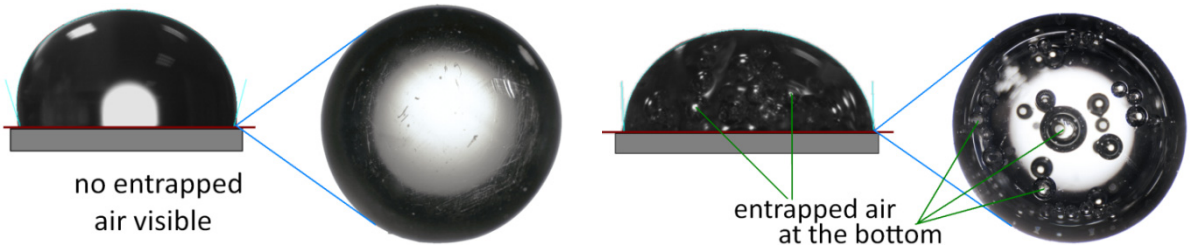

Figure 60: Photos the side and bottom view for Topas 8007 (left) and 5013 (right) on FDTS coated nickel. The photo of the bottom view was taken after detachment. For Topas 5013 (right) the many areas of previous air/nickel interface can be observed. For Topas 8007 (left), no entrapped air and no damage of the bottom can be observed. Scratches were caused during storage.

TOPAS 8007 AND 5013 ON NICKEL VERSUS SILICON. On the one hand, silicon achieves 2 – 20 ° higher contact angle for both Topas grades compared to nickel (Table 4 versus Table 7, Figure 61). For example Topas 8007 and 5013 obtain contact angles of 80 ± 4 ° and 66 ± 3° for native silicon and 60 ± 4 ° and 48 ± 2 ° native for nickel, respectively. The contact angles for Topas 8007 and 5013 on FDTS coated silicon achieved values of 97 ± 3 ° and 88 ± 2 °, respectively. On the other hand, water results in lower contact angles for native and oxygen plasma cleaned silicon compared to nickel. Hexadecane achieves higher contact angles on all surfaces. Water and hexadecane obtain with 106 ± 2 and 60 ± 1 °on FDTS coated silicon, respectively, significant higher contact angles than on nickel (89 ± 2 ° and 47 ± 4°).

Furthermore, contact angles measured on FDTS coated silicon before and after thermal treatment resulted in considerably less change than for nickel. Water displayed 113 ± 3 ° on FDTS before and 106 ± 2 ° after thermal treatment. Hexadecane resulted in contact angle of 59 ± 2 ° before and 60 ± 1° after thermal treatment.

Table 7: Contact angles of Topas 8007 and 5013 on silicon of different surface treatments[21].

Surface treatment	T8007	T5013
Native	80 ± 4 °	66 ± 3 °
Oxygen plasma	81 ± 3 °	62 ± 1 °
Oxygen plasma → FDTS	118 ± 3 °	102 ± 1 °
Oxygen plasma → FDTS → Oxygen plasma	85 ± 1 °	63 ± 2 °

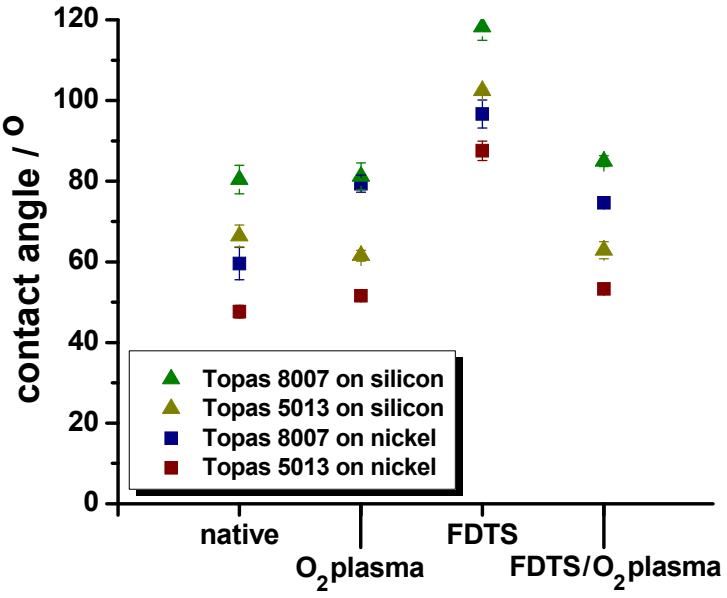

Figure 61: Contact angles of Topas 8007 and 5013 on nickel and silicon of different surface treatments[21].

XPS revealed that FDTS covered shim contain 31.21 at.% of fluorine atoms which is in the same range as measured for FDTS coated nickel. Small amount of fluorine atoms were found on oxygen plasma cleaned samples as well. Similar to nickel almost all fluorine is removed by oxygen plasma cleaning of previously FDTS coated silicon (1.95 at.%). The amount of carbohydrates was with 5 – 14 at.% much lower on all tested silicon samples than found on nickel surfaces.

[21] Surface treatments. Native: silicon without treatment; O2 plasma/oxygen plasma: oxygen plasma cleaned silicon; FDTS: oxygen plasma cleaned silicon followed by coating with FDTS; FDTS/O2pl: oxygen plasma cleaned silicon followed by coating with FDTS followed by a 2nd oxygen plasma cleaning.

Table 8: Elemental composition of the differently treated silicon surfaces measured by XPS. Values are given in atomic percentage (at.%).

Element	Oxygen plasma	Oxygen plasma → FDTS	Oxygen plasma → FDTS → Oxygen plasma
Si2p	61.38	35.00	53.51
C1s	5.22	14.38	6.68
O1s	33.09	19.41	37.86
F1s	0.31	31.21	1.95

The lateral ball shear test of Topas droplets on silicon surfaces confirms results obtained for nickel. It was not possible to remove Topas 8007 from native and oxygen cleaned silicon surfaces. However, Topas 5013 and 8007 were possible to detach from FDTS coated silicon resulting in a normalized shear force of 1.0 and 1.4 N mm^{-2}, respectively. Furthermore, it was possible to detach Topas 5013 from the oxygen plasma cleaned, previously FDTS coated silicon surface. This was not possible for similar treated nickel shims.

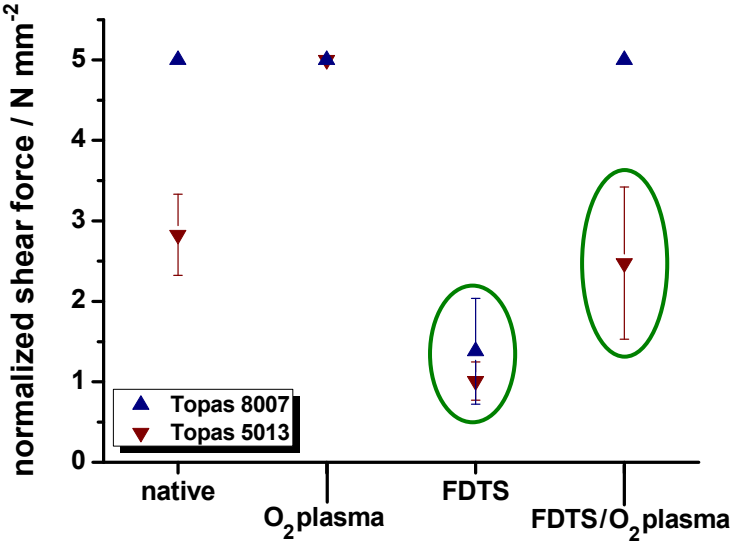

Figure 62: Normalized shear force (pressure) applied to remove droplets of Topas 8007 or 5013 from different nickel surfaces. Differences to nickel are high-lightened by green circles.

DISCUSSION. Contact angles measured on native silicon and nickel are difficult to compare due to different surface chemistry. Especially contact angles of hexadecane clarify that the behavior is very differently. Hexadecane is wetting all nickel surface well (contact angle ≤ 5 °), except for FDTS coated nickel (70 ± 1). In case of silicon contact angles of 13 – 23 ° were measured for native and oxygen plasma treated silicon. However, in case of FDTS coated surfaces, the rather CF_3 is presented to the test liquids instead of the underlying material. The contact angle obtained with water and

hexadecane can thereby give a good estimation of the uniformity of the coating, especially in comparison to values stated by manufacturer[22].

A higher contact angle was measured for water and hexadecane on thermally treated FDTS coated silicon compared to nickel. Considering that FDTS is expected to bonds less well to nickel than to silicon the temperature increase has most probably caused a stronger degradation for FDTS on nickel than for silicon. This especially expressed by the change in contact angle of hexadecane before and after thermal treatment. The contact angle decreased about 23°, from 70 ± 1 to 47 ± 4 ° for FDTS on nickel while silicon did not exhibit any significant change.

The worse coating (and/or higher degradation) of FDTS is also supported by the fact that Topas 8007 and 5013 obtain 14 and 21 ° higher contact angles on silicon, respectively. Furthermore, much lower shear force was necessary to detach Topas 8007 from FDTS coated silicon. However, there is still a lower shear force required to remove Topas 5013 than for 8007. Assuming that the higher contact angles lead to lower wetting and thereby lower adhesion, Topas 8007 should require less shear force to detach droplet from silicon and nickel. Since this is not the case, Topas 5013 droplet contained most probably some locations with air/silicon interface reducing the effective polymer/silicon interface and thereby reducing the adhesion strength of Topas 5013 compared to 8007. Interestingly, Topas 5013 required high shear force to remove droplets from FDTS coated silicon than necessary for nickel. This may be caused by smaller total area of air/silicon interface inside the droplet leading to larger Topas 5013/silicon interfacial area and thereby higher adhesion strength.

XPS measurements proved that a higher content of fluorine (1.95 at.%) is left on the silicon surface most probably due to incomplete removal of FDTS. Thereby, the adhesion of both grades could be lower explaining the removal of Topas 5013 from the oxygen cleaned surface. This could explain why Topas 5013 was removed from oxygen plasma coated silicon but not from nickel.

4.2.2. Mechanical Stability during Injection Molding

The stability of antistiction coatings, especially FDTS, during injection molding was investigated. Contact angles of water and hexadecane were measure on nickel shims before, during and after injection molding. It is difficult to investigate the thermal and mechanical stability of antistiction coatings separately. Since only a decrease in contact angle can be measured, it is not possible to verify the reason for the degradation. Based on results presented by Devaprakasam et al. at least FDTS should be thermally stable for mold temperature used in this project (T_{mold}: 40 – 165 °C) [Devaprakasam 2004].

The uniformity of freshly deposited antistiction coatings is very good exhibiting a maximum standard deviation of less than 5° for commonly 3 drops measured per surface, coating, and test liquid[23]. A deviation of the contact angle of below 5 ° for samples used to analyze the stability during injection molding is considered as negligible small.

[22] Applied MicroStructures Inc., manufacturer of the molecular vapor deposition system used in this project, states a maximum contact angle for FDTS coated silicon of 110 and 68 °, respectively.

[23] Water, hexadecane, Topas 8007, Topas 5013.

STABILITY OF CHF_3. CHF_3 coated nickel shims were used to injection mold Topas 5013 applying temperatures of up to 135 °C. The contact angle of water did not show any significant change (< 3 °) for injection molding of more than 175 pieces at mold temperatures of about 135 °C. The contact angle for hexadecane decreased from 39 ° down to 25 °. The mold temperature is the maximum tested for Topas 5013 (Figure 63).

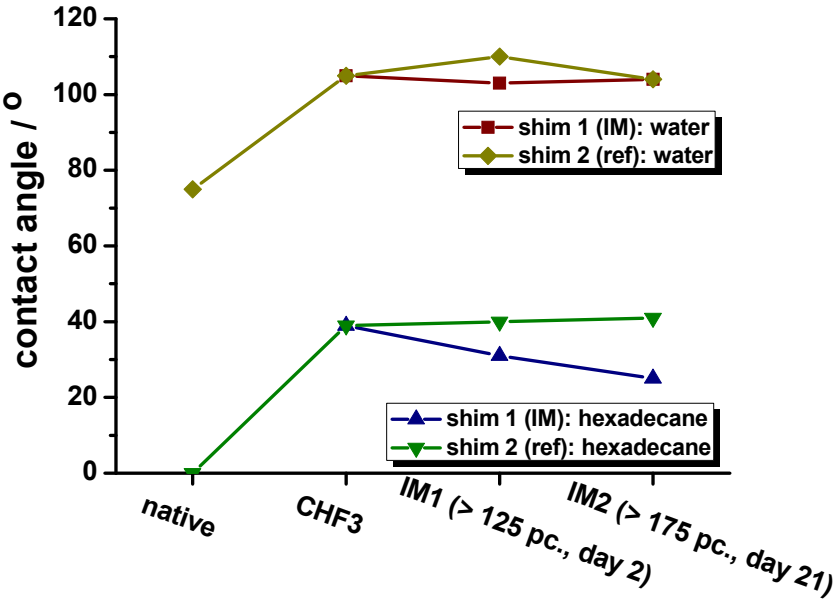

Figure 63: Contact angles of water and hexadecane measured on CHF_3 coated shims at different process steps during polymer replication. A reference shim (shim 2) was used to follow the coating stability without application in injection molding (shim 2)[24].

DISCUSSION. Hexadecane seems to be more sensitive towards changes in the surfaces chemistry than observed for water. While the contact angle of water would imply no changes of the FDTS coating, the changes for hexadecane rather prove degradation of some extent. Unfortunately, XPS measurements of this shim were not recorded but could have revealed a possible decrease in fluorine concentration caused by degradation during injection molding. However, few XPS measurements conducted on Topas 5013 samples injection molded using a CHF_3 coated shim did not show any trace of fluorine suggesting a good mechanical stability during injection molding.

[24] Data shown are presented without error bars. The standard deviation was < 3 ° for all measurements and was removed to improve clarity.

STABILITY OF FDTS. The contact angles of water and hexadecane on two freshly FDST coated nickel shims were analyzed before and after injection molding of about 75 pieces. No substantial decrease in the contact angle of water and hexadecane was observed. The contact angles of water and hexadecane decreased from 108 ± 1 ° to 104 ± 1 ° and 63 ± 1 ° to 57 ± 1 °, respectively, which is in the same order of magnitude as statistical variations of the contact angle (≤ 5 °).

Additionally, one shim was monitored over a longer period (≥ 500 pieces, about one month) to investigate the long-term stability of frequently used FDTS coatings (Table 9, sample 1; Figure 64). The contact angle of water did almost not change over a period of at least 500 molding cycles, decreasing from 108 ± 1 ° to 101 ± 1 °. The contact angle of hexadecane decreased from 71 ± 1 ° to 47 ± 5 °. The strongest decrease was observed during the first 150 pieces leading to a contact angle of 57 ± 1 ° (equally to sample 1 and 2). Pieces were injection molded at a mold temperature of 80 ° and a melt temperature of 220 – 280 °C. However, the initial contact angle of hexadecane on the freshly coated nickel shim was higher for sample 3 than for sample 1 and 2. Following pieces were injection molded at a mold temperature of 40 – 100 °C and a melt temperature of 250 °C leading to a decrease of further down to 47 ± 5 °. Lastly, a fourth shim was used to investigate the "annealing" of FDTS at 130 °C prior to injection molding. Similar to sample 1 and 2, no decrease of the contact angle was measured for at least the first 50 pieces. It has to be investigated in further detail if and at what temperature exactly, annealing may improve the coating quality.

Table 9: Contact angle measured for FDTS coated samples examined during injection molding.

	Sample 1	**Sample 2**	**Sample 3** [25]	**Sample 4**
Pieces	> 75	> 75	> 500	> 50
Mold temperature	135 °C	135 °C	100 °C	80 - 100 °C
Melt temperature	260 – 280 °C	260 – 280 °C	220 – 280 °C	250 °C
Annealing	130 °C	130 °C	130 °C	No
Water before IM	108 ± 1 °	108 ± 1 °	108 ± 1	112 ± 1 °
Water after IM	108 ± 1 °	104 ± 1 °	101 ± 1 °	113 ± 1 °
Hexadecane before IM	60 ± 1 °	63 ± 1 °	71 ± 1 °	74 ± 1 °
Hexadecane after IM	56 ± 2 °	57 ± 1 °	47 ± 5 °	66 ± 2 °

[25] Data presented in Figure 64.

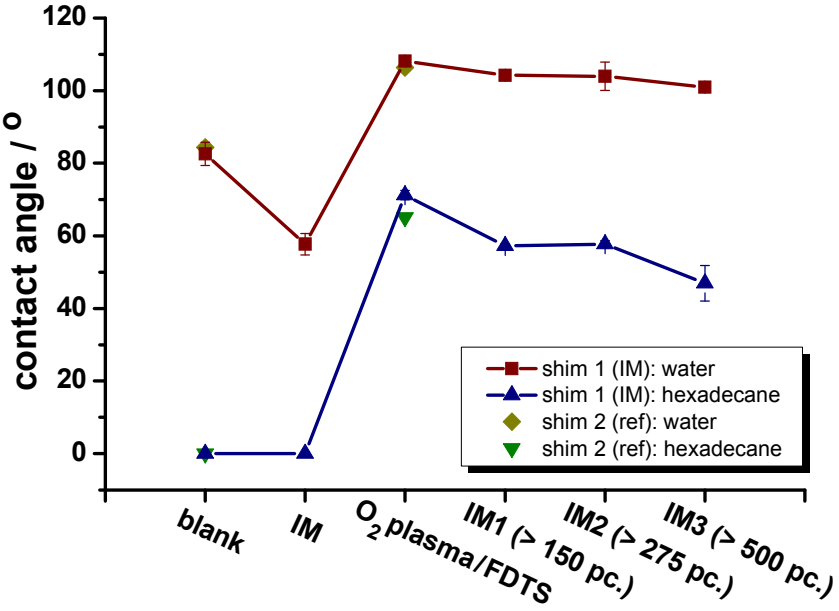

Figure 64: Contact angles of water and hexadecane measured on FDTS coated shim (shim 1 = sample 3) at different process steps during injection molding of Topas 8007 (T_{mold} = 40 – 100 °C). A reference shim (shim 2) was used to follow the coating stability without application in injection molding (T = 23 °C).

XPS measurements were conducted on different Topas 8007 samples injection molded from FDTS coated nickel shims (annealed). An extensive measurement was performed for a freshly FDTS coated nickel shim (annealed). Thereby, the 1st piece contains 0.75 at.% and the 2nd piece 0.32 at.% fluorine. From the 27th piece on, no fluorine was found on Topas 8007 samples injection molded from that shim[26]. These pieces were molded at a mold temperature of 100 °C. From the 83rd piece on, no fluorine was found on Topas 8007 samples injection molded from that shim. Another XPS measurement done on the 25th piece molded from the nickel shim presented as sample 2 showed no fluorine traces as well.

[26] 83rd, 110th and 137th piece did not show any fluorine as well. These samples were molded at T_{mold} of 60 – 80 °C.

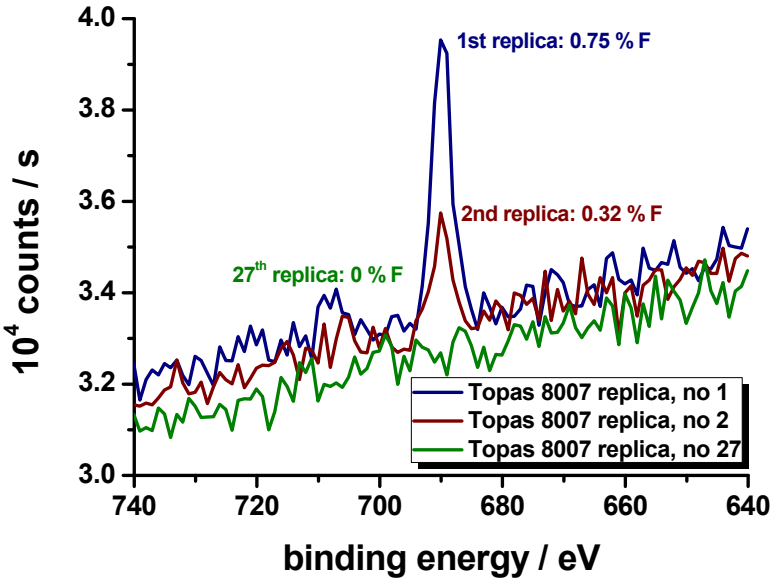

Figure 65: Fluorine peak extracted from XPS measurements for a set of Topas 5013 pieces injection molded from a freshly FDTS coated nickel shim. Injection molding was done at a mold temperature of 100 °C.

DISCUSSION. The contact angles of water and hexadecane on two freshly FDST coated nickel shims (sample 1 and 2) showed no substantial decrease in the contact angle of water and only to small extent for hexadecane was observed for the first 150 pieces. Similar contact angles were obtained for sample 3 after injection molding of 150 pieces, though the initial contact angle of hexadecane was about 10 ° high indicating better initial FDTS coating. This indicates that FDTS possibly degrades but only to a small extent. The monitoring of the contact angles for sample 3 show that after 150 pieces the contact angle of hexadecane decreases to a substantially smaller extent. The first 150 pieces of sample 3 as well as pieces of sample 1 and 2 were injection molded at a mold temperature up to 280 °C. Considering that FDTS degrades at temperatures of 300 °C [Devaprakasam 2004], it is very likely that the FDTS layer is damaged upon contact with hot polymer melt (250 – 280 °C) even though the melt cools rapidly. This is supported by the fact that for sample 3, the the contact angles of water and hexadecane decreased slower for subsequent molded pieces where only a melt temperatures of 250 °C was applied. The fact that the contact angle of hexadecane decreased to about 57 ° even though the initial contact angle varied about 10 ° suggests that if FDTS is damaged by high temperatures, the coating quality after applied temperature is constant. Comparison of the contact angle obtained for an unannealed FDTS coating used at a melt temperature of 250 °C showed no noticeable difference. This indicates that rather the melt temperature is might influence the coating than the annealing step. Results presented for sample3 (shim 1) were recorded simultaneously to the injection molding of 40 nm wide and 100 nm high pillars in Topas 8007 presented in Section III-4.2.

XPS measurements showed that fluorine is transferred from the nickel shim to the Topas replicas during the molding of the first 27 pieces (sample 3 and one additional sample) to a small extent (0 – 0.75 at.%). Afterwards, no fluorine traces were observed. Therefore FDTS is assumed to be applicable in injection molding for mass-fabrication of polymer replicas (up to 500 pieces). This is quite the

opposite of the stability of the fluorocarbonsilane[27] described by Pranov et al. In their setup an antistiction layer formed from fluorocarbonsilanes were only able to withstand one replication cycle [Pranov 2006]. Linear intrapolation allowed to calculate the maximum concentration possibly transferred to Topas for the first 27 pieces. Summing up these values, a maximum fluorine concentration of 0.19 at.% could possibly be removed from the nickel shim during injection molding of the first 27 pieces at a mold temperature of 100 °C. Considering a total fluorine concentratrion of 33 at.% for the freshly coated nickel shim, 0.19 at.% is a negligable amount.

STABILITY OF PFDT. The thermal stability of PFDT on gold coated nickel is not as good as for CHF3 or FDTS on native nickel as shown in Figure 66 and described above. The contact angles measured for water and hexadecane decrease from 98 ± 1 ° and 52 ± 4 ° on freshly coated PFDT to 90 ± 1 ° and 33 ± 2 °, respectively, after injection molding of only 25 to 50 pieces at 80 °C (Figure 66).

XPS measurements revealed that a large amount of fluorine (3.23 at.%) is present on the first injection molded piece. The sample was injection molded at a mold temperature of 80 °C.

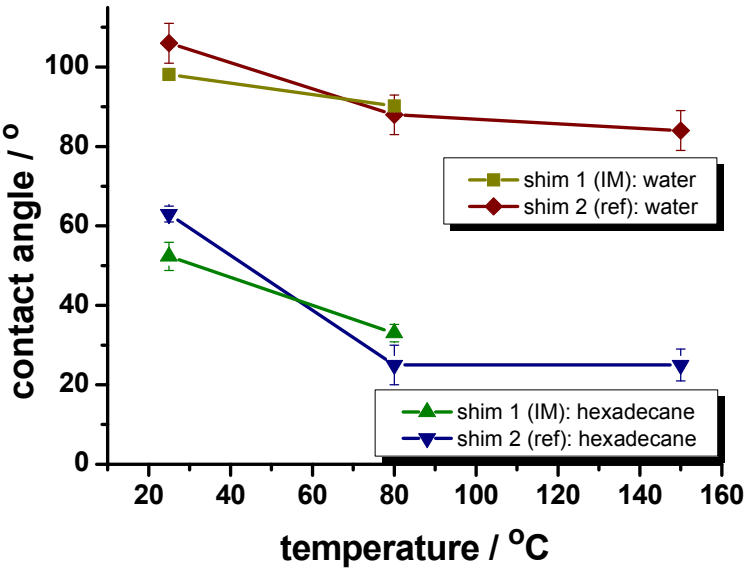

Figure 66: Contact angles of water and hexadecane measured on PFDT coated gold/nickel used for injection molding (shim 1, < 50 pc.) and heated to different temperatures (shim 2). The stability at increased temperatures of 80 or 150 °C as well as for injection molding of Topas 8007 (T_{mold} = 80 °C) seemed to be rather low.

DISCUSSION. The large decrease of the contact angle for water and hexadecane suggests a worse adhesion of the PFDT to gold or faster degradation of PFDT compared to FDTS and CHF3. This results in a gradual damage during injection molding. Fluorine is thereby transferred to a larger extent to the molded Topas samples as measured for FDTS. PFDT does therefore not seem to be an applicable antistiction coating for injection molding.

[27] Tridecafluoro-1,1,2,2,-tetrahydrooctyl trichlorosilane ($C_8F_{13}H_4SiCl_3$).

4.2.2.1. Summary

The uniformity of freshly deposited antistiction coatings is very good exhibiting a maximum standard deviation of less than 5° for commonly 3 drops measured per surface, coating, and test liquid[28].

CHF_3 and FDTS seem to be valuable antistiction coatings exhibiting no substantial degradation during injection molding[29]. However, FDTS is assumed to be the superior antistiction coating for injection molding on nickel compared to CHF_3. Contact angles achieved for Topas 8007 and 5013 are higher and loss in adhesion strength was stronger for FDTS coated nickel. Moreover, the FDTS is deposited in a self-assembled monolayer with higher precision than possible for CHF3. Considering nanoholes of 50 nm in diameter the thickness of the coating can have a substantial influence on the final structure dimension.

[28] Water, hexadecane, Topas 8007, Topas 5013.
[29] unstructured, flat nickel shims

4.3. Injection Molding

4.3.1. Injection Molding on Native Nickel Molds

Microfluidic structures were injection molded resulting in about 200 µm wide and about 49 ± 2 µm deep channels in Topas 8007 or 5013 (Figure 67, Figure 68). The structure dimensions of the Topas replica comply very well with the SU-8 master and nickel mold. No difference between injection molding of microstructures in Topas 8007 or 5013 under adjusted parameters was observed. Both grades replicate even small defects such as sidewall scalloping from the original structures etched in silicon (master) (Figure 69) or undercut from the silicon master (Figure 70). Though the *flat* steel mold part was polished to mirror-like finish, the small grooves (several micrometers) from the polishing were replicated into Topas as well.

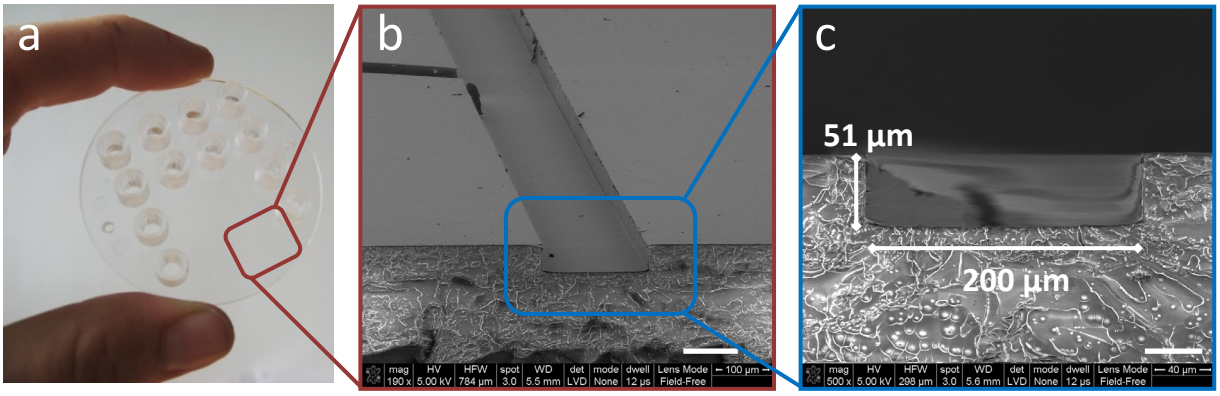

Figure 67: Photo of a microstructured polymer part in Topas 5013 (a) molded from the *luer* steel mold (movable mold part) and a microstructured nickel shim (stationary mold part). SEM images of a microchannel in Topas 5013 (b, 5 ° tilted) and the cross-sectional view (c). Scale bars: 100 µm (b), 40 µm (c).

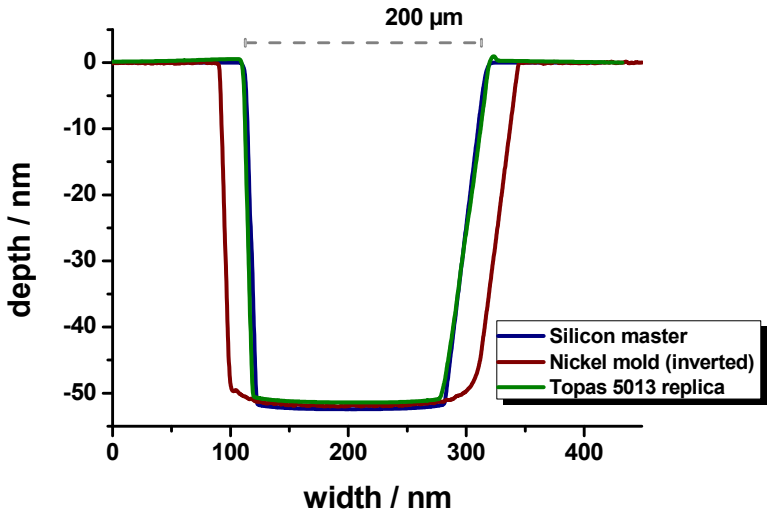

Figure 68: Cross-sectional profile of silicon master, nickel replica, and Topas 5013 replica.

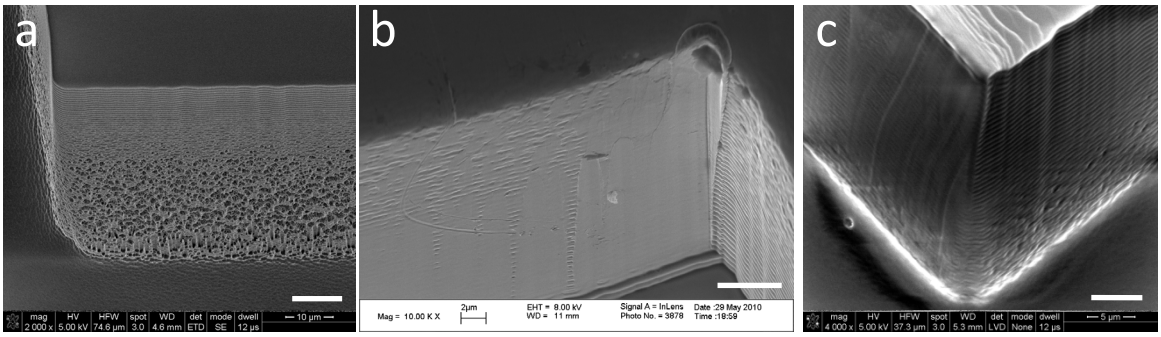

Figure 69: Tilted SEM images of silicon master (a), nickel mold (b), and Topas 5013 replica thereof (c). It is to note that the SEM images are representative but do not display the exactly same spot. Scale bars: 10 µm (a), 5 µm (b, c).

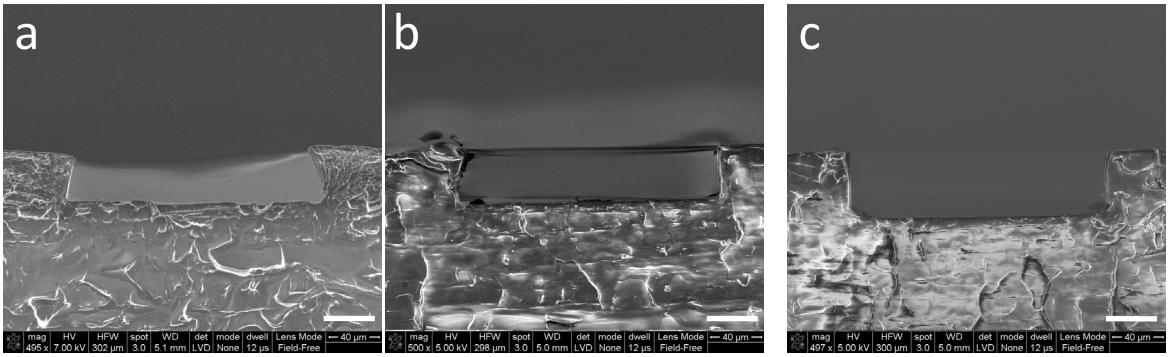

Figure 70: SEM images of cross-sections of Topas 5013 and 8007 replicated from nickel shims based on different masters. Topas 5013 replica based on SU-8 master (a), Topas 8007 replica based on SU-8 master (b), and silicon master (c). In images "a" and "b" small undercuts are visible, in "c" straight sidewall were achieved. Scale bars: 40 µm.

MOLDING DEFECTS. The injection molding of both grades was often accompanied by machinery failure (e.g. tool heating break-down) and demolding problems. The solidified part repeatedly remained in the stationary part (in case of flat mold) or movable part (in case of luer mold), increasingly at injection or holding pressures above 800 bars, mold temperatures above 100 °C for Topas 8007 or 135 °C for Topas 5013. Similar occurs for melt temperature above 270 °C and ejection temperatures above 60 °C for Topas 8007 and 70 °C for Topas 5013. If a solidified polymer part adhered too strong to the luer mold ejector pins partially fractured the part. The strong adhesion of solidified polymer parts to the luer mold is mainly caused by sub-optimal mold design. Twelve movable steel pins are integrated in the luer mold to form female luer connectors into polymer. The dimensions of these twelve pins are very concisely designed to allow moving of the pins while avoiding excess material flowing into the mold cavity between pins and steel mold. Sub-optimal process parameters led also to common injection molding errors like burn marks[30], flashes[31], flow lines[32], sink marks[33]or micro

[30] Burn marks are caused by air entrapped in the mold and compressed by injected polymer. At a certain point the entrapped air auto-ignites burning the plastic surrounding polymer. Burn marks evolve in molds with insufficient venting and for too high injection velocities.

[31] Flashes are excessive polymer forced out of the cavity. Flashes are caused by for example too low clamping force, too high injection speed or too high injection pressure.

[32] Flow lines are off-tone (for Topas: opaque) lines parallel to the flow direction. Flow lines appear when the polymer melt cools and solidifies before the cavity is filled caused by e.g. too low injection speed or too low mold temperature.

cracking[34]. Other errors typical appearing in injection molding of thermoplastics [WIKI 2011-IM] were not observed if sufficient filling of the mold was achieved.

Molding defects and part release were strongly reduced by optimizing process parameters (Section II-4.1., Table 3) though sink marks and micro cracks could not be removed completely. Sink marks first appeared after removing the external water cooling system (thermostat) and switching to cooling setup 3 (Section II-4.1.1.). Micro cracks and sink mark commonly appeared on the nickel shim side while the steel mold side remained defect free. The same result was obtained for a microstructured and unstructured (flat) nickel shim. Besides, a strong "clack" sound often accompanied the demolding when the molded part was released from the stationary mold. Although microstructures were well replicated in both Topas grades, in many cases sidewalls possessed a "tip" of excess material on top of the sidewall edge (Figure 71).

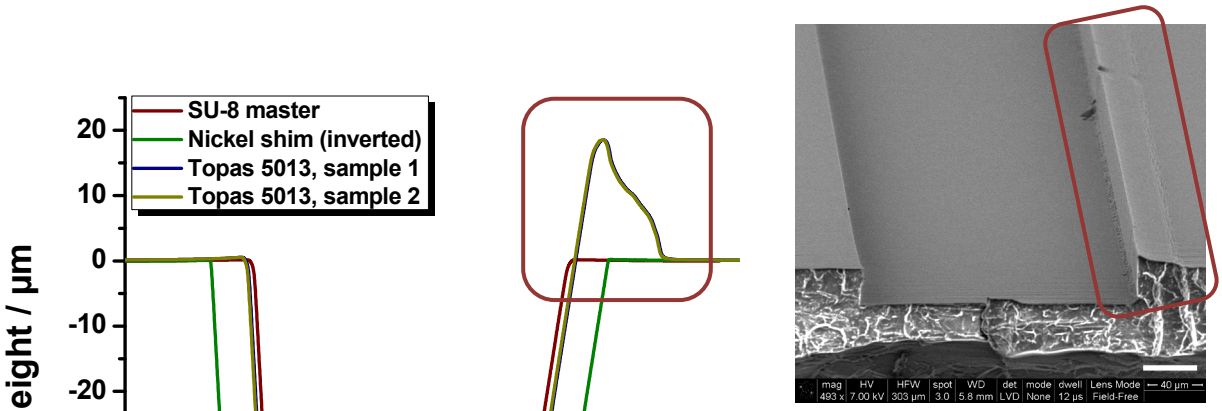

Figure 71: Cross-sectional profile of SU-8 master covered with gold and nickel and Topas 5013 replica thereof (left) and SEM of Topas 5013 replica (above). A "tip" of excess material is visible on the right hand side of the channel (red rectangle). Scale bar: 40 µm.

There are different stress-related factors such as mold temperature, cooling time, holding pressure. The inherit stress distribution was analyzed using a plane polariscope. Topas 5013 and 8007 parts injection molded from *luer* and *flat* molds were analyzed. Topas 8007 was injection molded at standard parameters. Topas 5013 was injection molded using a mold temperature of 125 °C. No significant stress was observed for Topas 5013 (Figure 72 d1-4). In fact it is difficult to obtain visible stress as shown in Figure 72 d4. The part was heated up to 150 °C and manually deformed. Topas 8007 retain little stress incorporated during injection molding (Figure 72 e1 - 2) compared to commercially injection molded polystyrene samples (Figure 72 b) and Topas of unknown grade (Figure 72 a).

[33] Sink marks are local depressions in the surface of the molded part. Sink marks are usually caused by non-uniform cooling result of inhomogene shrinkage of the polymer.

[34] Micro cracking is cracking of the surface of molded parts caused by internal stress due to e.g. too high injection or holding pressure, or stiction of the polymer to the mold.

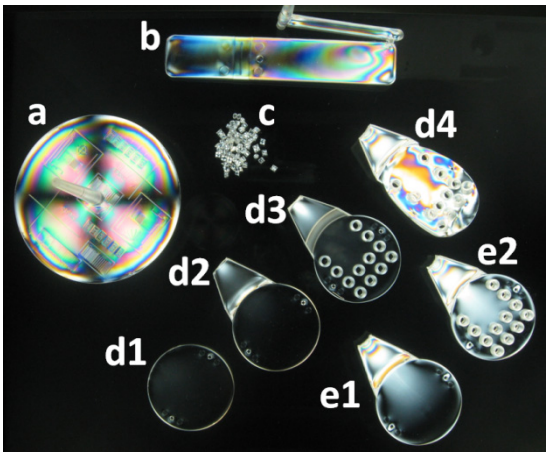

Figure 72: Photo of different polymer samples under plane polariscope showing tension lines as different colors. Topas of unknown grade (a), polystyrene (b), Topas 5013 pellets (c), Topas 5013 (d1 – 4), Topas 8007 (e1 – 2). Topas 5013 heated up to 120°C and mechanical deformed (d4).

DISCUSSION. Microstructures can be replicated with high fidelity by injection molding using Topas 8007 or 5013. No difference in replication quality was observed for either grade. A good surface finish was achieved for optimized process parameters (Section II-4.1., Table 3), though sink marks and micro cracks remained on the nickel shim side of the polymer parts. The *luer* or *flat* steel mold (movable mold part) has been treated with an antistiction coating facilitating the release on molded parts. The fact that the polymer part was molded with a very good surface finish on the steel mold side but with micro cracks on nickel mold side lead to the conclusion that micro-cracks are caused by strong adhesion of the solidified polymer to the nickel mold. An antistiction coating applied on the nickel mold is therefore expected to reduce micro cracks. However, sink marks are usually caused by insufficient or inhomogenous cooling. Heating and cooling of the steel mold holding the nickel shims is designed to provide a uniform cooling and heating rate over the whole shim surface. It is unknown why sink marks appeared frequently after the external cooling system (thermostat) was removed though process parameters were kept unchanged.

Problems arising during demolding can have different origins. On the one hand, the adhesion of the solidified polymer on the flat nickel shim can have a strong influence on the demolding. On the other hand, excessive packing of polymer can lead to high compression of the polymer during filling. Certain extend of shrinkage of the hot, low viscous polymer melt during cooling and solidification is necessary though unwanted to larger extend to be able to release and eject the molded part. Topas exhibits very small shrinkage (Topas 8007: 0.1 – 0.5%, Topas 5013: 0.4 – 0.7 % [35]) which allow for high-precision molding but also complicate demolding of structures such as used in this thesis. Commonly the application of tapered sidewall and round edges is recommended to facilitate demolding. Suboptimal mold design such as undercuts, steep sidewalls, large surface-to-volume ratio complicated demolding and led most probably to insufficiently demolded as fractured parts. For both microstructured molds, defects are present that affect smooth demolding; the sidewall scalloping (or porous sidewall surface) for molds based on silicon masters and re-entrant sidewall profiles in case of SU-8 based molds. Although microstructures were molded with good surface quality a “tip” of excess material was observed for all nickel shims. A metal hook in the movable mold part attached to polymer parts drags molded pieces out of the stationary mold containing the nickel shim with

[35] Values stated by the manufacturer (Topas Advanced Polymers GmbH). The extent of shrinkage depends heavily on the process parameters (values neither specified by the manufacturer nor measured experimentally in this project).

microstructures. Since the hook is only attached to one point the polymer parts are slightly tilted during demolding. It is very likely that the nickel shim sidewall moves polymer along the sidewall of the molded part and "deposits" it on top of the sidewall (Figure 73). This is supported by the fact that only one side of the channel walls are affected, commonly the side that is further away from the point where the molded part is dragged out of the stationary mold. The plastic deformation is facilitated by re-entrant (SU-8 master) or scalloped sidewalls (silicon master) of microstructures in nickel. In the few cases where no deformation was measured by a mechanical profilometer, deformations as stress lines were still visible by SEM (Figure 74).

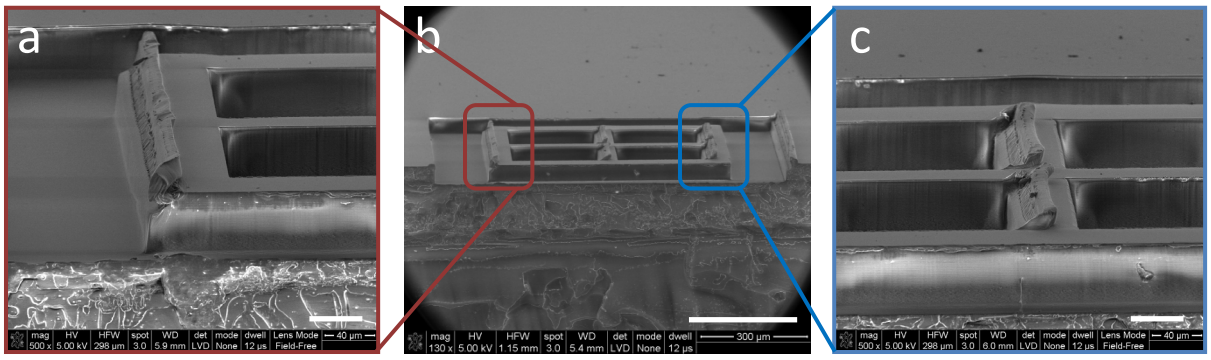

Figure 73: SEM images of the center alignment mark replicated in Topas 5013 visualizing the peak evolution. In the left images (a) it seems as if parts of the sidewall were scraped off and finally turn down on top of the alignment mark. Scale bars: 40 µm (a, c) and 400 µm (b).

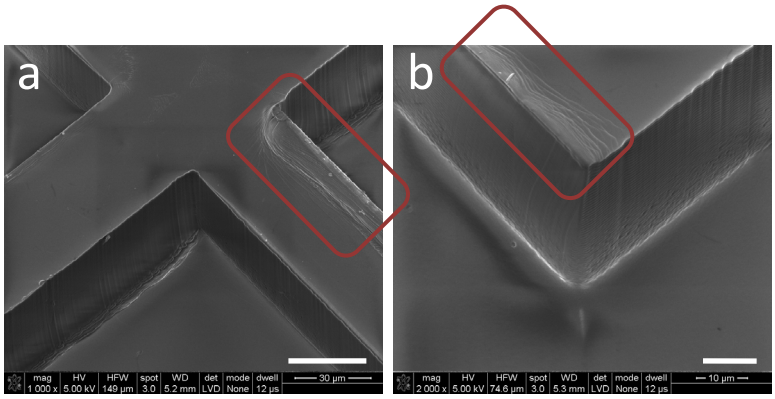

Figure 74: SEM images of Topas 5013 replicas visualizing beginning deformation of the sidewall (red squares). Structures shown posses the deformation on the same side, image b is rotated about 180 °. Scale bars: 30 µm (a) and 10 µm (b).

The application of antistiction coatings for injection molding of Topas 8007 and 5013 was investigated in detail and will be described in the following section. Special focus was set on investigating the "tip" problematic described above. Firstly, samples were injection molded for three different nickel molds based on structured silicon, SU-8, and SU-8 covered with gold to compare molding defects and their result on the injection molding quality. Secondly, parts molded on untreated (native) and fluorosilane coated shims were compared to evaluate the influence of the surface chemistry. Thirdly, the ejection temperature was varied for parts molded in Topas 5013 using the silicon based nickel shim with fluorocarbonsilane coating. Finally, parts from different molding cycles were analyzed to probe for wearing of the shim and related appearance of the "tip".

4.3.2. Injection Molding on Antistiction Coated Nickel Molds

Nickel shims coated with a monolayer of fluorosilane (FDTS) resulted in polymeric microstructures of similar replication fidelity as achieved for uncoated nickel molds. No differences in width or height were observed. The frequency of the injection molding cycle interruptions caused by problems in ejecting molded parts was significantly reduced. Micro cracks and the strong "clack" sound mentioned before disappeared completely. Furthermore, flow lines did not appear until the mold temperature was lowered to 40 °C (for Topas 8007 [36]). In case of Topas 8007, for example, parts molded on untreated nickel shims displayed flow lines on the nickel shim side for a mold temperature of 60 °C. The steel mold side resulted in a good surface finish. For fluorosilane coated nickel shims, the flow lines disappeared on the nickel shim side. For a mold temperature of 50 °C flow lines were visible on the steel mold side. For a mold temperature of 40 °C flow lines were visible on both sides of the molded part.

The "tip" of excess material as observed for uncoated shims appeared randomly as well. In the Figure 75 and Figure 76 shown below, the replication quality in terms of excess material deposited on top of the sidewall is worse for FDTS coated shims than for native shims.

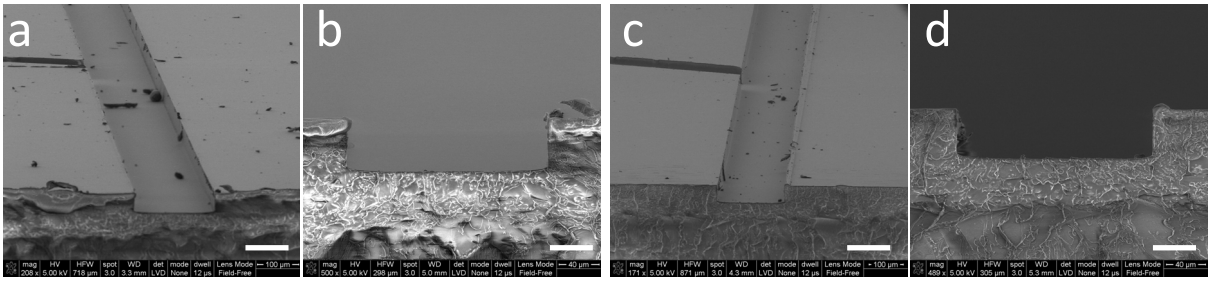

Figure 75: SEM images of Topas 5013 parts replicated from the native mold (based on silicon) (a (5° tilted) and b) and the FTDS coated mold (c (5° tilted) and d). Scale bars: 100 µm (a, c) and 40 µm (b, d).

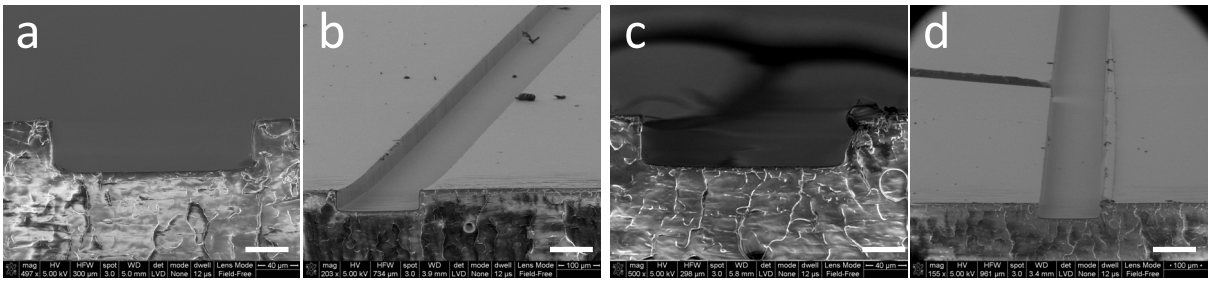

Figure 76: SEM images of Topas 8007 parts replicated from the native silicon based mold (a (5° tilted) and b) and the FTDS coated mold (c (5° tilted) and d). Scale bars: 100 µm (a, c) and 40 µm (b, d).

[36] The influence of antistiction coating on the appearance of flow lines was not tested for Topas 5013. Injection molding tests with Topas 5013 were only conducted in a range with good surface finish, without flow lines and micro cracks.

DISCUSSION. The application of fluorocarbonsilane on nickel molds did not significantly influence the molding quality but reduced defects such as micro cracks and flow lines. A broader range of parameters could be used with similar replication quality. Micro cracks are very likely to be caused be the very strong adhesion of Topas 5013 and especially, Topas 8007 to the nickel surface. Extremely strong adhesion of Topas to a steel plate with mirror-like finish was observed as well during thermal bonding of injection molded Topas parts as will be described in detail in Section IV-1. The Topas parts were adhering extremely strong to untreated steel bonding plate. After cooling down the Topas parts detached slowly from steel plate. The application of fluorocarbonsilane decreased the adhesion of Topas to nickel as has been investigated earlier (Section II-4.2.). The reduced adhesion improved the demolding significantly. Machine failure caused by demolding errors (part remained in the stationary mold) was seldom appearing. The "clack" sound observed during demolding disappeared as well. However, the major problems emerged during injection molding of microstructures, the "tip" of excess material, could not be visibly improved.

4.3.3. "Tip" of Excess Material

The extent of the "tip" of excess material may cause major problems during thermal bonding of micro- and nanostructured parts reducing the bonding quality. The "tip" may be deformed by the applied heat and pressure, but the bonding strength will most likely result in non-uniform bonding strength, hence leakage in the less bonded areas. Therefore a low tip height, if present, is crucial for achieving sufficient bonding strength.

The following four conditions were analyzed to investigate their influence on the amount of excess material on top of the channel sidewalls:

(1) Mold design (re-entrant or scalloped sidewalls)
(2) Mold surface chemistry (adhesion strength)
(3) Ejection temperature (part stiffness and shrinkage)
(4) molding cycles (mold wearing)

MOLD DESIGN AND SURFACE CHEMISTRY. The analysis of the "tip" evolution with respect to mold design and mold surface chemistry did not show any significant trend. Polymer parts molded from the native silicon based nickel shim resulted in lower "tips" for both polymer compared to the SU-8 based nickel shims (Figure 77). Topas 5013 exhibited lower "tip" heights than Tops 8007 for all shims. After application of a fluorocarbonsilane (nickel surface) or fluorocarbonthiol (gold coated nickel surface) this trend disappeared completely, resulting in a random height distribution for the different shims.

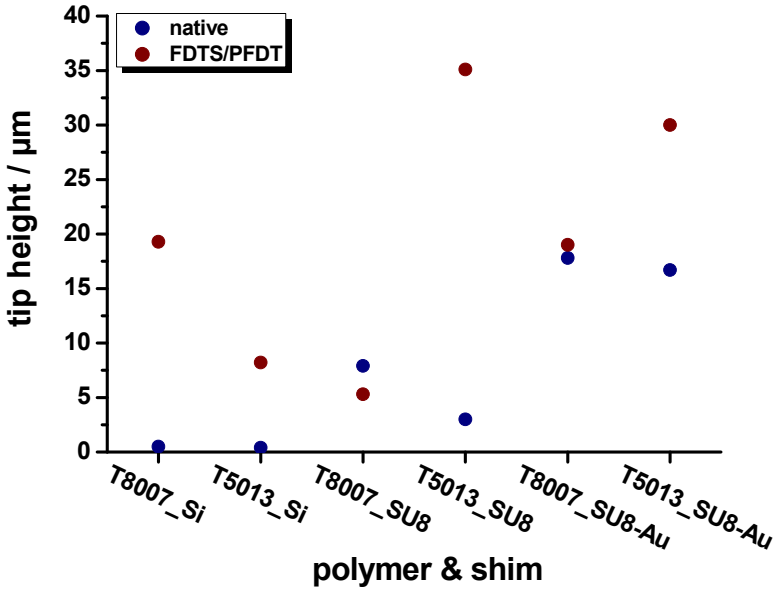

Figure 77: Height of the "tip" evolved for different nickel shims (based on structured silicon, SU-8, or gold covered SU-8).

DISCUSSION. The tip of excess material was substantial lower for Topas 8007 and 5013 for chips molded from the silicon based nickel shim compared to chips molded from the SU-8 based nickel shims. This leads to the conclusion that the slightly re-entrant sidewall observed fro SU-8 based master influences the demolding stronger than the scalloped sidewall from the silicon etching. However, the results obtained for FDTS coated shims do not comply with these observations. The tip height seems to vary randomly. This phenomenon has not been investigated in further detail.

EJECTION TEMPERATURE. Variation of the ejection temperature showed that with reducing ejection temperature the "tip" height decreases tremendously from about 19 µm at 70 or 80 °C to 0.7 µm at 39 °C (Figure 78). Although a very low ejection temperature reduces the problem of the "tip" to a sufficient level, it is to note that cooling of the mold from 125 °C down to 70 °C and 40 ° takes about 75 and 235 s, respectively. Lastly, pieces of different molding cycles (1, 25, and 80) were measured but showed no significant change of "tip" height (Figure 79).

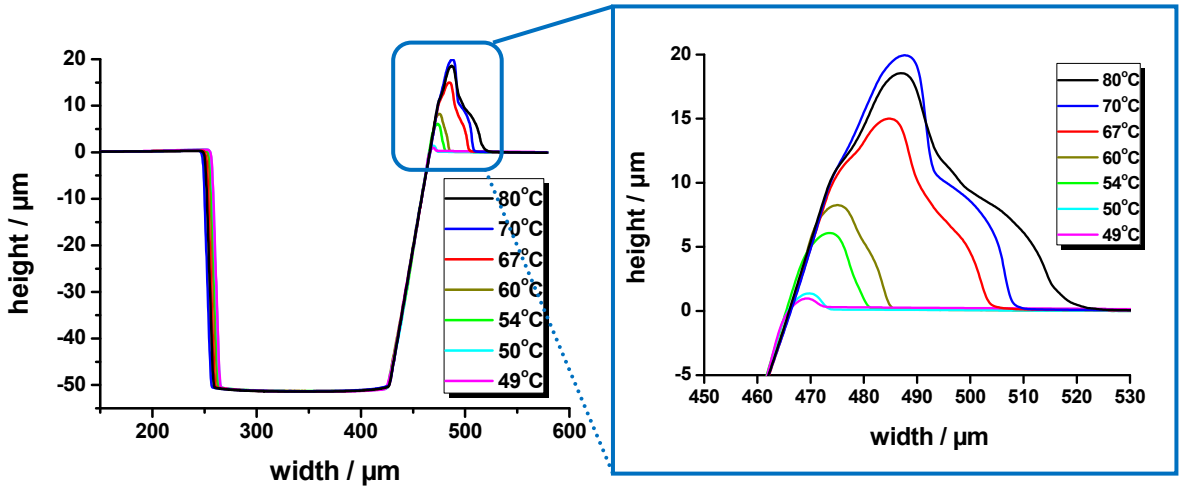

Figure 78: Evolution of the "tip" of excess material depending on the ejection temperature. The "tip" height decreases strongly with decreasing ejection temperature.

DISCUSSION. The ejection temperature had the strongest influence of any of the investigated parameters on the tip evolution. The tip height decreased from about 19 µm down to acceptable 0.7 µm. The strong decrease can be explained by either increased shrinkage of the polymer leading to detachment of the sidewalls before demolding or by increased stiffness for lower temperatures, especially in case of Topas 8007 with a glass transition temperature of only about 78 °C. On the other hand, the antistiction coating did not seem to have any visible influence on the tip height. In case of the mold design initially it seemed that the silicon based nickel shims would result in significantly lower tip height than for the SU-8 based shims. Considering that the microchannels formed in SU-8 most probably possessed re-entrant sidewall profiles this result would support the assumption that the tips are caused by structures in nickel grinding over the polymer moving material to the top of the sidewalls. The sidewalls in silicon were straight though scalloped which apparently caused less problems.

MOLD WEARING. Polymer replicas of varying cycle number injection molded in Topas 5013 were investigated to probe for possible wearing of the nickel shim. Mold wearing occurs when structures are deformed by the pressure applied during injection molding. Deformed structures present undercuts, re-entrant sidewalls or other defects that can influence the demolding, hence producing increasingly large tips for increasing cycle numbers. However, no significant increase was observed within the first 80 molding cycles leading to a tip height of about 8 – 13 µm (Figure 79). In fact, the first sample exhibited the largest tip height of about 13 µm.

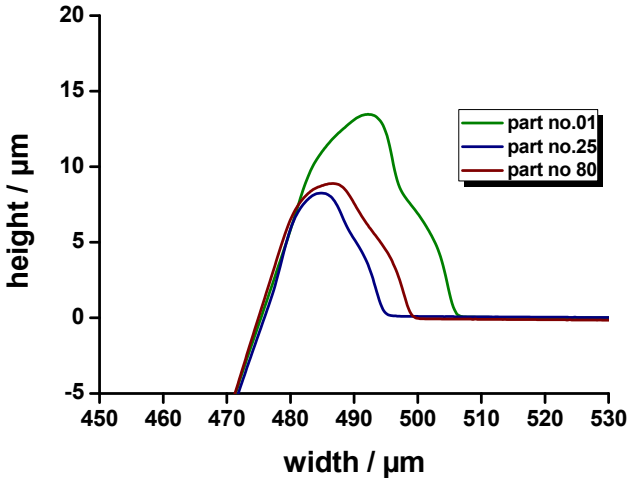

Figure 79: Evolution of the "tip" depending on the cycle number for Topas 5013 molded on the silicon based nickel shim. The "tip" height does not increase with increasing cycle number.

DISCUSSION. The analysis of Topas parts molded at different cycle numbers did not result in a visible increase of the tip height as would be expected in case of mold wearing caused by for example insufficient filling of the cavities on the backside of the nickel shim. However, no dependency of the "tip" height on the number of cycles was observed (for 80 pieces). Therefore it is assumed that the filling of the backside was sufficient and no mold wearing occurred on the investigated time scale. The difference in tip height for the first and the following samples might was possibly caused by a difference in ejection temperature. For standard injection molding experiments, the ejection temperature varied at least up to 5 °C.

Chapter 3

Fabrication of Polymeric Nanostructures

1. Design: Nanostructures for Cell Adhesion Modulation

The reaction of cells to nanostructured surface topography was shortly discussed in the introduction and examples of possible reactions of individual cell types to specific topographies and materials were given. The knowledge about the reaction of cells to specific polymeric materials (native or treated) is very limited and especially the introduction of nanostructured surface topographies has not resulted in any hypothesis that can predict behavior of a given cell type on a particular nanostructured topography. The cell can theoretically react in three different ways to nano- or microstructured surfaces: adhering to elevated surfaces only (Figure 80, left), adhesion of the full area by deformation of the cell body into the structures (Figure 80, center) or by penetration of the cell membrane by the structures (Figure 80, right). It is to note that in this thesis only option one and two were considered with respect to the design of nanostructured patterns. At this point no information was found regarding structures sizes at which nanostructures possibly penetrate the cell membrane.

Important length scales are still debated as shortly discussed in the introduction, and in more detail in the appendix. Nevertheless, assumptions about the cell adhesions can be made based on knowledge gained about the mechanisms and cell properties involved in the adhesion process:

(1) Length of the extracellular part of the integrin: about 15 – 20 nm in activated state
(2) Flexible cell body: complex function of membrane stiffness, cytoplasmic pressure, cytoskeleton flexibility, and others
(3) Sufficient integrin binding sites: 400 – 1200 integrins μm^{-2}, distance < 73 nm

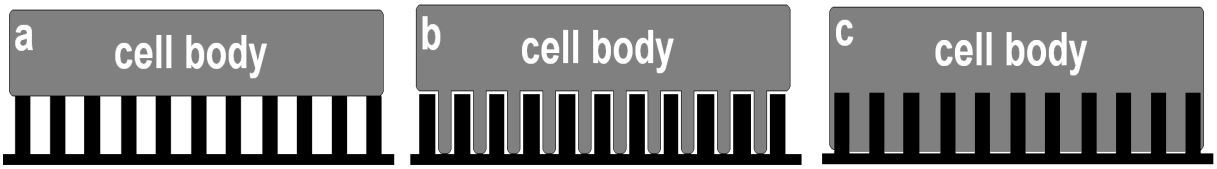

Figure 80: Sketch visualizing how the cell can react to nanostructured surface topographies. The cell cannot sense the bottom (a), the cell floats in nanostructured cavities sensing the full surface area (b), and the cell is penetrated by the nanostructures (c).

Nanostructured topographies were chosen based on knowledge gained by literature study compromised by fabrication limitations (resolution, time, and cost). The decision was made for nanostructured hole and pillar patterns with feature sizes of 50 – 500 nm in width and height-to-width aspect ratios of 1:2 to 2:1 since structures of these dimensions were expected to have a major impact on the adhesion strength of cells on nanostructured topographies. Special focus was set on the fabrication of about 40 nm wide and 100 nm high structures for process analysis and optimization. Due to their excellent characteristics with respect to injection molding and biocompatibility, Topas 5013 and 8007 were used for all injection molding experiments. An extensive description of both grades is given in the introduction, in Section I.4.3.

ASPECT RATIO, PITCH, AND SIZE. In order to regulate cell adhesion the cell must only be able to sense areas that are elevated but not the bottom in between. In other words, the cell should experience a discontinuous surface with only a certain area fraction presented to form adhesion points. There are two major issues to consider with respect to aspect ratio and pitch of nanostructured patterns: firstly, can a cell deform into nanostructured cavities, i.e. into holes or in between nanopillars? Secondly, can focal adhesions assemble in nanostructured cavities?

Estimation of the deformation of a cell into nanostructured cavities is a non-trivial problem. Various research groups have tried to simulate the deformation of a cell partially based on experimental values for cell properties such cell membrane elasticity or bond density (integrin bonds), but failed to accurately predict the deformability due to its complexity and lack of experimental support [Kong 2008, Palsson 2008]. The deformability of a cell depends on many factors such as membrane elasticity, cytoplasmic pressure, orientation of the cytoskeleton, and proteins incorporated in the membrane.

The elasticity of various cell types has been investigated and ranges commonly from 0.1 – 100 kPa, for example endothelia cells (0.2 – 18 kPa) [Ohashi 2002, Sato 2004, Pesen 2005], osteoblasts (0.3 – 20 kPa) [Simon 2003], astrocytes (2 – 20 kPa) [Yamane 2000], fibroblasts (3 – 12 kPa) [Rotsch 1999], or chicken cardiocytes (5 – 200 kPa) [Hofmann 1997]. Unfortunately one cannot easily calculate the actual deformability from the values of the tensile modulus even if leaving out other cell properties mentioned above. Firstly, forces exerted on the membrane by the cell itself are unknown. Secondly, the cell membrane is a dynamic system caused by constant local changes of its composition (lipids and proteins) generating a certain fluidity. Thirdly, intra- and extracellular signaling regulates cell membrane tension and cytoskeletal elasticity and local transmembrane proteins composition can restrict unhindered deformation of the membrane for example by their actual size, i.e. formation of partially large protein complexes, and by connecting the membrane with the cytoskeleton, i.e. at focal adhesion sites [Safran 2005, Vogel 2006, Palsson 2008, Schmitz 2008]. Fourthly, the membrane deformability is influenced by the rigidity and inertia of the cytoskeleton which results in an effective membrane tension and gives the cell its stability to maintain structure and shape. Furthermore, the cytoplasma imposes equally distributed pressure on the cell membrane which impedes any deformation. According to these assumptions some cell type with a higher bending modulus could probably deform into for example 50 nm wide holes sensing a continuous surface. In contrast, cells with lower bending modulus could most probably not sense the bottom sensing a discontinuous surface. Such cells could only adhere to the area presented by elevated structures and probably adhere less well.

Another approach can be taken in estimating the minimum dimensions of a cell membrane deforming into a nanostructured cavity. The cell membrane consists of a 5 – 10 nm thick phospholipid bilayer with embedded transmembrane proteins (extracellular part of an integrin: 15 – 20nm) and a glycocalyx which takes 20 up to 500 nm, for example20 – 30nm in chicken fibroblasts [Bailey 1985] or 70 – 500 nm in endothelia cells [Pries 2000, Reitsma 2007]. Unfortunately, it is not stated to what extent the measured values contain only membrane compounds or additional parts of the extracellular matrix. Considering only the deformation of a lipid bilayer and additional integrins in a 50 nm wide hole it leads to following conclusion: A tight bended lipid bilayer is about 10 – 20 nm thick (two lipid bilayers on top of each other). Adding integrins on each side of the folded lipid bilayer adds up twice 15–20 nm which results already in a final thickness of 40 – 60 nm. Assuming that a cell

is rather not able to form such a tight "double layer membrane" it is very unlikely that a cell will deform into cavities of 50 nm width independent of its elasticity. On the other hand a cell might be able to deform into 100 nm wide holes and form stable focal adhesion sites.

Estimating the deformability of a cell membrane is difficult, as discussed above, while estimation of possible formation of focal adhesion complexes based on dimensional characteristics appears to be simpler. Focal adhesions are formed by clustering of up to hundred integrins per focal adhesion site with areas up to 1 μm^2. Integrins have a diameter of about 8 - 10 nm and their extracellular part is about 15 – 20 nm long varying for different integrin types [Carrel 1985, Rivas 1991, Nermuth 1988]. Based on experiments it was shown that a maximum spacing of < 73 nm for integrin binding sites is required to allow for clustering and formation of focal adhesion sites [Arnold 2004, Cavalcanti-Adam 2007, Arnold 2008, Selhuber-Unkel 2010]. Others have shown that even a spacing of 140 nm is sufficient for fibroblasts to form $\alpha V\beta 3$-mediated focal contacts [Massia 1991]. Assuming that the cell cannot deform into nanostructures and leaving aside other cell characteristics, the cell will not be able to adhere in nanostructured cavities if the vertical distance between elevated and depressed surface is more than 25 nm, exceeding the length of the extracellular part of an integrin. Under this condition, the adhesion strength of a cell can be reduced by exceeding the distance for single integrins to cluster and form strong focal adhesion sites. Nanostructures with spacing larger than at least 73 nm [Arnold 2004] or 140 nm [Massia 1991] will not allow integrins on different nanostructures to by-pass the gaps in between and cluster to larger focal adhesions. The total adhesion strength will only rely on the focal adhesion sites formed on single elevated areas. It has been found that strong focal adhesion sites consist of up to 100 integrins. In areas of the cell membrane with densely packed integrins (about 1200 integrins/μm^2 [Wiseman 2004]) the average distance is about 32 nm which results in an average of about 10 and 40 integrins per pillar for a width of 50 and 100 nm, respectively (Figure 81). Since the strength of a focal adhesion site is dependent on its size the adhesion strength will vary between nanostructures of different widths.

The strongest effect in reducing the cell adhesion on nanostructures may be achieved by presenting the cell with areas where only one integrin can adhere, as previously done by J.P. Spatz and colleagues [Arnold 2004, Cavalcanti-Adam 2007, Arnold 2008, Selhuber-Unkel 2010]. They have used 8 nm wide gold dots to ensure that only one integrin (width: 8 nm by 10 nm) could bind to the surface. However, this exceeds the resolution possible in fabrication of polymeric nanostructures by injection molding. Smallest structures produced by injection molding so far were 25 nm wide and 40 nm deep structures [Schift 2000].

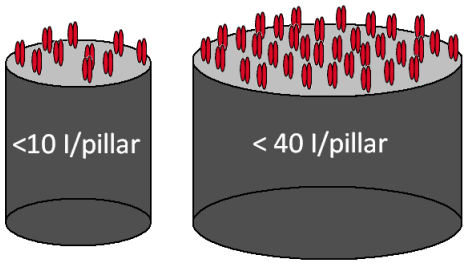

Figure 81: Integrin distribution on a 50 and 100 nm wide pillar at an integrin density of 1200 integrins/μm^2 (integrin concentration at strong focal adhesion sites according to Wiseman2004).

Besides theoretical assumptions of preferable structure sizes and fabrication limits such as stated above, economical considerations limit the nanostructured patterns that were fabricated for this project. Although features down to 5 nm lateral dimension can be written by electron beam lithography, process optimization is time consuming and cost intensive already for 50 nm wide structures. One nanostructured pattern takes about 25 min with additional 45 min for pumping and venting. With a cost of 1000 € per h for the electron beam writer available at DTU Danchip, the fabrication costs is about 800 – 1600 € per mold depending on the number of patterns per shim. Furthermore, injection molding of sub-micron structures is still a non-trivial problem and requires extensive process optimization. The aspect ratio is not only a critical point in molding of polymeric structures, but also in the development in electron sensitive resist. Already height-to-width aspect ratios of larger than three can cause problems during the final drying step after development. Especially nanopillars of widths smaller than 100 nm are likely to collapse.

In Figure 82, structure sizes used in this project are listed, based on the assumption that the adhesion strength will gradually decrease with decreasing structure sizes, expecting the strongest effect for 50 and 100 nm wide structures. For example, on a 50 nm round pillar focal adhesion can be formed containing maximal ten integrins. 200 nm wide pillars present enough area for almost 200 integrins (for 1200 integrin/μm^2) which allow for formation of large focal adhesion complexes. A distance of 200 nm or more is sufficient to separate focal adhesion sites from each other, assuming that the cell would not be able to deform into nanoscaled cavities. Furthermore, already a depth of 50 nm should be sufficient to avoid sensing of the bottom. However since the flexibility of a cell and thereby the extent of deformability is unknown, it was commonly aimed at fabricating structures with an aspect ratio of 1:1 or higher. To verify the effectiveness of attachment area towards changes in cell adhesion, two different patterns were designed introducing a variable surface fraction of about 2 – 75 % (pillars and holes).

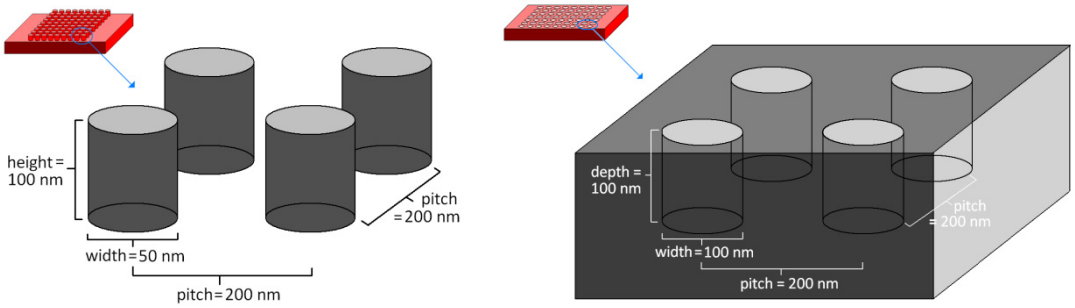

Figure 82: 3D sketch of nanopillar and –hole array used in this thesis exemplified for 50 nm wide and 100 nm high pillars (left)and 100 nm wide and 100 nm deep holes (right).

SHAPE. Not only dimensions but also the shape of structures might play a role in adhesion of cells to artificial surfaces. Though round shapes are dominant in nature, morphological preferences of cells are unknown. No information about any kind of response of cells to differently shaped structures such as change in adhesion or morphology, or cytoskeletal alignment was found. Based on information gained about the adhesion process and involved proteins, it is expected that the shape will rather play a minor role in cell adhesion modification. The adhesion depends on the ability of certain proteins like integrins to bind to their ligands such as the typical RGD motif (arginine (R),

glycine (G), aspartate (D)). It would be very unlikely if the final shape of the surface plays any role as long as the ligand is presented in the right orientation. However, the structures were designed as squared pillars or holes since the electron beam writer software converts any design into angular shapes such as rectangle and triangle. Depending on the precision of circular shape approximation circles take unevenly longer to convert than squares. However, experimental experience showed that squared features tend to round up depending on process parameters like grid and feature size. The effect increases with increasing grid size or decreasing structure size. Regular shapes were chosen to reduce time spend on conversion.

BIOCOMPATIBILITY OF TOPAS 8007 AND 5013. Cyclic olefin copolymer has rarely been used to study cell growth or adhesion. Johansson et al. showed that human epithelial carcinoma cells (HeLa) grow similar on oxygen plasma treated Zeonex (COC from Nipon Zeon) compared to equally treated polystyrene. Topas (COC from Topas Advanced Polymers) resulted in unsatisfactory cell growth [Johansson 2002]. Initial experiments conducted to probe for cell viability showed that 3T3 as well as HeLa cells behave comparable on low pressure oxygen plasma treated Topas 8007 and 5013 to tissue culture grade polystyrene. In contrast, adhesion and proliferation is limited on untreated Topas of both grades.

2. Experimentals

2.1. Fabrication of Nanostructured Topographies

2.1.1. Laser Lithography

The applicability of maskless laser lithography for the fabrication of sub-micrometer features was investigated using the DWL66 Printer from Heidelberg Instruments. The DWL66 is a high resolution pattern generator designed for low volume mask fabrication and direct writing into photo resist on e.g. silicon or silicon dioxide wafers. The system contains of a helium-cadmium laser system with a wavelength of 442nm. An integrated interferometer determines automatically the position of the substrate in all three dimensions and sets the focus length of the laser accordingly. The DWL66 software splits patterns into stripes of a certain width. These stripes are exposed by a highly focused laser while the stage moves fast in x-direction ("fast writing direction"). Stripes are stitched together with high precision (stage address grid: 4 nm) completing the exposed pattern in z-direction ("slow writing direction") (Figure 8). Detailed specifications are listed in Table 10.

Nano- and microstructures were designed using CleWin 4 Pro from PhoeniX, a mask layout design software. The most important process parameters are exposure dose (final laser intensity) and focus depth of the laser referred to as "defocus". The exposure dose can be adjusted by implementing filters (1 %, 10 %, and 31.62 %, 50% light transmission) directly into the laser optics or by modifying the dose in the software (10 – 100 %). The defocus value changes the focus depth of the laser in relation to the automatically determined value and can correct for possible errors.

Table 10: DWL66 properties

Laser	442 nm HeCd
Laser power	25 mW
Writing Head	4 mm
Pixel size	40 nm
Writing Mode	Uni- or bidirectional, high or low quality
Focus Depth	1.8 µm
Stage Address Grid	40 nm
Step Size	300 nm (high quality mode), 600 nm (low quality mode)
Resolution	640 nm (theoretical, 800 nm practical)
Writing Speed	≈ 1 Hz (for full line)
Writing Field	Max. 140 x 140 mm^2
Substrate	photomask, silicon wafer, silicon oxide wafer

Substrates (chrome mask or silicon) were pretreated with HMDS (Hexamethyldisilazane) to improve resist adhesion and subsequently spin coated with positive resist S1805 with 3000 rpm at 400 rpm/s for 60 s. Coated samples were baked at 115°C for 3 min aiming at 0.5 – 0.6 µm film thickness. To achieve maximum possible resolution nanostructured patterns of 300 – 500 nm wide holes were exposed using a 4 mm writing head in unidirectional high quality writing mode. Extensive dose tests were performed applying different filter sets: without filter, 10 %, 50%, 10 + 50%. For each dose test defocus and doses were tested ranging from 100 – 1600 (in 100 steps) and 10 – 100% (in 10% steps), respectively. Exposed patterns were developed in Microposit 15% MF-351 for 60 s at 21°C. Exposed patterns are partially etched into silicon.

2.1.2. Electron Beam Lithography

Most of the nanostructured patterns used for replication by injection molding were written by electron beam lithography applying. The electron beam writer JBX9300FS from JEOL was used for exposures. Detailed specifications of the JBX9300FS are listed in Table 11.

Table 11: JEOL- JBX9300FS properties

Acceleration voltage	max. 100 kV
Current	min. 0.1 nA
Pixel size	4 - 50 nm
Deflection rate	25 MHz
Writing Field	Max. 500x500 μm^2
Resolution	≥ 5 nm

Patterns of 50 – 500 nm designed width were written into positive electron sensitive resist, ZEP520A from Zeonex, at different thicknesses (Figure 83). The resist was either directly used as master for galvanic plating (structures ≤ 200 nm), or as mask for subsequent etching into silicon (structures > 200 nm) or deposition of nickel on masked nickel substrate (structures ≤ 100 nm). The maximum acceleration voltage of 100 keV, an aperture of 6 (aperture hole of 100 µm), and a grid size of 4 nm was used for all exposures to achieve minimum spot size and thereby best structure definition. A writing field of either 100 by 100 or 500 by 500 μm^2 was used. Dose and current were adjusted according to the design, but a dose between 170 and 260 $\mu C/cm^2$ and a current between 0.6 and 2.1 nA was commonly applied.

SPINNING OF ZEP520A. Poly(methyl-α-chloroacrylate-co-α-methylstyrene) (ZEP520A) is positive electron sensitive resists with dry etch resistance in SF_6 of 1:5 compared to silicon and high resolution (good contrast and superior sensitivity compared to PMMA). The layer thickness is very dependent on further process steps, e.g. anisotropic silicon etch mask or direct use as master for electroplating. In the former case layer thicknesses ranging from 50 – 100 nm are commonly used. In the latter case different resist thicknesses are required to achieve different aspect ratios. Spinning curves of different dilutions of ZEP520A with anisol were recorded using the automatic spinner Maximus 804 cluster system (Sister Semiconductor Equipment) and subsequent analysis using the Filmtek 4000 Spectrometer (Scientific Computing International). Wafers were spun for 60 s and subsequently baked at 180°C for 2 min.

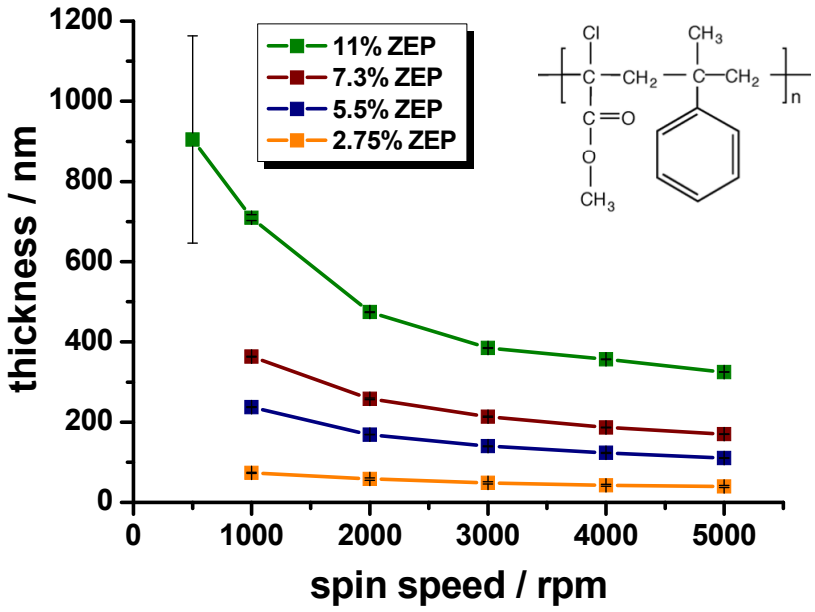

Figure 83: Spinning curve for different dilutions of ZEP520A with anisol; Insert: Chemical Structure of ZEP520 [Ikeurasekiguchi 2005].

The exposed samples were developed for 2 min in ZED-N50, rinsed with isopropanol for 15 s and carefully blow dried with nitrogen.

2.1.3. Silicon Etching

Nanostructured patterns written by either laser or electron beam lithography were partially transferred into silicon by anisotropic etching using the Cluster System C004 (Cluster1) from STS Microsystems. The exposed resist was etch using the recipe *fpe_nano* with an etch rate of about 0.5 – 1.0 nm/s. To achieve an etch depth of 100 and 200 nm samples were etched for 1:45 and 3:30 min, respectively. *fpe_nano* was optimized by Fredrik Persson, former Ph.D. student at the Department of Micro and Nanotechnology, Technical University of Denmark. The exact process parameters are stated in the Appendix I-3, Table 30. Residual resist was removed by immersing the sample in acetone.

Silicon residuals remaining on nickel molds after separation of silicon master and nickel molds were etched using a 30% potassium hydroxide solution. Samples were placed in a petri dish containing 30% potassium hydroxide at 100°C for 4 h. Subsequently, they were washed with ultrapure water.

2.1.4. Galvanic Plating of Nickel

The galvanic plating of nanostructured masters follows the same process as for microstructured masters, described in Section II-2.1.3. Structured resist on silicon or structured silicon wafers are coated with 50 – 100 nm nickel-vanadium alloy followed by electroplating of nickel. The nickel molds insert were cleaned from residual ZEP520A or silicon by applying Remover 1165 or acetone, or by applying potassium hydroxide, respectively. Finally, nickel plates containing nanoscaled patterns are cut into circular shape with radius of 85 mm and two straight cuts of varying sizes (Figure 37) to comply with the dimensions of the insert holder of the injection molder.

2.1.5. Injection Molding

Nanostructured surface topographies were similar to micrstructures replicated in cyclic olefin copolymer, Topas 8007S-04 and Topas 5013L-10, by injection molding using the ENGEL CC200 Victory 80/45 with a screw diameter of 18 mm (Figure 38a). The microstructured nickel mold insert is installed in the dedicated shim holed on the stationary mold. The mold consists of a disc-like cavity with a diameter of 50 mm and a thickness of 2 mm. One side is polished to mirror-like finish (movable mold) while the other holds the nanostructured insert (stationary part) (Figure 38b). Most nickel inserts contain alignment marks, one in the absolute center and four close to the edge, above and below the alignment holes. Nanostructures are commonly placed about 5 mm above the center (closer to the entrance).

Topas 5013 and 8007 were injection molded under various conditions. The range of values tested is given in Table 12. Extensive analysis of the injection molding process was performed for arrays of about 40 nm wide and 100 nm high pillars molded into Topas 8007. Structures were molded with various parameter sets to investigate their influence on the replication fidelity (width, depth, and shape), and molds of varying surface chemistry. The influence of mold temperature, melt temperature, demolding temperature, injection velocity injection pressure, and holding pressure was tested in the range stated in Table 12. For each parameter set only one parameter was changed out of the following standard parameters (Table 13): mold temperature of 80 °C[37], melt temperature of 250 °C, demolding temperature of 40 ± 3 °C, injection velocity of 100 mm/s, injection pressure of 750 bars, and holding pressure of 800 bars[38]. Based on our mold design the injection pressure and holding pressure could not exceed 1050 bars and 800 bars, respectively, to avoid excessive packing which causes insufficient demolding of solidified polymer parts. Injection pressures and holding pressures below 700 bars caused inacceptable macroscopic defects like strong depressions and wavy surface finish.

[37] Standard mold temperature was set to 80 °C, since most research groups recommended injection molding at a mold temperature of about the glass transtion temperature.
[38] Screw diameter: 18 nm, Filling velocity: 0.3 m s^{-1}.

Table 12: Standard process parameters used for injection molding of nanostructures in Topas 8007 and 5013

	Topas 8007	**Topas 5013**
Mold temperature T_{mold}	80 °C	125 °C
Melt temperature T_{melt}	250 °C	260 °C
Injection pressure P_{inject}	750 ± 25 bars	950 ± 25 bars
Injection velocity v_{inject}	100 mm s^{-1} [39] (2 - 30 cm^3 s^{-1})	40 mm s^{-1} [39] (4 cm^3 s^{-1})
Holding pressure P_{hold}	800 ± 25 bars for 10 s	400 ± 25 bars for 10 s
Ejection temperature T_{eject}	40 ± 3 °C	57 ± 5 °C
Pre-Drying (permanent)	50 °C	90 °C
Cycle Times	3 – 6 min	5 – 15 min

Table 13: Process parameters used to investigate the injection molding of nanopillars in Topas 8007 and–holes in Topas 5013.

	Topas 8007	**Topas 5013**
Mold temperature T_{mold}	40 – 100 °C	105 – 165 °C
Melt temperature T_{melt}	220 – 280 °C	260 – 290 °C
Injection pressure P_{inject}	750 – 1050 bars	950 ± 25 bars
Injection velocity v_{inject}	20 – 300 mm s^{-1} [39] (2 - 30 cm^3 s^{-1})	40 mm s^{-1} [39] (4 cm^3 s^{-1})
Holding pressure P_{hold}	700 – 800 bars	200 – 600 bars
Ejection temperature T_{eject}	30 – 70 °C	57 ± 5 °C
Pre-Drying (permanent)	50 °C	90 °C
Cycle Times	3 – 6 min	5 – 15 min

[39] Maximum speed at maximum width of 50 mm of the 2 mm thick circular mold.

2.2. Characterization of Nanostructures

The mass-fabrication of nanostructures into any kind of polymer requires (a) fabrication of a master or template in any kind of material, (b) replication into a resilient mold such as nickel, and (c) its mass-replication into polymer. In each process steps various errors can trigger a change in size and shape of the nanostructured surface. To assure uniformity and conformity with the original design and to be able to track sources of problems nanostructures were analyzed during all process steps.

Characterization of Nanostructures

(1) Resist master: control of exposure and development,
(2) Inverted nickel replicas, before and after injection molding: control of tool fabrication and mechanical stability,
(3) Polymer replicas molded under various conditions: control of molding process

The lateral and vertical dimensions of nanostructured patterns were analyzed by scanning electron microscopy (lateral dimension of features) and atomic force microscopy (lateral and vertical dimension of the features). A thorough study of dimensional stability during all process steps requires analysis of a large amount of samples. Only analysis of injection molded samples at different molding conditions with six parameter sets with each up to six different parameter values each injection molded with different mold coatings (native and with antistiction, and partially oxygen plasma cleaned) result in about 60 samples, leaving out analysis of master and mold fabrication. To limit the time consumption for imaging, especially by AFM, scanning electron images with different magnifications were taken from each sample, commonly 23^{rd} – 25^{th} piece. Exceptions were nanostructures written into resist since imaging accounts here for further exposure increasing the mechanical instability of structures. Analysis of macro- down to nanoscale defects and lateral dimensions were based on low and high resolution SEM images. Subsequently, AFM images were taken of one spot per sample. To verify that one AFM measurement is representative for the height or depth distribution of the nanostructured areas two or more spots were imaged for some of the samples. The absolute deviation was ± 5 nm and is considered within measurement accuracy supporting the assumption of acceptable uniformity. Larger deviations were only found in case of sub-optimal master fabrication were pillars closer to the center collapsed due to mechanical instability. These areas were taken out of consideration since their limited height does not represent the actual filling behavior.

SCANNING ELECTRON MICROSCOPY (SEM). High resolution scanning electron images were taken to observe shape of nanostructured areas as well as nano- and macroscaled defects. A Nova 600 NanoSEM (FEI company) was used to image nanostructured master in positive electron sensitive resist (ZEP520A, Zeonrex Electronic Chemicals) as well as Topas 8007 and 5013 samples of various magnifications (500 – 160.000 fold). Insulating samples were coated with 5 – 10 nm gold or titanium by either sputter-coating using Hummer from Anatech or electron beam evaporation using an SCM600 e-beam evaporator from Alcatel Vacuum Technology. Due to the ferromagnetic property of nickel, high resolution images using the through lense detector could not be taken by the Nova 600 NanoSEM. The nickel pieces were magnetized extremely fast and likely to be attracted by the column. Therefore imaging of nickel was limited to the field free detector limiting the resolution. In

contrast, the LEO 1550 Scanning Electron Microscope (Carl Zeiss NTS GmbH) enables high resolution imaging of nanostructures in nickel by employing the InLense detector with equally good resolution as obtained for metal coated resist or Topas using the Nova 600 NanoSEM. Lateral dimension were measured based on linear profiles created by Gwyddion2.21. Gwyddion is free software (GNU General Public License) for data visualization and analysis of scanning probe microscopy images. Gwyddion offers the possibility of setting the image dimensions before importing. The half field width (HFW) given in SEM images is used to precisely adapt the image dimensions. In fact, the half field width given in SEM images taken by the Nova 600 NanoSEM is the only reliable dimension usable for precisely measuring the lateral dimensions of nanostructures. The dimension of SEM images scales with the working distance and magnification whereby the scale bar displays not perfectly the actual dimensions of structures. The magnification has an inheriting error. The Nova 600 NanoSEM allows the user to record images in single or quad screen mode. The single screen mode displays thereby double the magnification as displayed in quad screen mode which is in principle true. Unfortunately the magnification is saved as displayed resulting in a double as high magnification in SEM images recorded in single screen mode[40].

SEM images, especially of sub100nm structures exhibited often diffuse edges, circumvent the determination of the exact size. Therefore, the width was determined by measuring the full width at half maximum. For each sample commonly 10 – 20 pillars were measured and averaged.

ATOMIC FORCE MICROSCOPY (AFM) AND GRAIN SIZE ANALYSIS. Atomic force microscopy images of uncoated Topas replicas commonly with a size of 2 by 2 μm^2 were taken at 0.5 Hz by a XE-150 (Park Systems Corporation) in intermittent mode using a super sharp silicon tip from Nanosensors™. Vertical dimensions of features were determined using the grain size analysis option of the XEI software package (Park Systems Corporation). This option enables the user to determine grains in for example polycrystalline silicon and measure their area, volume, length, perimeter, and peak-to-valley roughness (rpv). We employed this method to measure the average height or depth of polymeric pillars or holes, respectively. Height differences in a topography image result in an intensity distribution (pixel per intensity) represented by a histogram. Ideally nanostructures should exhibit a clear height difference compared to the “flat” background which results in a visible contrast in intensity. This difference in intensity can be utilized to separate structures from the background and measure their height or depth with respect to the overall background. For structures presented in this thesis the background commonly takes up the largest area resulting in a clear pixel-per-intensity peak (histogram). The value of height stated in the histogram is automatically defined during imaging and eventual image post-processing, i.e. leveling. It does therefore not necessarily reflect the actual height of features. The software enables the user to set a threshold (Figure 84, black flag) for excluding pixels representing a given height. Each spot containing a certain amount of “included pixels” surrounded by “excluded pixels” are counted as single “grain” representing one nanostructure (pillar or hole). The amount of pixels required to form such a grain is defined in the software and is not adjustable. The threshold is visualized in the topography image by coloring excluded pixels pink. This facilitates optimal adjustment of the threshold to separate but include all

[40] The problem of varying scale bar and magnification was discussed with a representative of FEI company resulting in the procedure as described in the text. Example for the varying magnification can be seen in Figure 93b. Compared to other SEM images shown, the magnification is obviously too high.

existing nanostructures while excluding the background (Figure 84, left). Excluded features were set to zero height or depth. The software automatically calculates the height or depth of structures by measuring the peak-to-valley roughness between each single grain (Figure 85, numbered and colored) relative to the user defined height threshold. As explained above, other values can be calculated as well based on the circumference of each spot. Often the threshold needs to be increased above the actual background height to avoid formation phantom spots which are caused by artifacts originating from either polymer processing or imaging. To calculate the actual height of nanostructures the "lost" height difference is regained by measuring the distance between threshold (Figure 84, black flag) and background (maximum of the pixel-per-intensity peak) by manually setting a cursor pair. As discussed above, the background commonly takes up the largest area. The resulting value is added to the previously calculated structure height.

The measurement accuracy is expected to be within few nanometers (< 5 nm). The accuracy mainly depends on the manual definition of cursor set point determining the distance between threshold and actual background. Tests were performed evaluating the influence of pillars or holes located at the border. Only a minor influence on the average pillar height was observed resulting in changes of the average height of less than 1 nm. Therefore all pillars were included in the calculation of the average pillar height. In contrast, holes located at the border contributed noticeable to the average hole depth and standard deviation leading to changes of up to 10 nm. For example an average hole depth of 73 ± 13 or 82 ± 11 nm results in 77 ± 5 and 84 ± 2 nm if holes located at the border are included or excluded, respectively. Holes located at the border are therefore very likely to exhibit an even smaller depth.

AFM images presented in this thesis show usually 3D and 2D rendering of the topography image containing two line profiles visualizing the depth or height of structures. It is to note that the grain size analysis is more precise as discussed later and resulted commonly in higher values for height and depth of structures than displayed in the line profiles presented.

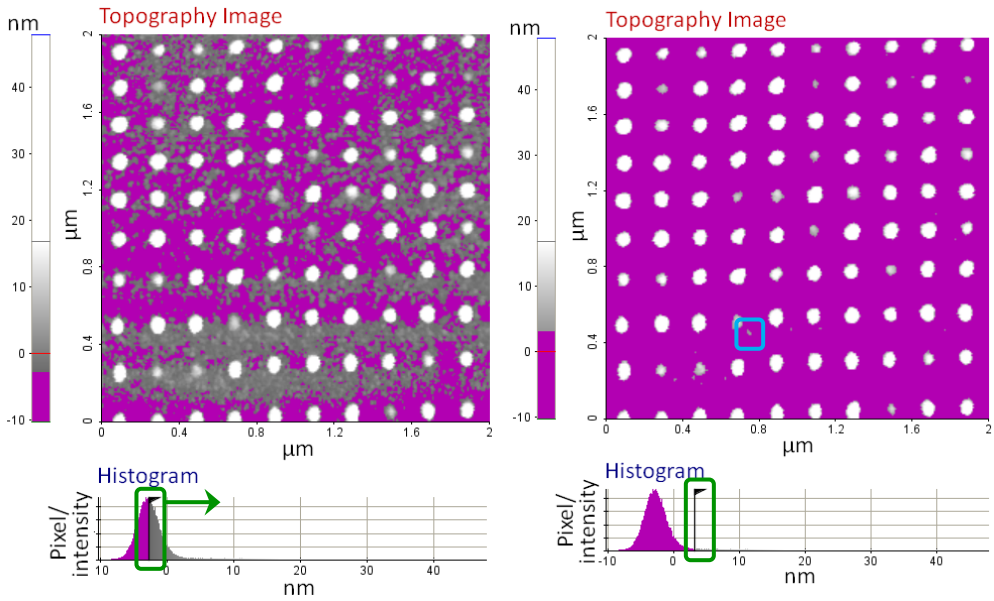

Figure 84: Grain size analysis based on XEI software package from Park Systems exemplified for 50 nm wide and about 35 nm high pillars. The threshold is set by moving the black flag (green square) towards larger heights. The maximum of pixel-per-intensity peak represent the average background (left). The final position of the threshold excludes pixels with intensities below the threshold (right, pink area). Areas containing too few pixels are excluded (right, blue square), residual grains are presented numbered and colored (Figure 85).

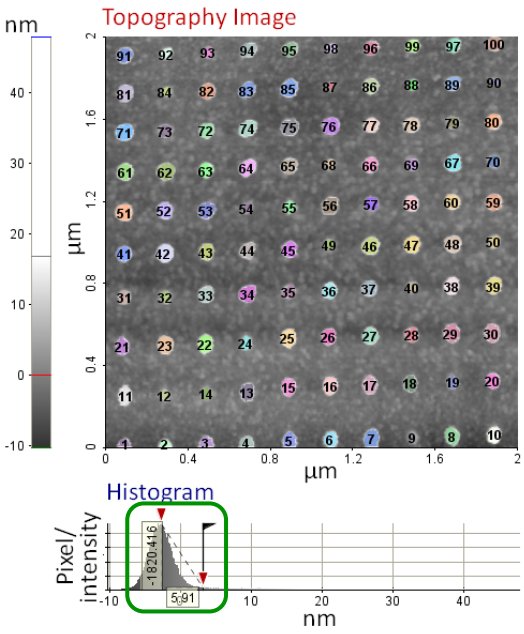

Grain	Rpv(nm)	Rpv corrected (nm)
Mean	*28.5*	*34.4*
Std.	*10.5*	*10.5*
1	31.2	37.1
2	26.7	32.6
3	44.1	50.0
4	30.9	36.8
5	34.0	39.9
6	30.6	36.5
7	38.9	44.8
8	36.8	42.7
9	9.1	15.0
10	31.5	37.4
11	39.5	45.4
12	12.4	18.3
13	38.5	44.4
14	9.6	15.5
15	36.0	41.9
16	41.3	47.2
17	36.5	42.4
18	31.4	37.3
19	16.1	22.0
20	34.2	40.1

Count: 20/100 Page: 1/6

Figure 85: Height extracted from the grain size analysis ("Rpv") and corrected by the distance of the threshold from the background (cursor pair, about 6 nm, "Rpv corrected").

3. Master and Mold Fabrication

The mass-fabrication of polymeric nanostructures requires a resilient mold presenting an inverted nanostructured relief. The mold is usually made of a metal providing sufficient tensile strength while providing certain plasticity as well. High ultimate tensile strength is required to avoid necking or fracture of nanostructures due to high pressure applied during injection and compression phase as well as frictional forces applied during demolding. On the other hand, a given ductility reduces fracture of the shim but also of the nanostructures. A deformation of few degrees might still be acceptable for injection molding purpose but avoids fracturing of the mold (or single nanostructures). For example, a silicon wafer will fracture under high pressure applied in injection molding in presence of small inhomogeneities such as dust particles on the backside. In contrast, nickel deforms plastically around particles of the same size though they will leave an imprint in the nickel. A simple test was performed using a silicon wafer as mold material for injection molding but failed due to complete fracture of the wafer. Though it is possible to use silicon as mold material by introducing an auxiliary sheet with a sufficient ductility nickel molds are easier to work with. Nickel molds were fabricated based on structured silicon or structured resist on silicon masters. Structured photoresist is commonly used for commercial fabrication of molds for injection molding of CDs and DVDs. Silicon as well has been repeatedly used as master material for electroplating NIL stamps [Park 2004, Schift 2005, Gadegaard 2007, Schift 2008] though only in limited extend for fabrication of nanostructured patterns. Two major issues determine whether structures are preferably written into resist or further etched into silicon. Firstly, the mechanical stability of the mold material is important, especially for height-to-width aspect ratios above unity. Secondly, master and electroplated mold replica need to be separated without deforming structures, especially structures in nickel.

MECHANICAL STABILITY. Resist has a very low ultimate tensile strength[41] (0.14 – 0.2 GPa) compared to silicon (5 – 9 GPa). The mechanical stability of structures in resist decreases with increasing aspect ratio. Thereby, structures can collapse during the final drying step after development of the resist caused by surface tension of the solvent. In the case that resist is directly used for electroplating, the initial resist thickness determines the aspect ratio of structures replicated in nickel which limits achievable aspect ratios. In the case that resist is used as etch mask for silicon etching, the etch depth determines the final structure height or depth and the initial resist thickness can be decreased to create more stable structures. Since the etch resistance of resist, i.e. ZEP520A is about 1:5 in SF_6 an etch depth of about 250 nm can be achieved for 50 nm thick resist.

SEPARATION OF MASTER AND MOLD. The separation of the silicon master from the nickel plate after electro-plating can be problematic. Already for microstructured patterns where the surface-to-volume ratio is comparable low, the adhesion between silicon and nickel is critical for complete separation of both. For nanostructures the adhesion increase about manifold due to highly increased surface-to volume ratio. Finally, the adhesion strength reaches the critical limit where structures start to break off. The separation could probably by improved by application of antistiction or sacrificial layers. In contrast, commonly used photon or electron sensitive resists like S1805 or ZEP520 can be dissolved by applying acetone or dedicated remover. Silicon can be etched away by either employing dry etching by reactive ion etching or wet etching using potassium hydroxide.

[41] Values are values are taken from “Engineering tables and data” A. M. Howatson, P.G. Lund and J.D. Todd, Chapman and Hall, London, 2nd edition, 1991, 181 pp.

3.1. Laser Lithography

The capability of fabricating nanostructures or at least sub-micron structures by laser lithography employing a 442 nm helium-cadmium laser was extensively tested. The DWL66 has a minimum step width of 300 nm. Therefore the simplest patterns at the resolution limit were chosen to test the limits, 300 nm wide holes (pitch: 600 nm) matching exactly the step width and 500 nm wide holes (pitch: 1000 nm) slightly off. A wide range of defocus (100 - 500) and dose values (10 – 100 %) were tested to find optimal parameter sets. Two set of dose tests are described in the following passages exemplifying the fabrication of holes and pillars and occurring problems.

EXPOSURE OF 500 NM HOLES. Initially patterns with holes of intended 500 nm width were exposed resulting in structure width of about 150 –850 nm. For example, 500 nm holes exposed in 600 nm thick S1805 and subsequently etched for about 250 nm into silicon resulted in 472 ± 161 nm for 5 % laser light transmission, dose of 90%,and defocus of 100 after etching into silicon. The sample exhibited a strong fluctuation in structure width containing holes with a diameter of 110 – 700 nm (Figure 86 a and c). For 100% dose the average hole diameter increases to 748 ± 108 nm (Figure 86d) while a reduced dose of 80% exposed only a very small fraction of the designed hole pattern (Figure 86 b). Residual holes have a diameter of about 180 nm. For a defocus of 300 and a dose of 80 % the hole pattern with a intended width of 500 nm resulted in 608 ± 157 nm wide pillars. Furthermore, features exhibited an elongation in x-direction (“fast writing direction”). It seems that the size distribution follows a linear pattern whereby the deviation within a line is small compared to a column or the overall size distribution. The width within two rows is 534 ± 131 nm and 298 ± 108 nm for a row with “wide” and “narrow” holes, respectively (Figure 86a, blue frame). The average diameter variation seems to follow a pattern of two or three rows with “wide” holes followed by one or two rows with “narrow” holes.

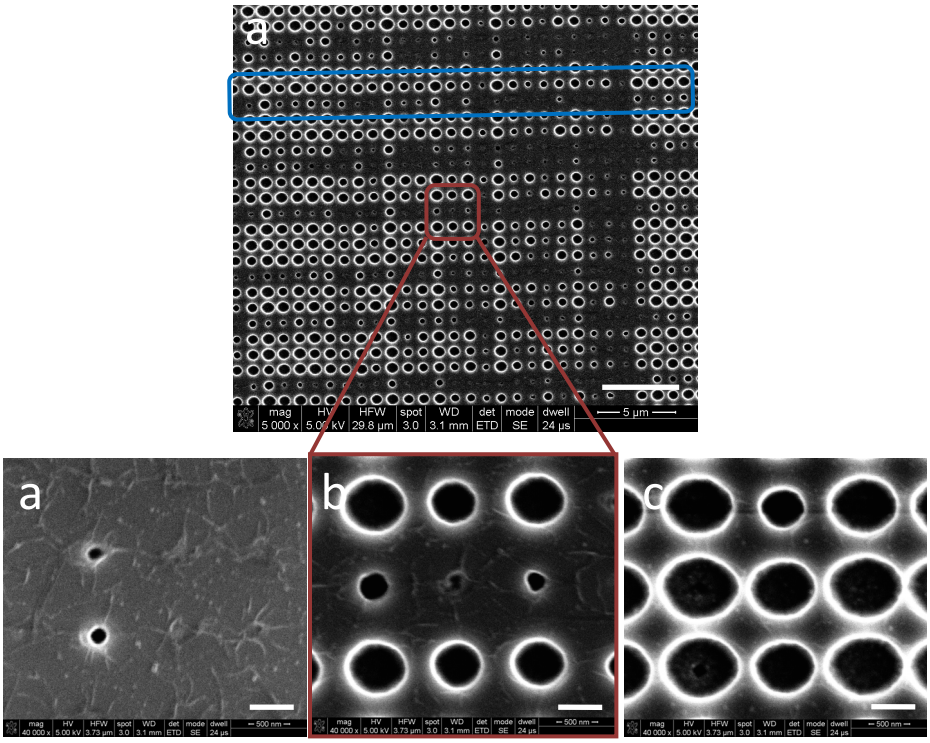

Figure 86: SEM images of 500 nm holes after etching into silicon. Structures were exposed using 5% laser light transmission at a defocus of 100 and dose of 80 % (b), 90 % (a, c), and 100 % (d). Scale bars: 5 µm (a) and 500 nm (c – d). Example rows containing "wide" and "narrow" holes are high lightened by the blue rectangle.

AFM measurements showed that 500 nm holes (508 ± 168 nm) exposed in 600 nm thick S1805 and further etched into silicon resulted in 277 ± 44 nm (Figure 87). The height of pillars has not been measure but is expected to have the same order of magnitude.

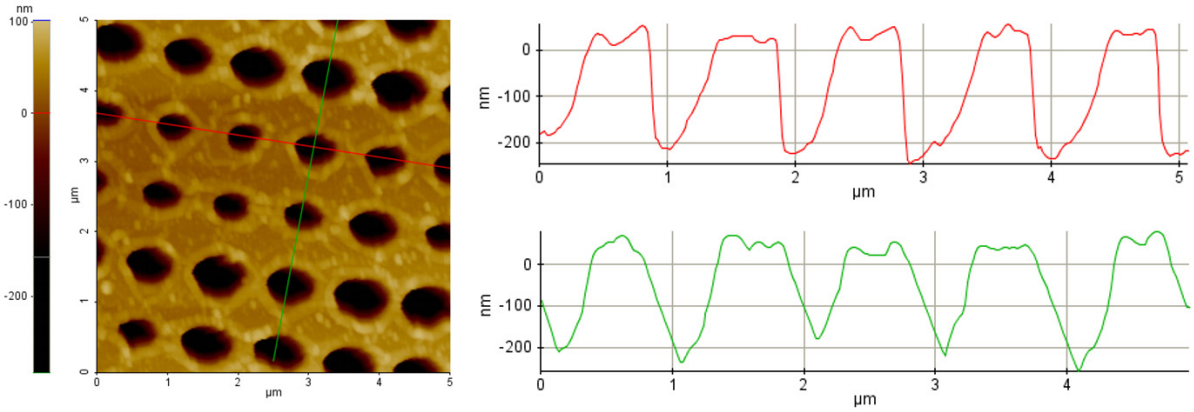

Figure 87: AFM image of 508 ± 168 nm wide holes etched 277 ± 44 nm deep into silicon (design: 500 nm round holes, defocus: 100, dose: 90%, filter: 50%).

DISCUSSION. It was not possible to fabricate nanostructures of 500 nm width with an acceptable uniformity (deviation < 10% of the structure width) though structure of down to about 180 nm in width were achieved. Neither defocus nor dose variation led to a parameter set that allows for fabrication of uniform structures close to 500 nm. However, the irregular size distribution is most probably caused by fluctuations in the exposure dose originate from an instable laser. The laser was already over-aged and broke down few weeks after that test. Furthermore, the shutter preventing resist from being exposed in between exposure spot seems to be too slow for patterns of such small

dimensions and pitch. Thereby, the exposed area is increased, especially in horizontal direction (fast stage movement) resulting in elongated features. The high standard deviation is not caused by large size distribution within a row but is mostly caused by regular variation of size between different rows ("narrow" and "wide"). The cause for the regularity of rows with "wide" and "narrow" holes is so far unknown.

EXPOSURE OF PILLARS BASED ON 500 NM HOLES. Another approach was tested by employing the over-exposure of holes to create pillar structures. 300 and 500 nm wide holes were exposed using defocus of 100 - 500 and dose of 10 – 100 %. Following parameter sets resulted in best structure homogeneity. Patterns of 300 nm wide holes resulted in holes of 459 ± 91 nm (defocus: 300, dose: 30%) (Figure 88a) and 656 ± 51 nm (defocus: 300, dose: 40%) (Figure 88b). Pillar structures were only achieved in case of 500 nm intended hole width resulting in rhomb-shaped pillars with an average diagonal width of 314 ± 94 nm (defocus: 300, dose: 70%) (Figure 88c) and 492 ± 91 nm (defocus: 500, dose: 70%) (Figure 88d). The Holes achieved an average width of 349 ± 59 nm (defocus: 200, dose: 10%). All patterns were extremely sensitive to changes in dose. While a given dose resulted in more or less homogenous structures, 10 % higher dose caused already an over-exposure leading to useless structures (merged holes or disappearing pillars). Furthermore, single rows of structures appear wavy in horizontal direction. A set of SEM images for hole and pillar structures illustrating the influence of defocus and dose are shown in the Appendix 1-2.1.

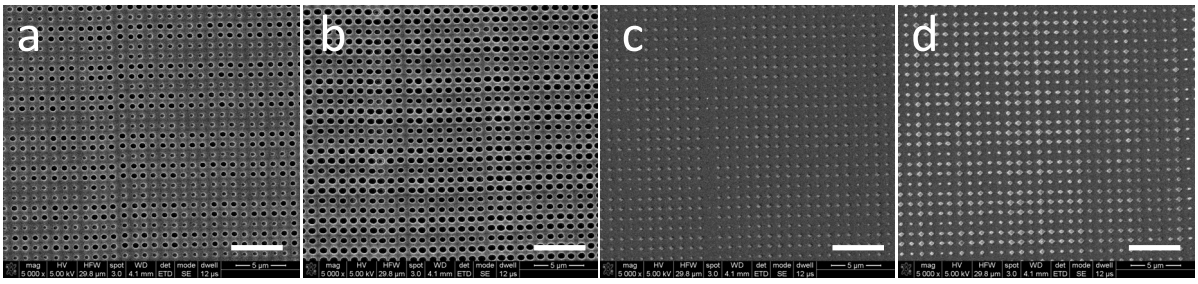

Figure 88: SEM images of the best hole and pillar patterns achieved from hole patterns of 300 (a, b) and 500 nm (c, d) intended width. (a) Hole pattern of 459 ± 91 nm (defocus: 300, dose: 30 %), (b) Hole pattern 656 ± 51 nm (defocus: 300, dose: 40 %), (c) Pillar pattern of 314 ± 94 nm (defocus: 300, dose: 70 %), (d) Pillar pattern of 492 ± 91 nm (defocus: 500, dose: 30 %). Scale bar: 5 µm.

AFM measurements showed that 656 ± 51 nm (300 nm intended width) exposed in 600 nm thick S1805 resulted in only 160 ± 30 nm (Figure 89) which is only about ¼ of the original resist height. Pillars fabricated by over-exposure of 500 nm wide holes were even smaller obtaining a height of only 129 ± 35 nm (Figure 90) which is only about ⅕ of the original resist height. A complete list of dimensions measured for exposed pillars and holes is given in Table 14.

Table 14: List of hole and pillar patterns for best dose and defocus

Intended width (nm)	Resulted Shape	Defocus	Dose (%)	Width (nm)	Height (nm)
300	Holes	300	30	459 ± 91	
300	Holes	300	40	656 ± 51	160 ± 30
500	Holes	200	10	349 ± 59	
500	Pillars	300	70	314 ± 94	129 ± 35
500	Pillars	500	70	492 ± 91	

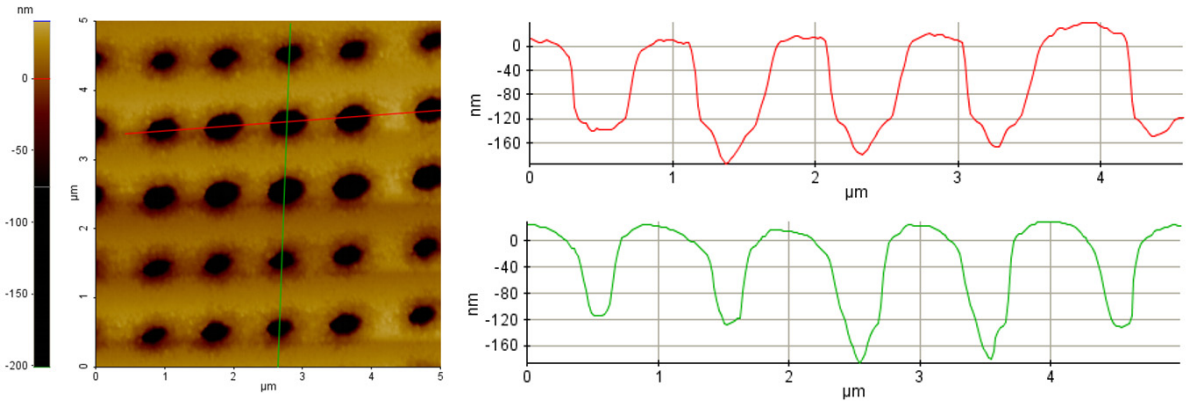

Figure 89: AFM image of about 656 ± 51 nm wide and 160 ± 30 nm deep holes in resist (design: 300 nm holes, defocus: 300, dose: 40%).

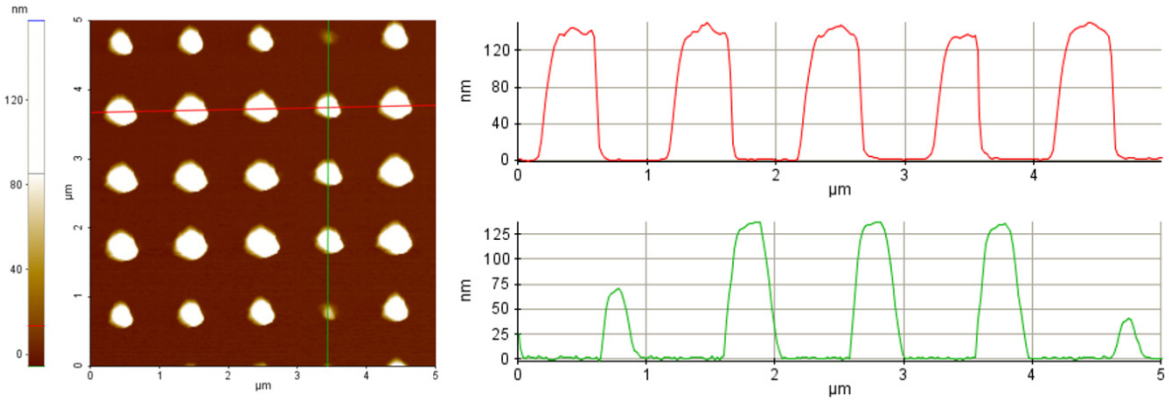

Figure 90: AFM image of about 314 ± 94 nm wide and 129 ± 35 nm high rhomb-shaped pillars in resist (design: 500 nm holes, defocus: 300, dose: 70%).

DISCUSSION. Optimal defocus and dose allowed for the fabrication of patterns with increased uniformity though the minimum standard deviation was commonly more than 10 % of the average structure width. A defocus value of 300 and a dose of 30 – 40 % for holes and 70 % for pillars achieved the most homogenous hole and pillar patterns though standard deviations of 50 – 100 nm were common. Surprisingly, a defocus of 200 and a dose of 10% resulted in the best hole pattern for 500 nm intended hole width. A similar pattern was obtained for a defocus of 300 though the homogeneity was worse and not all holes were visible. On the other hand an increased dose of 20%

led to a widely over-exposed hole pattern with holes partially merged making it unusable for further processing. The rhomb-shaped of pillars as observed in the SEM images (Figure 88c, d) originates from the overlapping exposure spots visualized in Figure 91.

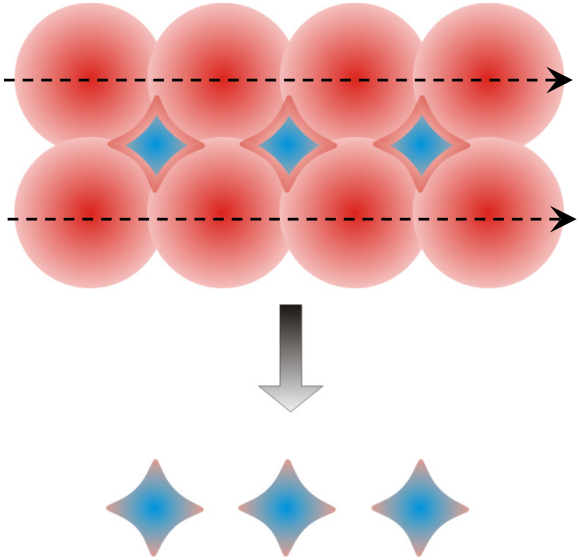

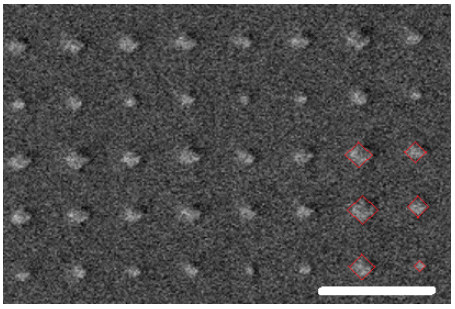

Figure 91: Schematic view of exposure profile for 500 nm wide holes leading to rhomb-shaped pillars (left) and cut-out from Figure 88d to magnify rhomb-shaped, scale bar: 2 µm (below).

The low height of structures can be explained by either limited exposure dose in vertical direction or exposure of the top layer of resist around the actual structures. The latter case is most likely the causes of the low structure height and depth. The laser beam exhibits a Gaussian intensity distribution and though the actual beam diameter is unknown the manufacturer, Heidelberg Instruments, specifies a minimum theoretical resolution of 640 nm (practical 800 nm). Thereby, it is most probable that a spot with a diameter of about 640 nm is exposed with a Gaussian intensity distribution. The maximum intensity in the center of the laser beam spot exposed holes down to about 300 nm while the area around the spot was exposed as well leading to a thinning of the resist after development. The hypothesis is supported by the low surface roughness of the bottom area observed for pillar patterns (Figure 90).

CONCLUSION. Careful optimization of dose and defocus combined with application of high contrast photo resists fabrication of structure below 500 nm is possible employing laser lithography. Further test need to conducted using a new laser to verify the cause for the size differences between lines with “narrow” and “wide” structures. If this problem can be solved fabrication patterns with high uniformity (≤ 10% of average structure width) will be possible. For example, separation of “narrow” and “wide” pillars leads to a significantly decreased standard deviation, from 314 ± 94 nm to 531 ± 30 nm and 361 ± 42 nm (defocus: 500, dose: 70%).

As discussed previously the adhesion of cells might be influenced gradually by decreasing structure size to dimensions below 100 nm. Structures fabricated with laser lithography cannot even approximately reach these dimensions. Therefore they were not considered for replication into nickel and polymer replication. Besides, investigation of real influence of nanostructured patterns requires a minimum in structure homogeneity over an area that covers at least a spread cell body (several tens of micrometers). Therefore focus was set on optimizing process parameters for writing nanostructures by electron beam lithography.

3.2. Electron Beam Lithography

Process parameters were optimized for hole and pillar patterns, in order to fabricate master in resist (ZEP520A) or silicon containing arrays of pillars and holes. Experiments were conducted to optimization writing parameters, especially exposure dose. As already described in the experimental section, silicon etching was performed employing a recipe *fpe_nano*. Due to reasonable etch results and limited application of silicon etching no further optimization of etch recipes was done.

In favor of mechanical stability and expecting that silicon can be etched without major problems initial test was conducted to produce two silicon wafer containing arrays of either 50 or 100 nm wide holes (Figure 92). Pattern were written into 100 nm thick ZEP520A and subsequently etched into silicon. Process parameters for exposure of nanostructured patterns were chosen based on experience of frequent users and process specialists at DTU Danchip: dose of 300 µC/cm^{2}and current of 2.1 nA. 50 and 100 wide holes were subsequently etched 100 and 200 nm into silicon applying *fpe_nano* for 105 and 210s, respectively.

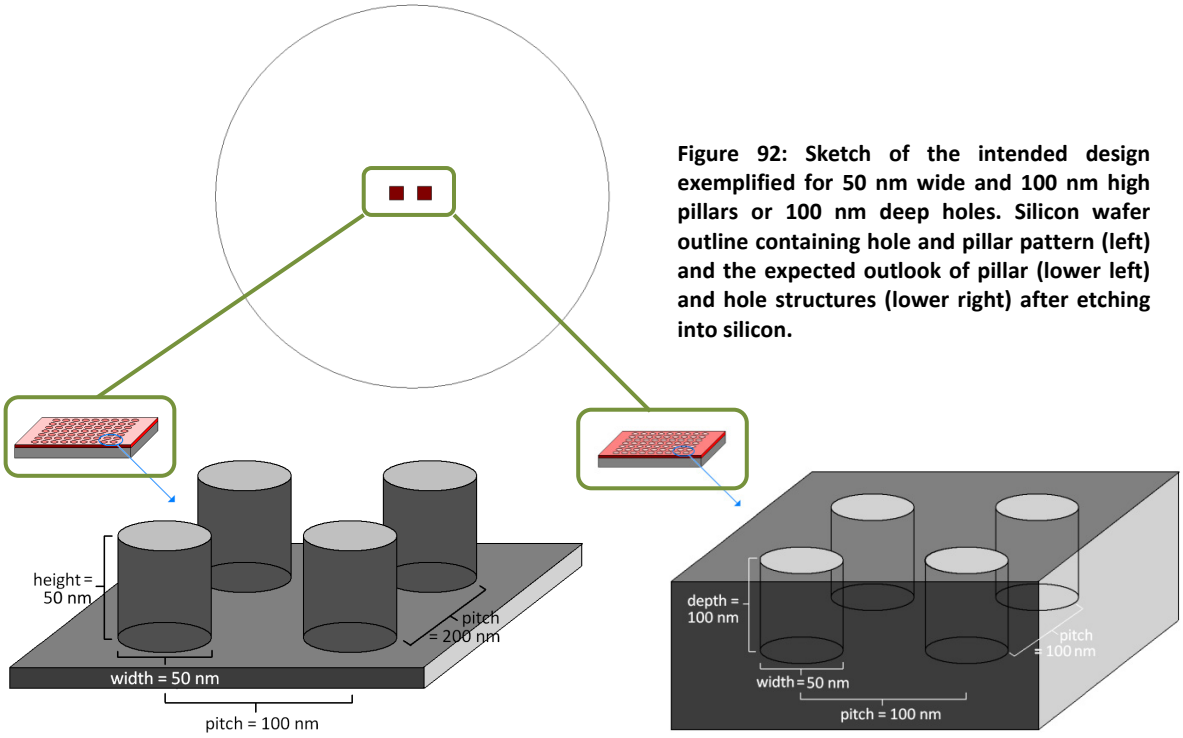

Figure 92: Sketch of the intended design exemplified for 50 nm wide and 100 nm high pillars or 100 nm deep holes. Silicon wafer outline containing hole and pillar pattern (left) and the expected outlook of pillar (lower left) and hole structures (lower right) after etching into silicon.

50 AND 100 NM WIDE HOLES. As it can be seen from Figure 93 all patterns were overexposed and distorted. Especially pillars collapsed to an increasing extent towards the center. Holes designed as 50 and 100 nm resulted in 79 ± 4 nm and 160 ± 3 nm, respectively. 100 nm wide pillars turned out to be about 94 ± 3 nm in short distance to the absolute center. Pillars in the absolute center were collapsed and could not be accurately measured (Figure 93c). Patterns of 50 nm wide pillars collapsed completely, in the center as well as corner.

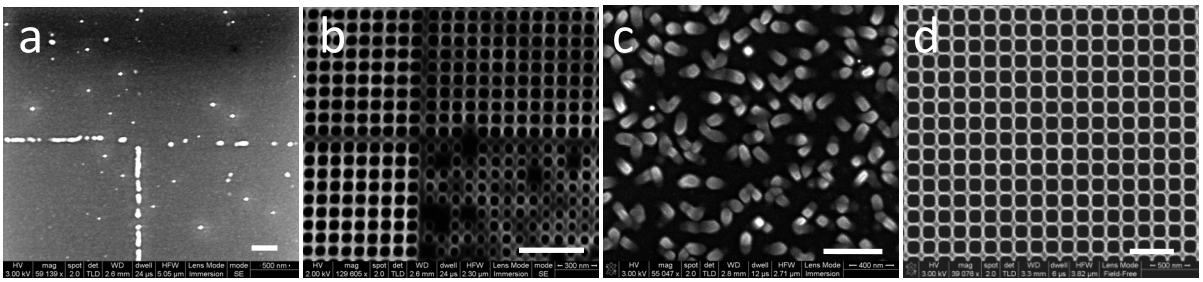

Figure 93: SEM images of pillar and hole arrays etched into silicon: pillars (a) and holes (b [42]) with intended width of 50 nm (pitch: 100 nm); and pillars (c) and holes (d) with intended width of 100 nm (pitch: 200 nm). Scale bars: 500 nm.

Even though structures were widely distorted, they were used to test the electroplating process of nanostructures performed by DVD Norden A/S. The resulting nickel plate demonstrated some major problems though structures were partially replicated with high fidelity. The major problem observed was related to the separation of silicon master and final nickel plate. The master/nickel mold pair for 50 nm structures was possible to separate with little effort. The resulting nickel shim reflects a fair replica of the master structure as presented in Figure 94. Very few holes replicated from the 50 nm pillar pattern were visible rendering the distorted master surface appropriately (Figure 94a). 50 nm holes were nicely replicated into nickel as well though many nickel pillars broke off (Figure 94b). The missing pillars allowed measuring the average pillar height using the bottom of defects in the pattern as zero level resulting in 102 ± 5 nm which agrees well with the initial etch depth of about 100 nm. It was not possible to separate master and nickel plate containing 100 nm wide structures without fracturing the silicon wafer. Small pieces of silicon were remaining on top of the nanostructured areas. The silicon residuals were etched away applying 30% potassium hydroxide. The silicon was removed though the nickel surface was heavily damaged (Figure 94c and d). The nanostructured areas were completely removed leaving only a visible frame of the original pattern. Instead nickel grains in the range of 0.2 – 4 µm are visible (Figure 96).

[42] The magnification stated in the image is incorrected due to an error in the SEM software. Images taken in single screen mode (instead of the common quad screen mode) displaying the doubled magnification.

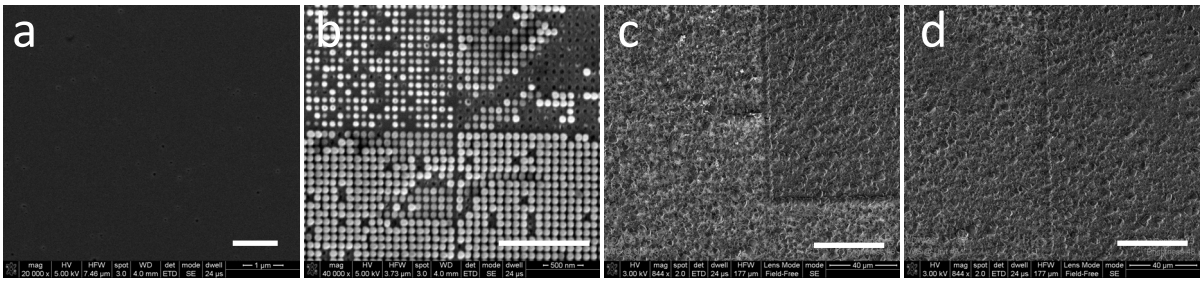

Figure 94: SEM images of nickel replicas of nanostructured patterns previously shown (Figure 93): 50 nm "holes" (a, 20.000fold) and pillars (b, 40.000fold). Scale bar: 1 µm (a, b) and 40 µm (c, d).

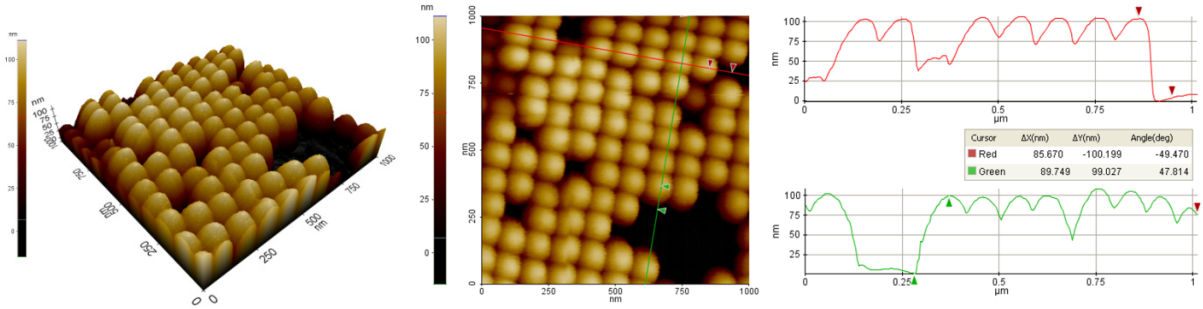

Figure 95: AFM image of 79 ± 4 nm wide pillars (design: 50 nm) in nickel. Pillars are partially broken off.

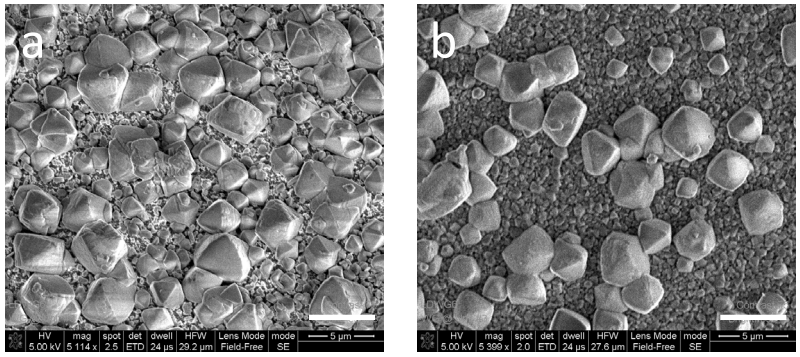

Figure 96: SEM images of nickel replicas representing flat (left, 5.000fold) and nanostructured areas (right, 5.000 fold) after etching in potassium hydroxide. Scale bars: 5 µm.

DISCUSSION. It was not possible to fabricate 50 nm wide pillars by electron beam writing into 100 nm resist and subsequent etching into silicon. Either the resist was not mechanical stable enough to produce standing pillars or the pillars were extensively over-etched by the silicon etching and collapsed. The strong broadening of 100 nm wide holes to about 160 ± 3 nm supports the latter case. However, 100 nm wide pillars obtained an average width of 94 ± 3 nm (close to the center) which almost equals with the intended width and supports rather the first case. In the first case, employing critical point drying can reduce the surface tension employed to fragile structures to zero and thereby allow fabrication of higher aspect ratios for smaller structure widths. However, to maintain simplicity of the process and reduce fabrication cost in favor of future commercialization critical point drying was not applied in this project. Differences between structures located at the center and corner are most probably caused by the proximity effect resulting in a larger dose towards the center

(described in detail in Section I.4.1.). Monte Carlo simulations have shown that especially backscattering events result in an energy distribution with a radius of about 30 µm in silicon whereupon less than 5% of the initial energy contributes to the exposure. To reduce pattern inhomogeneity caused by the proximity effect a "poor-man approach" was tested. A rectangular frame with a line width of 50 µm was placed in 2 µm distance of each structured pattern. However, it is difficult to estimate the influence of auxiliary structures on the exposed pattern without additional and commonly expensive software.

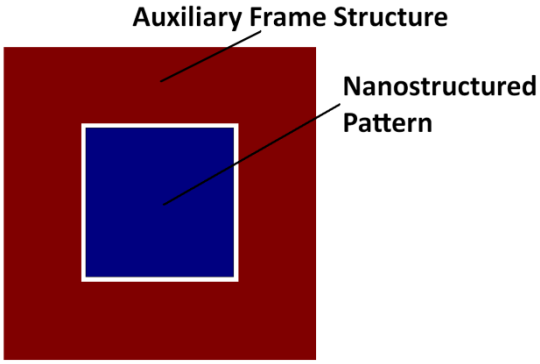

Figure 97: Auxiliary frame structure used as poor-man-approach to reduce inhomogeinities caused by proximity effect

The maximum writing area of the JEOL-JBX9300FS is 500 by 500 µm^2. Larger areas are split up into subareas of 100 by 100 or 500 by 500 µm^2 and automatically stitched together. Stitching errors resulted in an increased pitch between structures close to the section border as visible in Figure 93b. The difference in pitch resulted in a clear distinction between the four sections though in case of the pillar pattern only a dashed line remained.

A difference in contrast was observed for the 50 nm hole pattern which according to **P. Shi** (senior process engineer at DTU Danchip) results from contamination of electromagnetic lenses. Particles on the electromagnetic lenses can cause irregularities in the focus depending on the spot location. Different writing fields are thereby exposed with different foci causing defects in the written resist.

The separation of silicon master and nickel replica resulted in two damaged samples. The sample containing 100 nm structures was corroded by the etchant, potassium hydroxide, resulting only grains left on the surface. The etching of silicon from electroplated nickel has been successfully used employing other seed layers such as titanium or gold [Fritz 2002, Gadegaard 2003]. Titanium and gold are most probably not attacked by potassium hydroxide and thereby protect the electroplated nickel. The nickel of the nickel-vanadium seed layer and the electroplated nickel underneath are attacked by the etchant. In the sample containing 50 nm structures many nickel pillars were broken off which is most probably caused by friction applied at the silicon-nickel interface during separation. Since nanostructures are mostly formed during sputtering their mechanical strength depends mainly on the properties of the sputtered seed layer and the adhesion of the sputtered metal to the electroplated material. The layer consists hereby of a nickel-vanadium alloy containing 7% vanadium by weight. The vanadium acts mainly as reductant but it also improves the mechanical properties of the alloy. Pure nickel almost instantly oxidizes in air forming a natural insulating nickel-(II)-oxide layer. The vanadium prevents the formation of a nickel oxide layer, which would otherwise interfere with the galvanic process. The vanadium also improves the mechanical properties of the alloy by reducing the effect of temperature on the static tensile strength (Table 15) [Savitskiy 1961]. The

application of nickel-vanadium alloy as seed layer improves the stability of nanostructures, especially with increasing temperatures applied in injection molding. However, the adhesion of sputtered nickel-vanadium alloy to electroplated nickel can be poorly so that the alloy layer delaminates during processing.

Table 15: Mechanical Properties of Nickel and Nickel-Vanadium Alloy at elevated temperatures [Savitskiy 1961]

	Tensile strength at 20 °C [kg/mm^2]	**Tensile strength at 100 °C [kg/mm^2]**	**Tensile strength at 300 °C [kg/mm^2]**
Nickel	45	43	21
Nickel-vanadium alloy (7 wt%)	57	54	38

CONCLUSION. Although the etching of silicon by reactive ion etching is possible the applicability of resist based masters was tested. Additional experiments were conducted later-on using fluorocarbon based antistiction coated silicon master for nickel shim production. In the following sub-sections exposure and dose tests are presented.

3.2.1. Nanostructured Hole Patterns

An extensive dose test was performed to optimize exposure doses for frame and pattern. Arrays of holes with diameters of 50 and 100 nm holes and a pitch of 100 and 200 nm, respectively, were exposed into 105, 196, and 258 nm thick resist. Doses ranging from 210 – 290 µC/cm^2 for patterns and 50, 70, and 90 µC/cm^2 for frames were applied. The current was reduced to 0.8 nA. Patterns containing 50 nm wide holes were mainly used to verify the exposure while 100 nm structures were used to evaluate the electroplating process. The master containing 100 nm wide holes was directly used for electroplating. Firstly, results regarding the exposure of 50 nm wide holes are presented followed by the electroplating results for 100 nm wide holes.

EXPOSURE OF 50 NM HOLES. The dose test for intended 50 nm wide holes resulted in very homogenous arrays of holes depending on the exposure dose. A maximum hole width of 46 nm (105 nm resist, 290 µC/cm^2) for all patterns was achieved. The hole diameter increased slightly with increasing pattern exposure dose leading to structure broadening from about 37 nm to maximal 44 nm (Figure 98). For 105 nm thick resist holes obtain a width from 36 ± 2 nm (210 µC/cm^2) to 46 ± 2 nm wide (290 µC/cm^2). The resist thickness itself had only small influence (≤ 5 nm) on the structure width. A full list of average diameter for different resist thicknesses is given in Table 20. The exposure dose for the auxiliary 50 µm wide frame structures did not change pattern dimensions (at the corner) significantly resulting in a maximum difference of < 5nm on average (Figure 99). A set of SEM images and a table presenting the average width of intended 50 nm wide holes is given in Appendix 1-2.2.1.

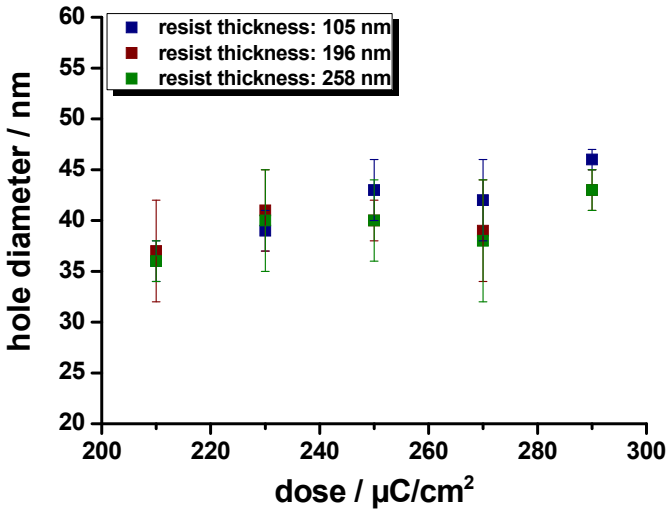

Figure 98: Dependency of hole diameter in the center of the pattern with respect to the pattern dose for different resist thicknesses.

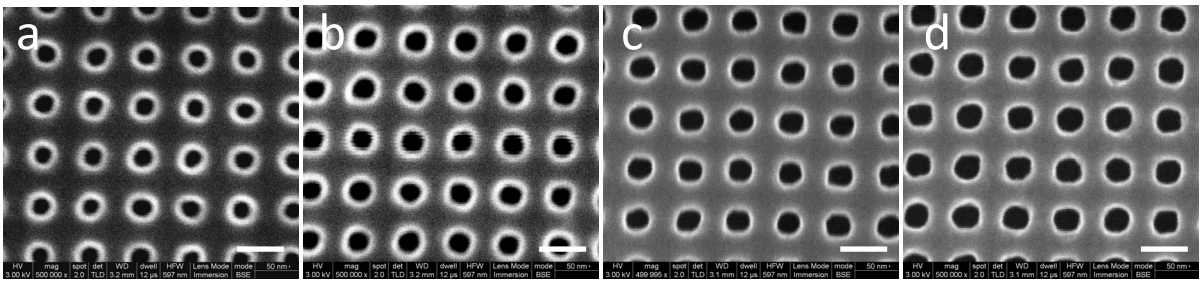

Figure 99: SEM images exemplifying the difference between holes located in the center (a, c) and corner (b, d) for a pattern dose of 210 µC/cm² (a, b) and 290 µC/cm² (c, d) with a frame dose of 90 µC/cm². Scale bars: 100 nm.

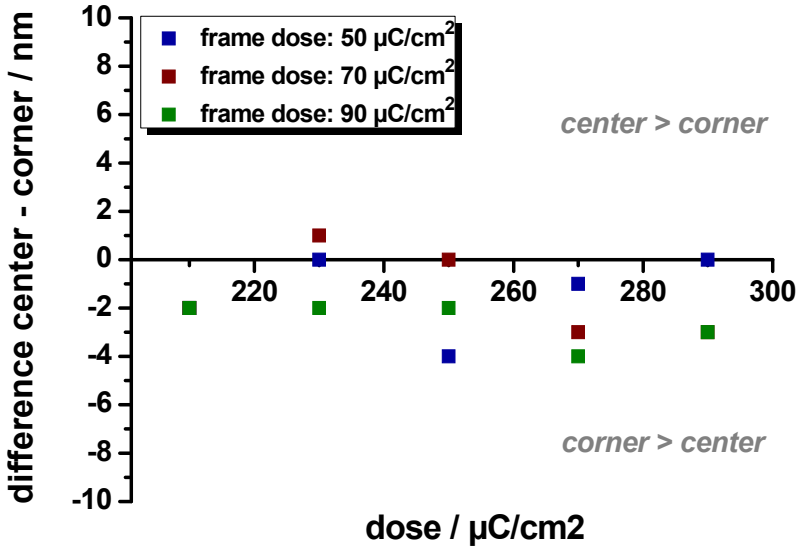

Figure 100: Difference between center and corner holes for different frame dosage. Error bars (≤ 4 nm) were removed with respect to clarity.

The maximum depth resolved for 50 nm wide holes by AFM was about 20 nm. Holes written into 258 nm thick resist showed an average hole depth of 17 ± 3 nm. The hole depth was decreasing with increasing number of scanned lines. The first row of holes was 20 ± 1 nm deep while the last only reached 14 ± 1 nm. No flat bottom was observed. Another approach failed to measure the depth of nanostructures in resist. Nanostructured pattern in ZEP520 on silicon wafers were fractured along the crystal line of silicon. The resist deformed heavily preventing a clear cross-section (Figure 101).

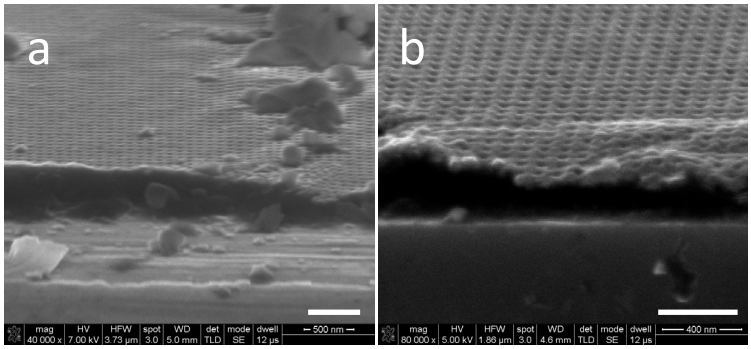

Figure 101: SEM image of a fracture silicon wafer carrying 50 nm wide holes written into 196 nm (a) and 258 nm (b) thick resist. Scale bars: 500 nm (a) and 400 nm (b).

ELECTROPLATING OF 100 NM HOLES. Resist based master and resulting nickel replica were easily separated almost without applying force. No substantial nano- or microscaled defects were observed. The electroplating replicated 100 nm wide pillars with high fidelity (shape and depth) into a nickel mold insert though random macroscopic defects were visible (Figure 102). Macroscopic defects are unknown contamination and disrupted or tilted pillars. The diameter of nickel pillars showed no significant dependency on either exposure dose of the original holes or resist thickness (Figure 103). The average pillar diameter ranged from 102 ± 3 nm (resist thickness: 196 nm, dose: 290 µC/cm^2) to 114 ± 3 nm (resist thickness: 258 nm, dose: 230 µC/cm^2). For example, holes written into 105 nm thick resist resulted in nickel pillars with an average diameter of 105 ± 7 nm for 210 µC/cm^2 and 112 ± 7 nm for 290 µC/cm^2. A set of SEM images and a table presenting the average width and height of intended 100 nm wide pillars replicated in nickel is given in Appendix 1-2.2.1.

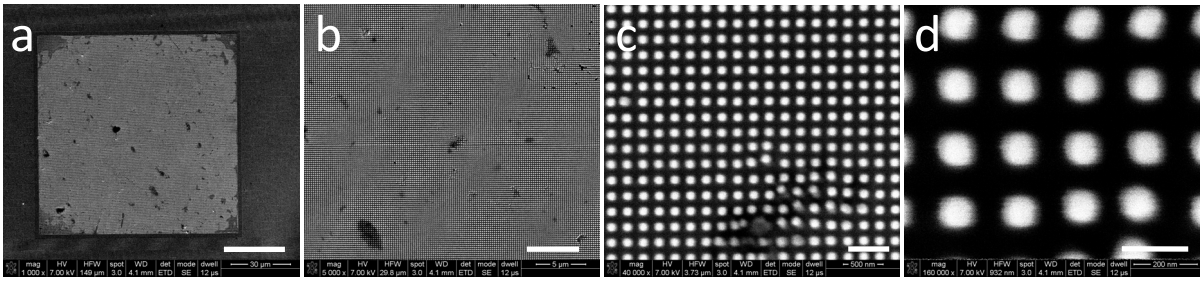

Figure 102: SEM images of replica containing 100 nm wide pillars in nickel at different magnification of 1.000fold (a), 5.000fold (b), 40.000fold (c), and 160.000fold (d). Scale bars: 30 µm (a), 5 µm (b), 500 nm (c), and 200 nm (d).

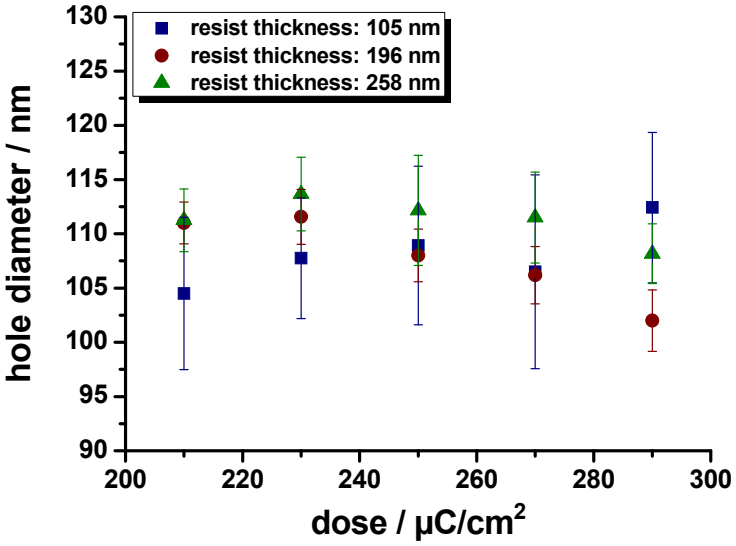

Figure 103: Diameter of pillars replicated into nickel for different resist thicknesses

The maximum depth of 100 nm wide pillars measured by AFM resulted in about 150 nm height. Holes written into 105 nm thick resist resulted in uniform pillars of 105 ± 7 nm in width and 99 ± 5 nm in height for a pattern dose of 210 (frame dose: 70 µC/cm^2). For 196 and 258 nm thick resist only an average pillar height of about 150 nm for 210 µC/cm^2 could be measured (Figure 104).

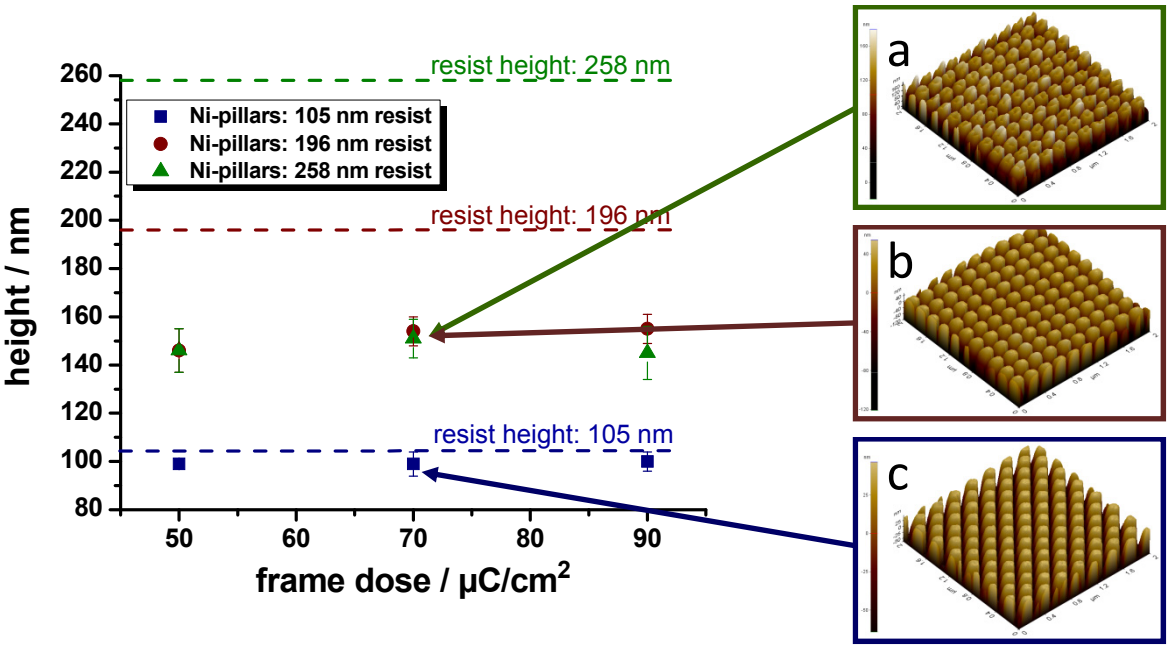

Figure 104: Average pillar height measured for varying exposure doses. AFM image representing 3D view of 100 nm wide pillars replicated from nanoholes written into 105 nm (a), 196 nm (b), and 258 nm (c) thick resist (210 µC/cm^2, frame: 70 µC/cm^2).

DISCUSSION. The influence of exposure dose (210 – 290 μC/cm^2) on lateral dimensions of 50 and 100 nm holes was less distinct than expected from the initial exposure. All patterns containing 50 nm wide holes were underexposed reaching 36 – 46 nm while patterns containing 100 nm were slightly overexposed obtaining diameters of 105 – 112 nm. Exposure especially of structures below 100 nm is heavily influenced by e.g. development conditions, resist sensitivity, or filament ageing. Besides, the deviation in structure width can be easily caused by statistical errors originating from the measurement method whereby the structure width is measured based on a cursor pair set on a line profile as described in the experimentals. The exposure of an auxiliary frame structure lead to improved homogeneity with respect to diameter of holes located at the center and corner. There was no significant difference (≤ 5 nm) between 50 and 90 μC/cm^2 observed. Since patterns exposed with a frame dose of 70 μC/cm^2 exhibited the least deviation this dosage was used for the following exposures of hole patterns.

The resist thickness did not show any significant influence on the diameter and most probably depth of 50 nm and 100 nm wide structures though the full depth could not be resolved. Unfortunately, only a depth of up to 20 nm for 50 nm wide holes in resist and a height of up to 150 nm for 100 nm wide pillars in nickel were measured by AFM using a super sharp silicon tip. Fracturing of 50 nm holes in resist on a silicon wafer failed to provide a sharp cross-section preventing depth measurement by SEM as well. Nickel cannot be fractured as silicon due to its ductility which circumvents the preparation of a sharp cross-section.

Since the resist based master was directly used for electroplating, the pillar height should equal the initial resist thickness in case of a full exposure (down to the bottom). A pillar height of about 100 nm corresponds well with the original 105 nm thickness of the resist. The 5 nm differences, though considered negligible, were possibly caused by resist drying and thereby shrinkage during processing. The sputter process prior to electroplating is known to replicate features down to few nanometers [Gadegaard 2003]. For higher resist thickness only a maximum of 150 nm was measured. Since line profiles based on AFM images did not show flat bottom in between pillars it is assumed that the super sharp silicon tip could not reach down to the bottom to resolve the full depth. The official specifications of the super sharp tips allow theoretical measuring of about 100 nm in depth for 50 nm wide holes. However, the theoretical resolution is compromised by contaminations on the sample surface which instantly increases the tip radius upon contact reducing the resolution. Gradually decreasing hole depth as observed for 50 nm wide holes support the hypothesis of increasing radius by accumulated contamination or wearing of the tip. Furthermore, SEM images were taken of different super sharp silicon tips revealing their tip shape (Figure 105). Except for the first image (Figure 105b) none of the imaged cantilevers possessed a super sharp tip which explains the low resolution of AFM images. Precautions were taken to prevent tip wearing by electrical discharge during mounting or during imaging by carefully adjustment of gain and set point. Although very low scan speeds of 0.5 Hz for areas of 2 by 2 μm^2 were used, tip wearing and even fracturing occurred rapidly.

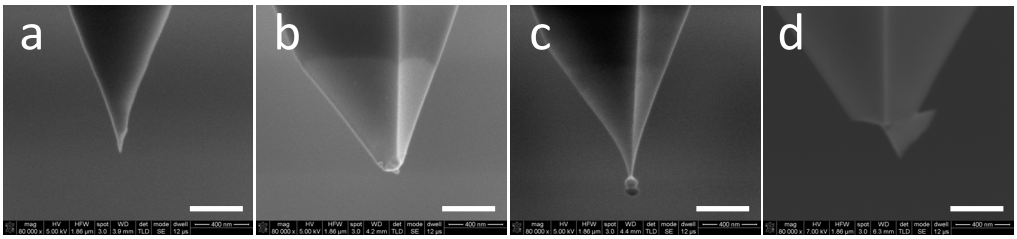

Figure 105: SEM images of super sharp silicon tips *after usage* in intermittent contact mode (AFM): sharpest tip imaged (a), worn down and round tip (b), contaminated tip (c), and fractured tip (d). Scale bars: 400 nm.

Furthermore, pillars replicated from 196 nm thick resist exhibit a fairly smooth tip surface with a large radius of curvature. Therefore it is most likely that the sample was full exposed and completely replicated by electroplating (Appendix 1-2.2.1, Figure 176). In contrast, 100 nm holes written into 258 nm thick resist result in pillars with non-flat tip shape though obtaining about the same width like for thinner resist (Appendix 1-2.2.1, Figure 177). This may be caused by either underexposure in vertical direction or limited coating capabilities of the sputtering process prior to electroplating. Monte Carlo simulation for 100 nm and 300 nm resist on silicon showed that the energy of the electron beam (for 100 keV) is highly focused while penetrating the resist and scatters significantly first inside the bulk silicon. 90 % of the energy is thereby penetrating more than 5 µm into the substrate. This should lead to a full exposure of even 300 nm thick resist. The sputtering of high aspect ratio holes is most likely the limiting process step if pillars on the nickel mold based on 258 nm thick resist in fact have a height below 258 nm.

The cause of randomly distributed macroscopic defects appearing after electroplating is still unknown. Problematically, the electroplating is done at an independent company, DVD Norden. They employed their standard process flow for master fabrication of CDs and DVDs to produce nickel replicas from nano- and microstructured masters used in this project. The electroplating is done in a clean environment but not cleanroom facility. Thereby, particles could easily interfere with the replication process. Furthermore, they separated master and nickel replica after electroplating and structures could probably be damaged during shipping.

3.2.2. Nanostructured Pillar Patterns

Based on results achieved for the fabrication of hole arrays dose tests for arrays of 50 and 100 nm wide pillar arrays were conducted. 50 and 100 nm wide pillars were written into 115 and 200 nm thick ZEP520. Pattern doses ranging from 180 – 260 µC/cm^2 [43] were tested at current of 0.6 nA and a frame dose of 40 µC/cm^2. Patterns written into 200 nm resist were used to evaluate the electroplating process of structures with an height-to-width aspect ratio above unity. The Resist was therefore coated with 5 nm nickel prior to SEM imaging.

[43] Pillars are created by exposing a major fraction of the resist. Thereby, lower doses are required compared to arrays of nanoholes.

EXPOSURE OF 50 AND 100 NM PILLARS. Most patterns showed major discrepancies from the original design. The width of pillars decreased with increasing dose yielding in 65 ± 6 nm to 32 ± 3 nm for pillars of 50 nm intended width, and 140 ± 8 nm to 88 ± 3 nm for 100 nm. 50 nm wide pillars collapsed gradually from center towards corner with increasing exposure dose above 220 and 180 µC/cm^2 for 115 and 200 nm thick resist, respectively. For doses above 220 µC/cm^2 even pillars located at the corner collapsed to an increased extent. 100 nm wide pillars were stable in both resist thicknesses, but holes exposed at 180 µC/cm^2 resulted in a wasp waist like rectangular shape (Figure 106). Some patterns such as 100 nm wide holes written in 115 nm thick resist at 240 µC/cm^2 consist in principle of regular pillar arrays but also containing randomly distributed areas with collapsed pillars by unknown reason.

In contrast to previously written arrays of 50 nm wide holes, pillar patterns resulted in a fairly large difference of up to 23 nm between center and corner for both resist thicknesses (Figure 107). Pillars located at the corners are larger than at the center. For example, 100 nm wide pillars written into 115 nm resist resulted in 97 ± 5 and 119 ± 4 nm at the center and corner, respectively. Only for an exposure dose of 180 µC/cm^2 50 nm wide pillars written into 200 nm resist seem to have about the same dimensions. However, this pattern seems to be underexposed. The bottom in between the pillars does not look flat (SEM image Appendix 1-2.2.2.). A set of SEM images of intended 50 and 100 nm wide pillars written into 100 and 200 nm resist is given in Appendix 1-2.2.2.

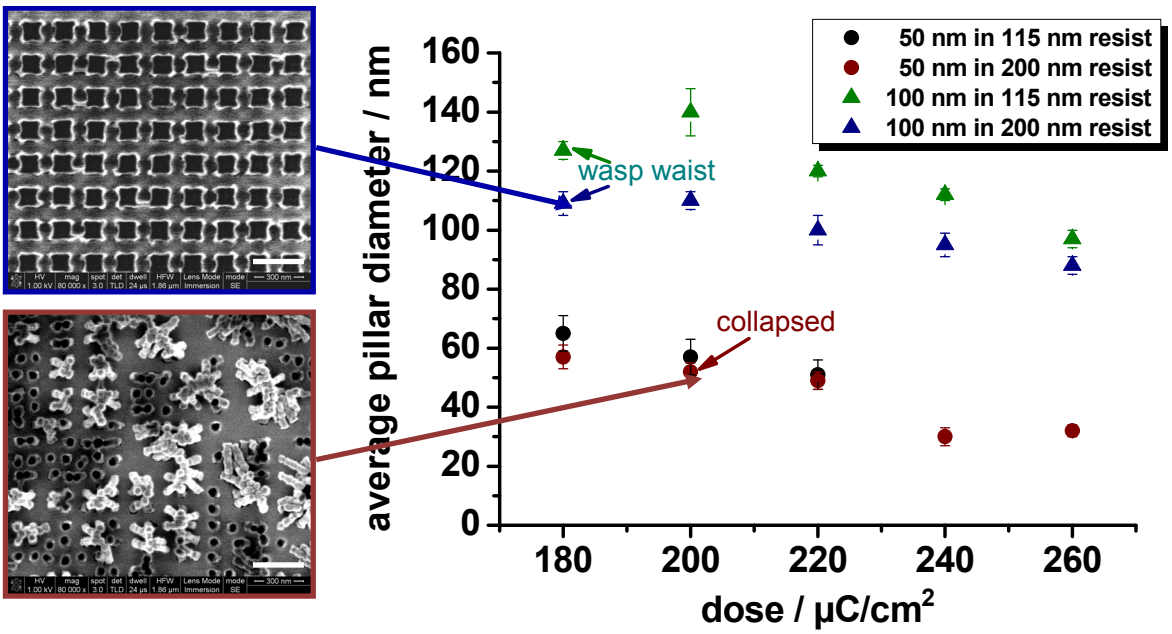

Figure 106: SEM images of 100 and 50 nm wide structures written into 200 nm resist visualizing two major discrepancies evolved from under- and overexposure (left). Width of 50 and 100 nm wide hole dependent on exposure doses (right). Scale bars: 300 nm.

Table 16: Diameter of 100 nm pillars replicated into nickel for different resist thicknesses

Dose \ Resist thickness	50 nm pillars, 115 nm resist	50 nm pillars, 200 nm resist	100 nm pillars, 115 nm resist	100 nm pillars, 200 nm resist
180 µC/cm²	65 ± 6 nm	57 ± 4 nm	127 ± 3 nm	109 ± 4 nm
200 µC/cm²	57 ± 6 nm	*52 ± 3 nm**	140 ± 8 nm	110 ± 3 nm
220 µC/cm²	51 ± 5 nm	*49 ± 3 nm**	120 ± 2 nm	100 ± 5 nm
240 µC/cm²	*collapsed*	*30 ± 3 nm**	112 ± 2 nm	95 ± 4 nm
260 µC/cm²	*collapsed*	*32 ± 2 nm**	97 ± 3 nm	88 ± 3 nm

** pillars collapsed, average width measured from laying pillars*

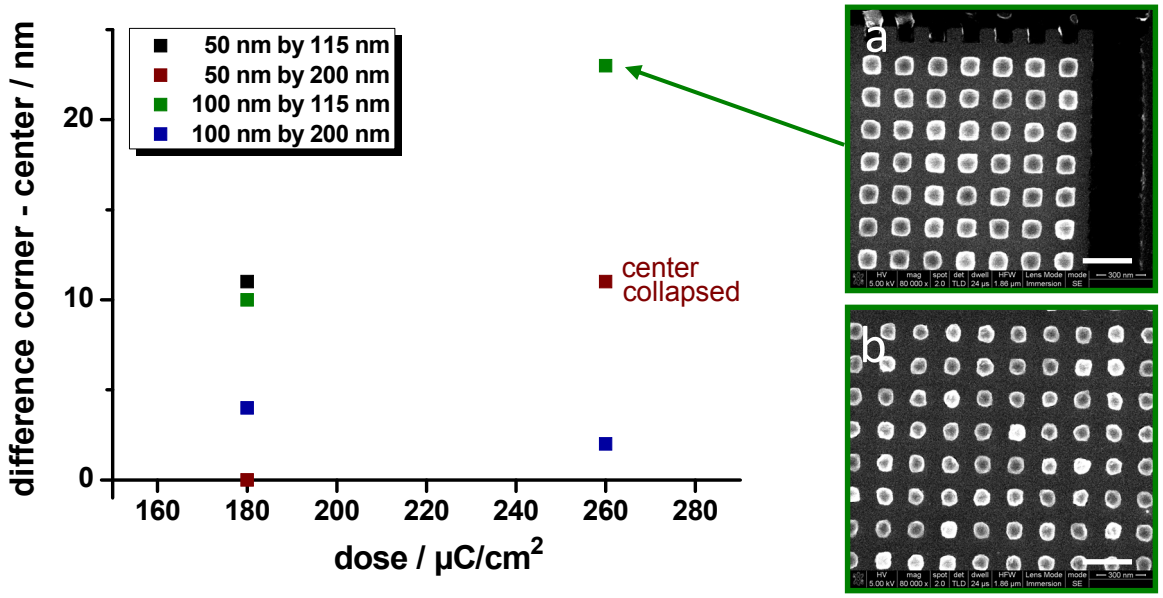

Figure 107: Difference between 50 and 100 nm holes located at center and corner. SEM images of 100 nm wide pillars located at the center (a) and corner (b) written into 100 nm thick ZEP520A (exposed at 260 µC/cm²). Scale bars: 300 nm.

The maximum depth resolved by AFM was about 30 ± 2 nm for 50 nm holes (115 nm resist, 200 µC/cm²) and about 90 ± 5 nm for 100 nm holes (115 nm resist, 260 µC/cm²) for both resist thicknesses. The measured height decreased with increasing number of scanned lines as observed before for other samples.

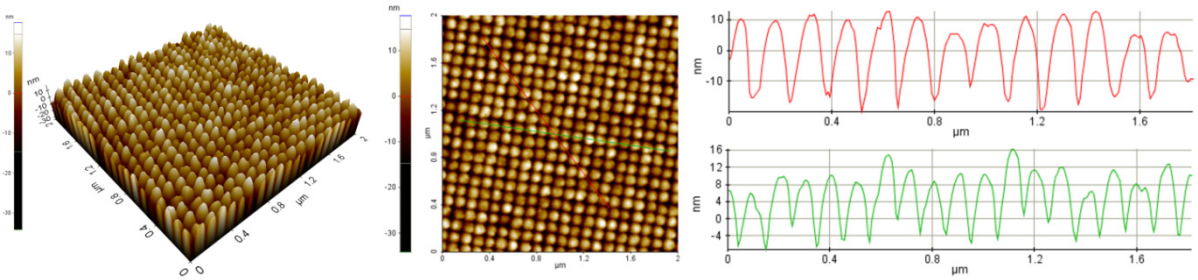

Figure 108: AFM image of 57 ± 6 nm wide pillars written into 115 nm thick resist (200 µC/cm²).

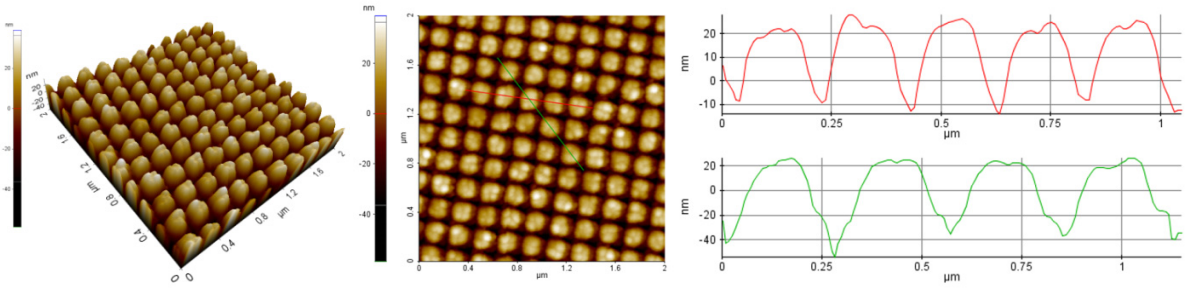

Figure 109: AFM image of 140 ± 8 nm wide pillars written into 115 nm thick resist (200 µC/cm^2).

ELECTROPLATING OF 50 AND 100 NM PILLARS. Nickel Shim and master were separated without problems. Residual resist was completely removed by Remover 1165 and acetone. As observed before for nanohole patterns, macroscaled defects appear, partially on the patterned area. Spots observed with by SEM prior to electroplating resulted in areas with structures further exposed by the electron beam. Holes in these areas display a broadening leading to broader pillars as well.

Otherwise patterns of 50 and 100 nm wide pillars were replicated into nickel with high fidelity. Most of the patterns containing intended 50 nm wide pillars collapsed during development of the resist. These collapsed pillars were nicely replicated into nickel leading to "cavities" with a maximum measured depth of 16 nm (Figure 110). Patterns containing intended 100 nm wide pillars were all replicated without problems resulting in very uniform arrays of holes of varying width complying with dimensions of pillars in resist for varying exposure doses (Figure 111). A maximum depth of 137 ± 9 nm was measured for 100 nm wide holes located in the corner (exposed at 260µC/cm^2). Holes replicated from pillar arrays exposed at the same dose but located in the center could only be measured down to a depth of 84 ± 5 nm. In both cases no "flat" bottom inside the holes was visible. A second AFM image using another tip was taken of the same pattern of holes located in the corner and resulted in only a depth of 17 ± 4 nm (AFM image in Appendix 1-2.2.2.).

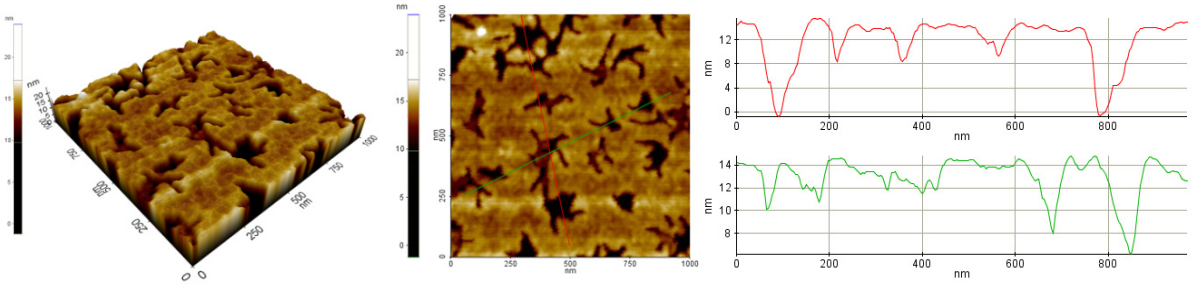

Figure 110: AFM image of cavities replicated from collapsed pillars of 50 nm intended width resulting in a maximum depth of 16 nm (resist thickness: 200 nm, dose: 220 µC/cm^2).

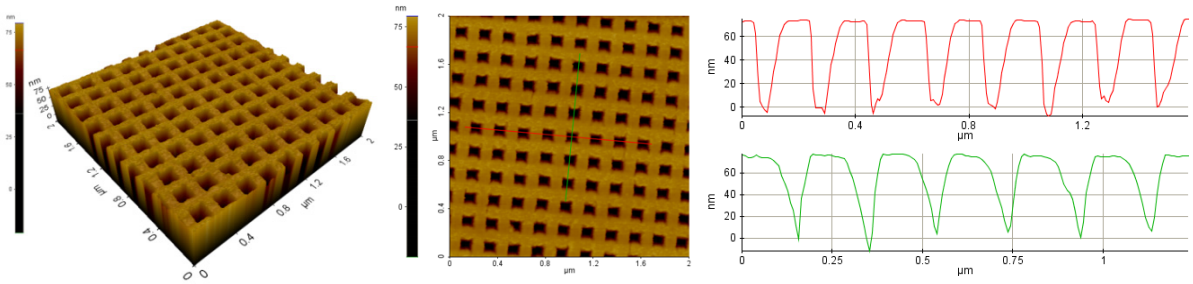

Figure 111: AFM image of holes located in the center replicated from pillars of 100 nm intended width resulting in a depth of 84 ± 5 nm (resist thickness: 200 nm, dose: 260 µC/cm^2).

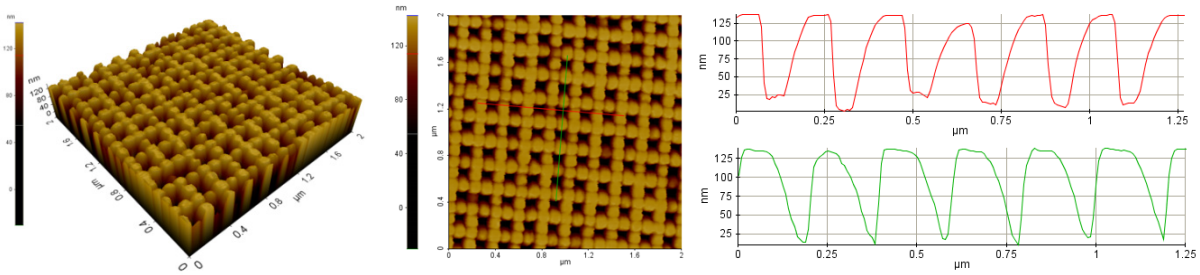

Figure 112: AFM image of holes located in the corner replicated from pillars of 100 nm intended width resulting in a depth of 137 ± 9 nm (resist thickness: 200 nm, dose: 260 µC/cm^2).

DISCUSSION. It is rather difficult to write high aspect ratio structures (above 2:1), mainly nanopillars, into ZEP520 without employing critical point drying. The resist is mechanically too instable. Most of the patterns containing 50 nm pillars collapsed, especially for 200 nm thick resist. Although only a depth of 30 and 90 nm for 50 and 100 nm wide holes, respectively, was measured we expect that the patterns were fully exposed. As discussed previously, especially the vertical resolution is heavily dependent on the tip shape. According to AFM images pillars obtain a shape with almost double the width as observed in SEM images. Therefore it is assumed that the depth was not fully resolved due to damaged or contaminated tip as explained previously. Presuming a full height of the pillars corresponding to the initial resist film thickness of 115 nm maximum aspect ratios of about 2:1 for 51 nm (50 nm exposed at 220 µC/cm^2) and 1:1 for 97 nm in width (100 nm exposed at 260 µC/cm^2) were achieved. For 200 nm thick resist aspect ratios of about 3.4 for 57 nm (50 nm exposed at 180 µC/cm^2) and 2.3 for 88 nm (100 nm exposed at 260 µC/cm^2) were achieved.

The nickel plating was able to replicate pillars written into resist, standing as well as collapsed pillars, with high fidelity though macroscaled defects were observed again. The low depth measured for 100 nm wide holes is most probably caused by limited resolution of the AFM as described before. This is supported by the fact that firstly, pillars exposed with a lower dose (holes located in the corner, Figure 112) resulted in a larger depth than obtained for those exposed with a higher dose (located in the center). Secondly, AFM images of the same area resulted in 17 ± 4 nm for one and 137 ± 9 nm (Figure 112) for another measurement. However, it could be seen from the AFM images that 100 nm pillars exposed with 260 nm are still underexposed in the corner. This shows that the frame dose of 40 µC/cm^2 was too low. The reason for macroscaled defects is still unknown. However, recently equipment for electroplating of nickel has been purchased by DTU Danchip prospectively allowing for better control of plating process and reducing defects by electroplating in a cleanroom environment.

CONCLUSION. Hole and pillar patterns of 50 and 100 nm diameter can be written into 100 and 200 nm ZEP520. 50 nm structures are mechanical instable and tend to collapse during drying after development. The electroplating of nickel resulted in uniform patterns replicated with high fidelity though unknown macroscopic defects are visible. Hole pattern can be fabricated with higher aspect ratio due to higher mechanical stability compared to pillar pattern of similar dimensions. Therefore another method was tested on their capability to produce nanopillars with height-to-width aspect ratios above unity. The original nickel mold ("father") replicated from the resist based master can be replicated again resulting in a second order nickel replica ("mother") which presents the structures originally written into resist. Thereby, holes can be written into ZEP520 producing a nickel mold presenting holes and allowing to fabricate a polymer replica containing nanopillars.

Two tests were conducting yielding similar results: it is not easily possible to produce a second order nanostructured replica from the first nickel replica. In both tests 50 nm pillars located on the "father" broke off together with a large amount of the initial sputtered nickel-vanadium from the first nickel replica and probably even parts of the electroplated nickel bulk (FIGURE). 100 nm structures seem to be replicated well but on the one hand, their depth seem to be low considering the low contrast, and on the other hand, the nickel seems to be cracked or distorted otherwise. On the one hand, the bad replication may be a result of suboptimal passivation of the nanostructures leading to increased adhesion between first and second nickel replica above common level. Therefore, structures broke off during separation of the nickel shims. On the other hand, structures could have possessed a slight undercut (or "T-shape") preventing smooth separation.

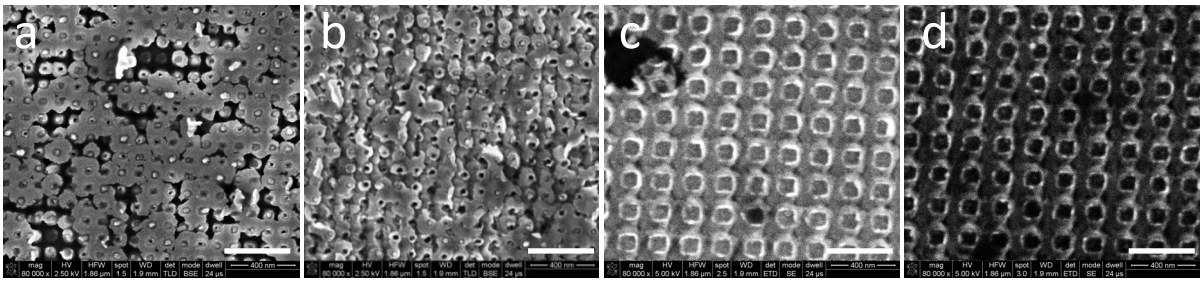

Figure 113: SEM images of the "mother" replica: 50 nm holes in resist exposed at 180 µC/cm^2 (a) and 260 µC/cm^2 (b); 100 nm holes in resist exposed at 180 µC/cm^2 (c) and 240 µC/cm^2 (d). Scale bars: 400 nm.

3.3. Summary

Nanostructures were successfully fabricated by laser lithography and electron beam lithography and subsequent etching into silicon. The replication into nickel resulted in homogene nanostructures though randomly distributed macro-defects were observed. The choice of different materials, i.e. resist or silicon, caused different problems during their development from master to mold. i.e. mechanical stability and separation issues.

MASTER FABRICATION. Laser lithography can be employed to fabricate nanostructures above 300 nm though with very low height-to-width aspect ratios of 1:4 for about 650 nm wide holes and 1:2.5 for about 315 nm wide pillars. The major problem was the large standard deviation of 50 – 100 nm caused by the row to row width deviation of structures. The irregular size distribution is most probably caused by fluctuations in the laser intensity as explained before. Further test need to conducted using a new laser to verify the cause for the size differences between lines with “narrow” and “wide” structures. If this problem can be solved fabrication patterns with high uniformity (≤ 10% of average structure width) will be possible.

Sub-micrometer structures can be fabricated by means of electron beam lithography. Nanostructures with lateral dimensions above 250 nm can be written with high precision with standard parameters. But with downscaling feature size and increasing structure density, the complexity of optimization required increases, especially to achieve nanostructures smaller than 100 nm. A major drawback of EBL is the ageing of filament used to emit electrons. Optimized dose value last only for short periods, about 1 – 2 month, according to P. Shi. Beside adjustment of important process parameters such as exposure dose, grid size and current, the mechanical stability of nanostructures in resist and silicon plays an increasing role. The less cross-linked polymer remains after development the more fragile the nanostructures become. For example, it is unproblematic to develop nanoholes of 100 nm diameter with heights up to 300 nm whereas nanopillars of equal dimensions become mechanical instable and collapse during the final drying step after resist development. Different methods can be applied to decrease the surface tension and allow for higher aspect ratios, such as critical point drying. Critical point drying was not used in this project to limit optimization effort to the EBL process and to keep the process steps and machines used limited with respect to commercial applicability. The fabrication of pillars with larger height-to-width aspect ratios can be done by using the exposed resist for subsequent dry etch of silicon by reactive ion etching. However, while the mechanical stability of resist causes problems during development and final drying step, nanostructures in silicon adhere extremely strong to sputtered/electroplated nickel. The adhesion between silicon and nickel caused fracture of either silicon pillars or nickel pillars.

Three aspects play a role in the choice of method for writing nanostructures (or sub-micron structures), resolution, speed, and cost. Since the adhesion of cells is most probably influenced by gradually decreasing structure size to dimensions below 100 nm electron beam lithography with a minimum resolution of several nanometers is the method of choice. In terms of cost is laser lithography definitely the better choice. While electron beam lithography cost about 800 €/h apart from actual acquisition cost, the running cost of the DWL66 is almost negligible. The speed of both processes is heavily dependent on pattern dimensions (total area) and process parameters. For

example, a 1000 by 500 μm^2 pattern is written in about 1.5 h using laser lithography. The same pattern takes about 20 min employing similar parameters as used in this thesis (current of about 1 nA). For an increased current the writing speed can be increased but resolution will decrease. On the other hand, the DWL66 needs the largest part of the writing time per line to accelerate and decelerate the stage. An extension of the pattern length (in "fast writing direction") will therefore not lead to a noticeable increase in writing time, even for up to the full length of about 140 mm. In contrast, for the electron beam writer each exposed dot plays a role in the exposure time. However, by increasing the current the exposure time can be increased tremendously allowing wafer-scale production on the same time-scale as laser writing with probably higher resolution but of course also much higher cost. Since nanostructures of about 100 nm or smaller were the dimensions of choice for this project, electron beam lithography was employed for all structures used for injection molding.

MOLD FABRICATION. Electroplating was used to produce a resilient mold into nickel from a resist or silicon based master structure. The electroplating is capable of replicating nanostructures from both types of substrate with high fidelity though randomly distributed macro-defects of unknown origin were observed. The major issue of electroplating features into nickel is, however, the separation of master and nickel mold. In case of resist based masters the separation is unproblematic as long as the resist is dissolvable in a polar solvent such as acetone. In case of silicon based masters the silicon and nickel, i.e. nickel-vanadium alloy, is adhering too strong. The silicon fractures during separation and etching of residual silicon with potassium hydroxide results in a corroded nickel surface exposing a grain structure. The application of fluorocarbon-based antistiction or sacrificial layers may result in improved release. However, since resist based master provide a simple and functioning process for nanostructures with aspect ratios up to 2:1, the application of antistiction or sacrificial layers was not tested extensively for nanostructure. A nickel mold was fabricated by using a silicon based master containing 250 and 500 nm holes coated with FDTS with minor success as will be described later-on.

To maintain certain simplicity of the process and due to suboptimal results of alternative methods, resist based masters were used to fabricate nickel molds used for injection molding experiments. The height-to-width aspect ratios of nanostructured molds fabricated for polymer replication were kept below 2:1.

VISIBILITY OF NANOSTRUCTURED PATTERNS. Nanostructured patterns are almost invisible and very difficult to find using light microscope, especially if not perfectly in focus. To facilitate orientation and visibility during SEM, AFM, and for cell experiments, five alignment marks of about 1 by 1 mm^2 and labels to identify nanostructured patterns were introduced. Structures were exposed in positive photo resist AZ5214E by standard UV lithography and further etched into silicon applying the same recipe as used for etching microfluidic structures as described in Section II-3.2.2.

4. Polymer Replication by Injection Molding

Injection molding is a suitable method to mass-produce nano- and microstructures as it has been shown by many research groups as described in Section I-2. In this chapter results towards the fabrication of especially sub100nm structures with an aspect ratio above unity are described and discussed. Different injection molding conditions (varying process parameters) and mold surface chemistry (untreated and fluorocarbon silane covered) were investigated to reduce molding defects and maximize structure height or depth. Nickel shims used for injection molding experiments are described in Appendix I-2.3.

As already described in detail in Section I-4.1.6., injection molding of nanostructures is dependent on the ability of the polymer melt to fill and, after solidification, to leave the nanostructured cavities. On the one hand, filling is facilitated by a high surface energy that allows the polymer to wet the surface (Figure 114, left). Surfaces with low surface energy lead to insufficient wetting and possibly even repulsion of the polymer melt. This is very likely to prevent polymer to fill nanostructured cavities (Figure 114, right). On the other hand, a good wetting is usually connected with good adhesion. A good adhesion will interfere with the demolding of solidified structures and possibly lead to fracture of nanostructures (Figure 115, left). This is especially important for the demolding of nanopillars which are mechanical less stable than nanoholes. A low surface energy implies worse wetting but also lower adhesion of the polymer melt to the mold surface. The decreased adhesion strength may allow the solidified polymer to demold without damaging single structures (Figure 115, right).

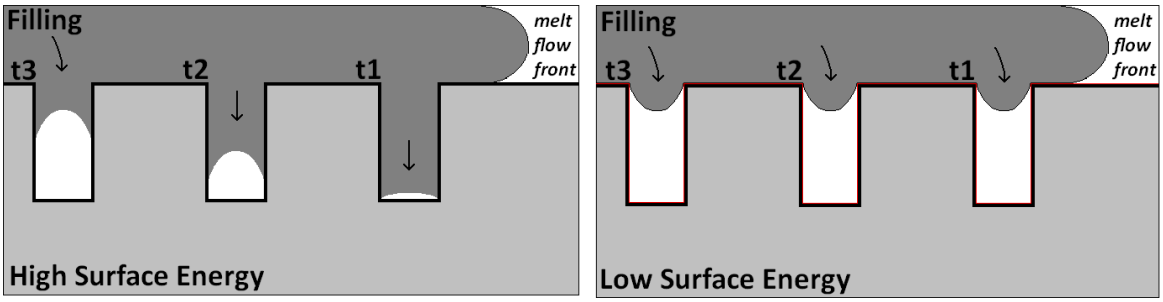

Figure 114: Sketch of assumed scheme for filling of nanostructures in molds with high (left) and low surface energy (right).

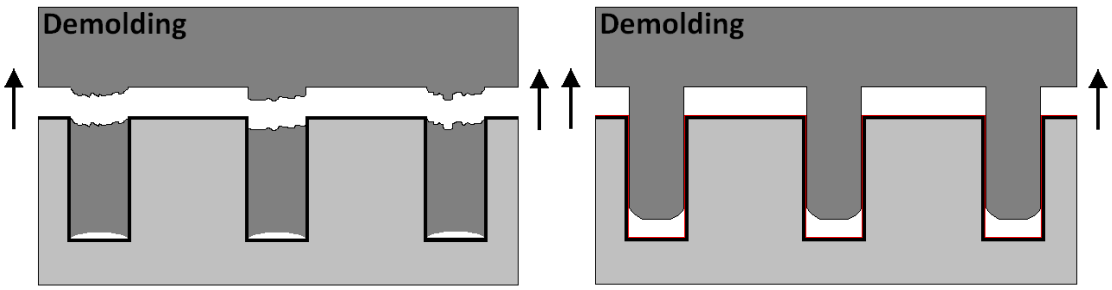

Figure 115: Sketch of assumed scheme for demolding of nanostructures in molds with high (left) and low surface energy (right) assuming equivalent filling depth.

In Section II-4.2., the wetting ability and adhesion strength of Topas 8007 and 5013 was analyzed for different surface treatments of nickel molds. The wetting and adhesion strength of Topas 8007 and 5013 was significantly reduced by application of fluorocarbon based coatings that lead to nickel molds with decreased surface energy. According to the higher contact angle of Topas 8007, this Topas grade exhibits worse wetting to native and antistiction coated nickel molds compared to Topas 5013. Nevertheless, lateral shear experiments with droplets of Topas 8007 and 5013 on differently treated nickel surfaces showed higher adhesion strength of Topas 8007 to antistiction coated nickel than Topas 5013. As discussed in Section II-4.2., this is most probably caused by air entrapped inside Topas 5013 drops possibly interfering with lateral shear force measurements. Therefore, it is assumed that Topas 5013 adheres as strong as 8007 for the same interfacial area if not stronger taking contact angle measurements into account.

Investigated Process Parameters:

- Mold and melt temperature
- Injection and holding pressure
- Injection velocity
- Ejection temperature
- *Application of different antistiction layer onto nickel shims*
- *Topas 8007 and 5013*

4.1. Injection Molding of Topas 5013

The higher glass transition temperature of Topas 5013 makes it a suitable material for cell handling system since it can be sterilized with ethanol as well as steam-sterilized. Furthermore, it has a higher flowability (Topas grade with highest melt flow index) than Topas 8007, which should facilitate filling of nanoscaled cavities in the mold.

Nanoholes were assumed to be easier to replicate by injection molding and are therefore used for initial experiments. Firstly, injection molding of nanopillars (holes in nickel shim) requires the polymer melt to flow into nanoscaled cavities. In case of holes (pillars on nickel shim) the polymer melt can flow around the pillars (in nickel) with more effective area for the polymer to fill than possible for holes in nickel. Secondly, pillars injection molded into Topas 5013 are less mechanical stable than holes, hence more sensitive towards forces exerted during the molding[44].

Injection molding of Topas 5013 was tested employing two different nickel shims, one containing 60 and 120 nm wide and 100 nm high pillars (shim ID: 100nm60h120h[45]). The other one holding 350 and 600 nm wide and 250 nm high pillars (shim ID: 250nm350h600h[46]). A variety of parameter sets were tested: T_{mold}: 125 – 135 °C, T_{melt}: 270 – 290 °C, v_{inject}: 40 – 80 mm s^{-1}, P_{inject}: 975 ± 25 bars, P_{hold}: 400 – 600 bar, T_{eject}: 57 ± 3 °C. Injection molding was done on native and fluorocarbon coated nickel shims in order to investigate the influence of mold surface and process parameter on the replication quality.

4.1.1. Native Nickel Molds

Initially results for the replication of 60 and 120 nm wide holes into Topas 5013 using a native nickel mold are presented, followed by results for 350 and 600 nm wide holes.

60 AND 120 NM WIDE HOLES. Injection molding of 60 nm wide holes resulted in heavily deformed shapes with up to 10 nm in depth (mold depth: 100 nm). 120 nm patterns were replicated with small areas of well defined holes but mostly exhibiting major distortions. The overall surface of nanostructured patterns often showed regular nanoscale defects and distortions such as elongation of holes and randomly distributed large-scale defects (Figure 116). Partially the nanostructured polymer surface seemed to be disrupted or torn apart. Furthermore, micro-scale “motifs” were observed on the nickel shim and transferred with high fidelity to subsequently molded objects (Figure 116). None of the above stated parameter sets resulted in major improvement towards fabrication of uniform patterns with regular arrays of nanoholes. The maximum achievable depth of 60 and 120 nm wide holes using uncoated nickel molds was not explored since the lateral shapes obtained were heavily distorted and therefore irrelevant as structural targets.

[44] Pillars collapsed partially during the development after exposure into ZEP520A, especially in the center of the patterns. The tensile strength of resist and pillars are of the same order of magnitude indicating that pillars injection molded into Topas 8007 or 5013 will be more sensitive towards forces excerted during the molding process than holes replicated into Topas.
[45] Shim ID 100nm60h120h: 59 ± 3 nm and 124 ± 3 nm wide and 100 nm high pillars.
[46] Shim ID 250nm350h600h: 349 ± 8 and 591 ± 10 nm wide and 249 ± 6 nm high pillars.

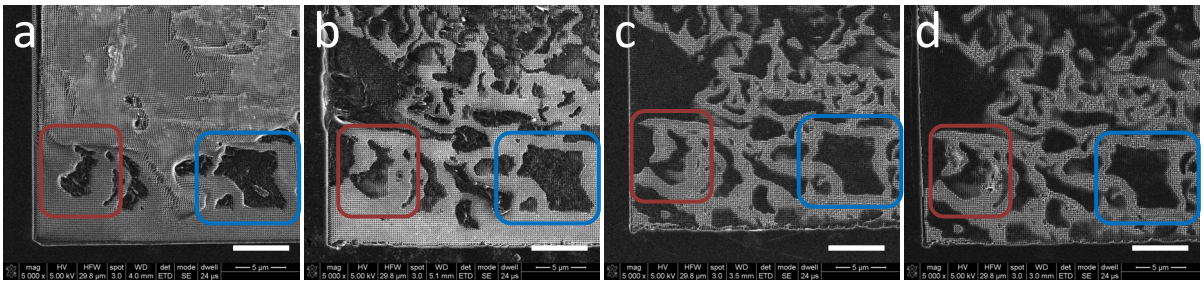

Figure 116: SEM image of Topas 5013 replicas (shim ID: 100nm60h120h) displaying contamination patterns, exemplified for red and blue rectangles. Replica no. 7 (a), no. 26 (b), no. 45 (c), and no. 71 (d). Molding parameters: T_{mold}: 120 °C, T_{melt}: 270 °C, v_{inject}: 60 mm s^{-1}, P_{inject}: 975 ± 25 bars, P_{hold}: 450 bars, T_{eject}: 57 ± 3 °C. Scale bars: 5 µm.

It was not possible to achieve patterns of 60 and 120 nm wide holes in Topas 5013 with acceptable uniformity. Therefore, injection molding of larger structure dimensions (350 and 600 nm wide holes) was performed.

300 AND 600 NM WIDE HOLES. Injection molding of 350 and 600 nm wide holes resulted in similar defects as observed for 60 and 120 nm wide hole patterns. The overall surface of nanostructured areas showed regular nanoscale defects, distortions and randomly distributed large-scale defects (Figure 117). It was not possible to achieve uniform patterns in the analyzed parameter range. A depth of 250 ± 35 nm was measured for 600 nm wide hole pattern. 350 nm wide holes were not explored since the lateral shapes obtained were heavily distorted and therefore irrelevant as structural targets.

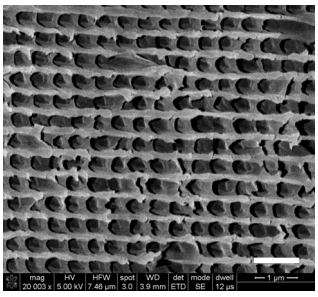

Figure 117: SEM images of about 350 nm wide holes (left) and 600 nm wide holes (right) with intended depth of about 250 nm injection molded into Topas 5013 (shim ID: 250nm350h600h). Patterns were widely distorted (b, c, d). Molding parameters: T_{mold}: 135 °C, T_{melt}: 280 °C, v_{inject}: 4 cm^3/s, P_{inject}: 975 ± 25 bars, P_{hold}: 400 bars. Scale bars: 1 µm.

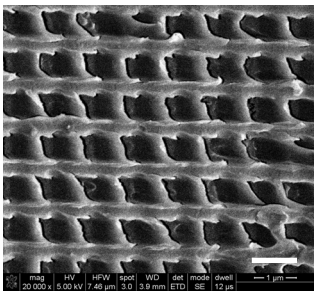

DISCUSSION. The replication of uniform arrays of 60, 120, 350, and 600 nm wide holes on native nickel molds injection molding failed completely though small areas of well replicated 120 nm wide holes were observed. The bad replication quality is possibly caused by suboptimal parameter sets though different parameters[47] were tested without any obvious effect. Mönkkönen et al. presented similar results for Topas 5013 demonstrating that complete filling was not achieved[48]. 100 nm wide grooves were replicated in Topas 5013 with a depth of about 24 nm (mold depth: 75 nm) at mold temperatures “above normal” [Mönkkönen 2002].

Nano- and large-scale defects were most probably caused by stiction of the polymeric nanostructures to the nanostructured mold during demolding. Frictional forces applied on the nanostructures during

[47] T_{mold}: 125 – 135 °C, T_{melt}: 270 - 290°C, v_{inject}: 40 – 80 mm s^{-1} (40 – 80 mm s^{-1}), P_{inject}: 975 ± 25 bars, P_{hold}: 400 – 600 bar.
[48] T_{mold}: not stated, T_{melt}: 270 and 310 °C, v_{inject}: 75 and 150 mm s^{-1}, P_{inject}: 800 and 1100 bars, P_{hold}: 800 – 1000 bar.

demolding of the solidified polymer caused nano-scale deformation and even delamination of polymer from the bulk. Polymer contamination on the nickel mold, deposited during the first molding cycles, remained on the mold surface even after further molding cycles. The additional "motif of polymer contamination" was transferred with high fidelity to subsequently molded objects (Figure 116a). The polymer contaminations were removed by applying oxygen plasma as described in Section II-2.2.

A strong adhesion of nanostructured Topas to nickel can be caused by either strong physical adsorption or by suboptimal structure shape such as undercuts which prevent demolding. Topas 5013 exhibited with 48 ± 2 ° a low contact angle on native nickel which indicates a good wetting, but also a strong adhesion (≥ 3 N mm^{-2}). The large surface-to-volume ratio of especially 60 nm wide pillars (in nickel) can complicate demolding even though nanostructures possess straight sidewalls. Moreover, undercuts possibly produced during electron beam exposure of the nanoholes in ZEP520A[49] could additionally interfere with the demolding. However, SEM images taken of collapsed pillars exposed in 200 nm ZEP520A did not show undercuts though sidewalls of collapsed pillars in 200 nm resists appeared rough (on nanoscale) (Figure 179).

All results obtained so far lead to the assumption that frictional forces applied on polymeric nanostructures during demolding are of major importance for the replication quality of injection molded features, especially nanostructures. Therefore, injection molding was investigated applying fluorocarbon-based antistiction coatings such as CHF_3 and FDTS.

[49] ZEP520A has been shown to produce re-entrant sidewalls for low acceleration voltage (30 keV) [Conway 2005].

4.1.2. Antistiction coated Nickel Molds

Antistiction coatings like CHF_3 and FDTS have been shown to decrease the adhesion of Topas 5013 substantially. FDTS turned out to be the superior material as antistiction coatings due to stronger decrease in adhesion strength of Topas 5013 compared to CHF_3 (Section II-4.2.1.). However, based on results obtained by Pranov et al., fluorocarbon based antistiction coatings[50] may limit the filling of nanoscaled cavities due to their lower surface energy. Thereby, the polymer is repelled from the mold unable to fill nanostructured cavities [Pranov 2006]. Topas 5013 wets CHF_3 coated nickel considerably better than FDTS coated nickel. CHF_3 is therefore a good compromise in terms of reduced adhesion versus good wetting.

Injection molding experiments were performed on nickel molds coated with approximately 10 nm plasma-polymerized CHF_3 using two shims: 110 nm wide and 115 nm high pillars in nickel (shim ID: 115nm110h[51]), and 60 and 125 nm wide and about 55 nm high pillars (shim ID: 55nm60h125h[52]). The influence of mold temperature (105 – 165 °C), melt temperature (260 - 290°C), injection velocity (20 – 80 mm s^{-1}), and holding pressure (200 – 600 bar) on the replication quality was investigated. Parameters were varied in relation to following standard parameters: T_{mold} = 125 °C, T_{melt} = 260 °C, v_{inject} = 40 mm s^{-1}, P_{hold} = 400 bars, P_{inject}: 975 ± 25 bars, and T_{eject}: 57 ± 3 °C. The only exception was done for the analysis of different melt temperatures whereby a mold temperature of 135 °C was applied.

MOLD AND MELT TEMPERATURE. The replication fidelity of nanoscaled structures was substantially improved. Nano- and large-scale defects of the overall patterned surface were fully removed. No micro cracks were observed. Only flow lines were observed for 105 and 115 °C.

Neither mold temperatures between 105 and 165 °C, nor a melt temperature of 260 – 290 °C did show any significant effect on the replication depth. Pillars injection molded at different mold temperatures obtain average hole depth of 68 ± 6 nm regardless of mold temperature (Figure 119). The melt temperature led to an average depth of 74 ± 6 nm regardless of melt temperature. A maximum depth of 79 ± 6 nm was measured for holes replicated at a mold temperature of 135 °C and a melt temperature of 280 °C. A smooth surface without visible height differences or nanoscaled deformations was observed for all samples.

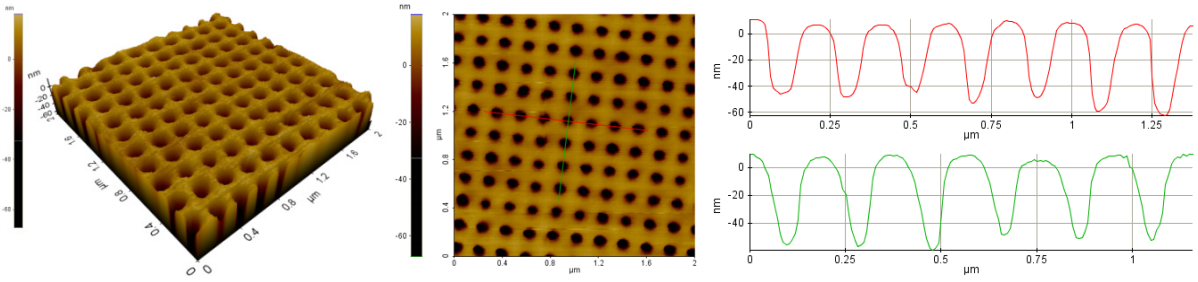

Figure 118: AFM image of 110 nm wide and 67 ± 6 nm deep holes replicated into Topas 5013 (v_{inject} = 40 mm s^{-1}, P_{hold} = 400 bars, T_{mold} = 125 °C, T_{melt} = 260 °C).

[50] Pranov et al. used FOTS evaporated in vacuum (tridecafluoro-1,1,2,2-tetrahydrooctyl trichlorosilane, $CF_3(CF_2)_5(CH_2)_2SiCl_3$).
[51] Shim ID 110nm110h: 107 ± 4 nm wide and 116 ± 4 nm high pillars.
[52] Shim ID 55nm60h125h: 59 ± 3 and 124 ± 3 nm wide and 54 ± 2 nm high pillars.

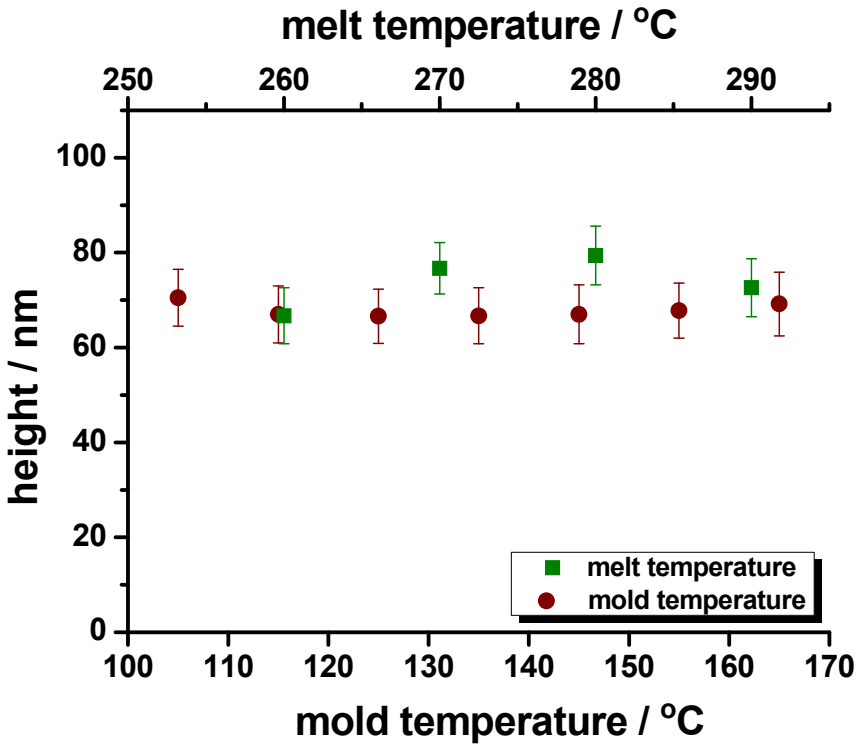

Figure 119: Replication depth of 110 nm wide holes (shim ID: 115nm110h) as a function of mold and melt temperature (P_{hold} = 400 bars, v_{inject} = 40 mm s^{-1}, T_{mold} = 135°C, T_{melt} = 260 °C).

DISCUSSION. The application of a fluorocarbon based antistiction coating[53] was tested with the known caveat that they may limit the filling of nanoscaled cavities in the mold [Pranov 2006]. Nevertheless, a layer of 10 nm fluorocarbon on the nickel mold surface enhanced the replication fidelity of nanoscaled structures substantially without reducing the replication depth. Nano- and large-scale defects of the overall pattern surface were fully removed. It was possible to replicate 110 nm wide and up to about 79 ± 6 nm deep holes with homogenous shape[54].

At least the mold temperature was expected to have a major influence on the replication of nanostructures. The absence of any effect caused by a change in mold temperature can be explained if the heat transfer at the melt/mold interface is examined with close attention. The theory of a nanometer thick skin layer formed at the polymer melt/mold interface is based on the assumption that the heat of the polymer is transferred to the mold were it diffuses further into the bulk (of the mold). Thereby, the first few nanometers of the polymer melt are cooled down and solidify upon contact with the mold which can restrict the filling of nanoscaled cavities.

The limited resolution of AFM, even if applying super sharp silicon tips, is well known and was discussed previously. This is supported by the additional samples injection molded at 135 °C exhibiting almost the full depth of about 100 nm (mold with about 115 nm high pillars). Moreover, none of the recorded images contains holes with cylindrical form and flat bottom as visualized from inverted AFM images. This issue will be discussed later in “Injection Velocity and Holding Pressure”.

[53] CHF_3 coated nickel shims: plasma-polymerized from CHF_3 monomer.
[54] P_{hold} = 400 bars, v_{inject} = 40 mm s^{-1}, T_{mold} = 135°C, T_{melt} = 280 °C.

The fact that additional samples molded at the same parameter set as the “main set of chips” (Figure 119, s1) proves that, on the one hand, a depth of 100 nm can be replicated. On the other hand, at least a depth of 100 nm can be resolved for 110 nm wide holes.

The absence of any effect caused by a change in mold temperature can be explained if the heat transfer at the melt/mold interface is regarded with close attention. The theory of a nanometer thick skin layer formed at the polymer melt/mold interface is based on the fact that the heat of the polymer is transferred to the mold were it diffuses further into the bulk (of the mold). Thereby, the first few nanometers of the polymer melt are cooled down and solidify upon contact with the mold which can restrict the filling of nanoscaled cavities (Section I-4.1.6.). This is most likely true for structures which display a low “initial contact area” for the polymer melt at the melt/mold interface. The “initial” contact area is defined by the area that the polymer can wet before solidification occurs. For example, patterns with array of holes and pillars can have the same surface-to-volume ratio by varying structure width, pitch and especially depth. However, the “initial contact area” for the polymer melt is smaller for holes than for pillars of the same width, pitch and height (or depth).

The amount of heat that is transferred from polymer melt to mold depends heavily on this intial contact area. In case of an array of nanoholes presented in the mold, the polymer is wetting the top surface and immediately transfers heat from the melt to the mold at the interfacial area between melt and mold. The polymer solidifies and restricts the filling depth. Pillars in polymer will therefore have a low replication height. For the opposite case, pillars presented on the mold, the initial contact area is much larger. Upon contact of the polymer melt with the tip of a pillar heat is immediately transferred with the same rate as for the hole pattern. In contrast, the heat in single pillars cannot dissipate into the bulk of the mold due to spatial limitations. The polymer around the pillars will cool down much slower, hence increasing the “initial contact area”. The melt can flow along the pillars and down to the bottom without substantial cooling of the polymer melt. Based on these consideration following assumption appears very likely. In case of a high initial contact area the polymer melt is cooled and a skin layer formed while in case of a low initial contact area rather the mold is heated up. Supported by these assumptions it is very unlikely that the holes were not replicated to the full depth. For the very same reason, no effect of the melt temperature was observed. The mold is “heated up” faster than the polymer melt at the melt/mold interface can “cool down”, hence leading to equal replication depths. The low measured depth may be caused by limited vertical resolution of the AFM, especially since the images do not display holes with a flat bottom.

All molded chips possessed very smooth surfaces with well shaped holes which rather indicate a complete replication to full depth. In the case that AFM images would represent the actual depth, the polymer melt would have to solidify very precisely at the same position in between all present pillars to achieve such a smooth surface. However, it is seems more likely that the polymer melt filled up the space in between the pillars completely down to the bottom, hence presenting a smooth surface. In that case, the spatial limitations of the AFM would have caused too low hole depth. However, the sample molded at a mold temperature of 105 and 165 °C was re-measured with different super sharp silicon tips resulting in a similar depth but not larger. The reason for the small replication depth despite a good surface quality is yet unknown.

INJECTION VELOCITY AND HOLDING PRESSURE. Optimization of process parameters resulted in the highest replication fidelity for width and depth at a holding pressure of 400 bars and injection velocity of 40 mm s^{-1}. The replication depth increased from 13 ± 2 and 38 ± 1 nm at 20 mm s^{-1} with increasing injection velocities up to 34 ± 6 and 54 ± 2 nm at 40 mm s^{-1} and decreased for higher velocities down to 15 ± 2 and 34 ±1 nm at 80 mm s^{-1} for 60 and 120 nm wide holes, respectively. The holding pressure followed the same behavior with highest replication depth at 400 bars. 60 nm wide structures were replicated with a maximum depth of 35 ± 6 nm while 120 nm wide structures were replicated with 54 ± 2 nm (mold with about 55 nm high pillars) at an injection velocity of 40 mm s^{-1} and holding pressure of 400 bars (Figure 120 and Figure 121).

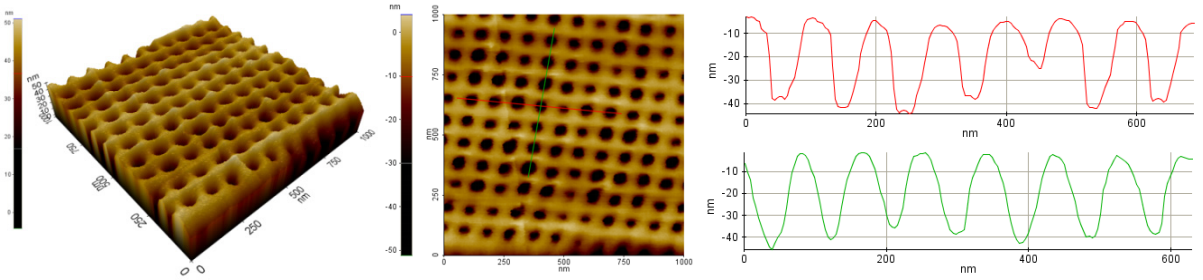

Figure 120: AFM image of 60 nm wide and 35 ± 6 nm deep holes replicated into Topas 5013 [55] (v_{inject} = 40 mm s^{-1}, P_{hold} = 400 bars, T_{mold} = 125 °C, T_{melt} = 260 °C).

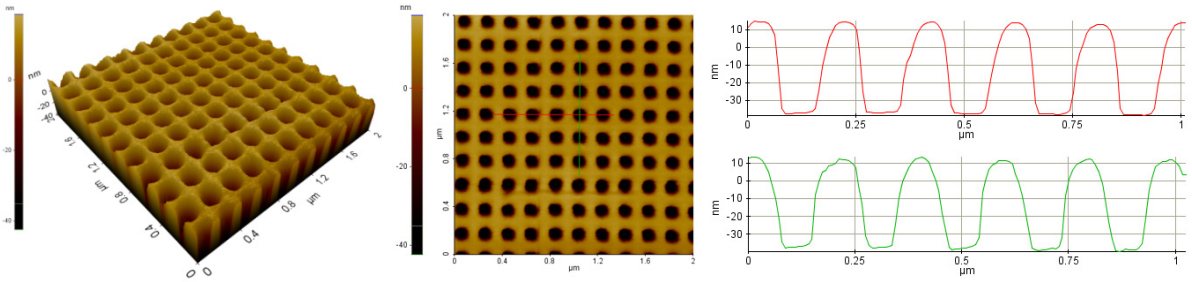

Figure 121: AFM image of 120 nm wide and 54 ± 2 nm deep holes replicated into Topas 5013 (v_{inject} = 40 mm s^{-1}, P_{hold} = 400 bars, T_{mold} = 125 °C, T_{melt} = 260 °C).

[55] The curved course of subsequent rows of holes visible in the AFM images was caused by drifting of the sample. Subsequent recorded images showed did not exhibit drifting. However, the depth of 60 nm wide holes decreased with each scan. To demonstrate the maximum possible depth, this image is presented.

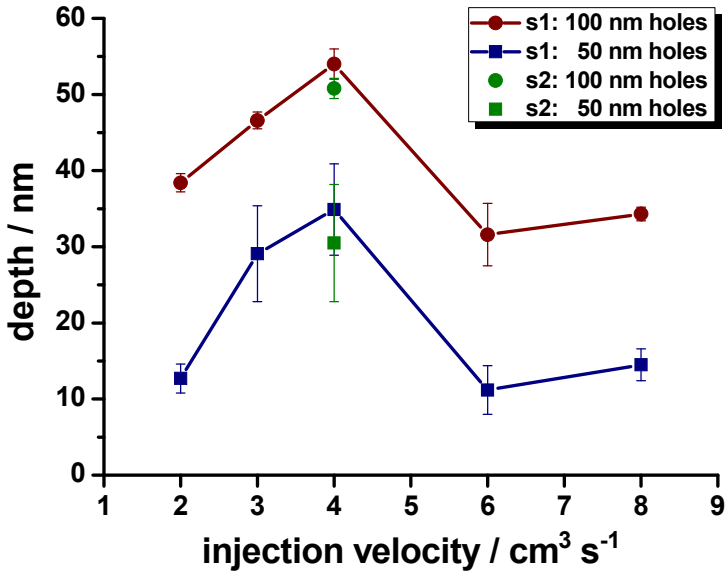

Figure 122: Replication depth of 60 and 120 nm wide and about 55 nm deep holes (shim ID: 55nm60h120h) as a function of injection velocity (P_{hold} = 400 bars, T_{mold} = 125 °C, T_{melt} = 260 °C).

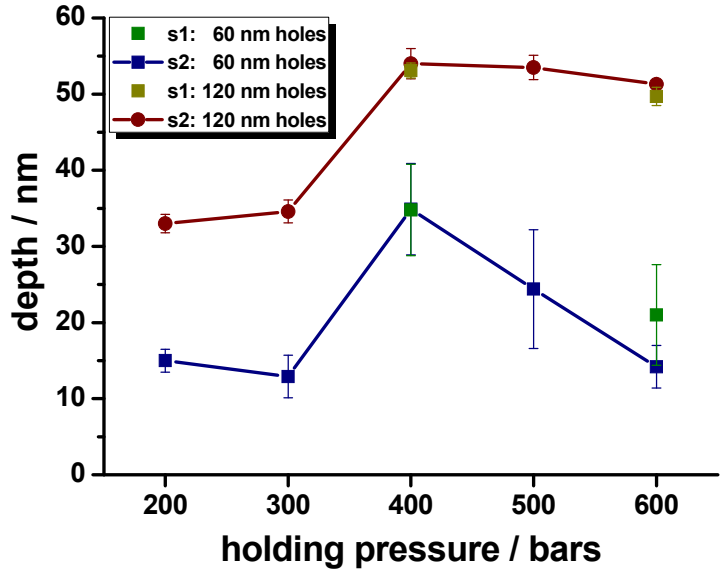

Figure 123: Replication depth of 60 and 120 nm wide holes (shim ID: 55nm60h120h) as a function of holding pressure (v_{inject} = 4 cm^3 s^{-1}, T_{mold} = 125 °C, T_{melt} = 260 °C).

DISCUSSION. It was possible to replicate 60 nm wide and 35 ± 6 nm deep and 120 nm wide and 54 ± 2 nm deep holes with homogenous shape. The replication depth increased with increasing injection velocity up to 40 mm s^{-1} and decreased for higher injection velocities. A similar trend was observed for increasing hole depth with increasing holding pressure until 400 bars and decreasing hole depth for decreasing holding pressure. It was expected that the replication depth would increase monotonously with increasing velocity and/or pressure until the full height of the mold structures is reached.

AFM images of different molding parameters were taken at different days, most likely using different AFM tips. Thereby, it is possible that the AFM images for a holding pressure of 500 and 600, as well as an injection velocity of 60 and 80 mm s^{-1} were recorded with tips of varying spatial dimensions leading to lower depths. This could be the reason that 60 and 120 nm holes follow the same trend. If the AFM tip exhibited larger spatial dimensions, the depth of 60 nm wide holes decreases to a similar extent as observed for 120 nm wide holes. A comparison of inverted view of AFM images presenting 120 nm wide holes was performed (Figure 124). It clarified that even though holes obtained equivalent shape on the "top", the bottom looked differently. For most of the samples, the holes exhibit a tapering shape towards the bottom (Figure 124, right). This supports the assumption of a limit vertical resolution of the AFM.

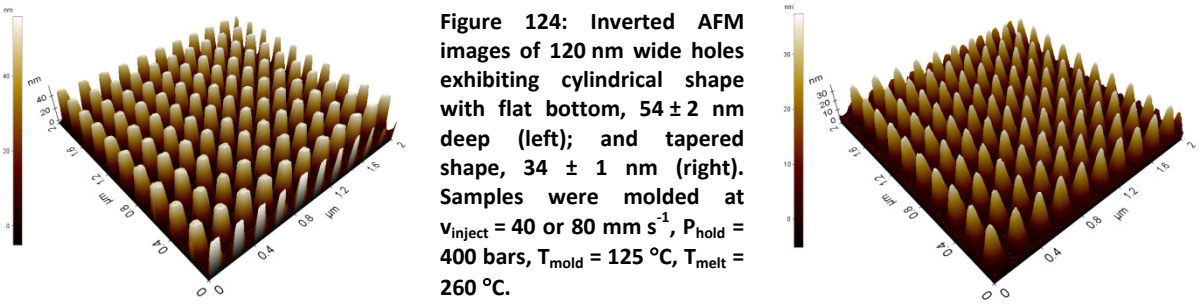

Figure 124: Inverted AFM images of 120 nm wide holes exhibiting cylindrical shape with flat bottom, 54 ± 2 nm deep (left); and tapered shape, 34 ± 1 nm (right). Samples were molded at v_{inject} = 40 or 80 mm s^{-1}, P_{hold} = 400 bars, T_{mold} = 125 °C, T_{melt} = 260 °C.

DEGRADATION OF CHF_3. X-ray photoelectron spectroscopy was employed to probe for inadvertent transfer of the fluorocarbon coating on the nickel mold to the injection molded pieces. No traces of fluorine were observed on molded items which lead to the conclusion that no degradation of the antistiction layer has occurred, even after hundreds of injection molded pieces. The degradation of CHF_3 was studied in detail and is described in Section II-4.2.2.

INJECTION MOLDING OF NANOHOLES VERSUS NANOPILLARS. Nanoholes of dimensions below 100 nm and a height-to-width aspect ratio above unity are often difficult to image reliable by AFM even though super sharp silicon tips were used. Trials to obtain a cross-section that can be imaged by SEM failed due to strong deformation appearing (Section III-3.2.1, Figure 101). Hence, it was decided to employ sub100 nm pillar patterns to investigate injection molding conditions thoroughly. Injection molding of 40 nm wide and up to 107 nm high pillars (height-to-width aspect ratio of up to 2.7:1) will be described in the following section.

4.2. Injection Molding of Topas 8007

Motivated by the improvement in replication quality for nanoholes in Topas 5013 using CHF_3 coated shims, the injection molding of more problematic patters such as arrays of pillars was investigated.

In the previous sub-section the main focus was set on the improvement of injection molding applying an antistiction coating, hence changing the mold surface energy. A comparison of the effect of process parameters on the actual replication depth was difficult due to large distortions of the hole patterns on native shims. Moreover, limited resolution of the AFM may have resulted in deception of the influences of process parameters on the replication depth. The actual height of pillars is less less problematic to resolve if the pitch in between them is large enough demonstrated by a flat bottom in between. Therefore small pillars (40 nm wide) with a large pitch (200 nm) were chosen. A large depth (intended 110 nm) was chosen to explore the filling as well as demolding of high aspect ratio structures (up to almost 3:1).

In this sub-section focus was set on the effects of the process parameter such as mold temperature on the replication height of pillars, especially for antistiction coated molds, but in comparison to native molds.

MOLDING OF PILLARS. Arrays of pillars, especially of such small dimensions (40 nm width and 100 nm intended height), provide a better model for the investigation of process parameters but also the effect of mold conditions. Very small but deep cavities (depth-to-width aspect ratio above unity) need to be filled while a large initial contact area is presented. The polymer melt will obtain the temperature of the mold at the melt/mold interface within few nanoseconds [Biancardo 2008, Section I-4.1.6., Section III-4.1.2.). In case of a "cold" mold, meaning a mold temperature below glass transition temperature the hot polymer melt will cool within nanoseconds forming a nanometer thick solidified skin layer. It is expected that the polymer once solidified cannot flow or deform further into the nanoholes leading to low replication depth. In contrast, if a mold temperature above glass transition temperature is applied, the polymer will only "cool" down from the bulk temperature to the mold temperature. Thereby, the polymer is kept in a deformable if not fluid state and probably able to fill the nanoholes completely.

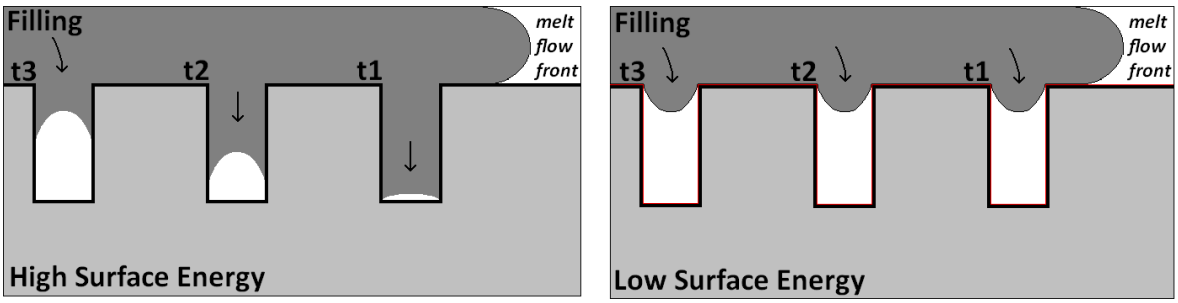

Figure 125: Theoretically assumed filling of nanostructures on native (high surface energy) and fluorosilane coated (low surface energy) nickel shims at different moments (under zero pressure condition as described [Pranov 2006]).

DEMOLDING OF PILLARS. The replication of pillars is not only more sensitive in case of filling but also regarding demolding. Given adequate filling, the adhesion of the polymeric pillars to the holes in the mold will determine whether the pillars can be demolded or not. If the adhesion strength exceeds a certain limit, frictional forces applied on the pillar cause deformation and finally fracture of structures (Figure 126). Due to the lower mechanical stability of pillars compared to holes, pillars will fracture easier. They will thereby react more sensitive towards changes in the adhesion of polymer to mold. To prevent deformation and fracture a low adhesion of polymer to mold is favorable namely a low surface energy of the mold. As already discussed, FDTS is expected to be the superior antistiction coating for nickel molds during injection molding. FDTS (as well as CHF_3) showed no substantial degradation during injection molding, at least for the first 75 pieces. However, FDTS resulted in a thermally more stable coating than CHF_3 based coatings[56]. FDTS coated nickel produce also substantially higher contact angles for Topas 8007 (and 5013) implying a lower surface energy. Injection molding experiments of Tops 5013 conducted on CHF_3 coated nickel shims indicated that rather high frictional forces during demolding are problematic for nanostructured patterns than a limitation in the filling. Hence, FDTS coatings resulting in even lower surface energy were investigated on the influence of filling and demolding of polymeric nanostructures. Lastly, FDTS can be deposited in a more controllable way, depositing an oriented monolayer while CHF_3 is plasma-polymerized to randomly oriented multilayer with a common layer thickness of 10 nm[57].

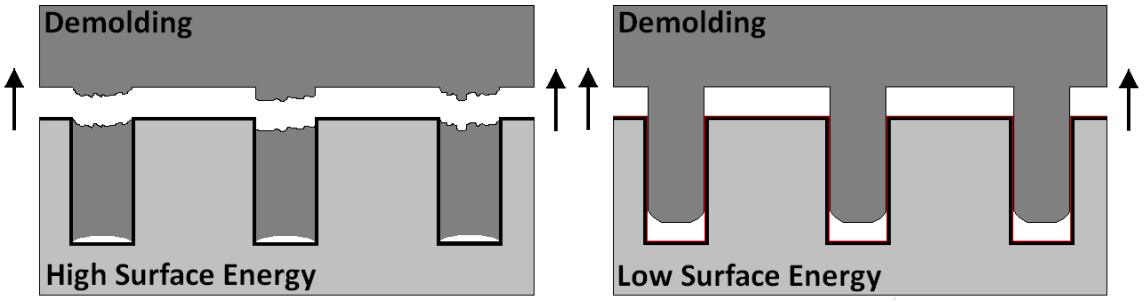

Figure 126: Theoretically assumed demolding of nanostructures on native (high surface energy) and fluorosilane coated (low surface energy) coated nickel shims.

TOPAS 8007. Topas possess excellent properties for a wide range of applications (Section I-4.3.1.). The two grades used in this thesis differ mainly due to a lubricant[58] added to Topas 5013 to increase flowability and thereby improve injection molding. The lateral ball shear test showed that Topas 5013 is wetting the FDTS coated nickel surface better than 8007, most probably caused by this lubricant. In fact, Topas 8007 shows a repelling character for FDTS coated surfaces (97 ± 3 °). Based on the contact angle measurements, the adhesion strength of Topas 8007 was expected to be lower than of 5013. The opposite was found from lateral shear experiments, but with the caveat that air entrapped inside of Topas 5013 droplets used to measure the adhesion strength lead to a lower measured adhesion than actually present. Moreover, Topas 8007 has a lower glass transition temperature leading to shorter cycle times for heating and cooling. For the last cooling system used

[56] Nickel shims coated with FDTS and CHF_3 were heated up to 300 °C for about 5 min. The contact angle of especially hexadecane decreased much stronger for CHF_3 than observed for FDTS after that treatment (Section II.4.2.1.).
[57] Layer thickness of below 10 nm might be possible to achieve similar contact angles. However, lower thicknesses were not analyzed, especially towards layer uniformity.
[58] Chemical composition not stated by the manufacturer.

(setup 3[59]), temperatures above 135 °C result in cycle times for heating and cooling of the mold of above 10 min. The cycle time can be kept below 6 min for temperatures up to 100 °C. The low glass transition temperature has, however, the drawback that sterilization can only be done by applying ethanol.

Based on these facts, Topas 8007 was chosen for thorough investigation of molding conditions for two different mold conditions (native and FDTS coated). Knowledge gained about the influence of various molding conditions and relevance of mold surface chemistry helps understanding mechanism and driving forces relevant in injection molding. It is expected that effects of process conditions will applying for Topas 5013 as well though possibly to different extent. Major problems addressed are firstly, how do certain molding parameters influence the replication quality? Secondly, which surfaces enable filling and release of high aspect ratio nanostructures?

Injection molding was performed using a nickel shim containing 40 ± 3 nm wide holes and 109 ± 2 nm wide and 109 ± 2 nm high pillars. The analysis of the pillar pattern was done by imaging areas close to the corner (about 40 nm wide) instead of pillars located in the center (about 33 nm wide). During the master fabrication pillars located in the center collapsed partially. On the final polymer replica, it would be impossible to distinguish between pillars of low height caused by limitations in the polymer replication and those caused by pillars (partially) collapsed or deformed during master fabrication. To avoid false measurements originating from defects in the master fabrication only pillars located within 100 µm from the corner.

It is to note that two nickel shims containing equal patterns were used to analyze the process parameters, fabricated with the same process parameters. Both shims possess structures equal dimensions and will therefore be referred to as shim ID: 110nm40p110h[60]. The first nickel shim was used to analyze the mold temperature (native and fluorosilane), melt temperature (fluorosilane), injection pressure (fluorosilane), and holding pressure (fluorosilane). The second shim was employed to study the melt temperature (native), injection velocity (fluorosilane), and ejection temperature (fluorosilane). Samples analyzed on fluorosilane coated nickel were done after one single coating process without cleaning and re-coating in between. This also allows gaining information about the long-term stability of FDTS coatings.

The order of different injection molding parameter set was as follows:

(1) Shim no. 1
   a. Mold temperature (native): 60 – 100 °C (150 pieces)
   b. Melt temperature (fluorosilane): 220 – 280 °C (175 pieces)
   c. Injection pressure (fluorosilane): 750 – 1020 bars (100 pieces)
   d. Mold temperature (fluorosilane): 40 – 100 °C (200 pieces)
   e. Holding pressure (fluorosilane): 700 – 800 bars (50 pieces)

(2) Shim no. 2
   a. Melt temperature (native): 220 – 280 °C (175 pieces)
   b. Injection velocity (fluorosilane): 50 – 300 mm s^{-1} (175 pieces)
   c. Ejection temperature (fluorosilane): 30 – 70 °C (5 pieces)

[59] Different cooling systems are described in Section II.4.1.
[60] Shim ID 110nm40p110h: 40 ± 3 nm wide holes (pitch: 200 nm) and 109 ± 2 wide nm and 109 ± 2 nm high pillars (pitch: 200 nm).

4.2.1. Mold Temperature

The mold temperature is widely considered as the molding parameter with the strongest influence on the replication quality, as also observed in this project. The different parameters are, of course, difficult to compare since they are not related to each other. The weighting is done based on the effect strength on the replication depth in the tested parameter range.

Structures were mold applying standard parameters (T_{melt}: 250 °C, v_{inject}: 100 mm s^{-1}, P_{inject}: 750 ± 25 bars, P_{hold}: 800 ± 25 bars, t_{eject}: 40 ± 3 °C) at varying mold temperature (T_{mold}: 40 – 100 °C).

40 NM WIDE PILLARS[61]. The influence of the mold temperature on the replication depth was analyzed for mold temperatures of 60 – 100 °C[62]. The mold temperature strongly influenced the replication quality of nanostructures and appearance of defects, on native as well as fluorosilane coated nickel molds.

Polymer pieces injection molded on a native nickel mold showed visible inhomogeneities of the nanostructured patterns and large-scale defects, especially for mold temperatures below 80 °C. Moreover, micro cracks[63] were found on polymer pieces molded on native shims. In contrast, all patterns molded on the FDTS coated shim exhibited excellent uniformity of nanostructured patterns without visible defects (nano- and large scale) regardless of mold temperature. A mold temperature of 40 °C flow resulted in uniform patters as well though flow lines were observed. The native shim showed increasing amount of polymer remaining on the nickel shim for increasing molding cycles at mold temperatures below 80 °C. The lower the mold temperature the more the polymer remained on the nickel mold. By applying mold temperatures of 90 °C or higher, polymer contaminations on the shim can be reduced to a large extent. Within about ten injection molding cycles after applying a mold temperature of 90 °C[64]polymer was reduced substantially and homogenous pattern (by eye) were obtained on the shim. No polymer residuals were observed on FTDS coated shim for any mold temperature.

The average pillar height increased with increasing mold temperature, observed for native as well as FDTS coated shims (Figure 127). Pillars molded from the native shim resulted in only a small increase in pillar height from 10 ± 4 nm at a mold temperature of 60 °C to a maximum replication height of 30 ± 10 nm for 80 – 100 °C (Figure 127, b). Pillars injection molded on FDTS coated nickel shim showed significantly larger average pillar heights, increasing from 4 ± 1 nm at 40 °C and 17 ± 4 nm at 60 °C up to 69 ± 38 nm at 100 °C (Figure 127, a). The standard deviation increased tremendously for mold temperature above 60 °C. The average pillar height was constantly larger for the FDTS coated nickel shim compared to the native shim.

[61] Shim ID 110nm40p110h: 40 ± 3 nm wide holes (pitch: 200 nm) and 109 ± 2 nm wide and 109 ± 2 nm high pillars (pitch: 200 nm).
[62] Glass transition temperature of 8007: 78 °C (manufacturer), 83 °C (experimentally determined).
[63] Micro cracks are described in more detail in Section II-4.3. (injection molding of microstructures).
[64] "Cleaning" was performed after the shim was used to injection mold pieces at a mold temperature of 60°C.

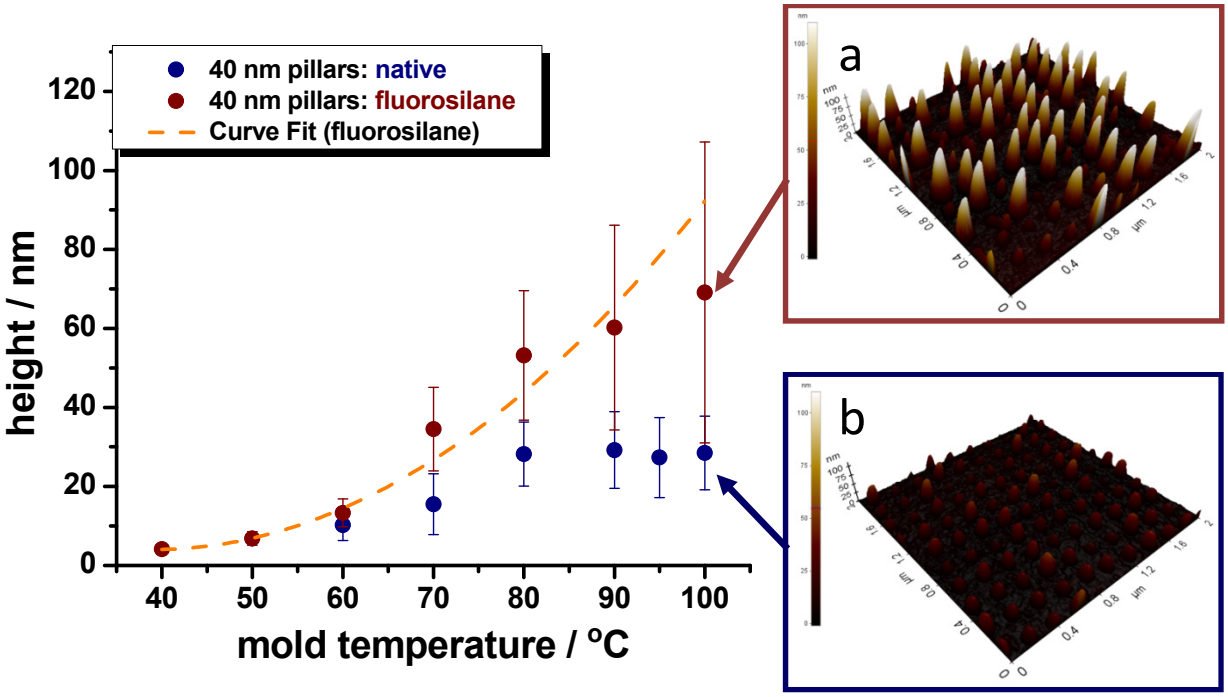

Figure 127: Average height of pillars injection mold into Topas 8007 on native and fluorosilane coated nickel shim at varying mold temperatures[65] (left). AFM images represent pillar patterns molded at 100 °C on FDTS coated (a) and native mold (b).

Table 17: Average height of pillars injection mold into Topas 8007 on fluorosilane coated nickel shim at varying mold temperatures

Mold temperature	Native	FDTS
40 °C	-	4 ± 1 nm
50 °C	-	7 ± 2 nm
60 °C	10 ± 4 nm	17 ± 4 nm
70 °C	16 ± 8 nm	35 ± 11 nm
80 °C	28 ± 8 nm	33 ± 15 nm
90 °C	29 ± 10 nm	60 ± 26 nm
100 °C	27 ± 10 nm	69 ± 38 nm

DICUSSION. The mold temperature strongly influenced the replication quality of nanopillars and appearance of defects, on native as well as fluorosilane coated nickel molds. Macroscopic defects, especially related to stiction of polymer to the mold surface, disappeared completely for polymer replicas molded on FDTS coated nickel shims. Only for very low mold temperature of 40 °C flow lines were observed. Interestingly, the flow lines did not widely interfere with the replication of the nanostructures. Injection molding on FDTS coated molds improved the replication quality enormously, eliminating nano- and large-scale defects particularly related to adhesion of polymer to nickel mold surfaces. Macroscopic defects such as polymer contaminations on nickel or micro cracks disappeared completely. Deformation of single nanostructures and distortions on micro-scale were

[65] Process parameters: T_{melt}: 250 °C, v_{inject}: 10 cm^3 s^{-1}, P_{inject}: 750 ± 25 bars, P_{hold}: 800 ± 25 bars, t_{eject}: 40 ± 3 °C

strongly reduced. Sometimes, randomly occurring and randomly oriented nano-scale deformations such as tilting of pillars or tips of excess material on top of nanoholes[66] appeared which will be discussed later.

Phenomena related to filling and demolding are expected to decide on the final height of pillars replicated into polymer. Results obtained for different mold temperature on native and FDTS coated nickel shims help separating the influence of these factors on the final replication height of 40 nm wide pillars.

The replication depth increased significantly with increasing mold temperature, especially for the FDTS coated shim, as expected from theoretical considerations. For mold temperatures below glass transition temperature, the hot polymer melt cools and solidifies upon contact with the substantial cooler mold leading to formation of a skin layer within few nanoseconds. The cooler the mold the shorter is the flow path of the polymer melt before solidification, hence forming smaller pillars. Mold temperatures at or above glass transition temperature lead to improved replication. Although the polymer cools substantially, the viscosity remains low enough to allow for flow or at least deformation into the nanoholes in the shim.

The average pillar height increases for both shim surfaces about the same extent (about 30 nm) until a mold temperature of 80 °C, equal to the glass transition temperature, is reached. For higher temperatures, the average pillars height remains about 30 nm for the native shims while increases up to about 70 nm for the FDTS coated shim. This indicates that at low temperatures filling is limiting while at elevated mold temperatures demolding related phenomena such as friction become important. For elevated mold temperatures at which the FDTS coating resulted in a larger replication height that native nickel shims, the demolding must be the cause of the smaller pillar heights for native shims. Based on contact angle measurements carried out for Topas 8007 (and 5013) in Section II-4.2., and results obtained by Pranov et al., the lower surface energy of FDTS coated nickel shims should lead to rather limited filling of nanostructured cavities compared to native nickel.

Besides limited filling of holes in the shim, the increasing amount of polymer contamination indicates that polymer is partially fractured during demolding and remains on the nickel mold. Demolding exposes the molded polymeric pillars to high frictional forces at a large surface compared to the small volume and the relatively low mechanical stability of polymer[67]. The excessive friction leads to structural failure. Partially single nanopillars broke-off from the polymer bulk (invisible by eye), but also larger amount of polymer remained on the nickel surface (visible by eye). The question is now, if polymer remains in the holes due to structural failure, will that polymer "seal off" the hole preventing polymer of subsequent molding cycles to flow in? New polymer from the current cycle can only blend with "old" polymer if a certain flowability of is given. This requires at least a mold temperature above the glass transition temperature of the polymer. The higher the mold temperature, the better the blending will most probably be, especially since the polymer flow inside the hole is very limited. This effect was observed for a mold temperature of 90 °C. The polymer contamination was slowly removed within the first few cycles after increasing the temperature.

[66] Similar to the "tip of excess material" described for microstructures (Section II-4.3.).

[67] Yield Strength for Topas 8007: 63 MPa. Tensile stress at yield point (point in the stress-strain curve at which plastic deformation begins to occur) (50 *mm min*$^{-1}$), tensile strain at yield: 4.5 % (Topas Advanced Polymers).

FILLING OF NANOSTRUCTURED MOLDS WITH LOW SURFACE ENERGY. Nickel shims displaying a low surface energy were expected to show rather a decreased replication of nanostructures, pillars as well as holes, than gained for native molds. This effect has been shown by Pranov et al. They showed that the mold surface energy is highly important for the replication of sub-micrometer structures (lateral dimensions ≥ 100 nm). The filling of nanoscaled cavities is problematic and limited by the surface energy. Structures replicated with a low compression molding setup were replicated up to a depth of 350 nm (melt temperature of 320 °C, mold temperature of 60 °C, molding pressure of about zero bars). The filling decreased strongly down to below 10 nm (same molding conditions) after application of a fluorocarbonsilane coating [Pranov 2006]. The major difference to their setup is that in injection molding pressure is in fact applied (up to several hundred bars). The initial filling of structures during injection molding is mainly driven by capillary force with no additional pressure applied which results in a "zero pressure condition" similar to the low compression molding setup. Only when the mold cavity begins to fill, injection pressure raises up to a certain limit set in the process control. Additional "holding pressure" can be applied during packing or compression phase to push additional polymer into the mold while the mold is cooled, to compensate shrinkage. If the polymer is injected into a cold mold, the polymer at the mold interface solidifies within few nanoseconds most probably without complete filling of all cavities. The applied injection and holding pressure is not able to force sufficiently more polymer into the mold to complete the filling[68]. This problem can also cause short shots (incomplete filled mold cavity). However, for mold temperatures at or above glass transition temperature of the polymer, the melt will remain deformable or even low viscose. Subsequently, injection and holding pressure applied can "push" more polymer[69] into the nanoholes and thereby increasing the filling depth. The equal or even larger average pillar height for the FDTS coated compared to the native nickel shim indicate that the filling of nanoholes is largely independent on the surface energy. The applied pressure over-rules the repulsive forces of the mold surface. Nevertheless, without the injection and holding pressure applied it appears very likely that the nickel molds with a low surface energy will exhibit limited filling of nanostructures as stated by Pranov et al.

[68] Injection and holding pressure raises up to the value set in the process control (here: $P_{inject} \leq 1000$ bars, $P_{hold} \leq 800$ bars). If the polymer is completely solidified and undeformable the pressure limit is reached without pushing sufficient polymer into the mold to complete filling.

[69] The polymer melt has not cooled down due to the high mold temperature and remains deformable.

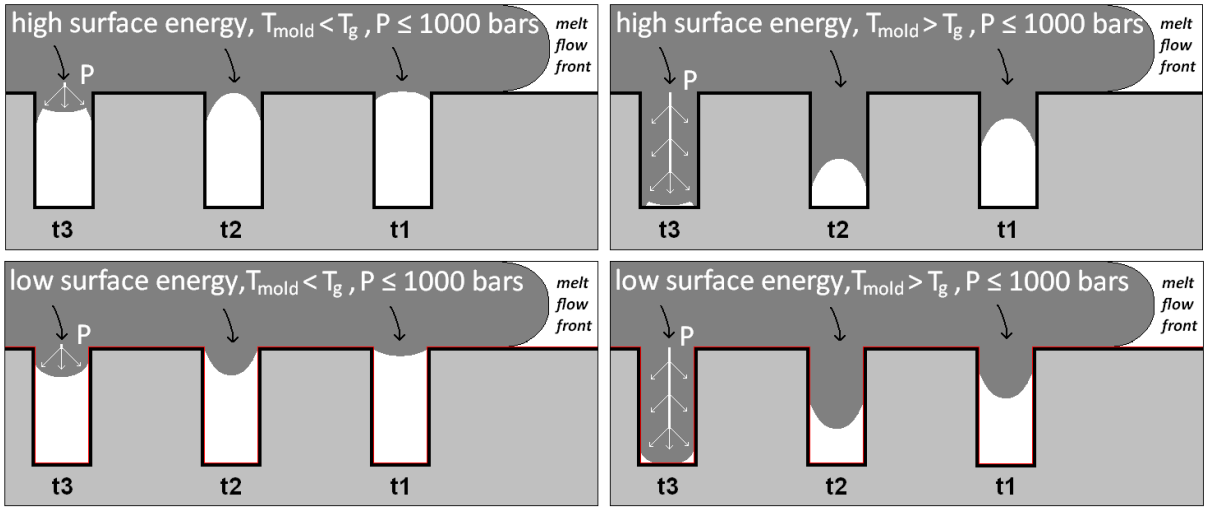

Figure 128: Theoretically assumed filling of nanostructures on native (high surface energy) and fluorosilane coated (low surface energy) nickel shims during injection molding.

DETERMINATION OF "SWITCH-OVER-POINT". The "switch-over point" at which the demolding related phenomena become important can be determined by plotting the minimum and maximum height of pillars replicated on native and FDTS coated molds (Figure 129). The minimum value is thereby either caused by limited filling or, given better filling, the lowest "point of fracture" during demolding.

The "point of fracture" is the distance of the fracture from the polymer bulk determining the the final length of single pillar. If demolding cannot be achieved due to too string adhesion of polymer to the mold, the pillars will fracture at a predetermined breaking point that is related to the shape and diameter of each single pillar. The diameter of the pillars varies up to 10 % (± 5 nm) resulting in a slightly different breaking point (or "point of fracture"). In case of limited filling this point might not be reached. Considering the average height of structures molded at 80 – 100 °C, the average "point of fracture" is about 30 nm from the bulk.

By extracting the maximum pillar height it can be seen that even though the average height for pillars molded at 80 - 100 °C on the native nickel shim is about 30 nm, deeper filling can be achieved leading to pillars with heights of up to 65 nm (for 90 °C). Pillars molded at a mold temperature of 100 °C on a FDTS coated nickel mold showed a maximum pillars height of 120 nm which exceeds the theoretical possible depth of the holes in the nickel shim. This may be caused by stretching of single pillars which will be discussed later in a separate paragraph related to randomly appearing distortion such as stretching. However, at a mold temperature of 60 °C the maximum pillars height for native and FDTS coated samples is equal (about 25 nm) suggesting limitation by filling of the cavities (due to the skin layer).

The minimum pillar height averaged over all samples is 8 ± 4 nm regardless of mold surface and mold temperature which seems to be approximate lowest point of fracture for 40 nm wide pillars (if sufficient filling is given). In case of FDTS coated nickel, less "fracturing" appears leading to a higher average values. In contrast, almost all pillars fracture from the native mold resulting in a constantly low average height for molding temperature of 80 – 100 °C at which a similar good filling (if not better) to FDTS coated nickel is expected. The point of fracture is subject to local variations in the surface chemistry, statistically varying filling depth and local varying lateral pillar dimensions which

influence the mechanical stability. The pillar diameter varies up to 10 %. Thinner pillars will break-off closer to the polymer bulk due to lower mechanical stability while thicker pillars are more stable, probably leading to a fracture at some location inside the hole (in the nickel mold).

Nevertheless, based on the strong increase of the maximum pillar height (mold temperature of 70 – 100 °C) for native molds and FDTS coated nickel shims, it is assumed that the "switch-over point" lies between 60 and 70 °C for Topas 8007. For mold temperatures at or below 60 °C ($\leq T_g - 20$ °C) the filling process is dominant while temperature at or above 70 °C ($\geq T_g - 10$ °C) result in domination by demolding related factors.

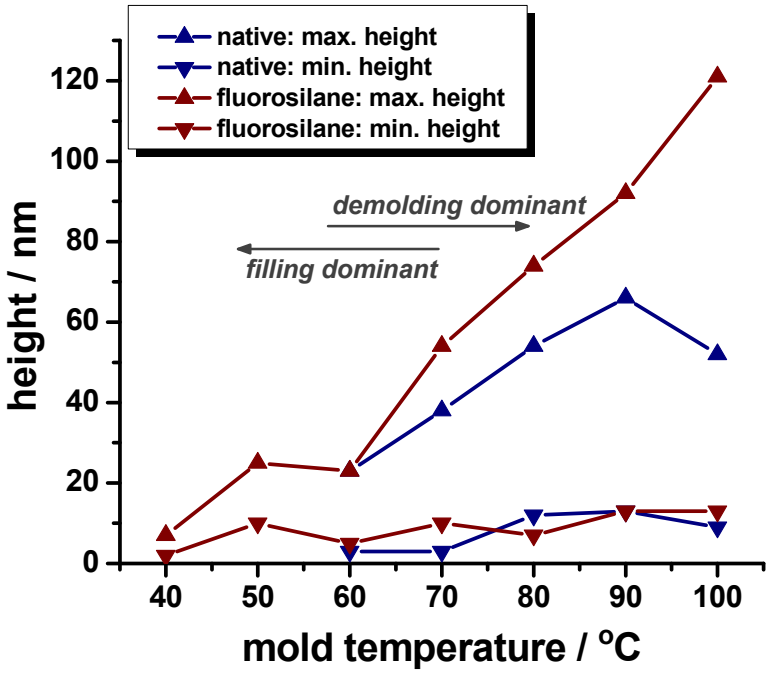

Figure 129: Minimum and maximum pillar height at different mold temperatures for native and FDTS coated nickel shim (hole depth in the mold: 109 ± 2 nm).

The increasing standard deviation of the average pillar height molded on FDTS coated nickel shims indicates a very irregular height distribution. It is most probable that a locally degraded or delaminated FDTS layer which lead to small partition of fractured pillars accounting for the high standard deviation. The increasing standard deviation from 15 nm at 80 °C to 38 nm at 100 °C is caused by the increasing difference between very tall and very small pillars. In principle, the pillar height increases for increasing mold temperature due to better filling of the structures (largest fraction of the pillars). However, a small fraction of the pillars breaks at a constant distance from the bulk polymer, here referred to as "lowest point of fracture". Averaging both fraction leads to the increasingly high standard deviation. To clarify the origin of the high standard deviations, dot plots were generated by binning the height of single pillars (original data) with a binning width of 5 nm.

DOT PLOTS. The dot plots resulted in a unimodal distribution of the pillar height for structures molded on the native shim or molded on the FDTS coated shim for mold temperatures below 70 °C (Figure 130). Structures molded on the FDTS shim display a bimodal height distribution (Figure 131) where lower peak of the bimodal distribution superimpose well with the single peak for the native nickel shim. This indicates that the polymer on the FDTS coated shim partially sense a native-like surface, i.e. area of delaminated (or degraded) FDTS layer. The accuracy of overlap is measured by determining the center of each appearing peak assisted by a Gaussian curve fit on the discretized data. The center of width of each peak is plotted against the height, presented in Figure 132[70]. The peak of the unimodal height distributions superimpose almost perfectly with the lower peak of the FDTS coated nickel. The accuracy of the superimposition is ≤ 5 nm. The center of width of the second peak increases strongly with increasing mold temperature. Pillars belonging to the "higher peak" resulted in a center-of-width (approximate average height) of 106 nm at a mold temperature of 100°C. This corresponds to a complete filling.

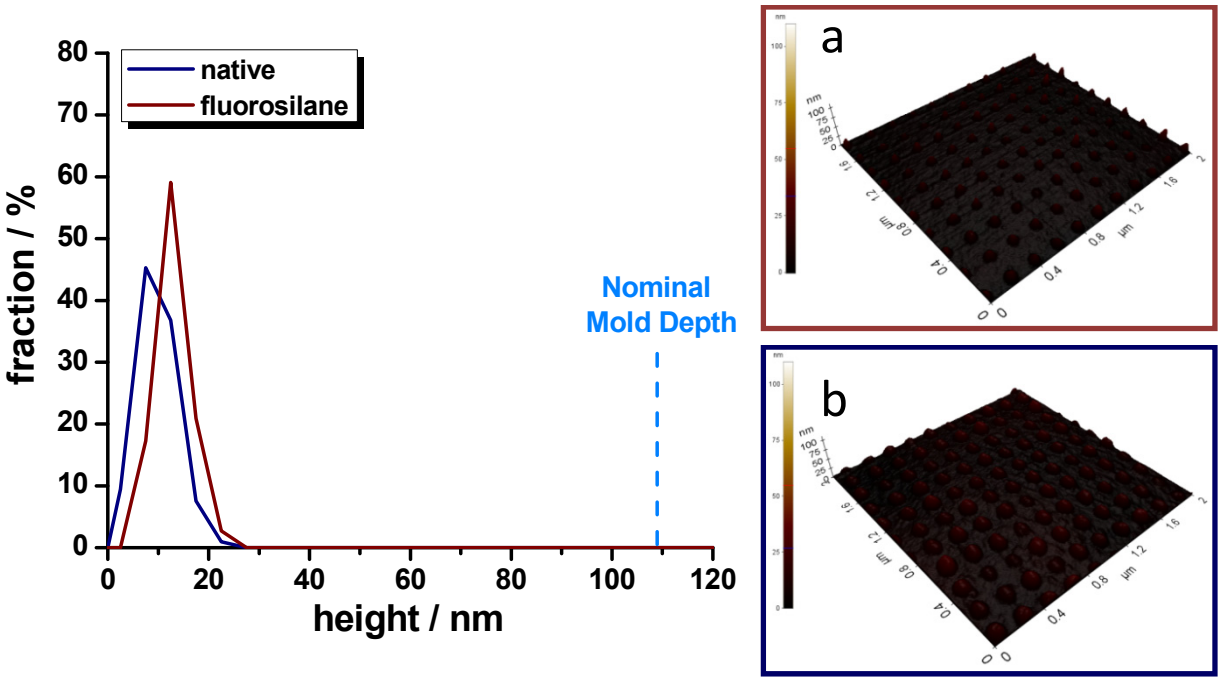

Figure 130: Dot plot of the discretized pillar height distribution (binning = 5 nm) exemplified of for a mold temperature of 60 °C (unimodal distribution for both shim surfaces) (left). AFM images (right) represent the corresponding pillar patterns molded at 60 °C on FDTS coated (a) and native mold (b).

[70] Only data for mold temperatures of 60 – 100 °C is shown, since no data was recorded for the native shim for mold temperatures of 40 – 50 °C due to excessive large-scale defects.

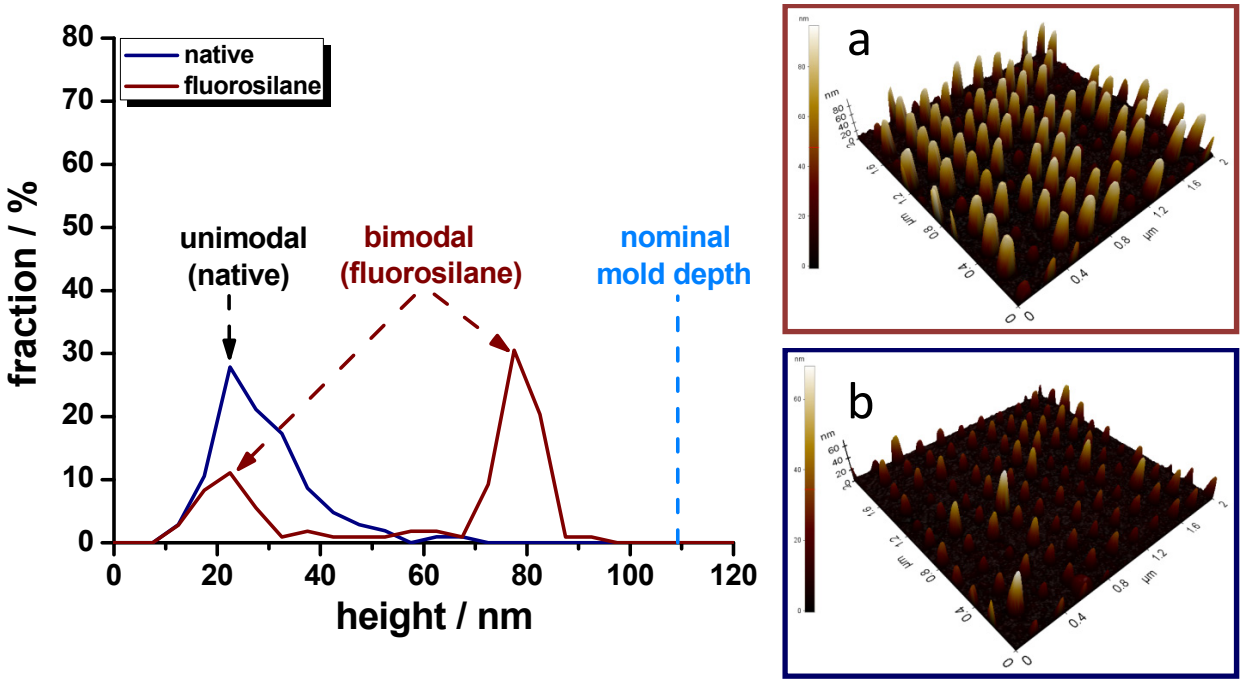

Figure 131: Dot plot of the discretized pillar height distribution (binning = 5 nm) exemplified of for a mold temperature of 90 °C (unimodal distribution for native nickel shim and bimodal for FDTS coated nickel shim) (left). AFM images (right) represent the corresponding pillar patterns molded at 90 °C on FDTS coated (a) and native mold (b).

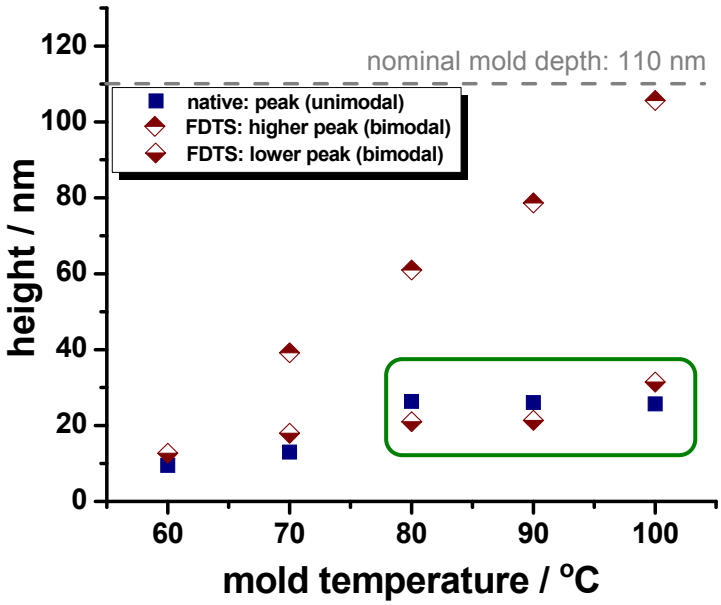

Figure 132: Center of width determined based on a Gaussian curve fit on the discretized pillar height distribution. The peak of the unimodal distribution for the native and FDTS coated nickel shim[71] superimposes almost perfectly (deviation ≤ 5 nm). Pillars which are most probably fractured are high lightened by the green rectangle.

[71] Structures molded from the FDTS coated nickel shim at a mold temperature of 60 °C resulted in a unimodal pillar height distribution.

DICUSSION. AFM images presented in Figure 130 and Figure 131 show the different appearance for nanostructures molded at different temperatures applying nickel shims with different surface chemistry. The average pillar height for structures molded at 60 °C is lower than for structures molded at 90 °C. The sample molded at 90°C on a FDTS coated nickel shim posses the largest pillars but also some missing (or very small) pillars resulting in a bimodal distribution. The data analysis done on the dot plots showed that the peak of the unimodal height distributions (native shim) superimposes almost perfectly (deviation ≤ 5 nm) with the lower peak of bimodal distribution (FDTS coated shim). This strongly indicates that the FDTS coated shim behaves locally like a native shim most probably caused by local delamination or degradation of the FDTS layer. Thereby, the lower peak contains mostly fractured pillars. It is to note that the sample representing the injection molding of pillars at a mold temperature of 100 °C on the FDTS coated shim was at least the 425th piece injection molded on that shim after a single coating[72].

In Section II-4.2., the thermal and mechanical stability was measured showing only a very low degradation of the FDTS layer during injection molding. However, the local defects can have two different origins. Firstly, it is possible that the adhesion of the FDTS to the nickel is high enough for surfaces with a low surface-to-volume ratio, i.e. flat or presenting low aspect ratio structures. For interfacial areas with a large surface-to-volume ratio the adhesion of polymer to FDTS is substantially higher and could have caused local delamination of the FDTS layer. Secondly, it is possible that FDTS was not optimal deposited forming a homogenous layer due to limited transport of active FDTS molecules inside the holes.

The contact angles of water, hexadecane, and Topas were only measured on flat surfaces and cannot resolve the wetting on nanoscale. Unfortunately it is not possible to measuring the fluorine content on the surface with nanometer resolution. The lateral resolution of XPS is about 50 µm.

A treshold was applied on samples exhibiting a bimodal distribution to extract pillars which are assumed to represent the filling and demolding behaviour of optimal FDTS coated nickel shims (Figure 133). The treshold was set based on the dot plots removing all pillars belonging to the lower peak. As a result, the standard deviation decreased to below 10 nm as observed for samples molded from the native shim. Considering only pillars above the threshold, the influence of the mold temperature on the replication height becomes similar to that described by other research groups [Huang2007, Pranov2006, Mönkkönen2002, Theilade2007]. A mold temperature of 100 °C (T_g + 20 °C) enabled the replication of 40 nm wide and 107 ± 6 nm high by complete filling and antistiction coating assisted demolding. This shows that injection molding of pillars with an aspect ratio well above two is possible (2.6:1). The problem of the most probably damaged FDTS coating needs to be investigated in further detail to assure stable coating and thereby uniform pillars heights.

[72] For each set of parameters at least 25 pieces were molded, but partially up to 50 pieces (80 °C: at least 350th piece, 90 °C: at least 375th piece).

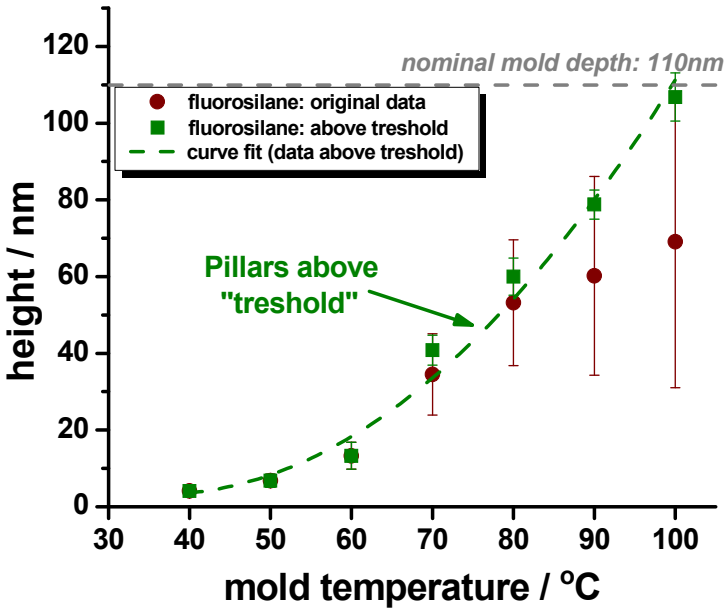

Table 18: Modified average pillar height excluding pillars below the threshold.

T_{mold}	Height above threshold
40 °C	4 ± 1nm
50 °C	7 ± 2nm
60 °C	13 ± 4 nm
70 °C	41 ± 4 nm
80 °C	60 ± 6 nm
90 °C	79 ± 4 nm
100 °C	107 ± 6 nm

Figure 133: Average height of pillars injection molded into Topas 8007 at different mold temperatures on fluorosilane coated nickel shims[73] (left). The red data points represent the original data while the green data points represent the average pillar height above the threshold. The data is given in the table shown above.

100 NM WIDE HOLES. 110 nm wide holes were replicated down to 99 ± 6 nm for mold temperatures ≥ 50 °C. For a mold temperature of 40 °C very limited replication depth was observed (46 ± 8 nm). The surface of the nanostructures molded at 40 °C exhibited a very high roughness.

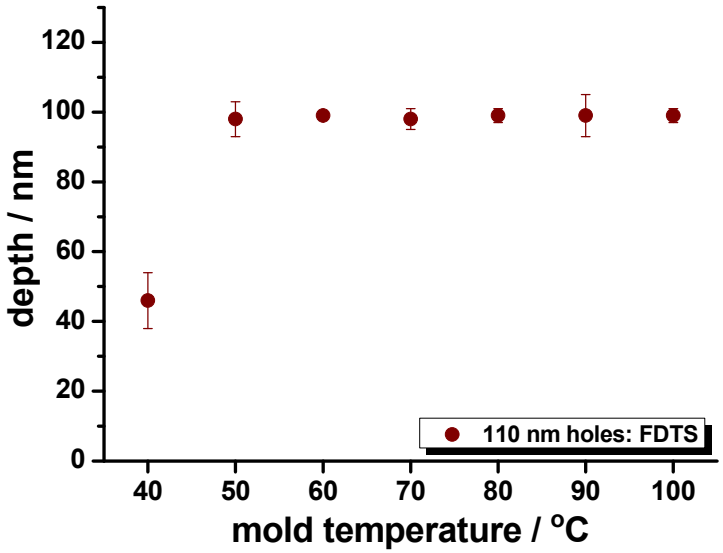

Figure 134: Average depth of holes injection molded into Topas 8007 at different mold temperatures on fluorosilane coated nickel shims[74]. A decreased replication depth was only observed for a mold temperature of 40 °C.

[73] Process parameters: T_{melt}: 250 °C, v_{inject}: 10 cm^3 s^{-1}, P_{inject}: 750 ± 25 bars, P_{hold}: 800 ± 25 bars, t_{eject}: 40 ± 3 °C
[74] Process parameters: T_{melt}: 250 °C, v_{inject}: 10 cm^3 s^{-1}, P_{inject}: 750 ± 25 bars, P_{hold}: 800 ± 25 bars, t_{eject}: 40 ± 3 °C

DISCUSSION. 110 nm wide holes were measured down to a depth of 99 ± 6 nm at mold temperatures of 50 – 100 °C. The measured depths comply well with maximum values commonly obtained for holes of these lateral (and vertical) dimensions [75]. Therefore, it is expected that patterns were replicated to the full depth of about 109 nm. The low average hole depth achieved for mold temperature of 40 °C shows that holes as well dependent on the mold temperature though to a lower extent. For mold temperature of 40 °C (T_g – 40 °C) the polymer melt cooled too fast to fill the space in between the pillars completely. The high surface roughness of the nanostructures molded at 40 °C support the assumption made previously that the polymer melt, if solidifying before reaching the bottom in between the pillars, does not stop perfectly at the same position. Thereby, polymer replicas exhibit higher surface roughness than pieces replicated to full depth. This also supports the assumption that 120 nm wide holes injection molded into Topas 5013 at mold temperature of 105 – 165 °C were in fact molded to full depth but spatial limitations of the AFM tip led to the low depths.

[75] Maximum average depth measured for 110 – 120 nm wide holes was about 100 nm. Compare with holes injection molded into Topas 5013 on CHF_3 coated nickel molds.

4.2.2. Melt Temperature and Velocity, and applied Pressures

Melt temperature and injection velocity are both related to the length of the flow path which the hot low viscose polymer melt can travel before solidification. An increase in melt temperature or injection velocity leads to an elongated flow path due to decreased melt viscosity (melt temperature) or increased velocity of the proceeding flow front (injection velocity). Solidification occurs at a later point enabling the polymer to flow further into the nanostructured cavities, especially for nanoholes in the mold. Thereby an increase in one of these parameters was expected to result in increased averaged pillar height.

Injection and holding are both related to packing of polymer material into the nanoscaled cavities. A mold temperature at or above the glass transition temperature of the polymer improves the filling depth if the mold surface favors filling and/or if pressure is applied to "pack" additional polymer into the nanoscaled cavities in the mold. A sufficient high pressure is therefore especially important if the mold surface energy does not favor filling but rather prevents filling at zero pressure condition as described in the previous sub-section. Injection pressure is build up once the polymer has filled the cavity (or is cooled down) while the holding pressure applies during the compression phase when the polymer is cooled down. The injection pressure is expected to have the stronger influence on the filling depth of nanoholes, since additional filling of nanoholes with polymer requires certain flowability, hence a mold temperature above the glass transition temperature. Unfortunately, only a small pressure range could be tested, limited by our mold design, to avoid excessive packing leading to insufficient demolding of polymer parts or deficient packing causing depression/sinkmarks.

MELT TEMPERATURE AND INJECTION VELOCITY. In the parameter range tested (residual parameters set to "standard"), no increase of the pillar height was observed for melt temperatures of 220 – 280 °C on the native nickel shim leading to an average of 18 ± 9 nm. The FDTS coating improved the replication height substantially leading to pillar heights of 63 ± 5 nm for melt temperatures of 240 – 280 °C (Figure 135). Lower melt temperatures lead to a maximal average pillar height of 95 ± 7 nm which is close to the full depth. Flow lines appeared for parts molded on native and FDTS coated nickel shims at a melt temperature of 220 °C. Micro cracks and polymer contaminations were observed for the native nickel shim at melt temperatures of 220 – 280 °C. No large-scale defects were observed for the FDTS coated shim.

The injection velocity did not show a significant difference for 100 – 300 mm s^{-1} for FDTS coated molds. Only for an injection velocity of 50 mm s^{-1}a strong reduction in the average pillar height down to 10 ± 9 nm was measured. An injection velocity of 20 mm s^{-1} was not able to fill the mold cavity even half before the injection pressure reached its set point. The average pillar height for FDTS coated nickel shims was constantly higher (≥ 30 nm). Problems with randomly tilted or stretched pillars appeared more frequently than during the test serial performed using the first nickel shim.

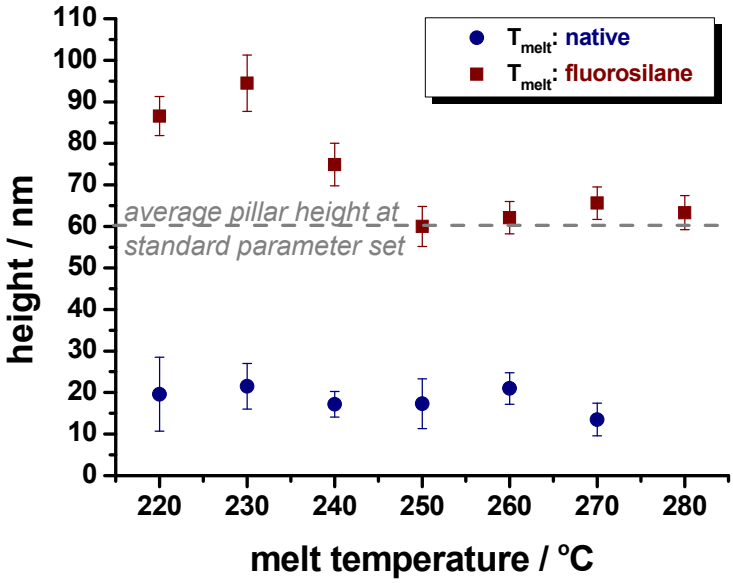

Figure 135: Average pillar height for different melt temperatures and injection velocities. Standard injection molding parameters: T_{mold}: 80 °C, T_{melt}: 250 °C, v_{inject}: 100 mm s^{-1}, P_{inject}: 750 ± 25 bars, P_{hold}: 800 ± 25 bars, t_{eject}: 40 ± 3 °C.

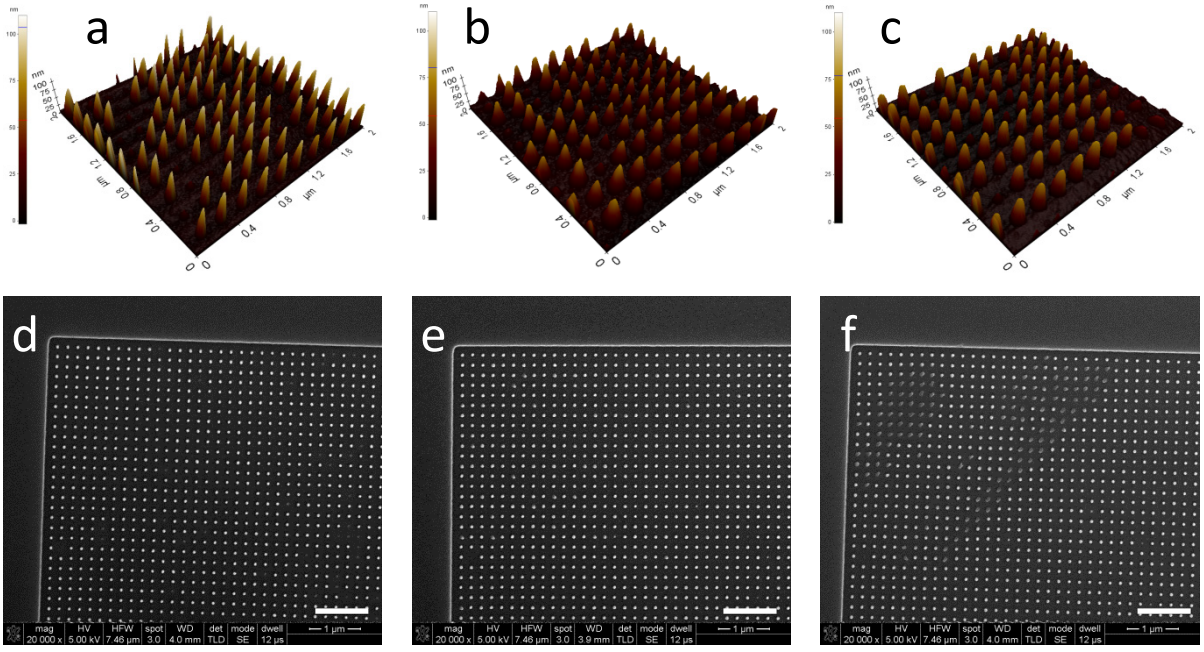

Figure 136: AFM (a – c) and SEM images (d – e) of pillars replicated in Topas 8007 at melt temperatures of 220 °C (a, d), 250 °C (b, e), and 280 °C (c, f). Standard injection molding parameters: T_{mold}: 80 °C, T_{melt}: 250 °C, v_{inject}: 100 mm s^{-1}, P_{inject}: 750 ± 25 bars, P_{hold}: 800 ± 25 bars, t_{eject}: 40 ± 3 °C. Scale bars (SEM images): 1 µm.

DISCUSSION. Melt temperatures of up to 280°C were tested exceeding the maximum melt temperature of 250°C recommended by the manufacturer. In our experiments, no significant improvement of the replication height (≤ 6 nm) was observed for temperatures above 240 °C. The increased replication height for decreasing melt temperatures cannot be explained. The bottom in

between the pillars is fully resolved thus sufficient good resolution of the AFM measurements is given. Distortion of pillars such as stretching and tilting was rarely observed for samples injection molded using the first shim, as for example seen in the SEM image in Figure 136f (T_{melt} = 280 °C). This problem will be addressed in the following sub-section. Considering only result obtained for melt temperatures of 250 – 280 °C, it is assumed that the polymer cools and solidifies at equally timescale. Therefore no difference in pillar height can be observed. It is assumed that sufficiently higher melt temperatures are required to obtain a visible effect. For lower melt temperatures than 220 °C at mold temperature at or below glass transition temperature, the overall mold surface will most probably exhibit flow lines and other large-scale defects even though an effect on the replication height may become visible.

The injection velocity did not show any effect on the final replication height for injection velocities at or above 100 mm s^{-1}. An injection velocity of 50 mm s^{-1} yielded in nanopillars with strongly decreased height of 10 ± 9 nm. The polymer bulk cools too fast down and solidifies, hence resulting in a limited filling. This is supported by the fact that at 20 mm s^{-1} the mold cavity cannot even be filled half. It is expected that the initial filling of the structures is mainly governed by capillary forces until pressure (injection pressure) is applied. The capillary force is independent on the overall velocity of the polymer bulk. The injection velocity will therefore not influence such small structures nut only the filling of larger structures [REF]. In case of 50 mm s^{-1}, the mold cavity was most probably not completely filled before the maximum injection pressure was reached[76]. Therefore, only the capillary forces contributed to the filling resulting in such small pillar heights.

110 nm wide holes[77] were injection molded under equal conditions investigating the influence of mold temperature on the replication depth of nanoholes. Arrays of holes injection molded on the native nickel shim exhibited widely nano- and large-scale distortions and deformations[78] as described for 40 nm wide pillars. The hole pattern are more sensitive and develop stronger deformations leading to useless patterns while the pillars result in more homogenous patterns but with decreased replication heights. Holes injection molded on the FDTS coated shim resulted in a complete replication to the full depth of 100 ± 2 nm regardless of mold temperature. Few randomly oriented and randomly appearing nanoscale deformations were observed for unknown reason. This phenomenon will be described in the following sub-section.

INJECTION AND HOLDING PRESSURE. No difference in pillar height was observed for a holding pressure for pillar patterns molded at the FDTS coated nickel shim at 700 or 800 bars resulting in 62 ± 7 nm high pillars. The injection pressure as well did not show any significant effect on the replication height of pillars (60 ± 5 nm) molded on the FDTS coated nickel shim with injection pressures of 750 – 1050 bars (Figure 137). Only at an injection pressure of 950 bars a significantly lower pillar height of 34 ± 4 nm was measured by AFM.

[76] Mold cooling and switch-over to holding pressure occurs once the injection pressure limit is reached.
[77] Shim ID 110nm40p110h: 40 ± 3 nm wide holes (pitch: 200 nm) and 109 ± 2 wide nm and 109 ± 2 nm high pillars (pitch: 200 nm).
[78] 40 nm pillar pattern and 110 nm hole pattern are located on the same shim (shim ID: 100nm100hpp).

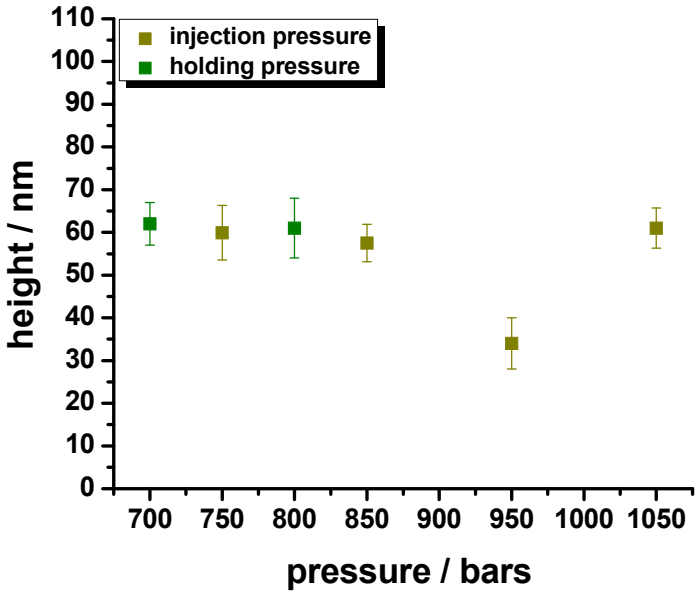

Figure 137: Average pillar height for varying injection and holding pressures. Standard injection molding parameters: T_{mold}: 80 °C, T_{melt}: 250 °C, v_{inject}: 100 mm s^{-1}, P_{inject}: 750 ± 25 bars, P_{hold}: 800 ± 25 bars, t_{eject}: 40 ± 3 °C.

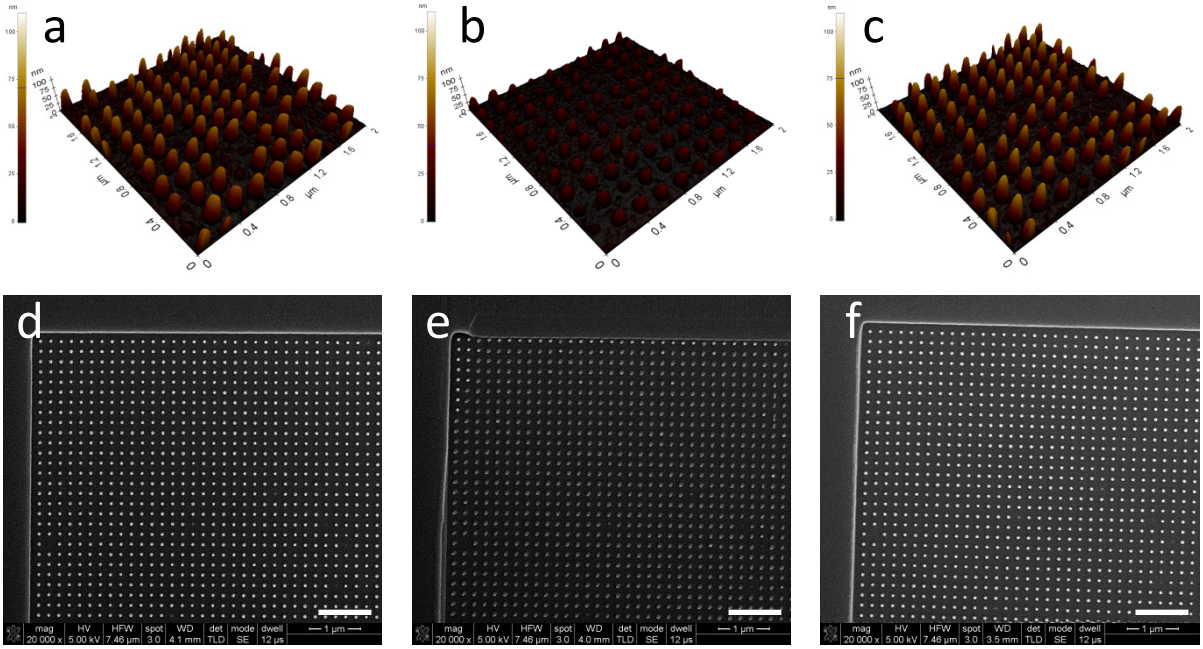

Figure 138: AFM (a-c) and SEM images (d-f) of pillars replicated in Topas 8007 at injection pressures of 850 bars (a, d), 950 bars (b, e), and 1050 bars (c, f). Standard injection molding parameters: T_{mold}: 80 °C, T_{melt}: 250 °C, v_{inject}: 100 mm s^{-1}, P_{inject}: 750 ± 25 bars, P_{hold}: 800 ± 25 bars, t_{eject}: 40 ± 3 °C. Scale bars (SEM images): 1 µm.

DISCUSSION. The injection pressure did not have any significant influence on the average pillar height (60 ± 5 nm). The substantially lower height of pillars molded at an injection pressure of 950 bars are caused by tilting of the pillars. This cannot be seen in AFM images but was observed from SEM images (Figure 138 e).

Based on the assumption that the filling of nanoholes with a low surface energy may be limited under zero pressure condition, at least the injection pressure is important to fill the holes. The higher the pressure, the more polymer can be forced into the nanoholes on the nickel shim, hence achieving larger fill depths. The heat transfer from the polymer melt to the nickel shim speeds up the cooling and thereby solidification of the polymer melt the deeper it penetrates into nanoholes in the mold. The increasing interfacial area between melt and mold compared to the low volume of each single pillar leads to a fast cooling, hence decreasing flowability of the melt and finally solidification. Even at increasing injection pressure, it may not be possible to push more polymer into the nanoholes in the nickel shim. An injection lower than 750 bars led to sink marks and voids which will influence the replication height, most probably decreasing the replication height.

It is difficult to make a reliable assumption based on only two measurements which led to the same replication height of 62 ± 7 nm. However, as long as sufficient but not excessive packing is achieved to compensate for shrinkage and decrease internal stress, no substantial effect is expected for lower or higher holding pressures.

4.2.3. Randomly oriented Nanoscaled Deformation

Initially, it was expected that these random defects are caused by strong adhesion of Topas to the nickel mold. However, random defects appeared for native nickel shims and FDTS coated shims as well. Process parameters which are most likely to decide on the replication quality of the overall surface as well as on single nanostructures were investigated; namely mold and melt temperature as well as injection velocity, injection pressure, and holding pressure. None of these parameters led to a reasonable explanation for randomly appearing and randomly oriented deformation of nanostructures (Figure 139).

Variation of the ejection temperature showed a huge effect on the appearance of the tip of excessive material found on top of microstructures molded into Topas 8007 (and 5013). Therefore the ejection temperature was investigated. Since the ejection temperature can only influence the demolding, but not the filling of injection molded samples, only SEM images were recorded to probe for tilting and other deformations. The effect of demolding (or ejection) of solidified polymer replicas at temperatures of 30 – 70 ± 1°C was investigated.

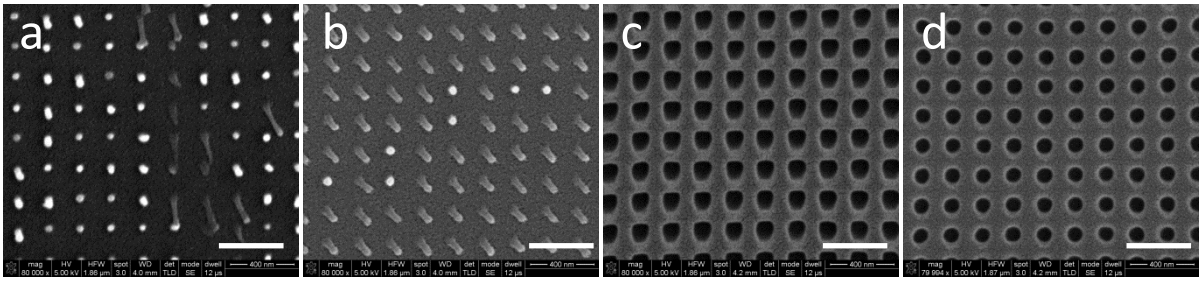

Figure 139: SEM images of 40 nm wide pillars (a, b) and 120 nm wide holes (c, d)exemplifying the appearance of randomly appearing and randomly oriented deformations. Partially only single pillars are tilted (a), partially a larger area (b). Directed deformation appeared sometimes differently for the corners (c) compared to the nicely replicated holes center (d). Scale bars: 400 nm.

No effect was observed for demolding temperatures above or below the standard temperature of 40 ± 3 °C (Figure 140). All chips showed randomly oriented tilted or deformed structures (Figure 140).

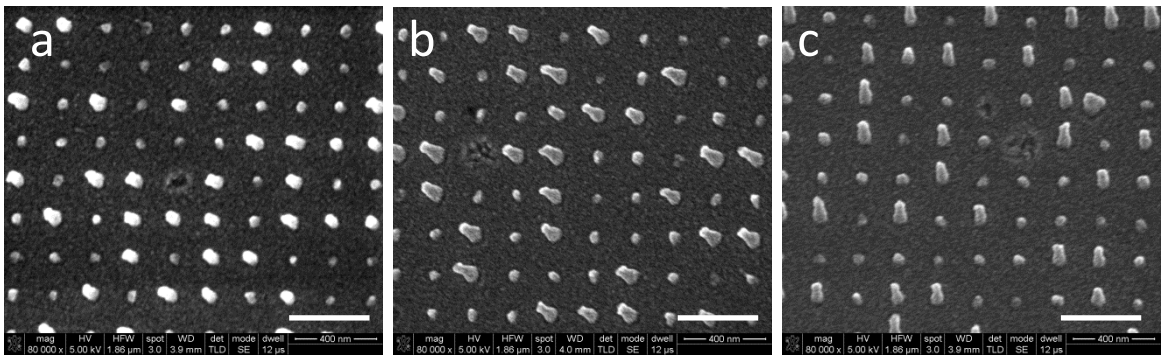

Figure 140: SEM images of 40 nm wide pillars ejected at different temperatures of 30 °C (a), 50 °C (b), and 70 °C (c). No difference can be observed. Scale bars: 400 nm.

DISCUSSION. Injection molding experiments applying varying demolding temperatures did not lead to any reasonable explanation for the appearance of the defects let alone the direction of tilting. As explained in section xx regarding the "tip" of excess material on top of the sidewall channels of microstructures, deformations could be caused by undesirable shape structure. Random defects were mainly observed for pieces molded on the second nickel shim. It is possible that small variations in the process chain led to structures with for example re-entrant sidewalls. In that case, nanopillars and holes deform easier, especially taking the way of ejection into account. As explained for microstructures, the polymer disk containing the nanostructures is pulled out of the stationary mold at a single point located on the opposite side of the sprue. Small tilting of the polymer sample is very likely and may have caused the deformations. However, in case of microstructured parts, the "tip" was commonly located at the same side while the nanostructures are tilted in random direction, even on the same piece.

Another explanation was given by Huang and Pranov et al. which assigned such defects to polymer shrinkage [Huang 2007] and thermally induced flow instabilities at the melt/mold interface [Pranov 2006] as main cause. The latter argument is supported by the fact that for pieces molded at a very low injection velocity of 20 mm s^{-1}, a varying filling was observed (Figure 141). Moreover, two flow fronts were observed entering the cavity from the sides and merging approximately in the middle of the cavity (Figure 141, red rectangle). The cause for the appearance of these two flow fronts is under investigation. The problem of randomly appearing nanoscaled deformations has not been solved yet.

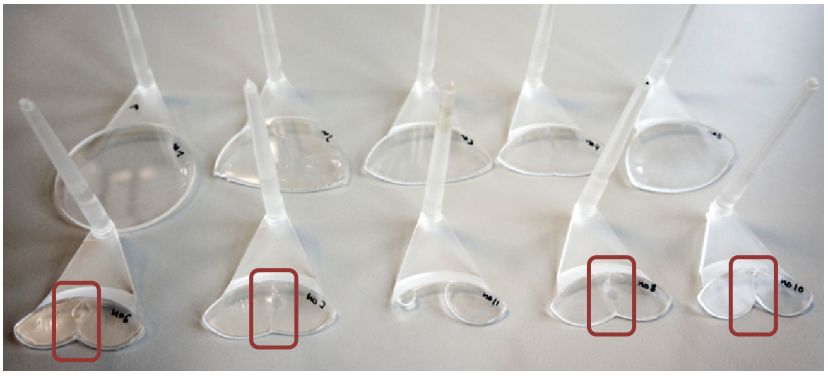

Figure 141: Photo of Topas 8007 chips injection molded at 20 mm s^{-1} at standard parameters[79]. The merging flow fronts are high lightened by the red rectangle.

[79] Standard parameters: T_{mold}: 80 °C, T_{melt}: 250 °C, P_{inject}: 750 ± 25 bars, P_{hold}: 800 ± 25 bars, t_{eject}: 40 ± 3 °C.

4.3. Summary

Observations from injection molding of Topas 8007 and 5013 on native as well as fluorocarbon-based antistiction coatings on nickel molds suggest that efficient demolding is of greater importance for the structural integrity than energetically favorable filling.

Arrays of 100 nm wide holes were molded with excellent surface quality applying a broad range of parameters such as mold temperature of 105 – 165 °C for Topas 5013 or 50 – 100 °C for Topas 8007. A mold temperature of 100 °C (T_g + 20 °C) enabled the replication of 40 nm wide and 107 ± 6 nm high by complete filling and antistiction coating assisted demolding. This shows that injection molding of pillars with an aspect ratio well above two is possible (2.7:1).

Based on results obtained for 40 nm wide pillars in Topas 8007, a “switch-over point” was found that reflects a change of the dominating cause limiting the average pillar height, i.e. filling or demolding. At mold temperatures of 60 °C or below, filling is limiting and leads to small pillar heights. For increasing temperature above 70 °C phenomena related to demolding such as frictional forces become important. Frictional forces applied during demolding lead to deformation and fracture of pillars causing a low average pillars height even though better filling was achieved. The lowest point of is thereby about 8 nm far from the bulk polymer. Considering the average height of structures molded at 80 – 100 °C, the average point of fracture is about 30 nm from the bulk, if cavities in the nickel shim are sufficient filling.

Samples molded from FDTS coated nickel shims possess a bimodal distribution most likely related to local defects in the FDTS coating. The lowest “point of fracture” was used as threshold to remove fractured pillars and to extract pillars which are assumed to represent the filling and demolding behaviour of optimal FDTS coated nickel shims. As a result, the standard deviation previously up to 40 nm high decreased to below 10 nm. The problem of the most probably damaged FDTS coating needs to be investigated in further detail to assure stable coating and thereby uniform pillars heights.

Chapter 4

Assembly of Polymeric Microfluidic Systems

1. Thermal Bonding of Polymeric Microfluidic Systems

Thermal bonding was used to combine nano- and microstructured injection molded polymer parts to a functional microfluidic system. The major drawback of thermal bonding, as described previously, is the softening and hence probable deformation of the microchannel, especially the channel lid[80]. The deformation can become critical for the application of the microfluidic channels and even close the channel. Deformation can be decreased while increasing the bonding strength by pre-treating the polymer surface with oxygen plasma. Another problem that could arise from thermally bonding microchannels to nanostructured patterns is deformation of the nanostructures caused by applied heat and pressure. However, the large surface-to-volume-ratio may facilitate heat dissipation from the nanostructures into the air trapped inside the microchannels keeping the polymer locally cooler than the surrounding bulk polymer. Thereby, deformation of the nanostructures could be avoided. The deformation of microchannels and nanostructures was analyzed by mechanical profilometer and SEM as will be described in detail in the following section.

1.1. Experimentals

Topas 8007 and 5013 chips were thermally bonded using a Hot Press from P/O/Weber with electronic pressure sensor. Experiments were performed to find optimal bonding conditions. The influence of bonding temperature T_{bond}, applied pressure P_{bond}, bonding time t_{bond}, and pre-treatment time with air plasma t_{plasma} on the bonding quality was investigated. The air plasma treatment was performed under constant conditions of 0.6 bar at 50 W in air for 10 – 60 s. Chips were bonded using either untreated or air plasma activated polymer parts.

The setup consists of the two steel plates with separate temperature control, force controller with digital display (precision: ≈ 0.05 bars), silicon pad, luer aluminum holder, and flat steel plate. The aluminum luer holder is placed on the silicon pad and heated up. The flat and luer Topas chips are aligned and placed together into the luer holder. The flat steel plate (thickness: 2 mm) is placed on top of the flat Topas chip. The upper heating plate is lowered and pressed down with a certain force. The silicon pad keeps the bonding setup in between the two heating plates parallel and provides thereby optimal distribution of the applied force. The force is adjusted manually (precision: ≈ 0.5 bars). The heating plates are heated up automatically and are always kept on the bonding temperature.

[80] Depending on the setup, the wall that is facing upward is usually deformed stronger. In the setup used in this project, the flat part containing the nanostructured patterns were facing upward and thereby referred to as “lid”.

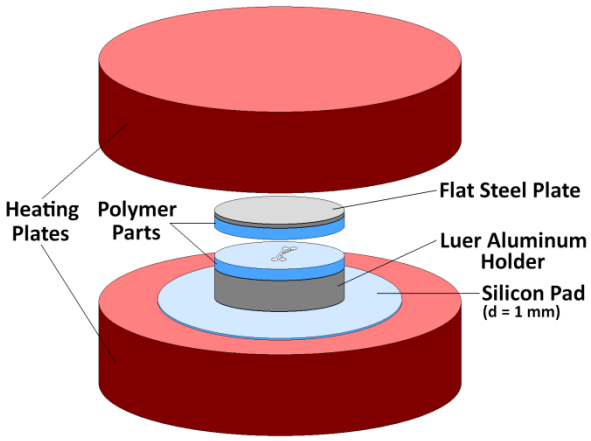

Figure 142: 3D Sketch of the thermal bonding setup used to bond Topas 8007 and 5013. The aluminum luer holder fits to hold the polymer chip with 12 male luer fittings.

To bond two chip parts the upper heating plate is lowered and a given pressure is applied. The temperature and pressure are kept constant (± 1 °C and ± 2.5 bar). After bonding the upper heating plate is released and the polymer chip is taken out together with the flat steel plate. The stack of polymer and flat steel plate is left to cool down and finally separated.

Table 19: List of bonding parameters used for Topas 8007 and 5013

	Topas 8007	**Topas 5013**
Plasma treatment	0 – 60 s	0 – 60 s
Bonding temperature	48 – 78 °C	105 – 125 °C
Pressure	50 – 100 bars	50 – 100 bars
Bonding duration	2.5 - 15 min	10 min

BONDING QUALITY. The bonding quality was initially analyzed visually by eye (interference rings and entrapped air). Subsequently, deformations of channel bottom and nanostructured lid were analyzed by a mechanical profilometer, Dektak 8 (Veeco Instruments Inc.). The bending was measured from the sidewall to the center (visualized in the Appendix I-2.4, Figure 202). Finally, deformation of nanostructures was analyzed by scanning electron microscopy after mechanical debonding. To investigate the deformation of nanostructures on nanoscale, several chips containing hole and pillar patterns were bonded applying 7.5 ± 0.5 bars for 15 min at 123 ± 1 °C for Topas 5013 [81] and 77 ± 0.5 bars for 10 min at 73 ± 1 °C for Topas 8007. After cooling down, bonded chips were mechanically debonded and imaged by SEM. Chips were sputter coated with gold prior to SEM imaging to prevent charging in high resolution image mode[82].

[81] For this experiment only, a similar bonding setup was employed where the maximum pressure possible (7.5 bars) was applied.
[82] Polymeric nanostructures can be imaged in low vacuum mode without or in high vacuum mode with metal coating (Nova 600 NanoSEM from FEI company). The resolution in low vacuum is not good enough too image nanostructures as small as 50 nm with sufficient quality.

1.2. Thermal Bonding of Topas 5013

Micro- and nanostructured parts injection molded from Topas 5013 were sufficiently well bonded to facilitate investigation of cell adhesion strength for different nanostructured surface topographies. Nanostructures were not deformed during the bonding for bonding temperatures of at least up to 125 °C. Commonly chips were air plasma treated prior to bonding. The effect of air plasma treatment on the bending quality and strength was investigated.

The bonding Topas 5013 parts at temperatures of 105 to 110 °C resulted in insufficient bonding quality, regardless of pre-treatment and pressure applied. Newton rings and voids[83] were formed at the bonding interface, and chips were easy to debond by hand without applying significant pressure. Channel lid (nanostructured) and bottom bended up to about 1 – 2 µm. Newton rings and voids disappeared for an increased bonding temperature and pressure of at least 115 °C and 50 bars, respectively. The bending increased from about 0.7 ± 0.1 µm (bottom) and 1.6 ± 0.1 µm (lid) at 115 °C and 50 bars to 4.3 ± 0.1 µm (bottom) and 13.4 ± 0.5 µm (lid) at the maximum temperature of 125 °C and pressure of 100 bars (Figure 143). Untreated chips were bonded without exhibiting Newton rings or pools at a temperature of 120 °C for pressures tested (50 – 100 bars).

In the parameter range tested, the temperature had the strongest effect on bonding strength and bending of microchannel lid (nanostructured part) and bottom. A change in bonding temperature from 105 – 125 °C resulted in an increased bending from 0.3 ± 0.1 µm (bottom) and 0.7 ± 0.1 µm (lid) at 105 °C to 4.3 ± 0.1 µm (bottom) and 13.4 ± 0.5 µm (lid) at 125 °C and about 100 bars. The lid bends considerably stronger than the channel bottom (Figure 143). A change in pressure from 50 – 100 bars resulted only in a maximum change of 0.8 µm (bottom) and 3.2 µm (lid) at the maximum bonding temperature of 125 °C. A change in plasma treatment time from 0 s (untreated) to 60 s did not result in a significant change in the bending. Typical profiles of chips bonded for different bonding parameters without and with 30 s air plasma treatment are given in the Appendix I-2.4.

[83] Areas of entrapped air at the bonding interface.

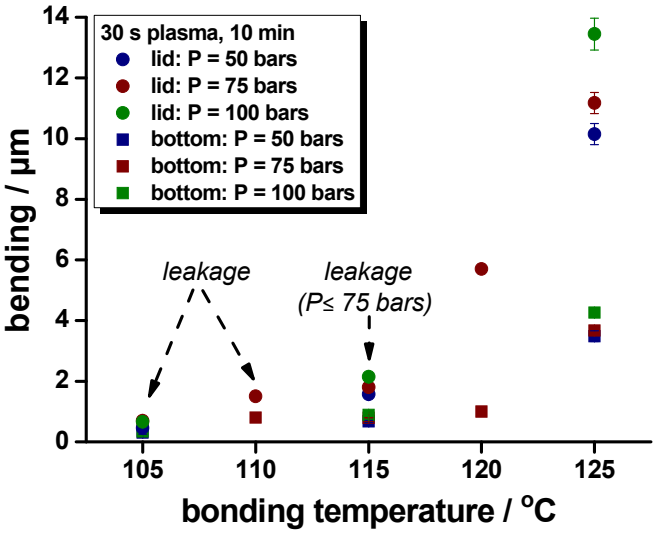

Figure 143: Bending of microchannel bottom and nanostructured lid of Topas 5013 chips dependent on the bonding temperature. Bonding was performed using 30 s air plasma treated chips bonded for 10 min at constant pressure stated in the figure.

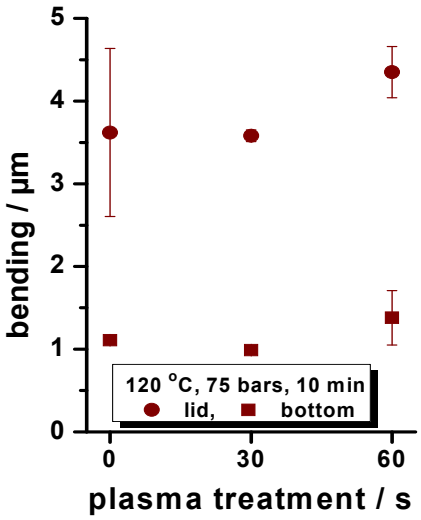

Figure 144: Bending of microchannel bottom and nanostructured lid of Topas 5013 chips dependent on the plasma treatment time. Bonding was performed at constant temperature of 120 °C and pressure of 75 bars for 10 min.

To measure the bending of the channel from a cross-sectional profile is an important though not perfect measure to evaluate the influence of the different bonding parameters. The profiles allow for precise measurement of actual bending of the channel measured from sidewall to center. However, it does not represent the total deformation (squeezing of the channel) properly. For example, the pressure seem to have only a minor effect on the channel bending measured based on cross-sectional channel profiles in the tested range. SEM images taken of a cross-section of chips bonded at varying pressures[84] show that the pressure has a tremendous effect on the absolute height of the channel, especially with increasing bonding temperatures (Figure 145 and Figure 146). While an increase in pressure did not show any visible influence on the channel height for a bonding temperature of 115 °C, the effect is significant for 125 °C. In the latter case, the channel is almost collapsed showing a height of about 5 µm in the channel center. Since the channel was also deformed close to the sidewalls the bending determined as stated above would result in an absolute difference of only 10 µm. The calculated bending and the overall deformation of the channel showed no significant difference for varying plasma treatment times. The “tip” of excess material resulting from injection molding was squeezed together and mostly not visible in the SEM images (Figure 145, Figure 146) or in the cross-sectional profile recorded from debonded chips parts (Appendix I-2.4). In some cases it caused formation of voids in the bond interface behind the “tip” (Figure 147).

[84] Residual bonding parameters remain constant.

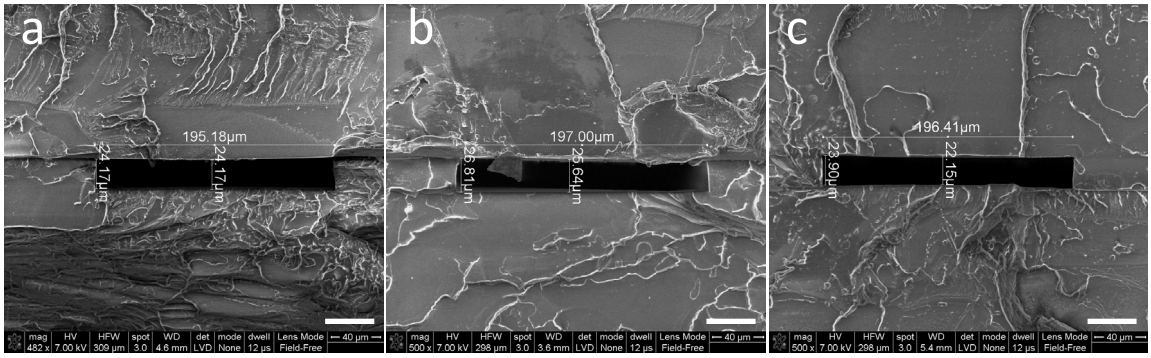

Figure 145: SEM images of channel cross-section from thermally bonded Topas 5013 chips. Bonding parameters: air plasma treatment = 30 s, T_{bond} = 115 °C, t_{bond} = 10 min, P_{bond} = 50 bars (a), 75 bars (b), and 100 bars (c). Scale bars: 40 µm.

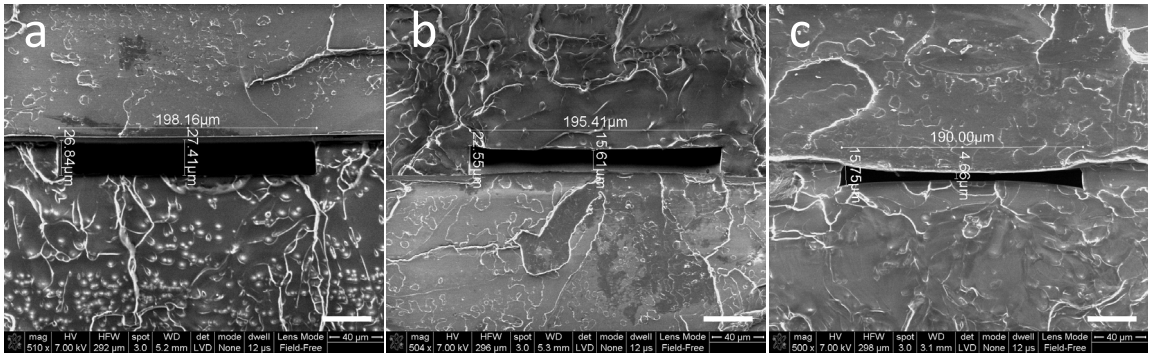

Figure 146: SEM images of channel cross-section from thermally bonded Topas 5013 chips. Bonding parameters: air plasma treatment = 30 s, T_{bond} = 125 °C, t_{bond} = 10 min, P_{bond} = 50 bars (a), 75 bars (b), and 100 bars (c). Scale bars: 40 µm.

Figure 147: SEM images of cross-section of microchannels fabricated in Topas 5013. The "tip" of excess material caused sometimes voids (indicated by white arrow) in the bond interface behind the "tip". Scale bars: 40 µm.

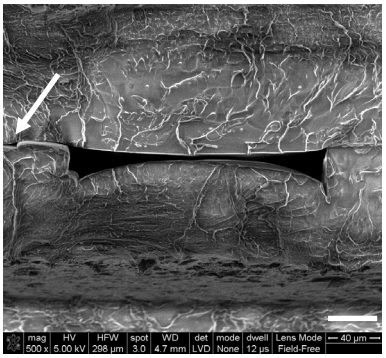

DEFORMATION OF NANOSTRUCTURES. 50 nm and 100 nm wide holes in Topas 5013 did not deform visibly as it can be seen from Figure 148 and Figure 149. The grainy surface was caused by the gold sputtering prior to SEM imaging. Although a different setup with lower pressure was applied the higher bonding temperature resulted in a bending of the channel lid comparable to the otherwise used setup.

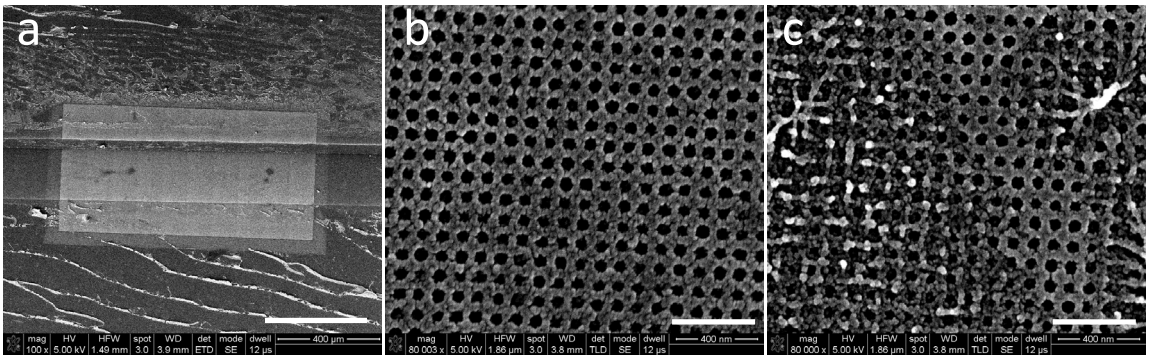

Figure 148: SEM images of arrays of 50 nm wide holes after bonding and subsequent mechanical debonding showing the whole nanostructured pattern (a) and magnified view of a center area (b) and a bonded area outside the microchannel (c). Bonding parameters: 30 s air plasma treatment, 123 °C, 15 min, 7.5 bars. The measured bending of the nanostructured lid reached about 4.7 µm. Scale bars: 400 µm (a) and 400 nm (b, c).

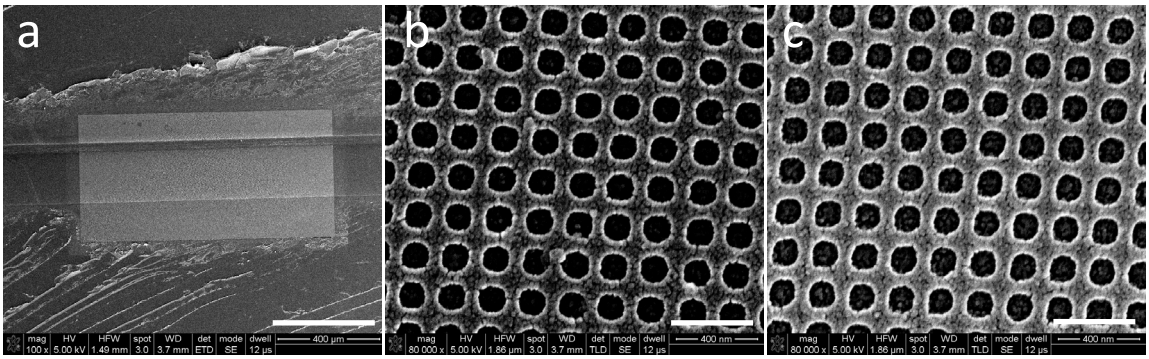

Figure 149: SEM images of arrays of 100 nm wide holes after bonding and subsequent mechanical debonding showing the whole nanostructured pattern (a) and magnified view of a center area (b) and a bonded area outside the microchannel (c). Bonding parameters: 30 s air plasma treatment, 123 °C, 15 min, 7.5 bars. The measured bending of the nanostructured lid reached about 4.7 µm. Scale bars: 400 µm (a) and 400 nm (b, c).

DISCUSSION. Air plasma treated Topas 5013 chips were well bonded at a temperature of 115 °C and pressure of 100 bars, able to withstand pump rates applied during cell adhesion experiments with pump rates up to 1 ml min^{-1} [85]. Lower bonding pressures led to insufficient bonding and delamination during cell experiments. Increased bonding temperatures to 120 or even 125 °C led to higher bonding strength but also increasingly high deformation. Patterns of 50 and 100 nm holes on parts displayed an overall bending of 4.7 µm. None of the imaged patterns showed significant deformations related to bonding. In fact, some even areas of nanostructures in bonded areas were still undeformed after mechanical debonding.

For a quantitative measurement of the adhesion strength of cells to various surfaces the area of channel cross-section is important. Different bonding parameters and thereby varying channel bending change the cross-sectional area of the microfluidic channel. Thereby, the hydrodynamic pressures inside the microfluidic system changes which complicate comparison of data obtain from cell adhesion experiments.

[85] Higher pump rates were not tested.

1.3. Thermal Bonding of Topas 8007

Micro- and nanostructured parts injection molded from Topas 8007 were appropriately bonded for application in cell experiments. Nanostructures were not deformed during the bonding for bonding temperatures of at least up to 73 °C.

Topas 8007 chips are more difficult to bond sufficiently well compared to Topas 5013. The parameter range is noticeable smaller for bonding chips with good quality (no Newton rings or pools) as well as creating acceptable high bonding strength. Bonding temperatures of 48, 58, and 68 °C[86] did not show any significant bending (< 0.6 µm), but were also not bonded exhibiting Newton rings and voids[87]. No significant change for varying pressure was observed for bonding temperatures of 48 – 68 °C. Chips were easy to debond by hand without applying significant pressure. An improved bonding quality was observed for a bonding temperature above 68 °C with widely reduced voids compared to lower temperatures. Bonding at a temperature of 73 °C resulted in the good bonding quality. No Newton rings or voids were observed. A bending of up to 1.6 ± 0.3 µm (bottom) and 3.0 ± 0.1 µm (lid) (Figure 150) was measured. Bonding of Topas 8007 slightly below glass transition temperature[88] at 78 °C led to complete collapse of the channel (Figure 151).

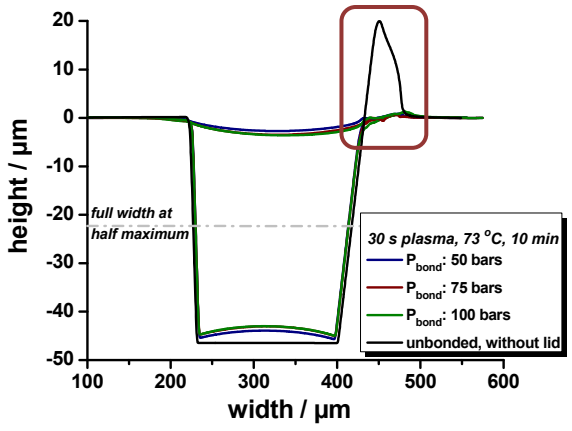

Figure 150: Cross-sectional profiles of Topas 8007 chip for bonding temperature of 73 °C and pressure of 50, 75, and 100 bars. The "tip" of excess material visible in the original channel profile (black profile, high lightened by red rectangle) is extremely squeezed.

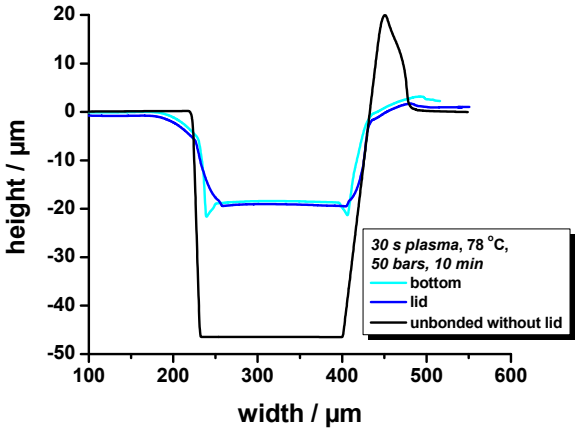

Figure 151: Cross-sectional profile of Topas 8007 chip bonded at 78 °C and 50 bars for 10 min. The chip collapsed completely.

Bonding temperature, pressure and plasma-treatment had similar effect on the bending as described for Topas 5013 though to considerable smaller extent. A strong effect was observed for bonding temperatures between 73 and 78 °C. Chips were bonded at 73 °C with good bonding quality while the channels were completely sealed at 78 °C caused by deformation of the channel bottom and lid (Figure 151). An increase in pressure from 50 – 100 bars had no substantial effect on the bending (≤ 3.0 µm at 100 bars for T_{bond} = 73 °C) and overall deformation (≤ 2.1 µm at 100 bars for T_{bond} = 73 °C)

[86] Equal bonding results for P_{bond}: 50 – 100 bars, t_{bond} = 10 min, t_{plasma} = 0 or 30 s.
[87] "Voids" or "pool": Air entrapped in between the bonding interface.
[88] Glass transistion temperature of Topas 8007 (and Topas 5013) was experimentally tested and resulted in a temperature of 83 °C, instead of 78 °C as stated by the manufacturer.

(Figure 153). The air plasma-treatment as did not cause any significant change in the bending leading to 1.5 ± 0.3 µm (bottom) and 2.8 ± 0.4 µm (lid). Chips bonded without pre-treatment resulted in the lowest bending of 1.1 ± 0.1 µm (bottom) and 2.3 ± 0.1 µm. Furthermore small voids were observed for bonded chips without air plasma treatment prior to bonding. Additionally, the influence of the bonding time was investigating showing that the bending increases with increasing bonding time from 0.2 ± 0.1 µm (bottom) and 1.1 ± 0.5 µm (lid) for 5 min to 3.1 ± 0.1 µm (bottom) and 6.2 ± 0.3 µm (lid) for 15 min bonding (Figure 154). Profiles of chips bonded exemplified for different bonding parameters without and with 30 s air plasma treatment are given in the Appendix I-2.4.

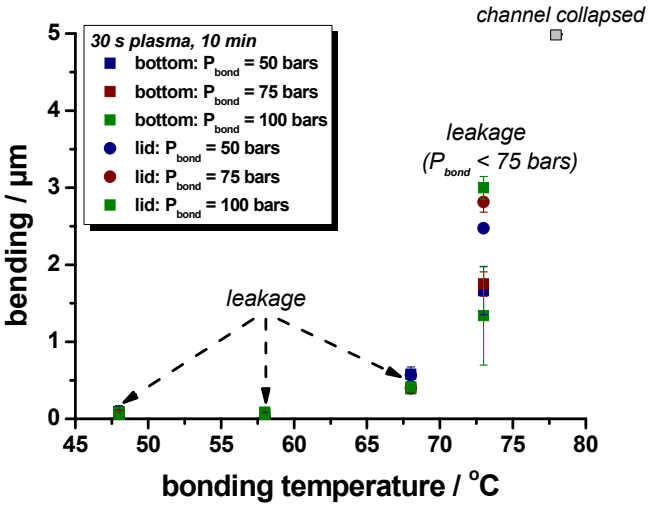

Figure 152: Bending of microchannel bottom and nanostructured lid of Topas 8007 chips dependent on the bonding temperature. Bonding was performed using 30 s air plasma treated chips bonded for 10 min at constant pressure stated in the figure.

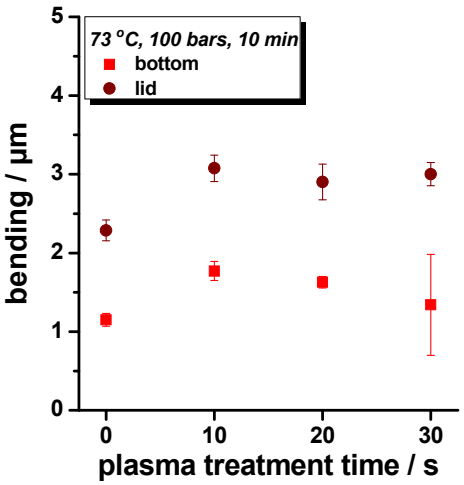

Figure 153: Bending of microchannel bottom and nanostructured lid of Topas 8007 chips dependent on the plasma treatment time. Bonding was performed at constant temperature of 73 °C and pressure of 100 bars for 10 min.

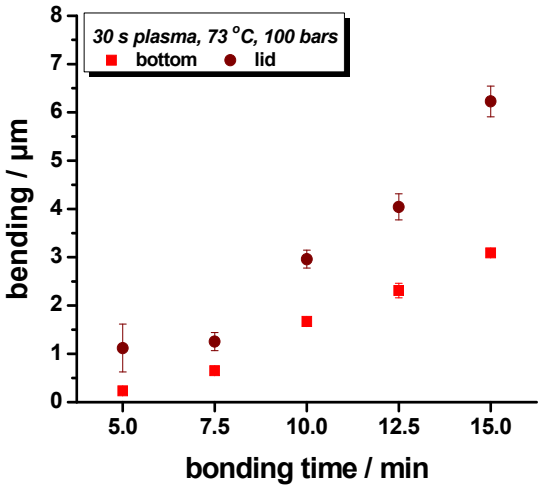

Figure 154: Bending of microchannel bottom and nanostructured lid of Topas 8007 chips dependent on the bonding time. Bonding was performed using 30 s air plasma treated chips bonded at constant temperature of 73 °C and pressure of 100 bars.

As described in the previous section, the bending of the channel from a cross-sectional profile is not the perfect measure to evaluate the influence of the different bonding parameters. It does not represent the overall deformation of the channel (caused by "squeezing") properly. The difference of the channel height and width compared to the original injection molded part was calculated based on the cross-sectional profiles. In case of bonding temperatures of up to 68 °C[89] no visible deformation occurred. Microchannels exhibited the same dimensions before and after bonding. At a bonding temperature of 73 °C a minor overall deformation was observed leading to a decrease of the channel height of 0.9 µm for 50 bars and 2.1 µm for 75 and 100 bars. The channel width decreased about 10 µm in total at full width at half maximum channel height (indicated by grey line in Figure 150). The "tips" of excess material emerged during injection molding were squeezed together and almost not visible in the cross-sectional profiles recorded from debonded chips for bonding temperatures of ≥ 73 °C (Figure 150, Figure 151).

DEFORMATION OF NANOSTRUCTURES. 50 nm and 100 nm wide pillars in Topas 8007 did not deform significantly as it can be seen from Figure 155 and Figure 156. The rough surface structures were caused by the gold sputtering prior to SEM imaging. Similar to Topas 5013, nanostructured patterns were partially still intact in areas at the bond interface (images not shown).

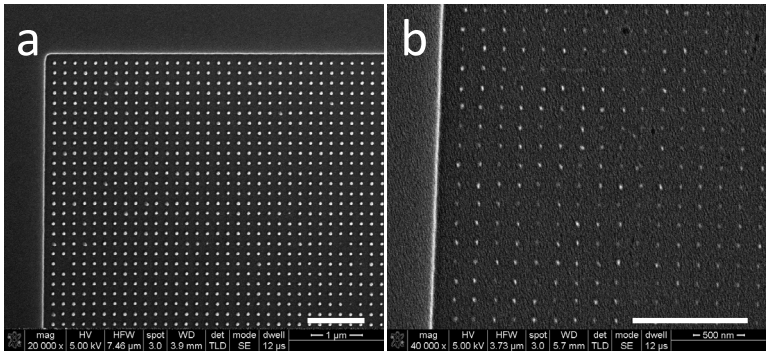

Figure 155: SEM images of arrays of 40 nm wide[90] pillars before (a), and after bonding and subsequent mechanical debonding (b). Bonding parameters: 30 s air plasma treatment, 73 °C, 10 min, 100 bars. Measured bending of the nanostructured lid: 4.6 µm. Scale bars: 400 nm.

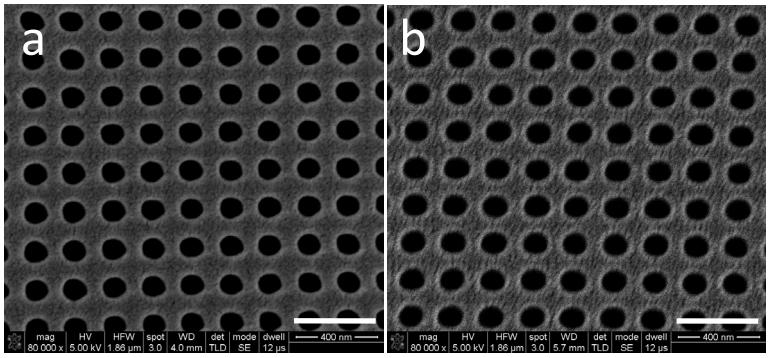

Figure 156: SEM images of arrays of 120 nm wide holes before (a), and after bonding and subsequent mechanical debonding (b). Bonding paramaters: 30 s air plasma treatment, 73 °C, 10 min, 100 bars. Measured bending of the nanostructured lid: 4.6 µm. Scale bars: 400 nm.

[89] Bonding parameters: P_{bond}: 50 – 100 bars, t_{bond} = 10 min, t_{plasma} = 0 or 30 s.
[90] Width of the holes in the corner and center

DISCUSSION. Topas 8007 chips pre-treated with air plasma for 30 s were well bonded at a bonding temperature of 73 °C and applied pressure of 75 – 100 bars (for at least 10 min). Chips were able to withstand pressures applied during cell adhesion experiments (pump rate ≤ 400 µl min^{-1}). Chips partially delaminated for higher pump rates. However, only very few tests were conducted using Topas 8007. To obtain reproducible data, additional experiments are required. Since neither plasma treatment time nor bonding pressure had a substantial influence on the bending of the channel lid and bottom, prolonged air plasma treatment and/or increased pressure might improve the bonding strength without largely increased bending. Patterns of 30 – 40 nm wide pillars and 120 nm wide holes on parts did not show any visible deformation though the overall bending of the nanostructured lid was about 4.6 µm. Even nanostructures in areas of the bond interface were partially still undeformed.

TOPAS 8007 VERSUS 5013. The bending of Topas 8007 during thermal bonding caused by heat and applied pressure is lower (3.1 ± 0.1 µm (bottom) and 6.2 ± 0.3 µm [91]) compared to Topas 5013 (4.3 ± 0.1 µm (bottom) and 13.4 ± 0.5 µm (lid)[92]). In contrast, the bonding strength observed from cell experiments was worse for Topas 8007. Both observations can be explained with with the better flowability (higher melt flow index) of Topas 5013 compared to 8007. The melt flow index for Topas 5013 is 24 ml min^{-1} while only 2 ml min^{-1} for Topas 8007[93]. Topas 5013 softens faster with faster decreasing viscosity for increasing temperatures compared to Topas 8007. Therefore, the bending of Topas 5013 channel structures but also the resulting bonding strength is higher for comparable bonding temperatures than for Topas 8007.

[91] Bonding parameters: T_{bond} = 73 °C, P_{bond} = 100 bars, t_{bond} = 15 min, t_{plasma}= 30 s.
[92] Bonding parameters: T_{bond} = 125 °C, P_{bond} = 100 bars, t_{bond} = 10 min, t_{plasma}= 30 s.
[93] Melt flow index measured at heat deflection temperature (HDT) plus 115°C with 2.16 kg load. Values stated by the manufacturer.

2. Micro Milling of Fluidic Connectors

Fluidic connectors containing male luer fittings were micro milled into Polycarbonate (PC) or Polytetrafluoroethylene (PTFE) providing connection to PTFE or silicon tubings, respectively. The male luer fittings were designed to comply into the twelve luer chip injection molded in Topas 8007 or 5013. Two types of male luer connectors were designed: one without external fluidic connectors made of PTFE (Figure 157) and one with external fluidic connectors made in PC (Figure 158). Both materials were purchased from (Nordisk Plast A/S, Denmark). In the first case, PTFE tubings are connected via a metal tip. Due to the self-sealing ability of PTFE, PTFE tubings can be connected to the micro milled PTFE luers simply via a metal tip. The diameter of the metal tip complies with the diameter of holes in the milled part and the outer diameter of the PTFE tubings. In the latter case, silicon tubings are directly connected to the "external" fluidic connector of the milled part.

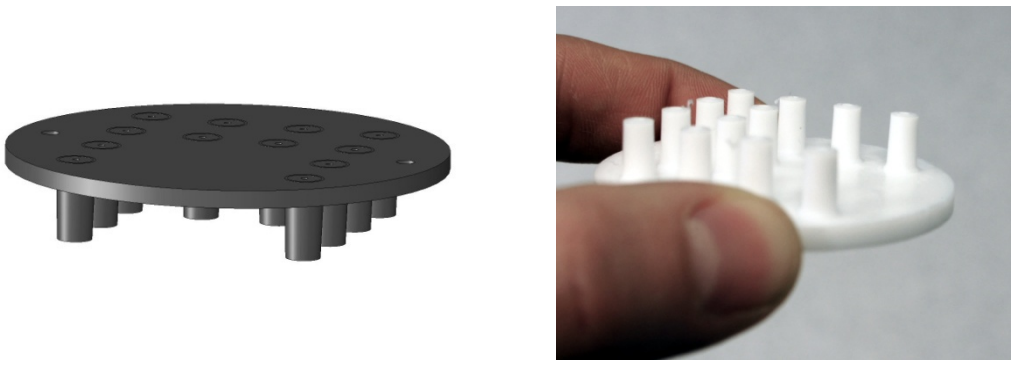

Figure 157: CAD drawing (a) and photo (b) of male luer fitting ports without internal fluidic connector micro milled in Polytetrafluoroethylene.

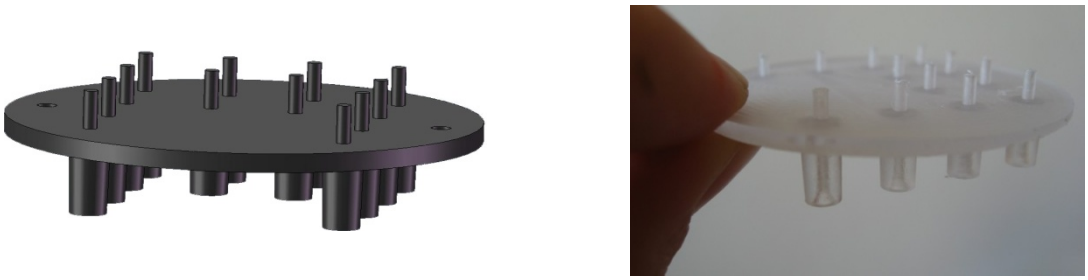

Figure 158: CAD drawing (a) and photo (b) of male luer fitting ports with external fluidic connector micro milled in Polycarbonate.

Chapter 5

Cell Experiments

Injection molded pieces of Topas 8007 and 5013 containing unstructured and nanostructured areas were investigated by studying proliferation and morphology of different cell types compared to tissue culture grade polystyrene (TCPS). Three different cell types were used for initial studies: mouse fibroplasts (NiH3T3), human epithelial carcinoma cells (HeLa), and immature dentritic cells were cultured over a period of several days on Topas 8007 and 5013 samples containing different nanostructured patterns.

Initial tests were performed to verify applicability of a setup to investigate the cell adhesion on injection molded nanostructured patterns integrated in a microfluidic channel system.

1. Experimentals

PLASMA TREATMENT. Samples were air plasma treated equal to treatment prior to bonding to assure similarity of the surface chemistry on single and bonded chips. Samples were treated in air plasma at 0.6 bars and 50 W for 30 s. Contact angles of untreated and air plasma treated Topas 8007 and 5013 were recorded on a DCA from dataphysics.

CELL CULTURING. NIH3T3 cells were grown in Dulbecco's modified Eagle's medium with Glutamax (GIBCO Life Technologies), 10% newborn calf serum (Sigma Aldrich) and 1% penicillin-streptomycin (GIBCO Life Technologies). HeLa cells were cultured in Dulbecco's modified Eagle's medium with Glutamax, 10% fetal bovine serum (Sigma Aldrich) and 1% penicillin-streptomycin. Immature dendritic cells (iDC) were cultured in X-vivo medium (Lonza Cologne GmbH) with 2 % human AB serum. Immature DCs are generated from monocytes isolated from human blood and stimulated to differentiate into iDCs. All cells types were cultured under standard conditions at a temperature of 37 °C and an atmosphere of 5 % carbon dioxide. Sterilisation was done by immersing chips for 10 min in 70 % ethanol, followed by washing in Dulbecco's phosphate buffer saline (DBPS; GIBCO Life Technologies). Chips were washed once in DMEM. The cell suspension was applied and about 3 ml medium was added.

CELL EXPERIMENTS ON SINGLE CHIPS. NiH3T3, HeLa, and immature dentritic cells were cultured over a period of several days (2 – 9 days) on Topas 8007 and 5013 samples containing different nanostructured patterns. The cell survival and morphology was investigated and compared to flat Topas and partially flat tissue culture grade polystyrene surface by light microscopy in phase contrast and fluorescence imaging after cell fixation.

For each experiment, one set of samples was air plasma treated while a second set was used without treatment. Chips were fixed with biocompatible adhesive tape in a small cell culture dish (52 mm diameter) and sterilized as described above. Cells were seeded with a density of about 4 10^4 cells/chip. Images were recorded once a day using an Axiovert 25 (Carl Zeiss NTS GmbH) with an

Exwave HAD camera SSC-DC54A (Sony), commonly in phase contrast at a magnification of 100fold or 200fold. Medium was changed every 2 – 3 days.

CELL ADHESION EXPERIMENTS ON BONDED CHIPS. The bonded microfluidic chip containing nanostructures (Topas 5013) was fixed in an Axiovert 100M (Carl Zeiss NTS GmbH) with computer controlled stage and an iXon camera (Andor Technology) (Figure 159). Chips were sterilized for 10 min in ethanol as described above. Subsequently, chips were rinsed for 1 min with DPBS, followed by 1 min with medium. Chips were filled with fresh medium and cells were injected. Cells were allowed to settle down for about 1 h. Cell medium was injected with a pump rate of 20 – 50 µl min^{-1} increasing in steps of 20- 50 µl min^{-1}. The experiment was controlled by a LabView program ("timelapse") written by Dávid Selmeczi (former group member at DTU Nanotech) which enables taking images at a given frequency at different locations of the chips for a set of pump rates. The pump rate was increased every 60 s. Images were recorded after 30 s to allow for flow stabilization. A syringe pump model NE-1000 (New Era Pump Systems, Inc.) was used for all experiments.

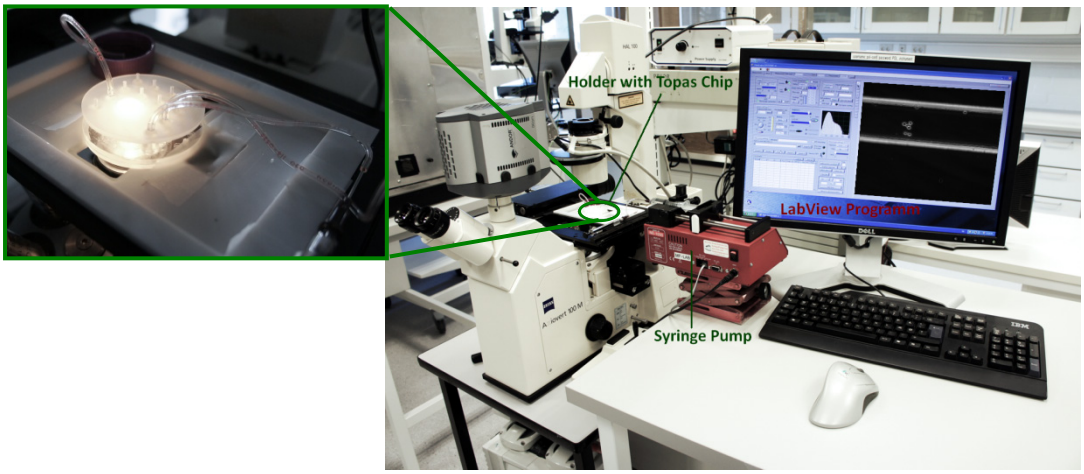

Figure 159: Photo of the setup used for initial cell adhesion experiments (top) and a close view of the installed chip (left).

CELL FIXATION AND FLUORESCENCE STAINING. Cells were fixed applying the fixation solution (2% glutaraldehyde in 0.05M cacodylate buffer) for 15 – 20 min. The solution was removed and the cell culture rinsed twice with DPBS (Lonza). Samples were stored in fresh DPBS at 4 °C. Fluorescence staining with TRITC-phalloidin (Sigma Aldrich) was performed to investigate changes in the actin filaments and stress fibers for varying nanostructured patterns. Cells were permeabilized with 0.1 % Triton X (Sigma-Aldrich) in DPBS for 1 – 5 min and washed twice with washing buffer (0.05 % Tween (Sigma-Aldrich) in DPBS). Staining was performed to investigate changes in the cytoskeleton by staining actin filaments. Samples were immersed in DPBS containing 0.23 µM TRITC-phalloidin for about 45 min. Subsequently, the sample was washed twice in washing buffer for 5 – 10 min. and once with DPBS. Samples were stored in fresh DBPS at 4 °C. The staining resulted in a very good fluorescence signal without strong background noise. Cells were imaged using a Zeiss Axio Observer Z1 (Carl Zeiss NTS GmbH).

2. Cell Culturing Experiments with Single Chips

Initial cell experiments of NiH 3T3, HeLa and immature dendritic cells (DC) on air plasma treated Topas 8007 and 5013 showed cell morphologies comparable to cells cultured on commercial tissue culture grade polystyrene (Figure 160).

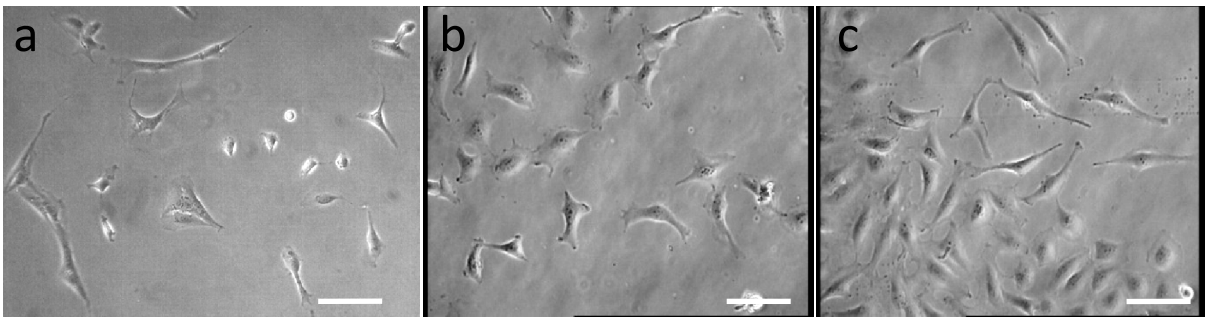

Figure 160: Light Microscope images of NiH3T3 cells on unstructured TCPS (a), air plasma treated Topas 8007 (b) and 5013 (c). Scale bars: approximately 100 µm.

In contrast, the proliferation of HeLa and NiH3T3 cells was strongly decreased on untreated Topas samples. HeLa cells exhibited an elongated shapes and spread less well on untreated Topas of both types. NiH3T3 cells did almost not adhere to the surfaces on untreated Topas of both types and thereby showing rarely spots (500 by 500 μm^2) with one or two living cells. These cells exhibited a contracted shape. However, although the proliferation of plasma treated Topas surfaces doe not seem to differ, staining of fixed HeLa cells with TRITC-phalloidin showed a clear difference in the organization of the cytoskeleton as well as cell spreading (difference in cell area). Immature DCs were found to spread less well on native Topas regardless of surface topography forming largely extended lamellopodia and filopodia compared to air plasma treated Topas. No obvious influence on immature DC morphology could be seen for nanostructures on treated or untreated Topas.

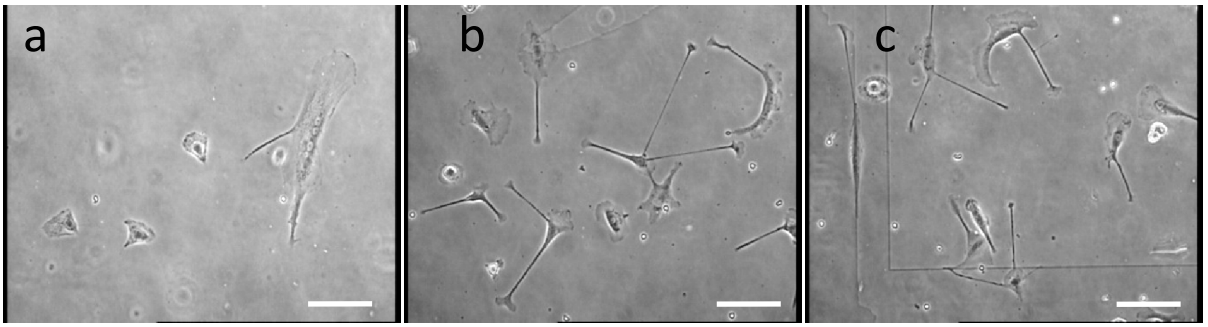

Figure 161: Phase contrast images of immature dentritic cell on the 2nd day after seeding. Cells spread well on air plasma treated, unstructured Topas 8007 without forming extended lamellopodia and filopodia (a) as observed for untreated, unstructured (b) and nanostructured Topas 8007, exemplified for 40 nm wide and high pillars (pitch: 400 nm) (c).

No visible difference in morphology was found for most of the tested pillar and hole pattern ranging in the dimensions of 40 – 120 nm in width compared to the unstructured surfaces of untreated or air plasma treated Topas 8007 or 5013. However, few examples for visible differences in morphology and/or cell spreading of HeLa and NiH3T3 cells on nanostructured topographies compared to unstructured Topas 8007 surfaces are described in the following paragraphs.

HeLa on Air Plasma treated Topas 8007 Replicas. HeLa cells showed an increasing spreading on 40 nm wide and high pillars with a pitch of 400 nm compared to cells cultured on unstructured surfaces (Figure 162 a, b). The fluorescence staining with phalloidin showed a strong increase in the amount of stress fibers. This might indicate that the cell prefers to attach to pillars even though they most probably can sense the bottom in between. Thereby the cells are stretching out generating a larger cell area. This does not necessarily mean that the cell is attaching stronger or weaker compared to the unstructured surface. 40 nm wide and high pillars with a pitch of 200 nm generated a decreased cell area (Figure 162). No stress fibers were observed. 110 nm wide and deep holes with a pitch of 200 nm resulted in an even smaller cell area (Figure 162). No stress fibers can be seen as well.

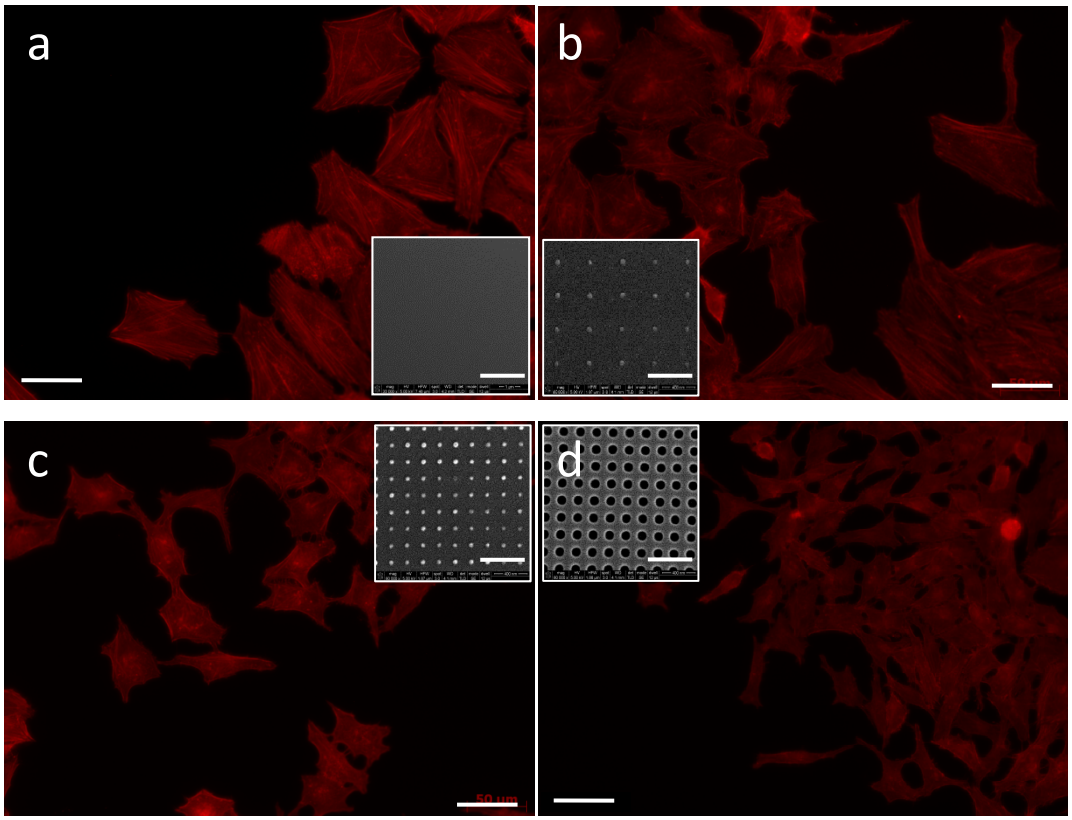

Figure 162: Fluorescence images of HeLa cells on different topographies stained with phalloidin against actin. Unstructured surface (a), 40 nm wide and high pillars (pitch: 400 nm) (b), 40 nm wide and high pillars (pitch: 200 nm) (c), and 110 nm wide and deep holes (pitch: 200 nm) (d). Scale bars: 50 µm. Insets: SEM images of respective nanostructures; scale bars: 500 nm.

HeLa on Untreated Topas 8007. It was found that HeLa cells definitely prefer arrays of 180 and 520 nm wide and 300 nm deep pillars as well as 350[94], 450, and 600[96] nm wide and 300 nm deep holes (Figure 163 a, c, d). In contrast, similar to about 100 nm wide and deep structures, arrays of 150 nm wide and 300 nm deep holes (pitch: 400 nm) did not show any significant influence on the HeLa cells (Figure 163 b).

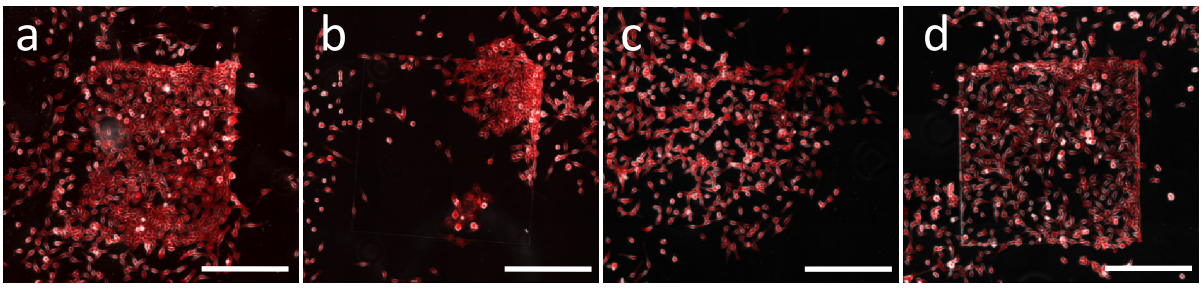

Figure 163: Merged phase contrast and fluorescence images of HeLa cells stained with TRITC-phalloidin (red) to visualize actin filaments. 180 nm wide pillars (a), 520 nm wide pillars (b), 150 nm wide holes (c), 450 nm wide holes (d). Scale bars: approx. 250 µm.

NiH3T3 on Air Plasma treated Topas 8007 Replicas. NiH3T3 cells showed a clear difference in proliferation on 50 nm wide and deep holes compared to unstructured surfaces for air plasma treated Topas 8007. It was clearly visible that cells were avoiding this pattern by growing around the pattern (Figure 164).

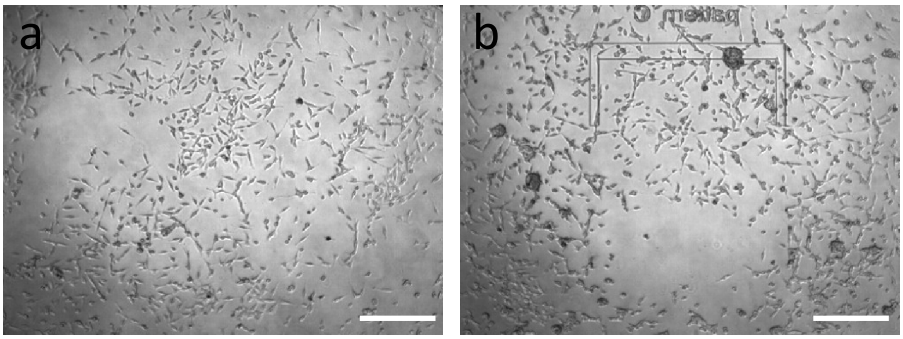

Figure 164: Light Microscope images of 3T3 cells on air plasma treated, unstructured Topas 8007 (a) and containing pattern of 50 nm wide and deep holes (b). The cells do not grow on the nanostructured pattern. Scale bars: 100 µm.

[94] Images not shown.

3. Cell Adhesion Experiments with Bonded Chips

Nanostructures were designed and injection molded in Topas 8007 and 5013 to modify the adhesion strength of cells. Ideally, areas should be generated were only one cell type adheres, or at least that specific cell type adheres stronger than others.

Experiments were conducted to set up a system enabling the user to investigate the adhesion strength of cells on nanostructured and flat polymer surfaces in a closed microfluidic chip. Thereby all process steps were successfully performed: (a) Injection molding of channel structures for a simple microfludic system in Topas 8007 and 5013, (b) injection molding of nanostructures in both Topas grades, (c) thermal bonding, and setting up a system to investigate the adhesion strength based on the applied flow rate. The system was developed in cooperation with other group members, including a program written in LabView by Dávid Selmeczi to control the experimental setup. The program enables precise control of pump rate and image taking (phase contrast and fluorescence) at specified locations and time.

Cell experiments were conducted using NiH3T3 cells on 600 nm wide and 250 nm deep holes in Topas 5013. Initially medium was injected with a pump rate of 50 µl min^{-1} increasing in steps of 50 µl min^{-1} was applied. The number of cells remaining on the surface 30 s after increasing the pump rate was counted. Cells elongated at applied flow and the number of cells remaining on the flat bottom of the microfluidic chip decreased with increasing flow rate from initially 24 cells (no flow) to 19 cells at 300 µl min^{-1} (79 % remaining), 6 cells at 450 µl min^{-1} (25 % remaining), and 1 cell at 500 µl min^{-1} (4 % remaining). The last cell is detached at a pump rate of 650 µl min^{-1}. Cells attached to 600 nm wide and 250 nm deep holes decreased from 19 cells (no flow) to 15 cells at 300 µl min^{-1} (79 %), 3 cells at 450 µl min^{-1} (16 % remaining), 1 cells at 500 µl min^{-1} (5 % remaining). The last cell is detached at a pump rate of 550 µl min^{-1}.

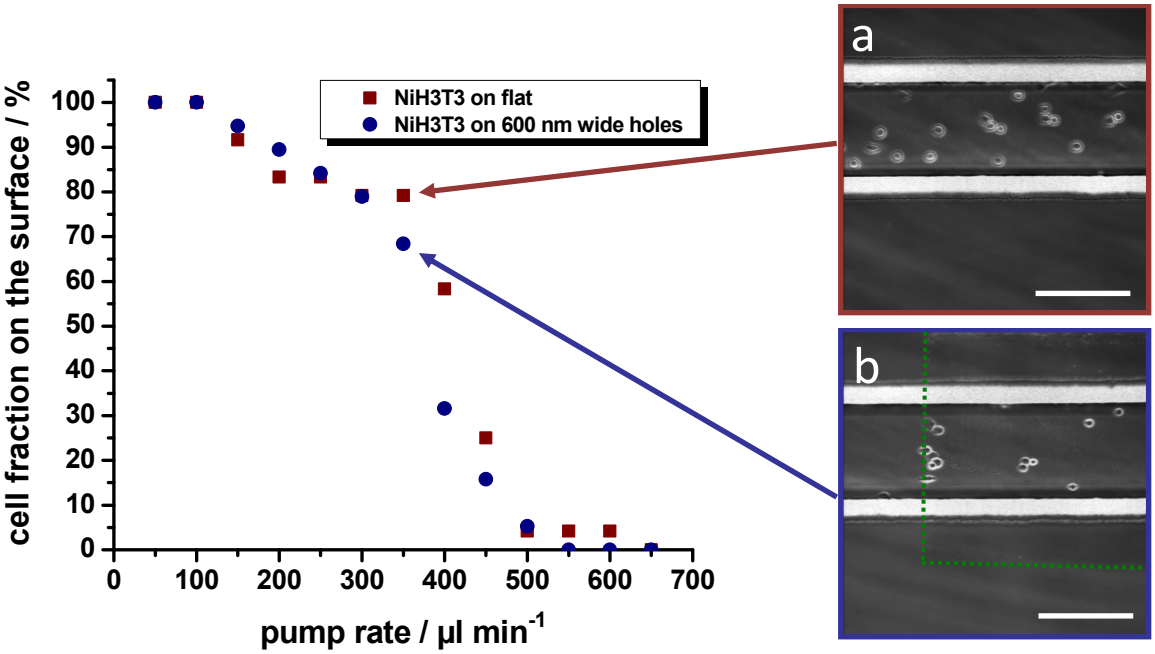

Figure 165: Cell adhesion of NiH3T3 on flat and nanostructured surfaces (600 nm wide and 250 nm deep holes, pitch: 1 µm). The amount of cells decreases with increasing pump rate with a step of 50 µl min^{-1}. Photos representing NiH3T3 cells on flat (a) and nanostructured surface (600 nm wide holes), (b) at a pump rate of 300 µl min^{-1}. Scale bars: 200 µm.

The resolution, especially between an applied pump rates of 300 – 500 µl min^{-1} required an adjustment to lower increase of the pump rate. A pump rate of 20 µl min^{-1} was employed and showed an improved resolution.

The number of cells remaining on the flat bottom of the microfluidic chip decreased with increasing flow rate from initially 13 cells (no flow) to 10 cells at 180 µl min^{-1} (77 % remaining), 3 cells at 320 µl min^{-1} (23 % remaining), and 1 cell at 340 µl min^{-1} (8 % remaining). The last cell is detached at a pump rate of 440 µl min^{-1}. Cells attached to 600 nm wide and 250 nm deep holes decreased from 15 cells (no flow) to 10 cells at 180 µl min^{-1} (79 %), and 1 cell at 340 µl min^{-1} (7 % remaining). The last cell is detached at a pump rate of 420 µl min^{-1}.

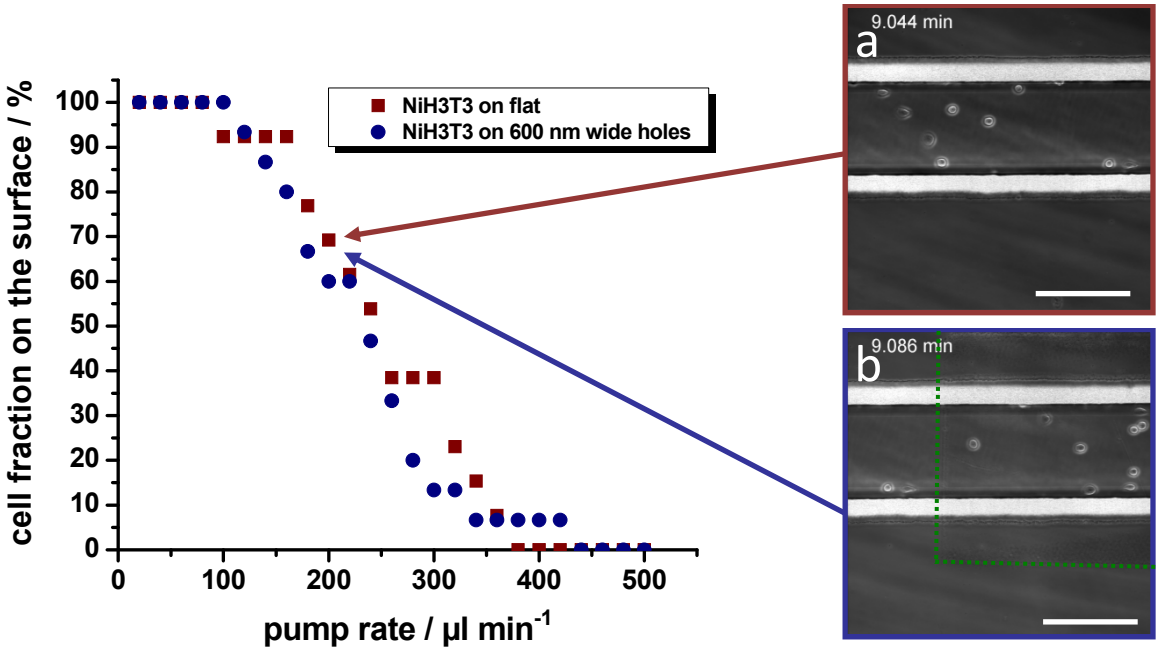

Figure 166: Cell adhesion of NiH3T3 on flat and nanostructured surfaces (600 nm wide and 250 nm deep holes, pitch: 1 µm). The amount of cells decreases with increasing pump rate with a step of 20 µl min^{-1}. Photos representing NiH3T3 cells on flat (a) and nanostructured surface (600 nm wide holes) (b) at a pump rate of 180 µl min^{-1}. Scale bars: 200 µm.

DISCUSSION. It was observed that the fraction of cells decreased with increasing flow rate whereby cells on 600 nm wide and 250 nm deep holes (pitch: 1 µm) whereby a larger number of cells was detached from the nanostructured surface than from the flat surface. These results indicate a possible reduction in the adhesion of NiH3T3 on 600 nm wide and 250 nm deep cells presenting a reduced area fraction of about to the cells. The actual adhesion strength has not been calculated so far. Additional experiments are required to gain statistical verification and to be able to calculate the adhesion strength more precise. Up to date, too many variables influence the calculation of the adhesion strength such as delay of image taking, frequency of increasing the pump rate, or interval between cell seeding and experiment start. For example, more cells might detach at a lower pump rate as detected for the described experiments if the flow is applied longer. The measured adhesion strength can vary depending on interval between cell seeding and experiment start, at least in the first few hours. Cells shown in the images above, for example Figure 127 a and b, did not spread as well as observed for NiH3T3 cultured over several days. Therefore, it is very likely that the adhesion strength of these cells will be much lower. Modelling of varying shear rates acting on the cell during these experiments may assist precise measurement of probably varying adhesion strength of different nanostructured topographies compared to flat surfaces. However, the major goal of these experiments was to show that injection molded nanostructures can be integrated successfully into a polymeric microfluidic system and its application for investigating the adhesion strength of cells on different surface topographies. All process steps towards that goal were successfully performed.

Chapter 6

Conclusion and Outlook

Nano- and microstructures were designed to match possible applications for investigating the adhesion strength of cells. The aim was to develop and optimize a process that allows the mass-fabrication of nanostructures below 100 nm to comply with adhesion relevant dimensions. A simple microfluidic system was designed that supports the transfer of cells to nanostructured patterns and enable application of varying shear rates applied on the cells.

A process flow was developed that allows fabricating nano- and microstructured masters and their replication into a resilient mold material by electroplating of nickel. The structured nickel shims were used for replication of the presented surface relief into Topas 8007 and 5013 by injection molding. The process flow demonstrated the mass-fabrication of high aspect ratio nanostructures up to a height-to-width aspect ratio of 2.7 to 1 as well as microstructures and their integration into the a sealed microfluidic chip. Cell experiments on single chips showed that Topas 8007 and 5013 are biocompatible materials comparable to tissue culture grade polystyrene. Few differences in morphology and/or cell spreading of HeLa and NiH3T3 cells on nanostructured topographies compared to unstructured Topas 8007 surfaces were observed. For example, NiH3T3 cells were clearly avoiding arrays of 50 nm wide and deep holes (pitch: 200 nm) of air plasma treated Topas 8007. In contrast, HeLa cells showed a tendency of preferring arrays of 180 and 520 nm wide and 300 nm deep pillars as well as 350, 450, and 600 nm wide and 300 nm deep holes compared to unstructured surfaces of untreated Topas 8007. Lastly, initial cell adhesion experiments demonstrated a successfully working setup for investigation of cell adhesion on nanostructured topographies by applied flow.

POLYMER REPLICATION OF NANOSTRUCTURES. The replication process by means of injection molding was thoroughly investigated. The effects of mold surface energy and injection molding conditions (varying process parameters) on the final nanostructure quality of high aspect ratio nanostructures in Topas 8007 and 5013 were explored. The major goal was to reduce molding defects and maximize structure height or depth. Optimized injection molding conditions[95] allowed the mass-production (> 500 pieces) of highly ordered nanostructures of controlled size. Arrays of pillars of 40 nm in diameter and 107 nm in height (ratio of 2.7:1) were successfully injection molded in Topas 8007 at mold temperatures above glass transition temperature (100 °C) using a fluorocarbonsilane coated nickel mold.

Observations from injection molding of Topas 8007 and 5013 on native as well as fluorocarbon-based antistiction coatings on nickel molds suggest that efficient demolding is of greater importance for the structural integrity than energetically favorable filling. It was found that though process parameters can improve the replication quality (uniformity, feature height and width), major improvement is only achieved by applying fluorocarbon-based antistiction coatings. The overall surface of nanostructured areas molded on native nickel molds often showed regular nanoscale defects and

[95] Possible process parameters for injection molding of high aspect ratio pillars: T_{mold} = 100°C, T_{melt} = 220 – 280 °C, v_{inject} = 10 – 30 $cm^3\ s^{-1}$, P_{inject} = 750 – 1050 bar, P_{hold} = 700 – 800 bar.

distortions, and randomly distributed large-scale defects. In contrast, a molecular vapor deposited fluorocarbon based antistiction coating was found to improve the replication fidelity significantly. Large scale defects of the overall patterned surface were fully removed while regular nanoscale defects decreased significantly. The application of antistiction coatings reduced also the sensitivity of process parameters on the replication quality. If sufficient filling of the mold cavity was given, only the mold temperature had a significant influence on the replication quality.

In this project, the mass-fabrication of arrays of nanopillars and -holes in polymer was demonstrated and process related effects analyzed. However, detailed analysis of nanostructures was often prevented by limited resolution of applied metrology methods (AFM and SEM), especially in vertical direction. To get an even better understanding, possible application of TEM or for example using carbon nanotube modified AFM tips might allow for better evaluation of the injection molding process of nanostructures. Even though fluorocarbon based antistiction coatings improved the replication quality tremendously, local changes (most probably damage) in the coating led to significant inhomogeneities in the pillar height. Therefore it is of major importance to optimize and verify the coating uniformity. Finally, the effect of polymeric nanostructures on the viability, morphology and other properties of various cell types need to be studied in detail. Especially, investigation of the adhesion strength of cells on nanostructured topographies is of major interest. Detailed information about the adhesion of cells on nanostructured surfaces may help to clarify the mechanism of adhesion as well as enable the application of nanostructured surfaces in cell handling, for example for sorting specific cells from a mixed cell suspension.

Appendix I

1. Mechanisms in Cell Adhesion

Cell adhesion is necessary for proliferation and differentiation of most (adherent) cell types. Cells build up connection to other cells or the extracellular matrix (ECM) using cell adhesion molecules such as selectins, cadherines (cell-cell), or integrins (cell-ECM). Adhesion of a cell to the extracellular matrix or an artificial surface (*in vitro*) is based on the adsorption of the transmembrane protein "integrin" on the surface. The ability of integrins to sense their ligands is largely dependent on the ability of the cell membrane to deform according to surfaces' topography. In this section focus is set on giving an introduction to the mechanisms relevant for cell adhesion to natural (ECM) as well artificial surfaces (nanostructured polymers) and requirements such as size of adhesion points as well as cell membrane stiffness and dimensions (Figure 167).

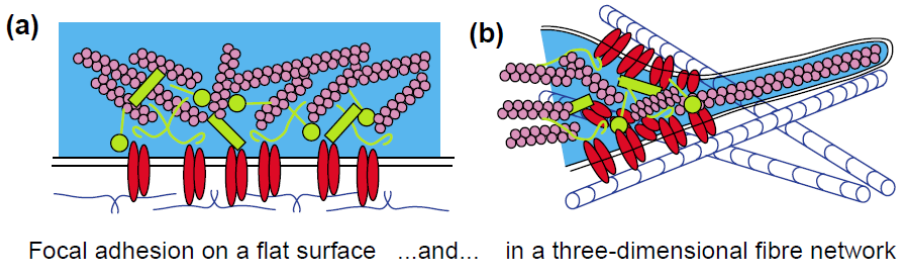

Figure 167: The topology of focal adhesions and their components on a flat surface such as a fibronectin-coated glass cover slip (a) or formed within a three-dimensional network of collagen fibers (b) [Wehrle-Haller 2002].

INTEGRINS. Integrins are transmembrane proteins of type I that bind to peptide motives such as RGD (arginine (R), glycine (G), aspartate (D)) which can be found in the ECM proteins such as fibronectin, vitronectin and fibrinogen. Integrins are diffusely distributed in the plasma membrane as long as the cell is in suspension. The COOH-terminus of integrins is facing towards the cytoplasm while the N-terminus containing the active binding site is located extracellular. Integrins are heterodimers consisting of two domains, a single chain "α-subunit" and double chain "β-subunit". One of the most studied integrins is the αIIbβ3-integrin which has an 8 by 10 nm wide elliptical "head" with two 15 – 17 nm long and 2 – 3 nm wide tails separated by 4 – 6 nm. The full length of an integrin is about 21 – 25 nm [Carrel 1985, Rivas 1991]. Another integrin, αVβ1 (also called "fibronectin receptor"), obtains a full length of 28 nm with a globular head of 8 by 12 nm and two tails with a length of 18-20 nm and a width of about 2 nm [Nermuth 1988]. Inactivated integrins are present in a folded state with a low affinity to their ligand. Upon intra- or extracellular activation, e.g. magnesium or calcium ions (Mg^{2+} or Ca^{2+}), the chains unfold and elongate and affinity to ligands such as fibronectin increases.

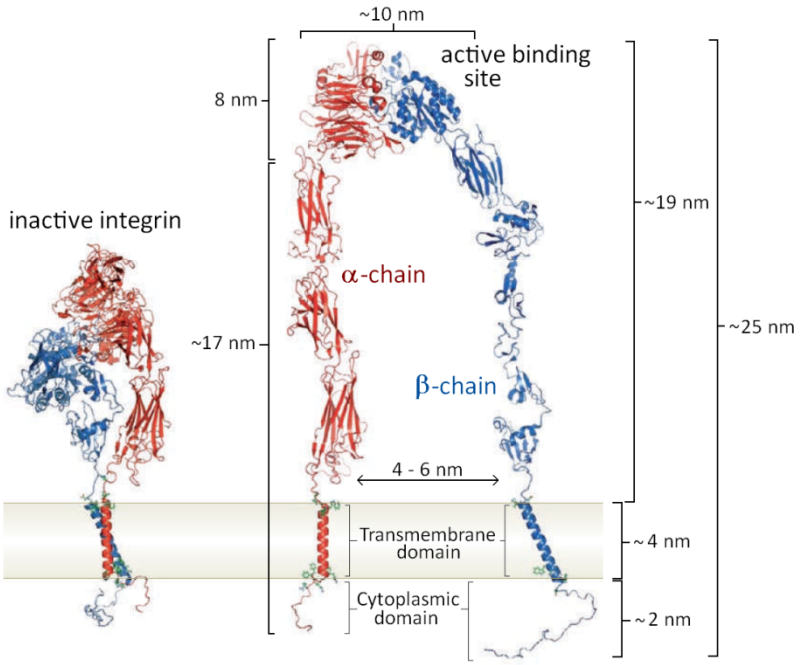

Figure 168: Typical structure of inactivated and activated integrins showing α-chain and β-chain and typical dimensions [adapted from Shattil 2010 with dimensions added based on Carrel 1985].

CELL ADHESION BY FORMATION OF FOCAL ADHESION COMPLEXES. Integrins located at the edge of lamellipodias bind to components of the extracellular matrix such as fibronectin, vitronectin, collagen, or laminin, attaching the cell to the underlying substrate, e.g. ECM. They are linked to the actin cytoskeleton and stabilized by binding of cytoplasmic proteins like talin. The adhesion of the integrin to actin fibers at that state is usually weak and allows to slip under small forces (pico-Newton range) applied to the integrin. However, the adhesion of integrins to actin fibers can be reinforced by assembling proteins like tensin and vinculin forming multi-protein complexes, so called "focal contacts". Focal contacts are formed within 0.001 s to 1 min and withstand forces in the upper pico-Newton range (5 – 170 pN) [Vogel 2006]. When the cell continues moving forward, the focal contacts are dissolved, allowing the cell to detach from the surface and re-attach at another point.

However, initiated by applied shear forces focal contact can undergo a second transition towards more stable connection between cell and surface, into "focal adhesion sites" (Figure 169). Focal adhesions are formed by assembling additional cytoplasmic proteins such as paxillin or α-actinin creating stable complexes that can withstand forces in nano-Newton range. Tens of focal adhesion sites can cluster together with typical areas < 1μm^2 increasing the bonding strength at that specific location sufficiently [Nicolas 2006]. Shear force applying on integrins can originate from either the cell's own contractile apparatus or externally, e.g. through the substrates rigidity, or actively applied by mechanical manipulation such as micropipettes. Upon cells' detachment from the surface, integrin molecules are recycled into the cell by endocytosis, transported to the moving front of the cell and re-integrated into the membrane [Owen 2005, Besser 2006, Vogel 2006, CML 2011]. Kanchanawong et al. have for the first time measure the actual position of the various proteins assembled to focal adhesion site (Figure 169) by interferometric fluorescent super-resolution

microscopy [Shtengel 2009]. They showed that integrins are located in the first 30 nm connecting the cell to the substrate). The inner plasma membrane is about 32 nm separated from the substrate.

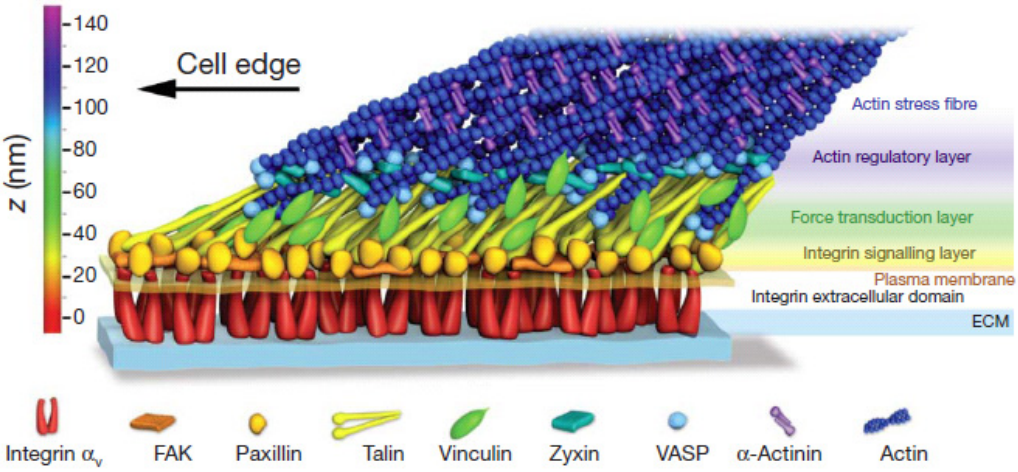

Figure 169: Schematic model of focal adhesion molecular architecture, depicting experimentally determined protein positions. Note that the model does not depict protein stoichiometry [Kanchanawong 2010].

Integrin Binding Sites. The distance between integrin binding sites plays a critical role in formation of focal adhesion sites and thereby cell adhesion and spreading. The research group around J.P. Spatz has shown that the spacing of adhesion sites for cells affect the strength of the cell adhesion, i.e. amount of formed focal adhesions [Cavalcanti-Adam 2007, Arnold 2004, Selhuber-Unkel 2010]. They investigated the reaction of MC3T3-osteoblasts and REF52 rat fibroblasts on gold dots of 8 nm in diameter with spacing of28, 58, 73, 85, 103, and 108 nm. The dimensions of the gold dots allow only one integrin molecule to bind to adsorbed RGD-containing molecules and thereby allow for direct evaluation of the formation of focal adhesion sites dependent on the distance between integrin binding sites. MC3T3-osteoblast exhibit strongly reduced adhesion to gold dots arrays with spacing of 73 nm and above. They observed normal adhesion on substrates with 28 and 58 nm spacing between gold dots. They proposed that a spacing of 58 ± 73 nm can be considered as universal length scale for integrin clustering and activation, since these properties are shared by a variety of cultured cells (MC3T3-Osteoblasts, B16-Melanocytes, and 3T3-Fibroblasts) [Arnold 2008]. EF52 rat fibroblasts formed focal contacts only on gold dot arrays with spacing of 28, 50, and 58 nm. Cells exposed to larger integrin spacing (90 nm, 103 nm, and 108 nm) showed reduced adhesion with extended adhesion zones. They exhibit delayed spreading with repeated protrusion-retraction cycles, erratic and non-persistent cell motility. The density of integrin binding sites for flat, 28 and 58 nm spacing was calculated to be 40,000, 1473, and 461 molecules/μm^2, respectively. A maximum package density of focal contact points is reached on substrate with integrin spacing of 28 nm. They calculated a local detachment force of 9.4 nN/μm^2 for 28 nm and 5.9 nN/μm^2 for 58 nm spacing. These results indicate that a critical RGD density is essential for the establishment of mature and stable integrin adhesions, which induce formation of focal adhesions and efficient cell spreading [Cavalcanti-Adam 2007, Selhuber-Unkel 2010]. Patla et al. suggest that the formation of focal adhesion complexes is mediated through specific doughnut-shaped particles on the cell membrane with a diameter of 25 ± 5 nm and a spacing of about 45 nm [Patla 2010]. Although the theory of particle-mediated formation of focal adhesions is new, it complies well with findings from the results presented above.

2. Supplementary Material - Results

2.1. Laser Lithography

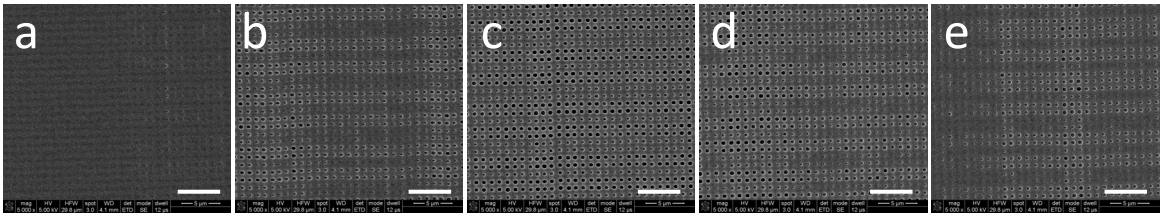

Figure 170: SEM images of intended 300 nm wide holes written into positive resist S1805 at varying defocus for a constant dose of 30 %. Defocus values of 100 (a), 200 (b), 300 (c), 400 (d), 500 (e). Scale bars: 5 µm.

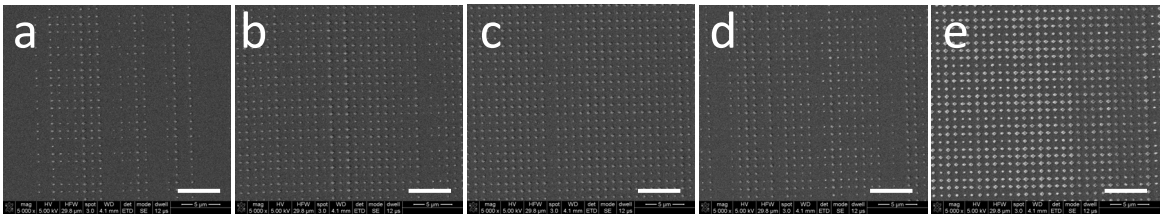

Figure 171: SEM images of intended 500 nm wide holes written into positive resist S1805 at varying defocus for a constant dose of 70 %. Over-exposure led to rhomb-shaped pillars. Defocus values of 100 (a), 200 (b), 300 (c), 400 (d), 500 (e). Scale bars: 5 µm.

2.2. Electron Beam Lithography in ZEP520

2.2.1. Dosetest for 50 and 100 nm wide Holes in ZEP520A

EXPOSURE OF 50 NM HOLES.

Table 20: Diameter of 50 nm holes written into ZEP520A resist of different thicknesses

Dose \ Resist thickness	105 nm	196 nm	258 nm
210 µC/cm^2	36 ± 2 nm	37 ± 5 nm	36 ± 2 nm
230 µC/cm^2	39 ± 2 nm	41 ± 4 nm	40 ±5 nm
250 µC/cm^2	43 ± 3 nm	40 ± 2 nm	40 ±4 nm
270 µC/cm^2	42 ± 4 nm	39 ± 5 nm	38 ±6 nm
290 µC/cm^2	46 ± 1 nm	43 ± 2 nm	43 ± 2 nm

Following SEM images exemplify the difference of effect of proximity effect causing higher doses in the pattern centers compared to the corners.

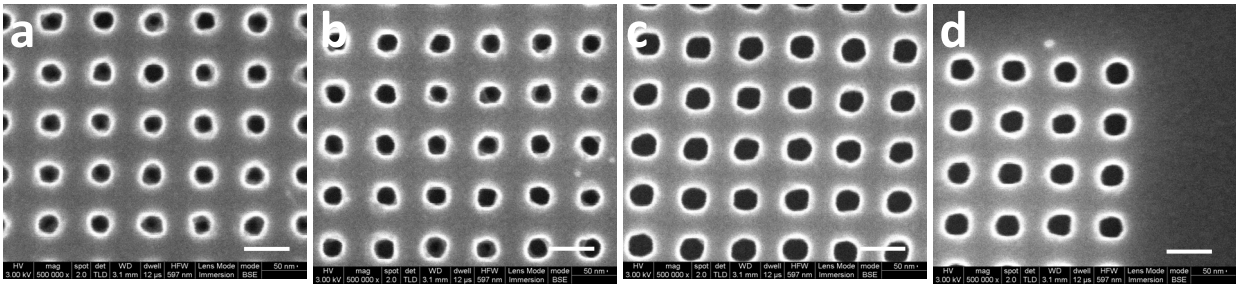

Figure 172: SEM images of 50 nm wide holes located in the center (a, c) and corner (b, d) for a pattern dose of 210 µC/cm^2 (a, b) and 290 µC/cm^2 (c, d) with a frame dose of 50 µC/cm^2. Scale bars: 100 nm.

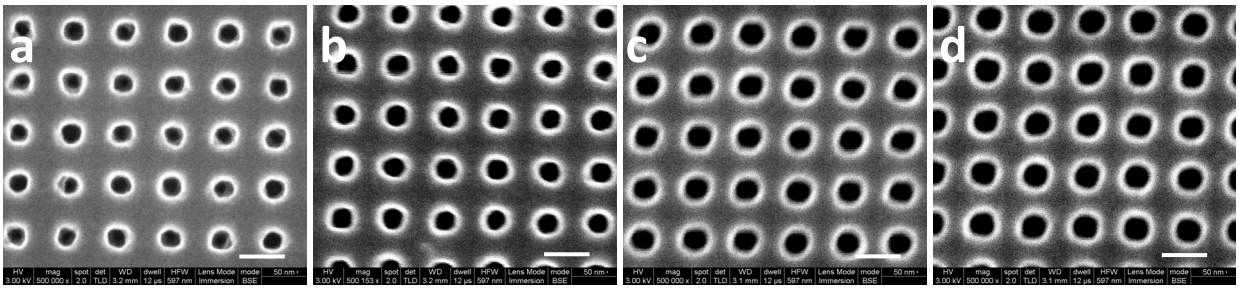

Figure 173: SEM images of 50 nm wide holes located in the center (a, c) and corner (b, d) for a pattern dose of 210 µC/cm^2 (a, b) and 290 µC/cm^2 (c, d) with a frame dose of 70 µC/cm^2. Scale bars: 100 nm.

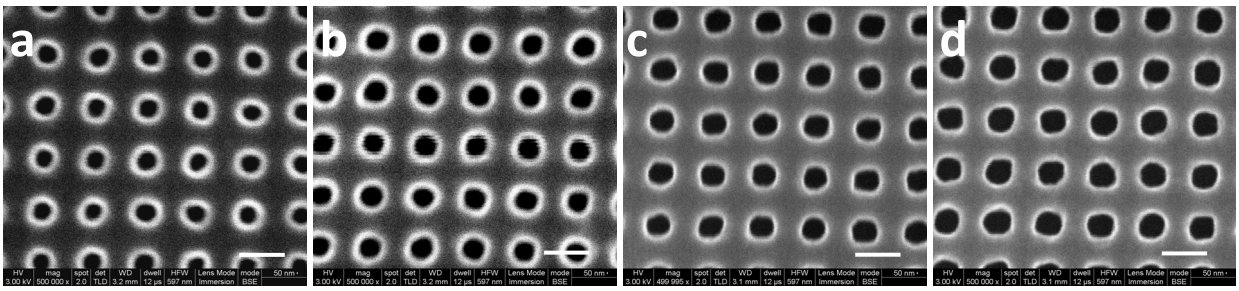

Figure 174: SEM images of 50 nm wide holes located in the center (a, c) and corner (b, d) for a pattern dose of 210 µC/cm^2 (a, b) and 290 µC/cm^2 (c, d) with a frame dose of 90 µC/cm^2. Scale bars: 100 nm.

ELECTROPLATING OF 100 NM HOLES.

Table 21: Average diameter of 100 nm pillars replicated into nickel for different resist thicknesses.

Dose \ Resist thickness	105 nm	196 nm	258 nm
210 µC/cm^2	105 ± 7 nm	111 ± 2 nm	111 ± 3 nm
230 µC/cm^2	108 ± 6 nm	112 ± 3 nm	114 ± 3 nm
250 µC/cm^2	109 ± 7 nm	108 ± 2 nm	112 ± 5 nm
270 µC/cm^2	107 ± 9 nm	106 ± 3 nm	112 ± 4 nm
290 µC/cm^2	112 ± 7 nm	102 ± 3 nm	108 ± 3 nm

Table 22: Average height of 100 nm pillars replicated into nickel for different resist thicknesses.

Dose \ Resist thickness	105 nm	196 nm	258 nm
50 µC/cm²	99 ± 2	146 ± 9	146 ± 9
70 µC/cm²	99 ± 5	154 ± 6	151 ± 8
90 µC/cm²	100 ± 2	155 ± 6	145 ± 11

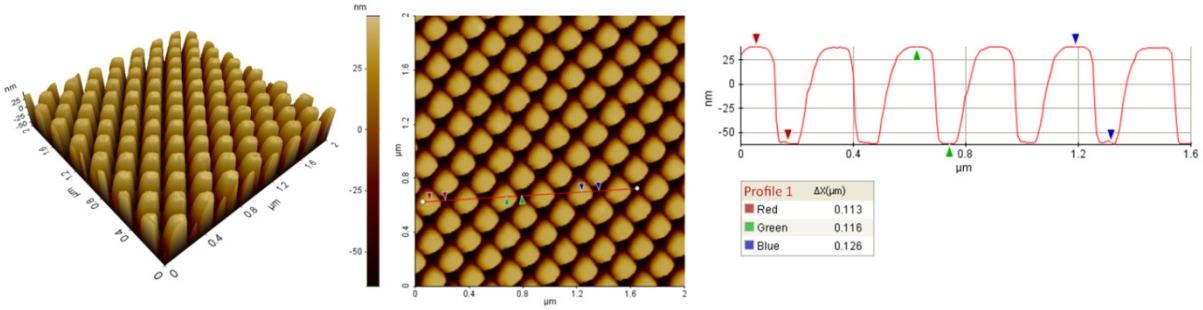

Figure 175: AFM image and line profiles for nickel pillars originally write into 105 nm resist (pattern dose: 210 µC/cm², frame dose: 70 µC/cm²), average width: 105 ± 7 nm, average height: 99 ± 5 nm.

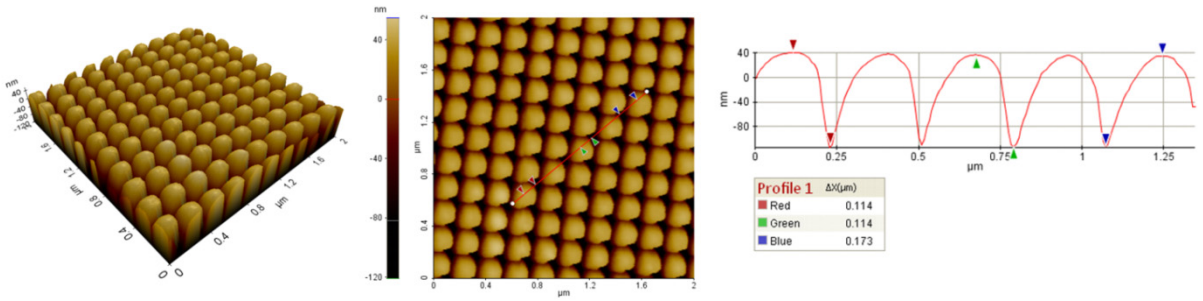

Figure 176: AFM image for nickel pillars write into 196 nm resist (pattern dose: 210 µC/cm², frame dose: 70 µC/cm²), average width: 111 ± 2nm, average height: 154 ± 6 nm .

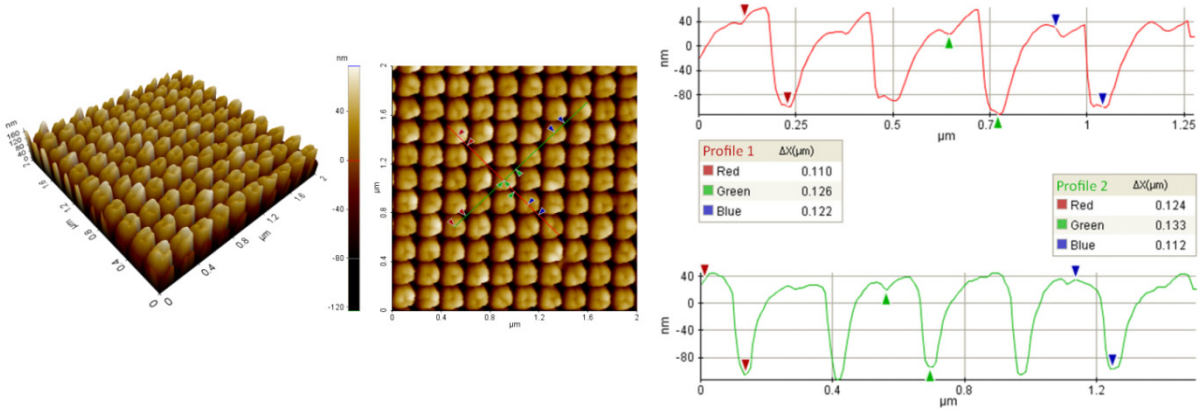

Figure 177: AFM image and line profiles for nickel pillars originally write into 258 nm resist (pattern dose: 210 µC/cm², frame dose: 70 µC/cm²), average width: 111 ± 3 nm, average height: 151 ± 8 nm.

2.2.2. Dosetest for 50 and 100 nm wide Pillars in ZEP520A[96]

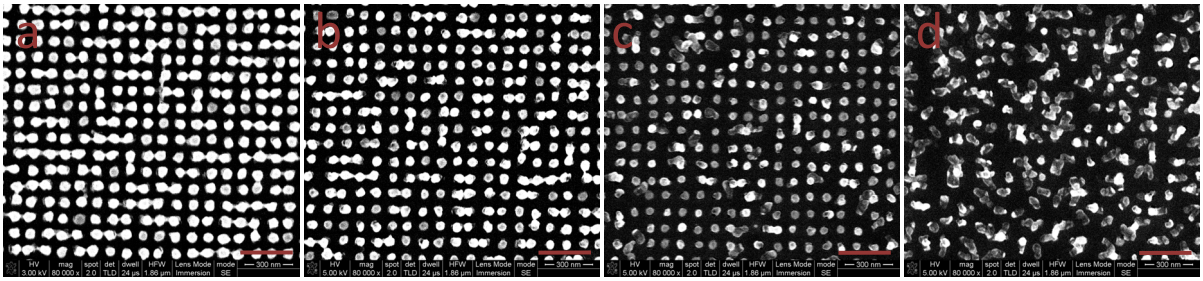

Figure 178: SEM of 50 nm wide pillars exposed in 100 nm resist at different doses: 180 µC/cm2 (a), 200 µC/cm2 (b), 220 µC/cm2 (c), 260 µC/cm2 (d). Scale bars: 300 nm.

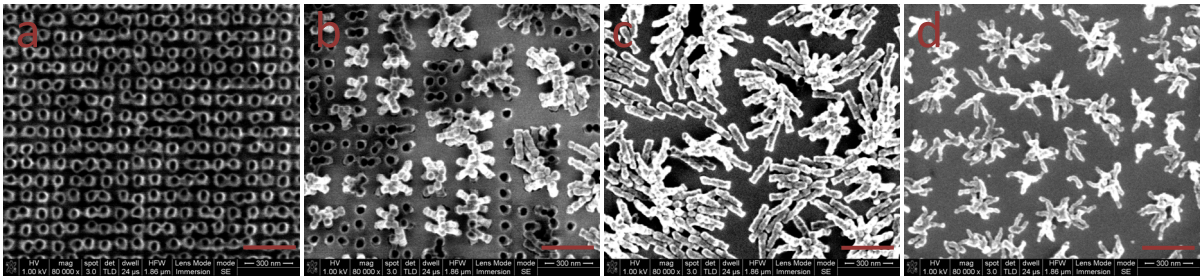

Figure 179: SEM of 50 nm wide pillars exposed in 200 nm resist at different doses: 180 µC/cm2 (a), 200 µC/cm2 (b), 220 µC/cm2 (c), 260 µC/cm2 (d).

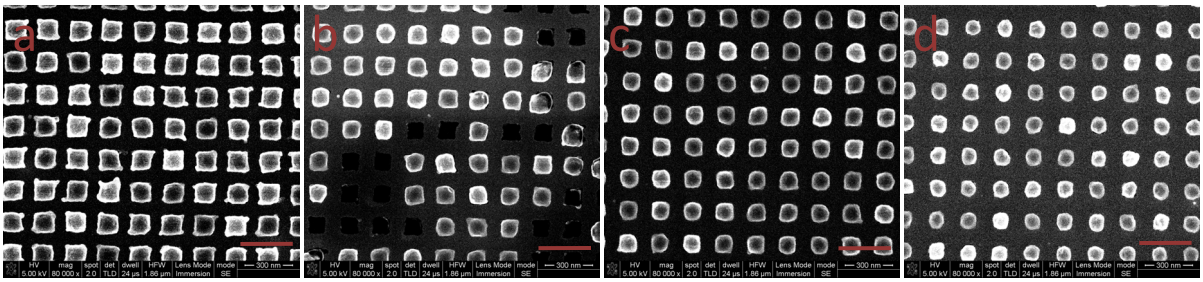

Figure 180: SEM of 100 nm wide pillars exposed in 100 nm resist at different doses: 180 µC/cm2 (a), 220 µC/cm2 (b), 240 µC/cm2 (c), 260 µC/cm2 (d).

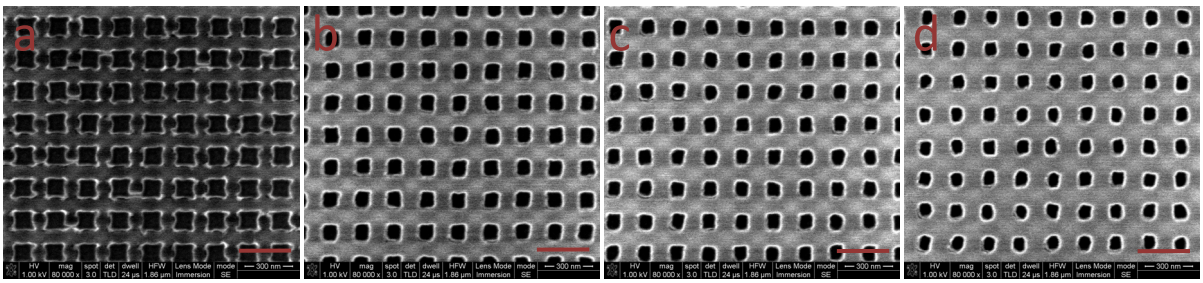

Figure 181: SEM of 100 nm wide pillars exposed in 100 nm resist at different doses: 180 µC/cm2 (a), 220 µC/cm2 (b), 240 µC/cm2 (c), 260 µC/cm2 (d).

[96] Figure numbers and scale bars are partially high lightened in red due to better visibility.

Following SEM images exemplify the difference of effect of proximity effect causing higher doses in the pattern centers compared to the corners.

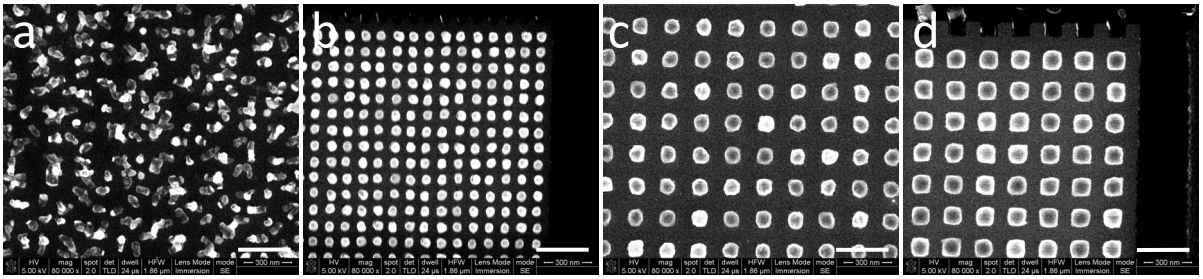

Figure 182: SEM images of 50 nm wide pillars exposed at 240 µC/cm^2 (center (a), corner (b)), and 100 nm wide pillars exposed at 260 µC/cm^2 (center (c), corner (d)) written into 100 nm thick ZEP520.

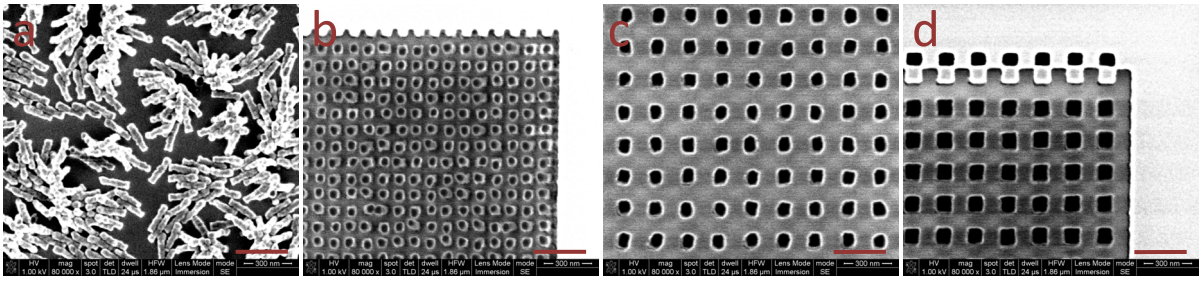

Figure 183: SEM images of 50 nm wide pillars exposed at 220 µC/cm^2 (center (a), corner (b)), and 100 nm wide pillars exposed at 260 µC/cm^2 (center (c), corner (d)) written into 200 nm thick ZEP520.

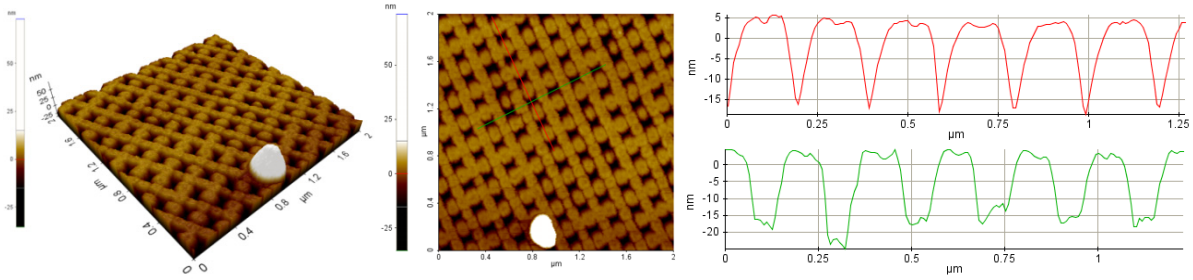

Figure 184: AFM image of holes located in the corner replicated from pillars of 100 nm intended width resulting in a depth of 17 ± 4 nm (resist thickness: 200 nm, dose: 260 µC/cm^2).

2.3. Nickel Shims

The shim ID represents the rounded height or depth of structures followed by the rounded width and an abbreviation related to the structure (“h” for holes”, “p” for pillars).

2.3.1. 60 and 120 nm Hole Pattern (ID: 100nm60h120h)

Nanoholes of intended width of 50 and 100 nm were exposed into 105 nm thick resist. Uniform pattern of 59 ± 3 and 124 ± 3 nm wide and 100 nm high pillars were replicated into nickel (Figure 185). Both patterns were widely over-exposed though the design contained smaller structures (45 and 90 nm) and the exposure dose should lead to maximal 50 and 100 nm wide pillars. The height was not measured but is expected to be of the same dimensions as the resist thickness.

During removal of the protection layer from this shim a metal film of about 82 nm thickness delaminated partially from the mold surface (Figure 186). This metal film is most probably the initial sputtered nickel-vanadium alloy. DVD Norden applies either a lacquer or blue tape on the electroplated nickel shims to protect the mold surface from particle contamination which could interfere with the injection molding process. Apparently the adhesion between sputtered and electroplated nickel can be poor so that the sputtered layer delaminates easily. DVD Norden changed most probable settings in the electroplating process, for example increasing the current to speed up the electroplating process. An increase in current causes also increase of inherent stress in the electroplated nickel. This stress could probably be the reason for the worse adhesion of nickel-vanadium to electroplated nickel than previously experienced. Some macro-scale defects were mostly located outside the nanopatterned area.

Table 23: Process Parameters for 50 and 100 nm holes (exposed on 04/11/2008)

Resist Thickness	105 nm
Current	0.6 nA
Dose	240
Frame Dose	40
Original Design	45nm holes (pitch: 100 nm) 90 nm holes (pitch: 200 nm)

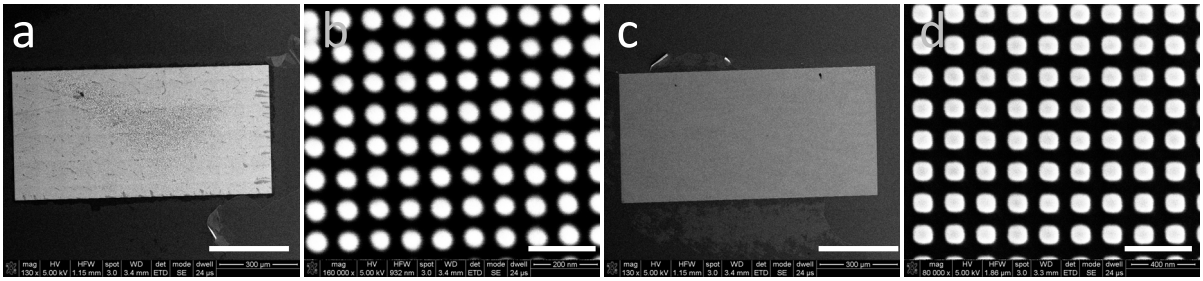

Figure 185: SEM images of 59 ± 3 nm wide and 124 ± 3 nm wide pillars replicated into nickel. Scale bars: 300 µm (a, c) and 400 nm (b, d).

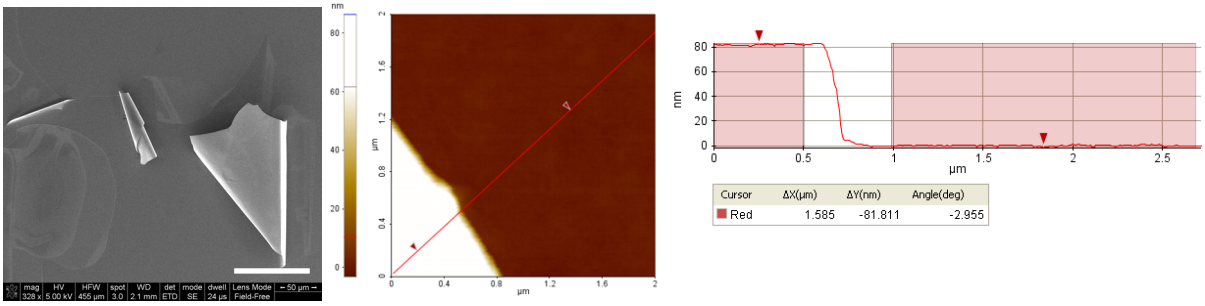

Figure 186: SEM and AFM image of NiV layer delaminated during separation of protection foil (e.g. blue tape) from the nickel mold. Scale bar (SEM image): 100 µm.

2.3.2. 60 and 120 nm Hole Pattern (ID: 55nm60h120h)

Table 24: Process Parameters for 50 and 100 nm holes (exposed on 04/11/2008)

Resist Thickness	58 nm
Current	0.6 nA
Dose	200
Frame Dose	80
Original Design	45nm holes (pitch: 100 nm) 90 nm holes (pitch: 200 nm)

Nanoholes of intended width of 50 and 100 nm were exposed into 58 nm thick resist. Uniform pattern of 59 ± 3 nm wide and 42 ± 2 nm high as well as 124 ± 3 nm wide and 54 ± 2 nm high pillars were replicated into nickel (Figure 185). It is to note that the bottom of 60 nm wide pillars was most likely not resolve due to limited resolution of the AFM. The pillars height of 60 and 120 nm is therefore assumed to be uniform 50 ± 2 nm. Both patterns were widely over-exposed though the design contained smaller structures (45 and 90 nm) and the exposure dose should lead to maximal 50 and 100 nm wide pillars. The height difference of about 8 nm could be caused by underexposure in vertical direction though not very likely as explained previously.

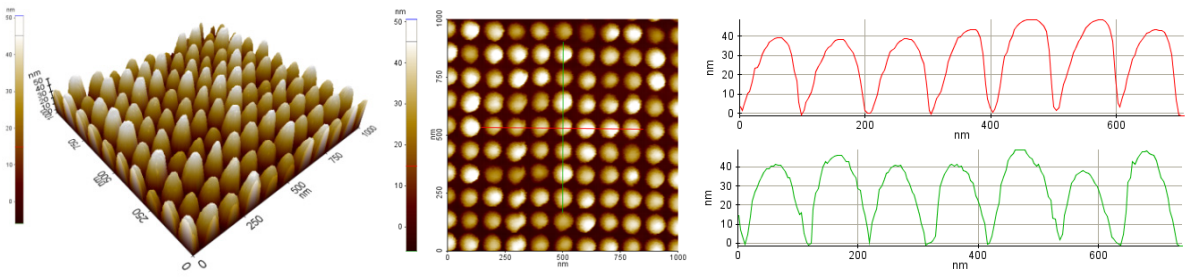

Figure 187: AFM image of 59 ± 3 nm wide and 42 ± 2 nm high pillars replicated into nickel.

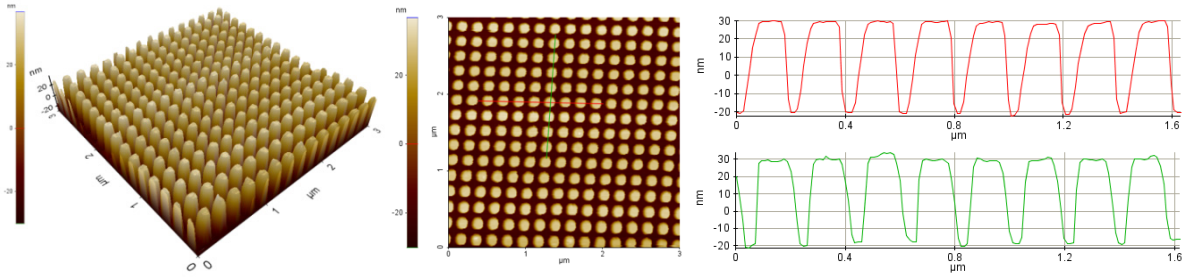

Figure 188: AFM image of 124 ± 3 nm wide and 54 ± 2 nm high pillars replicated into nickel.

2.3.3. 110 nm Hole Pattern (ID: 115nm110h)

Since previously exposed pattern of 100 nm hole array lead to an extensive over-exposure the dose was reduced to 180 µC/cm^2. A very uniform pattern of 107 ± 4 nm wide and 116 ± 4 nm high pillars replicated in nickel was produced. No macro-scaled defects were observed on the patterned area (Figure 189).

Table 25: Process Parameters for 50 and 100 nm holes (exposed on 30/06/2009)

Resist Thickness (nm)	120 nm
Current (nA)	0.6 nA
Dose (µC/cm^2)	180
Frame Dose (µC/cm^2)	80
Original Design	90 nm holes (pitch: 200 nm)

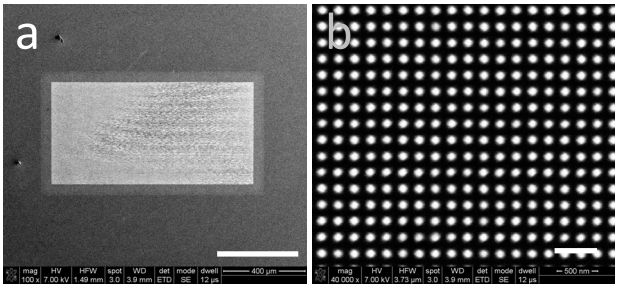

Figure 189: SEM images of 107 ± 4 nm wide and 116 ± 4 nm high pillars replicated in nickel. Scale bars: 400 µm (a) and 500 nm (b).

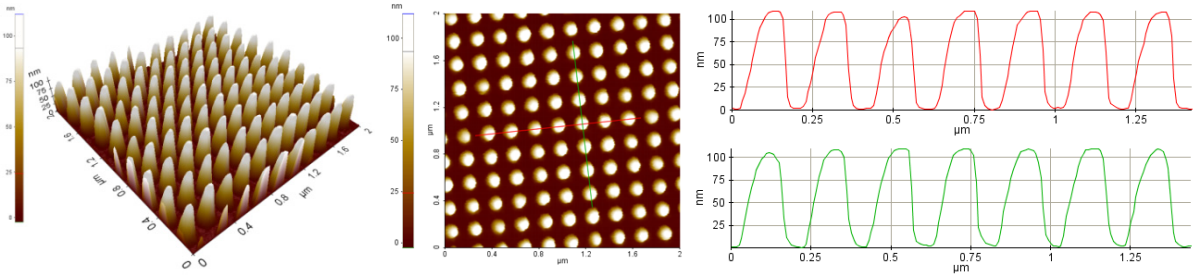

Figure 190: AFM images of 107 ± 4 nm wide and 116 ± 4 nm high pillars in nickel.

2.3.4. 40 nm Pillar and 110 nm Hole Pattern (ID: 110nm40p110h)

To reduce writing time the current was increased expecting only negligible broadening of structures (< 5 nm from intended with) compared to lower current. Microstructures, i.e. five alignment marks and labels to identify nanostructured patterns were included to improve orientation and visibility of nanostructured patterns.

All patterns, but especially patterns A and B containing pillars were widely over-exposed, most probably caused by the increased current. The electroplating resulted in a nickel mold containing 33 ± 4 nm holes (pattern A), 33 ± 3 nm holes (pattern B), and 109 ± 2 nm wide and 109 ± 2 nm high pillars. It is to note that for the determination of pillars width only perfectly round holes replicated from standing pillars were measured. Tilted pillars leading to elongated holes were left-out since they would adulterate the actual pillar width. Pillars in the center of pattern A and B were partially collapsed (Figure 191). Both patterns display very homogenous arrays of 40 – 43 nm wide holes in the corner of each pattern (Figure 192). Since several holes in the center of pattern A and B were tilted and thereby resulted in deformed holes (Figure 191), only the corner areas were investigated during injection molding experiments. The depth of 33 nm wide holes (or 40 – 43 nm in the corner) was measured to a maximum of 10 nm. From injection molding experiments resulting in pillars of up to 100 nm it is assumed that the pillars in ZEP520were fully exposed and replicated into nickel with high fidelity. The removal of the protection layer, i.e. blue tape caused again delamination of a large area of the nickel-vanadium layer though nanostructured patterns remained intact (Figure 194). Furthermore, small amounts of silicon fractured and remained on the nickel mold in the alignment mark located in the center and in the labels of the nanostructured areas.

Table 26: Process Parameters for 100 nm wide pillars and holes (exposed on 27/10/2009)

Resist Thickness (nm)	110 nm
Current (nA)	3.8 nA
Dose (µC/cm^2)	200
Frame Dose (µC/cm^2)	80
Original Design	Pattern A[97]: 100 nm pillars (pitch: 400 nm), Pattern B: 100 nm pillars (pitch: 200 nm), Pattern C: 90 nm holes (pitch: 200 nm)

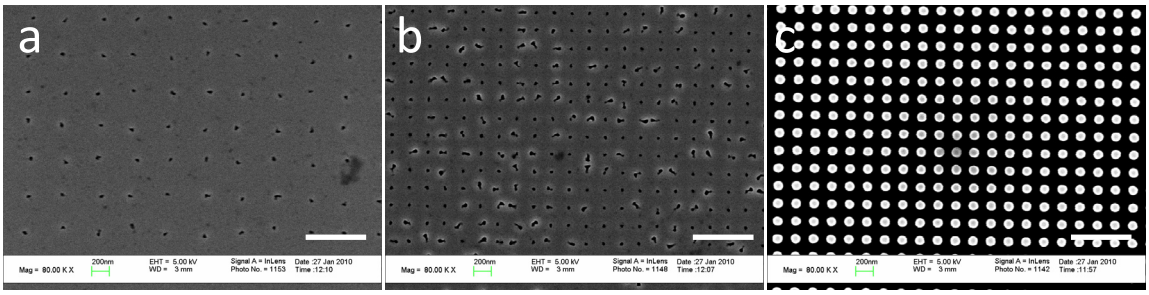

Figure 191: SEM images of structures in the pattern center: 33 ± 4 nm holes (pitch: 400 nm), 33 ± 3 nm holes (pitch: 200 nm) and 129 ± 2 nm pillars (pitch: 200 nm) replicated in nickel. Scale bars: 600 nm.

[97] Pattern A was not analyzed during for investigation of injection molding conditions, but were used for cell experiments.

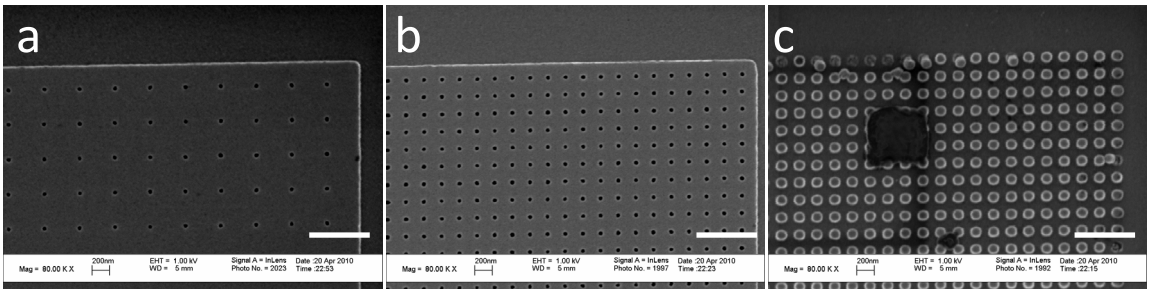

Figure 192: SEM images of structures in the pattern corner: 43 ± 5 nm holes (pitch: 400 nm), 40 ± 3 nm holes (pitch: 200 nm) and 109 ± 2 nm pillars (pitch: 200 nm) replicated in nickel. SEM images taken after injection molding experiments. Scale bars: 600 nm.

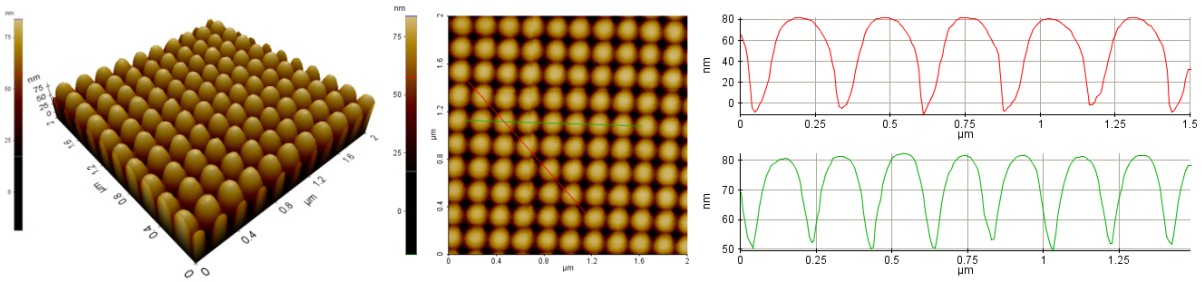

Figure 193: AFM image of 109 ± 2 nm wide and 100 ± 2 nm high pillars in nickel.

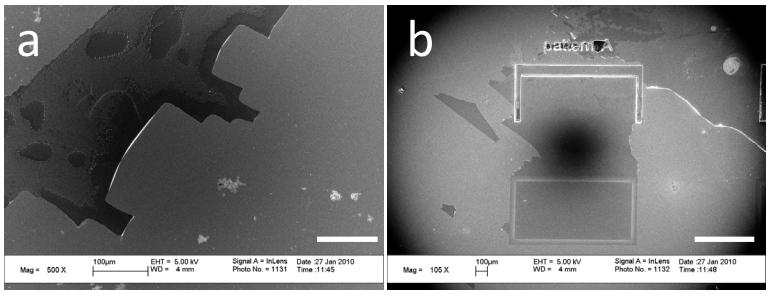

Figure 194: SEM images of defects visible after electroplating of nickel. Scale bars: 100 µm (a) and 400 µm (b).

2.3.5. 250 and 500 nm Hole Pattern (ID: 250nm350h600h)

Structures were exposed into 100 nm thick resist and subsequently etched (*fpe_nano*) into silicon. Prior to electroplating samples were coated with FDTS aiming to improve separation of silicon and nickel.

Exposure of ZEP520 and subsequent etching into silicon resulted in a uniform pattern of 343 ± 9 nm and 595 ± 5 nm [98] wide holes. Structure were etched for 260 s to achieve an etch depth of about 250 nm. The structures showed an average depth of 256 ± 9 nm. The silicon master was separated from nickel mold without fracturing the silicon. Nickel pillars partially fractured and broke off, and even remained fully integrated in the nanoholes of the silicon mold. Together with the actual pillar about

[98] Values were determined by applying a cursor pair on a line profile and measuring from intensity peak center to peak center. Commonly widths were determined at full width at half maximum intensity. The values obtained for e.g. intended 500 nm wide structures in silicon (520 ± 8 nm) differed widely (> 50 nm) from values measured for nickel (573 ±15 nm) if measured at full width at half maximum intensity.

150 – 200 nm additional material break off from the nickel bulk (Figure 196a). In other areas the nickel-vanadium layer seemed to be delaminated from the shim adhering to the silicon holes (Figure 196b). The nickel shim contained 349 ± 8 and 591 ± 10 nm wide and 249 ± 6 nm high pillars. Height differences were most probably caused by nickel residuals, i.e. “frame” on the silicon holes and unknown contaminations, i.e. “blob” on top of the nickel pillars. Many of the contamination were removed by oxygen plasma.

The FDTS improved the separation of silicon mold and nickel replica though single nickel pillars fractured. Either the coverage of the antistiction coating was insufficient or FDTS is not applicable for electroplating purpose.

Table 27: Process Parameters for 50 and 100 nm holes (exposed on 04/11/2008)

Resist Thickness (nm)	100 nm
Current (nA)	0.6 nA
Dose (µC/cm^2)	240
Frame Dose (µC/cm^2)	40
Original Design	250 nm holes (pitch 500 nm) 500 nm holes (pitch: 1000 nm)

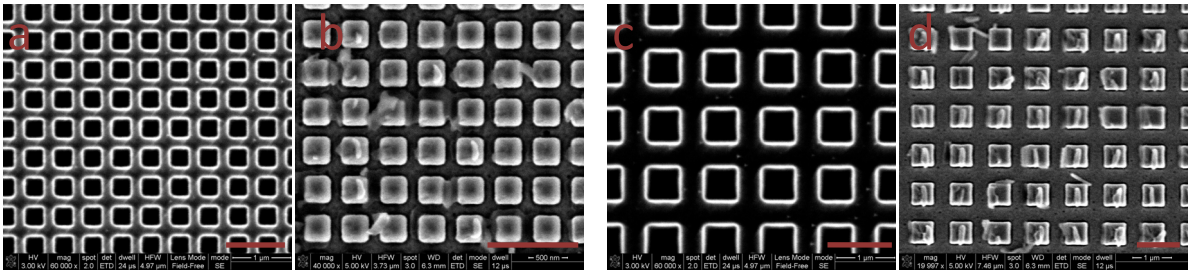

Figure 195: SEM images of about 250 nm (a, b) and 500 nm (c, d) hole pattern etched into silicon (master) (a, c) and replicated into nickel (mold) (b, d). Scale bars: 1 µm.

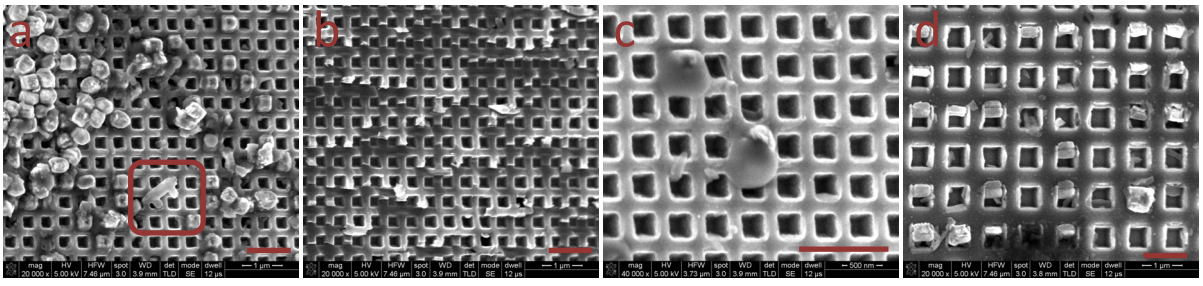

Figure 196: SEM images of 250 nm (a, b) and 500 nm (c, d) hole pattern etched into silicon after separation from nickel mold. Nickel pillars broke partially off the mold and partially remained on the silicon master. Scale bars: 1 µm.

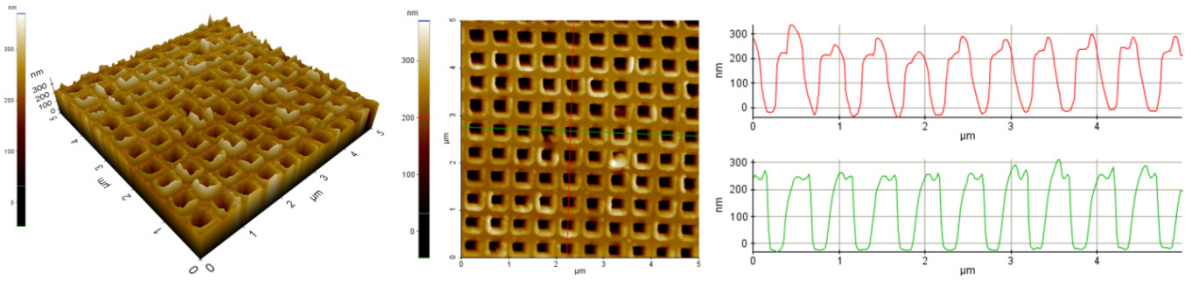

Figure 197: AFM images of 250 nm holes in silicon <u>after</u> separation from the electroplated nickel mold.

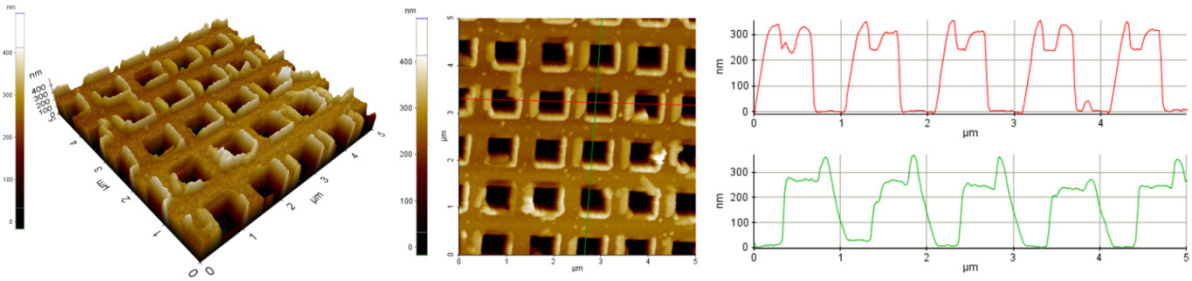

Figure 198: AFM images of 500 nm holes in silicon <u>after</u> separation from the electroplated nickel mold.

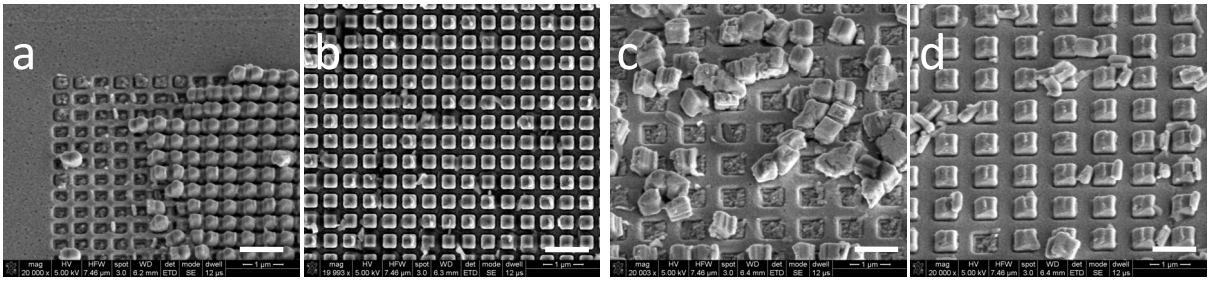

Figure 199: SEM images of 250 and 500 nm pillar pattern in nickel *after* separation from silicon master (before cleaning with oxygen plasma) visualizing various defects in the mold. Scale bars: 1 µm.

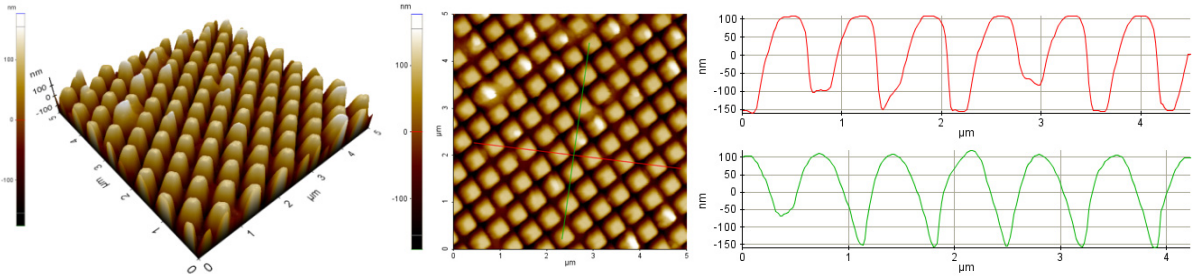

Figure 200: AFM images of 349 ± 8 wide and 249 ± 6 nm high pillars in nickel after cleaning with oxygen plasma.

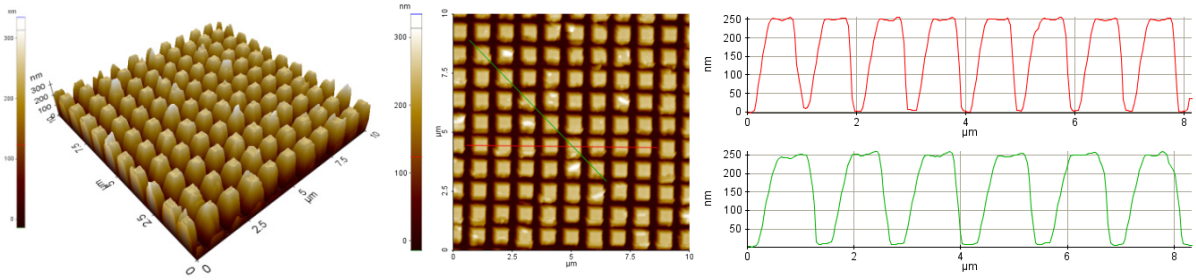

Figure 201: AFM images of 591 ± 10 nm wide and 249 ± 6 nm nm high pillars in nickel after cleaning with oxygen plasma.

2.4. Thermal Bonding

2.4.1. Topas 5013

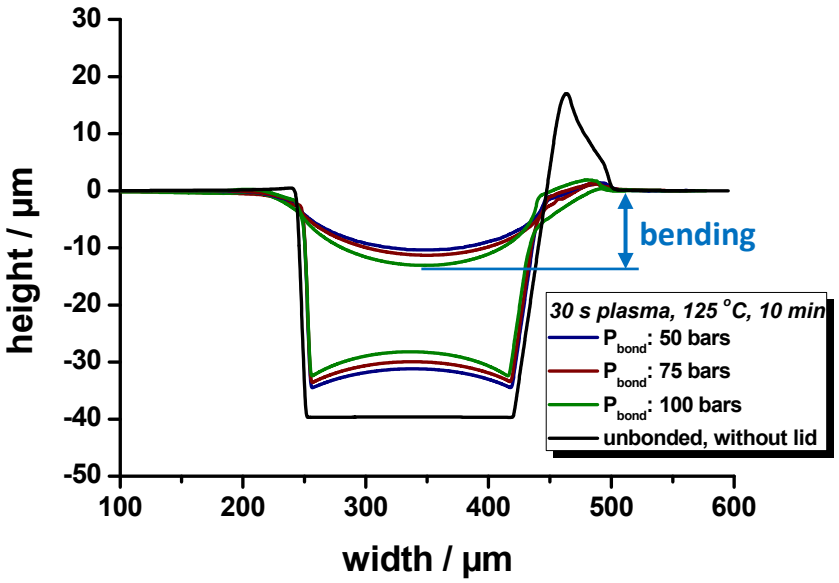

Figure 202: Cross-sectional profiles of microchannels (bottom) and nanostructures (lid) in Topas 5013 bonded with different bonding pressures. The blue arrow indicates the extent of bending at P_{bond} = 100 bars.

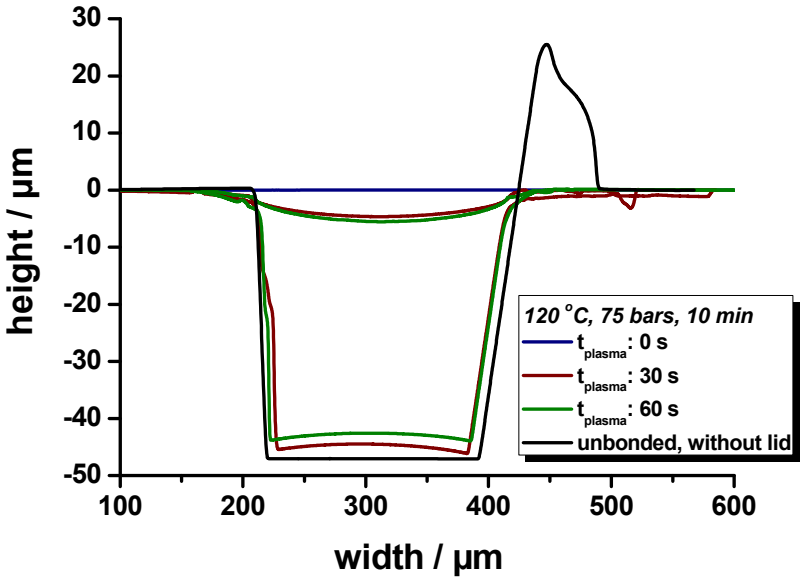

Figure 203: Cross-sectional profiles of microchannels (bottom) and nanostructures (lid) in Topas 5013 bonded with different pre-treatments.

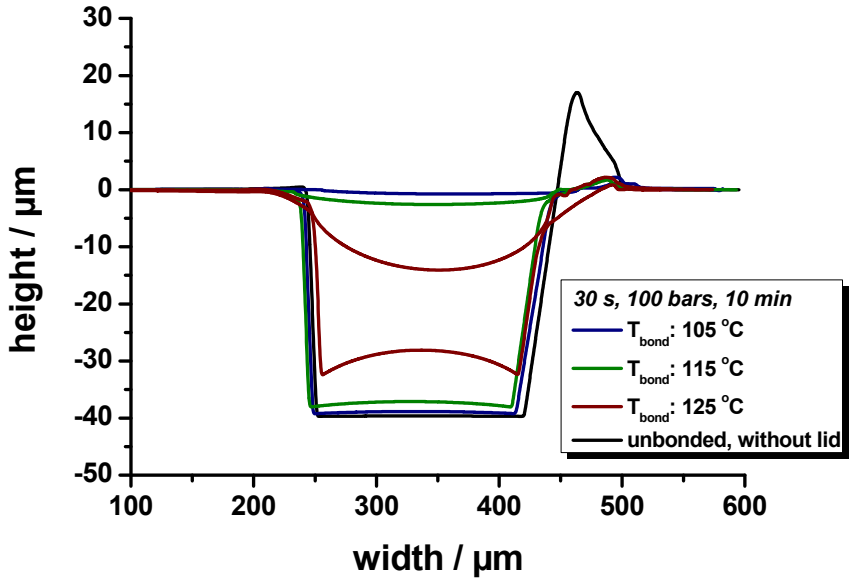

Figure 204: Cross-sectional profiles of microchannels (bottom) and nanostructures (lid) in Topas 5013 bonded with different bonding temperatures without plasma treatment.

2.4.2. Topas 8007

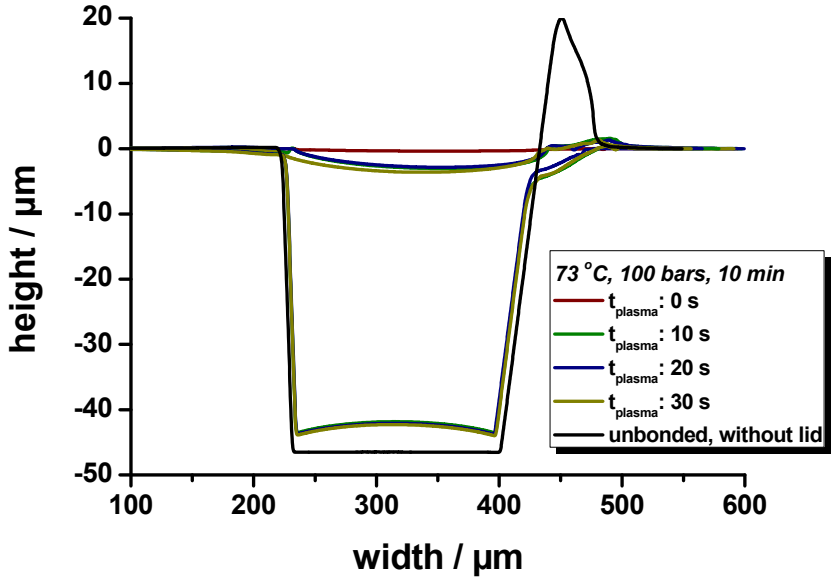

Figure 205: Cross-sectional profiles of microchannels (bottom) and nanostructures (lid) in Topas 8007 bonded with different pre-treatments.

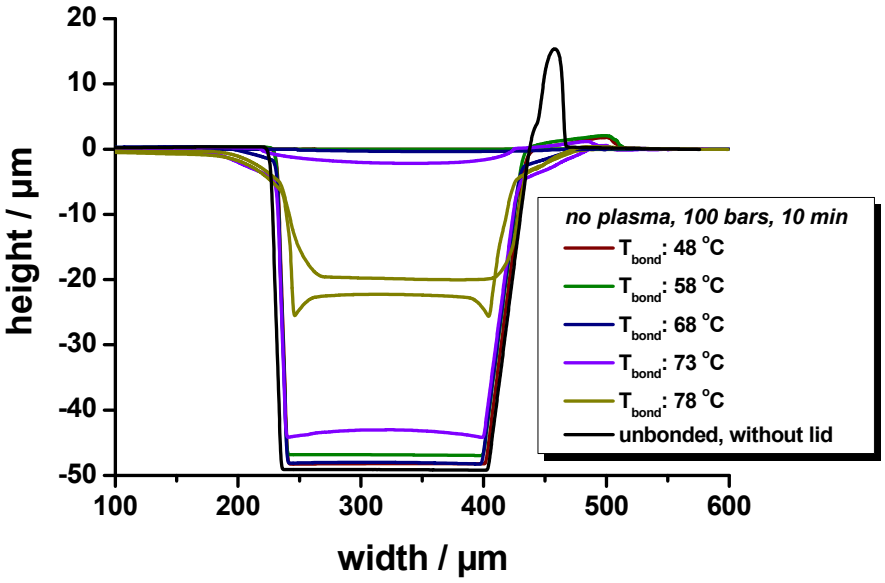

Figure 206: Cross-sectional profiles of microchannels (bottom) and nanostructures (lid) in Topas 8007 bonded with different bonding temperatures without plasma treatment.

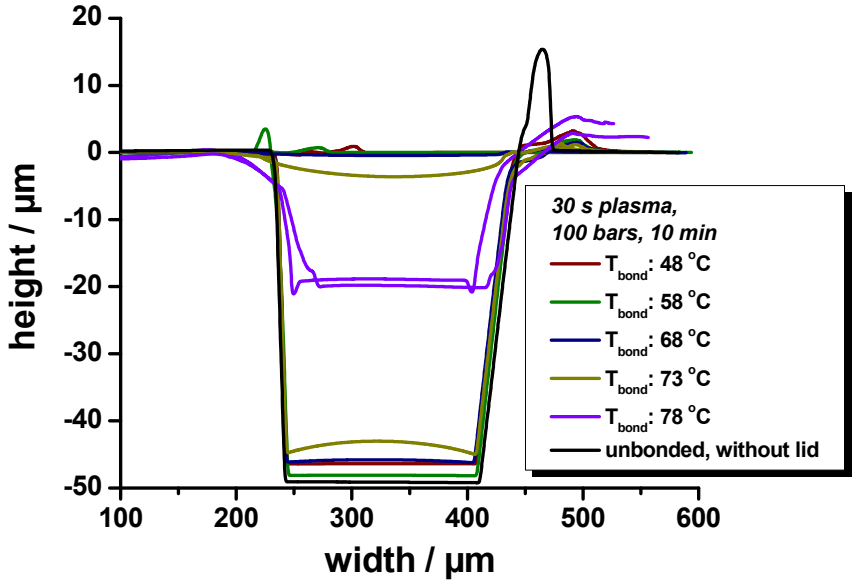

Figure 207: Cross-sectional profiles of microchannels (bottom) and nanostructures (lid) in Topas 8007 bonded with different bonding temperatures with 30 s plasma treatment.

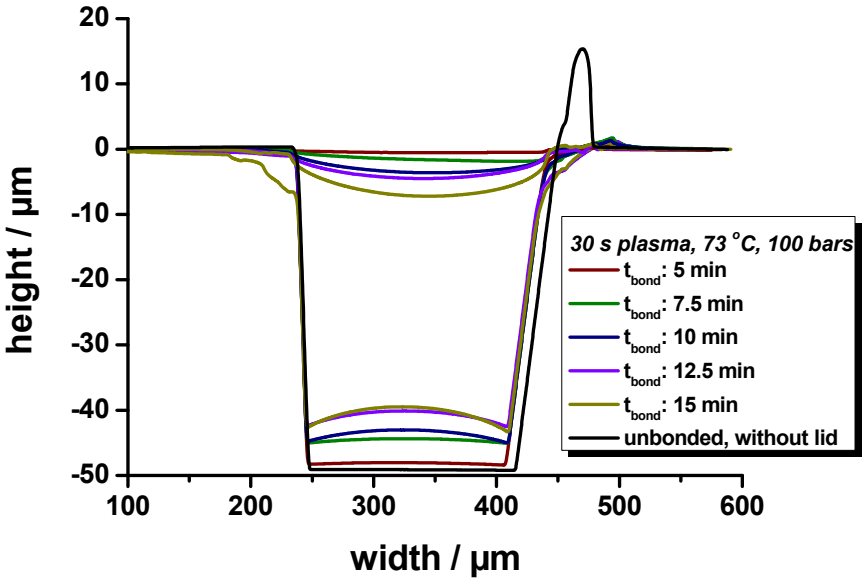

Figure 208: Cross-sectional profiles of microchannels (bottom) and nanostructures (lid) in Topas 8007 bonded with different bonding times.

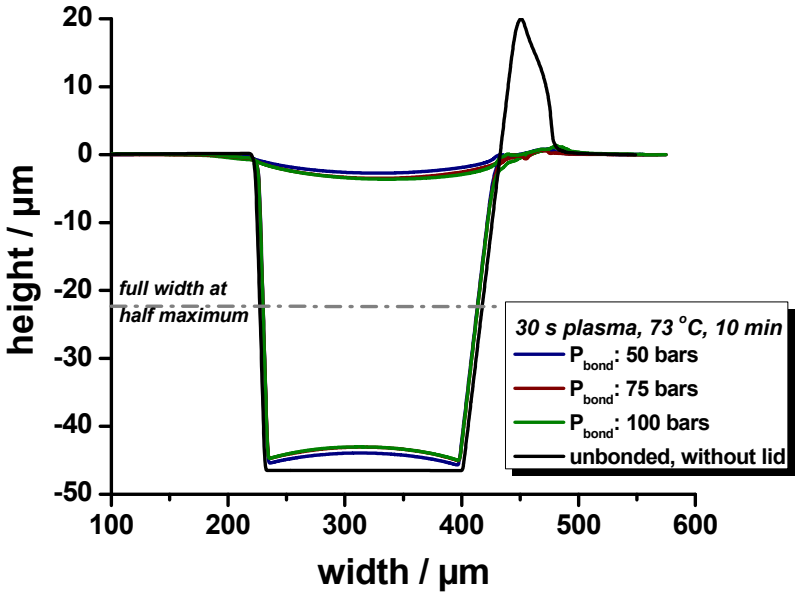

Figure 209: Cross-sectional profiles of microchannels (bottom) and nanostructures (lid) in Topas 8007 bonded with different bonding pressures.

2.5. Cell Experiments

2.5.1. Cell Culturing Experiments with Single Chips

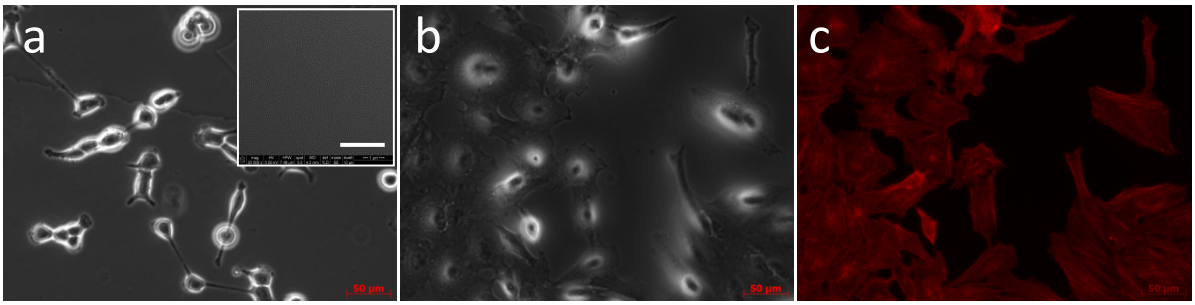

Figure 210: Phase contrast images of HeLa cells on untreated (a) and air plasma treated (b), unstructured Topas 8007 and the complying fluorescence image (c) of the air plasma treated, unstructured surface. Scale bars: 50 µm. Inset: SEM images of the surface structure, scale bar: 500 nm.

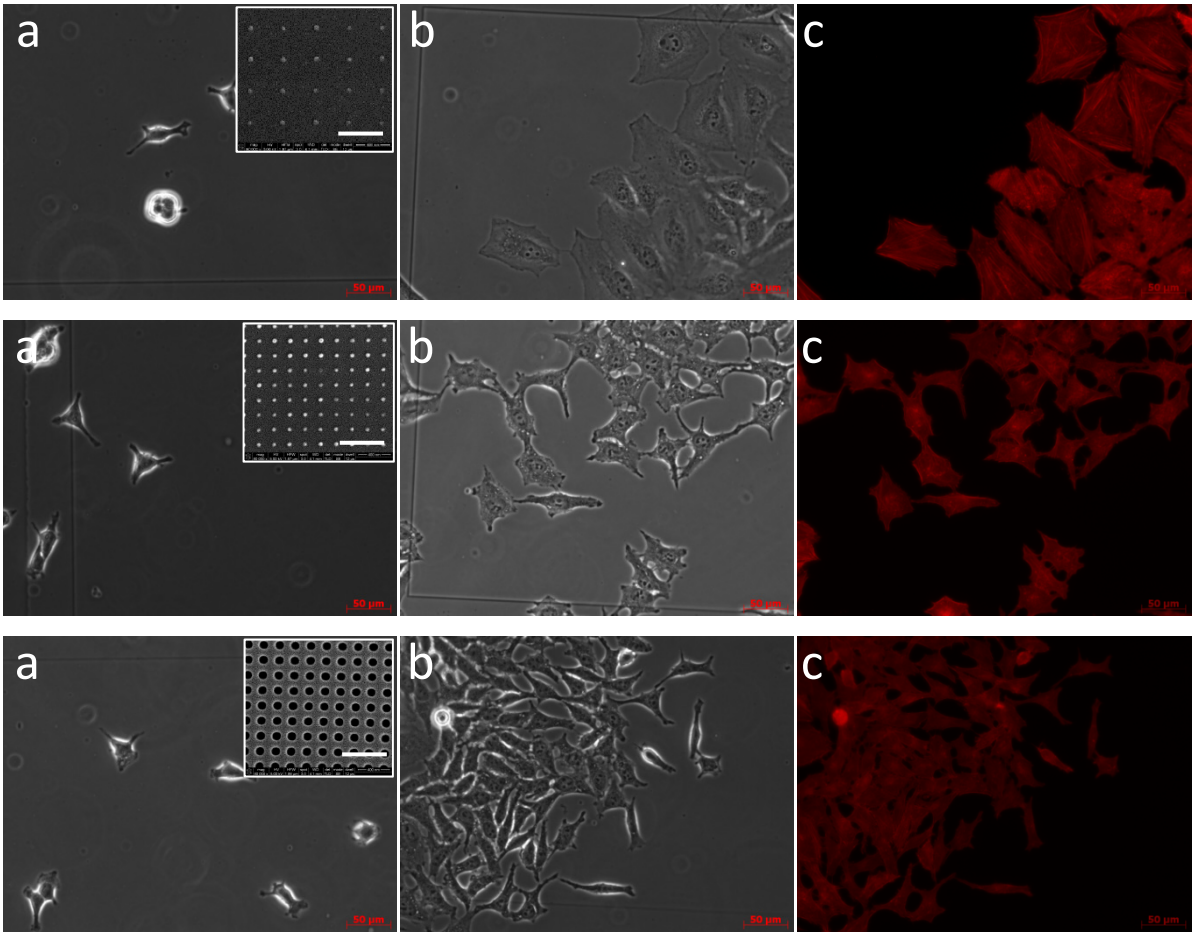

Figure 211: Phase contrast images of HeLa cells on untreated (a, d, g) and air plasma treated (b, e, h), unstructured Topas 8007 and the complying fluorescence image (c, f, i) of the air plasma treated, unstructured surface. Scale bars: 50 µm. Inset: SEM images of the surface structure, scale bar: 500 nm.

2.5.2. Cell Adhesion Experiments with Bonded Chips

Phase contrast images of NiH3T3 in a bonded microfluidic chip containing 600 nm wide and 250 nm deep holes taken during an adhesion experiments. A pump rate of 50 µl min^{-1} increasing in steps of 50 µl min^{-1} was applied.

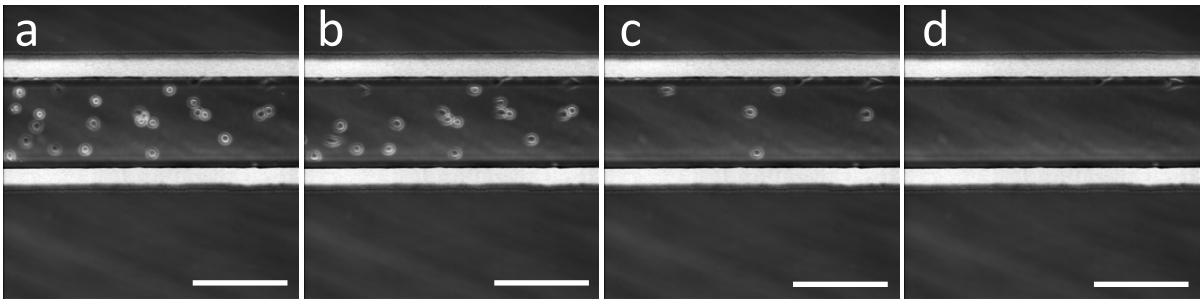

Figure 212: Phase contrast images of 3T3NiH cells on flat Topas 5013 (microfluidic system). The number of cells remaining on the flat bottom decreased with increasing pump rates (steps: 50 µl/min): 24 cells at 0 µl min^{-1} (a), 19 cells at 300 µl min^{-1} (b), 6 cells at 450 µl min^{-1} (c), 1 cell at 500 µl min^{-1} (d). Scale bars: 200 µm.

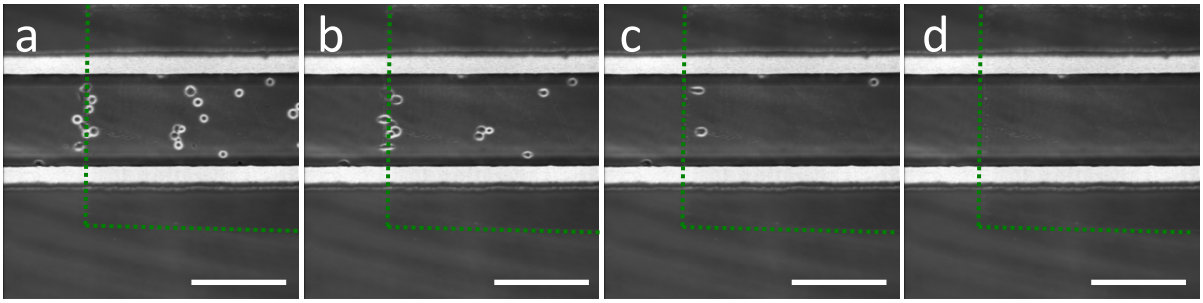

Figure 213: Phase contrast images of 3T3NiH cells on 600 nm wide and 250 nm deep holes in Topas 5013 (microfluidic system). The number of cells remaining on the flat bottom decreased with increasing pump rates: 19 cells at 0 µl min^{-1} (a), 15 cells at 300 µl min^{-1} (b), 3 cells at 450 µl min^{-1} (c), 0 cells at 500 µl min^{-1}. The green dotted line high lightens the nanostructured area. Scale bars: 200 µm.

Phase contrast images of NiH3T3 in a bonded microfluidic chip containing 600 nm wide and 250 nm deep holes taken during an adhesion experiments. A pump rate of 20 µl min^{-1} increasing in steps of 20 µl min^{-1} was applied.

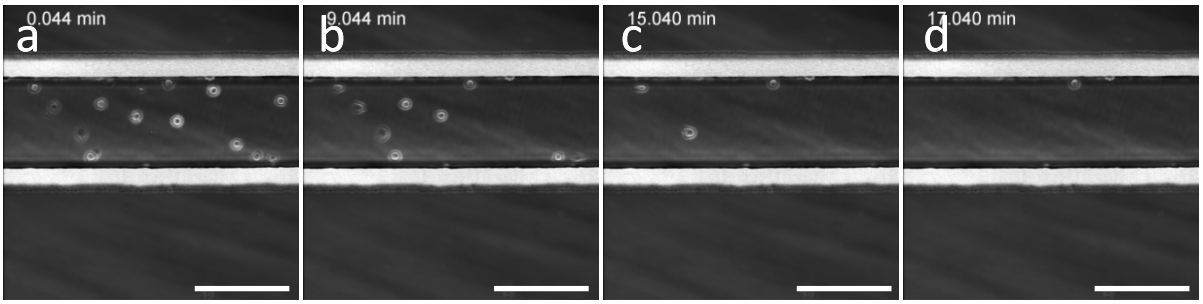

Figure 214: Phase contrast images of 3T3NiH cells on flat Topas 5013 (microfluidic system). The number of cells remaining on the flat bottom decreased with increasing pump rates (steps: 20 µl/min): 13 cells at 0 µl min^{-1} (a), 10 cells at 180 µl min^{-1} (b), 3 cells at 320 µl min^{-1} (c), 1 cell at 340 µl min^{-1}. Scale bars: 200 µm.

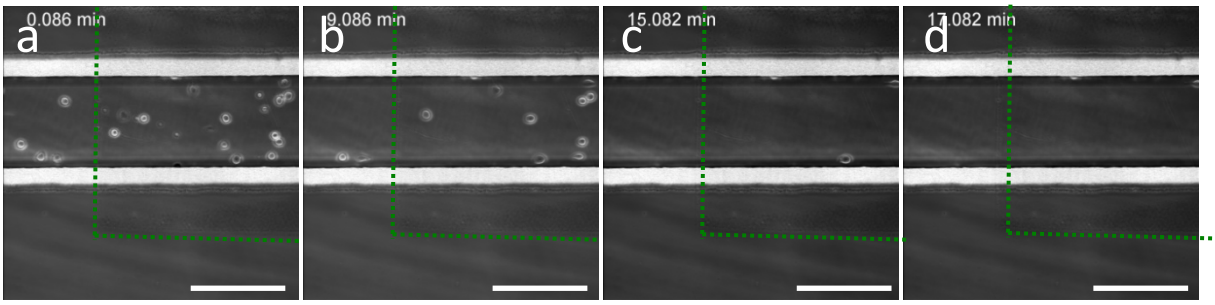

Figure 215: Phase contrast images of 3T3NiH cells on flat Topas 5013 (microfluidic system). The number of cells remaining on the flat bottom decreased with increasing pump rates (steps: 20 µl/min): 15 cells at 0 µl min^{-1} (a), 10 cells at 180 µl min^{-1} (b), 1 cells at 320 µl min^{-1} (c), 1 cell at 340 µl min^{-1}. The green dotted line high lightens the nanostructured area. Scale bars: 200 µm.

3. Recipes and Process Parameters

Table 28: Recipes for Galvanic Plating (DVD Norden A/S)

Nickel sulfamate bath:	**Passivation bath:**
- 450-500 g/l nickel sulfamate Ni (NH2SO3)2 · 4 H2O - 70 g/l Boric Acid H3Bo3 - 0-5 g/l Nickel Chloride NiCl2 · 6 H2O - 0.02 – 0.1 g/l Wetting agent *Quantities correspond to 80 g/l nickel ions and max 1.5 g/l chloride ions.*	- 1125 g sodium carbonate suspended at 70°C in 3.5 l water - 22.5 g sodium dodecyl sulphate suspended in 1 l water - 675 g trisodium phosphate

Table 29: Process parameter of standard recipe *multilayer* STAMP for deposition of FDTS [DTU Danchip].

O_2-plasma	Flow	Power	Time
	200	**250**	**300**

Dual layer repeated **1** times

First layer repeated **4** times

O_2-Plasma	Flow	Power	Time
	0	**0**	**0**
	Line 1 Water	Line 2	Line 3 FDTS	Line 4
Pressure	**6**		**0.500**	
No. cycles	**1**		**1**	
Vapor order	**2**		**1**	
Time	**900** seconds			
Purge	**5** cycles			

Second layer repeated **0** times

O_2-Plasma	Flow	Power	Time
	0	**0**	**0**
	Line 1 Water	Line 2	Line 3 FDTS	Line 4
Pressure	**0**		**0**	
No. cycles	**0**		**0**	
Vapor order	**0**		**0**	
Time	**0** seconds			
Purge	**0** cycles			

Table 30: *fpe_nano - S*ilicon etching recipe for Cluster System C004 (Cluster1) from STS Microsystems.

Chamber conditioning with dummy wafer was performed prior to etching of samples.			
	Dummy	**nano50nm**	**nano100nm**
Forward Power	20	20	20
Reflected Power	0	0	0
Load Position	34.7	36.2	34.4
Tune Position	39.1	38.5	38.9
APC Angle	64	64	64.4
Chamber Peak-to-Peak Voltage	355	350	350
Chamber Bias Voltage	87	99	103
process time	1:45	1:45	3:30
etch depth	?	≈ 100 nm	≈ 200nm

Table 31: *Shallolr* - *S*ilicon etching recipe for Advanced Silicon Etcher or ASE (STS MESC Multiplex ICP).

Parameter		Shallolr
Chiller	Temperature	10 °C
General	Pump down	00:20 min
	Gas stab	00:10 min
	Process time	05:56 min
	Number of cycles	Standard: 31
	Cycle times (etch/pass)	6.5 sec / 5.0 sec
	Recipe process	Discrete
Pressure	APC mode	Manual
	APC setting	86.8 %
Gases	C_4F_8 flow (etch/pass)	0 sccm / 120 sccm
	SF_6 flow (etch/pass)	260 sccm / 0 sccm
	O_2 flow (etch/pass)	26 sccm / 0 sccm
RF	Coil power (etch/pass)	2800 W / 1000 W
	Coil load/tune matching	50 % / 80 %
	Coil matching	Automatic
	Coil power tolerance	50 %
	Platen power (etch/pass)	16 W / 0 W
	Platen load/tune matching	45 % / 61 %
	Platen matching	Automatic
	Platen power tolerance	50 %
HBC	HBC	Active
HeLUR	Helium pressure	9.8 Torr
	Helium flow (max min^{-1})	40 sccm / 10 sccm
	Test time	01:00 min
	Maximum HeLUR	15 mTorr min^{-1}

Appendix II

Paper published in Journal of Microelectronic Engineering (2010)

Nanostructures for All-Polymer Microfluidic Systems

M. Matschuk, N. B. Larsen

Microelectronic Engineering 87 (2010) 1379–1382

Contents lists available at ScienceDirect

Microelectronic Engineering

journal homepage: www.elsevier.com/locate/mee

Nanostructures for all-polymer microfluidic systems

Maria Matschuk *, Henrik Bruus, Niels B. Larsen

Department of Micro- and Nanotechnology, Technical University of Denmark, Building 345 East, DK-2800 Kongens Lyngby, Denmark

ARTICLE INFO

Article history:
Received 15 September 2009
Received in revised form 25 November 2009
Accepted 27 November 2009
Available online 3 December 2009

Keywords:
Injection molding
Nanostructures
Electron beam lithography
Electroforming
Nickel mold
Polymer
Cyclic olefin copolymer
Topas

ABSTRACT

We present a process for fabricating nanostructured surfaces with feature sizes down to at least 50 nm and aspect ratios of 1:1 by injection molding. We explored the effects of mold coatings and injection molding conditions on the final nanostructure quality. A plasma-polymerized fluorocarbon based antistiction coating was found to improve the replication fidelity (shape and depth) of nanoscale features substantially. Arrays of holes of 50 nm diameter/35 nm depth and 100 nm/100 nm diameter, respectively, were mass-produced in cyclic olefin copolymer (Topas 5013) by injection molding. Polymer microfluidic channel chip parts resulted from a separate injection molding process. The microfluidic chip part and the nanostructured chip part were successfully bonded to form a sealed microfluidic system using air plasma assisted thermal bonding.

1. Introduction

Recent years have shown an increasing need for mass-production of nanostructures with high-precision, for e.g. antireflection [1,2] or antistiction coatings [3], optical data storage (e.g. Blu-ray disk) and for biomaterial applications. Therapeutic uses of human mesenchymal stems cells are of immense current interest, and their differentiation into particular cell lineages has recently been demonstrated to depend sensitively on the order of nanoscopic hole arrays [4]. We aim at integrating this type of cellular control in disposable microfluidic chip units, which calls for cost-effective production of the required nanostructures and their stable integration in a microfluidic system. Injection molding is the industrially preferred technology platform for low cost fabrication of polymer items in large numbers, but the technology has not yet been established for fabricating nanostructures of higher aspect ratios ($\geqslant 1$) in all relevant polymer materials.

Molding of polymer nanostructures down to 25 nm in width has been reported using injection molding [5–8]. Schift et al. demonstrated the injection molding of 25 nm wide and 40 nm deep structures [8], although the replication uniformity is sub-optimal even over a small area (<4 μm^2). Most injection molded features have been of height-to-width aspect ratios below one [5,6,9]. Sub-100 nm-features with aspect ratios larger than one and uniform shape over a larger area are difficult to realize by injection molding, especially in the widely and increasingly used cyclic olefin copolymer (COC). In fact, COC has been shown to replicate sub-μm structures worse than materials commonly used for injection molding, like polycarbonate or PMMA [7]. Injection molding of sub-100 nm surface structures of aspect ratio one or larger in COC has not been reported to our knowledge.

Phenomena at nanometer length scales are strongly influenced by interfacial effects, including wettability and friction, due to the increase in surface-to-volume ratio for decreasing dimensions. Inability of the polymer melt to fill nanoscale cavities during injection will limit the resolution of injection molding. This may be caused by insufficient wetting of the polymer melt on the mold surface. Given adequate cavity filling, inability of the solidified polymer to leave the nanoscale cavity during demolding may lead to nanostructural failure. Demolding exposes the molded polymer nanostructures to high frictional forces compared to their relatively low mechanical stability which may lead to their break-off from the bulk of the molded polymer. Optimal molds and molding conditions should therefore target proper filling and ease of release from the nanocavities of the mold.

The application of antistiction coatings on the mold can reduce frictional forces between mold and polymer during demolding. Antistiction coatings of fluorocarbon-silanes [10], fluorocarbons [11] or self-assembled monolayers [12] have been shown to improve the replication fidelity of hot-embossed features. However, antistiction coatings have not been tested as extensively for injection molding. The pressure on the polymer melt at the time of its initial contact with the (cold) mold surface is very low in injection

* Corresponding author.
E-mail address: maria.matschuk@nanotech.dtu.dk (M. Matschuk).

0167-9317/$ - see front matter © 2009 Elsevier B.V. All rights reserved.
doi:10.1016/j.mee.2009.11.167

molding, in contrast to embossing processes where the polymer melt is forced into the (hot) mold cavities by the applied pressure. This implies that nanostructure filling in injection molding may be strongly dependent on the interfacial energy of the mold and the polymer melt. Thus, a low surface energy antistiction coating could limit the filling of nanoscale cavities in the mold due to insufficient wetting of the coating by the polymer melt [13].

We find that optimization of molding parameters only lead to slight improvements in replication quality (feature depth and width). In contrast, the application of an antistiction coating results in major improvements in replication quality, improvements that are largely insensitive to variations in the molding parameters. We were able to mass-produce (>500 pieces) 100 nm wide and deep holes with high replication fidelity and uniformity over a large area (0.5 mm^2). Furthermore, we demonstrate that polymeric nanostructures can be thermally bonded to polymeric microfluidic systems without deformation of the nanostructures and with very limited deformation of the microfluidic channels.

2. Experimentals

Micro- and nanostructured surface topographies were injection molded in cyclic olefin copolymer, Topas 5013L-10 (TOPAS Advanced Polymers), using a commercial injection molder, ENGEL Victory 80/45 (ENGEL Austria). A conventional injection molding (IM) process consists of polymer melting, filling of the mold cavity, packing, cooling, and part release. The structures were molded with various parameter sets to maximize the replication fidelity (width, depth, and shape). The influence of mold temperature (115–140 °C), melt temperature (270–290 °C), injection velocities (2.0–8.0 cm^3/s), and holding pressure (300–600 bars) were investigated. The parts were demolded and ejected at a mold temperature of 55 ± 5 °C. To assure stabilization of the IM process, at least 25 pieces were injection molded for each set of parameters and only the final pieces used in the quality assessment.

The mold consists of a base plate with exchangeable insert. Micro- and nanostructured inserts were produced as a replica relief by electroplating of nickel on a silicon wafer based master structure. Microstructures were formed by UV lithography in a negative photoresist, SU-8 2075 (MicroChem, Newton, MA), spin-casted on a silicon wafer. Nanostructured holes of nominal lateral dimensions of 50 nm or 100 nm, respectively, a pitch of two times the structure width, and aspect ratios of 1:1–1:2 (Fig. 1) were fabricated by electron beam lithography (JBX-9300FS, Jeol) in an electron sensitive polymer, ZEP520A (Zeonrex Electronic Chemicals). Subsequently, structures formed in SU-8 or silicon were coated with a monolayer of FDTS (CAS No. 78560-44-8), deposited by a MVD 100 Molecular Vapor Deposition System (Applied Microstructures) to support the release of master and nickel shim. The electroplating process is similar to that described by Mönkkönen et al. [7]. The micro- and nanostructured master were sputter-coated with 100 nm nickel–vanadium composite (7 wt.% vanadium) and subsequently electroplated in a galvanic nickel bath to a final thickness of about 300 μm (DVD Norden A/S, Denmark). The resulting nickel shim presented a replica relief of the original master relief. A set of nickel molds was coated with 10 nm fluorocarbon polymer by plasma-polymerization of CHF_3 monomer using a Plasmatherm 740 RIE system (Unaxis, St. Petersburg, FL).

Microfluidic chip parts and nanostructure chip parts were thermally bonded after activation of both chip parts in an air plasma (0.6 mbar, 50 W, 30 s). Bonding proceeded at an applied pressure and temperature of 7.6 bars and 123 °C for 15 min.

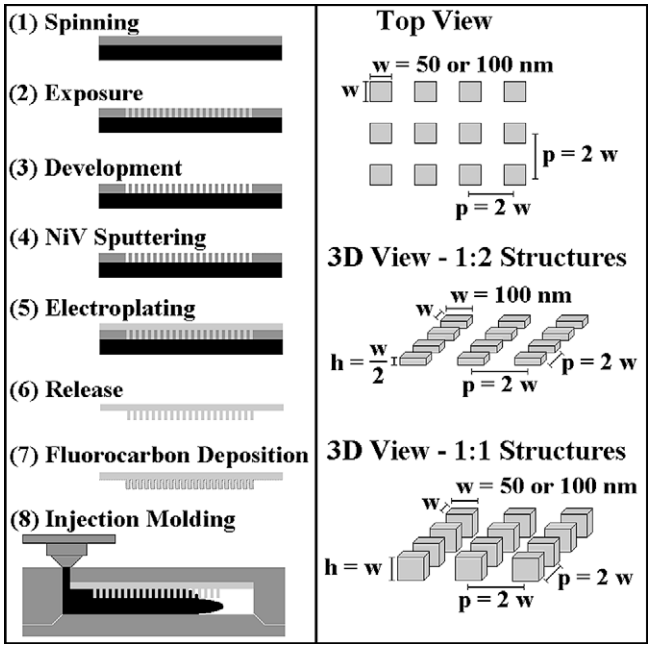

Fig. 1. (Left) Schematic diagram of the mold fabrication and replication, and (right) 2D and 3D sketch of fabricated nickel mold inserts: pillar array structures with features of w = width, h = height, p = pitch.

3. Results and discussion

3.1. Mold fabrication

Microfluidic channels of 200 μm in width and 25–100 μm in height were successfully fabricated in the negative photoresist SU-8 and replicated with high fidelity in nickel to form a mold insert for fabrication of a microfluidic chip part.

The fabrication of nickel molds containing 50 and 100 nm wide pillars, respectively, was successfully realized with pillars having aspect ratios of 1:2–1:1. Patterned surfaces were analyzed at different areas using atomic force microscope (AFM) and scanning electron microscope (SEM). All nanostructures written into ZEP520A were of high quality after development, i.e. without undercuts and of homogenous size over the whole patterned area. No substantial nano- or micro-scaled defects were observed. The electroplating replicated all nanostructures with high fidelity (shape and depth) into a nickel mold insert (Fig. 2a).

3.2. Injection molding

Micro- and nanostructured surface topographies were successfully injection molded in Topas 5013. Microstructures of 200 μm width and 25–100 μm in height were replicated. Randomly occurring micro-scaled cracks disappeared after application of an antistiction layer based on plasma-deposited fluorocarbon on the nickel mold. No effect on the replication fidelity (shape or depth) could be seen compared to uncoated nickel molds.

Holes of widths from 50 to 100 nm were replicated in Topas 5013 using an uncoated nickel mold. The overall surface of nanostructured areas molded on nickel molds without antistiction coating often showed regular nanoscale defects and distortions (Fig. 2b) and randomly distributed large-scale defects. Large-scale defects were most probably caused by stiction of polymer to the mold during demolding. Polymer contamination on the nickel mold, deposited during the first molding cycles, remained on the mold surface even after further molding cycles. The additional

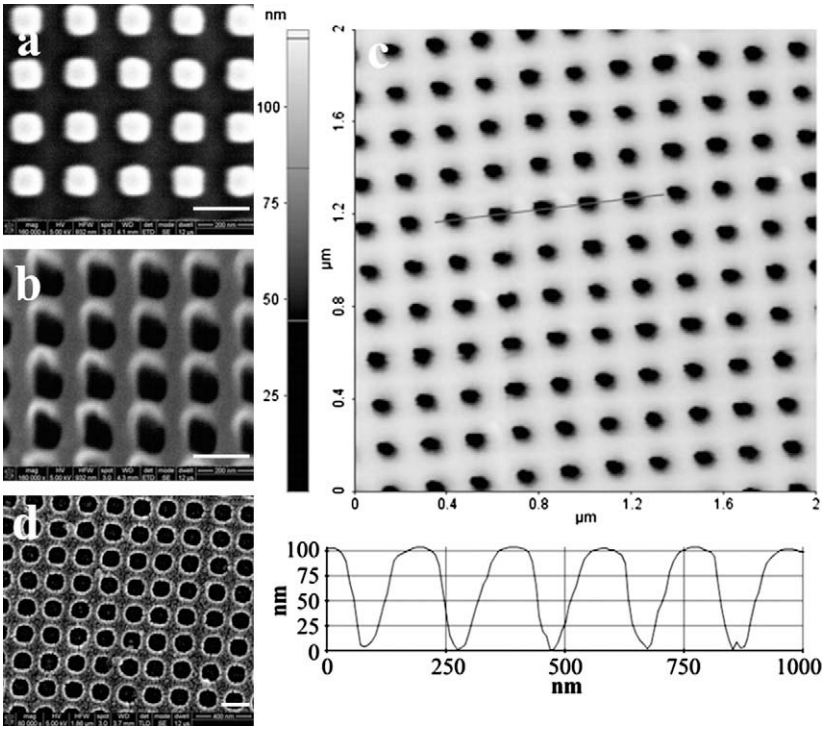

Fig. 2. Scanning electron micrograph of 100 nm wide and deep holes: (a) nickel mold, (b) polymer replica thereof molded without antistiction coating, and (c) atomic force micrograph with line profile of polymer replica molded with antistiction coating (same mold, scan size: 2 × 2 µm^2, profile length: 1 µm) and (d) scanning electron micrograph after their forced debonding from microfluidic structures. Scale bars represent 200 nm.

motif of contamination was transferred with high fidelity to subsequently molded objects. Injection molding of 50 nm wide holes resulted in deformed elongated shapes of depths of about 10 nm (mold depth 100 nm). The maximum achievable depth of 100 nm wide holes using uncoated nickel molds was not explored since the lateral shapes obtained were heavily distorted and therefore irrelevant as structural targets.

In contrast, we were able to replicate 50–100 nm wide holes with homogenous shape and without observable macroscopic defects over the whole structured area in Topas 5013, using a fluorocarbon based antistiction coating plasma-polymerized from CHF_3 monomers. The application of a fluorocarbon based antistiction coating was tested with the known caveat that they may limit the filling of nanoscaled cavities in the mold [13]. A layer of 10 nm fluorocarbon on a nickel mold surface enhances the replication fidelity of nanoscaled structures substantially without reducing the replication depth. The replication quality was improved and large-scale defects of the overall patterned surface were fully removed. 50 nm wide structures were replicated with a maximum depth of 35 nm (mold with 50 nm high pillars) while 100 nm wide structures could be replicated with full depth of 105 ± 5 nm (mold with 105 ± 5 nm high pillars) (Fig. 2c). X-ray photoelectron spectroscopy was employed to probe for inadvertent transfer of the fluorocarbon coating on the nickel mold to the injection molded pieces. No traces of fluorine were observed on molded items (data not shown). No degradation of the antistiction layer was observed, even after hundreds of injection molded pieces.

Optimization of process parameters resulted in the highest replication fidelity for width and depth at a holding pressure of 400 bars and injection velocity of 4 cm^3/s (Fig. 3). The replication depth increases with increasing holding pressure up to 400 bars and decreases for higher pressures. Holes replicated with up to 400 bars were about 100 ± 5 nm wide while higher holding pressures caused widening of the structures by about 40%. Holding pressure is required to compensate for polymer shrinkage during cooling (0.4–0.7%). However, the application of excessive pressure condenses the bulk polymer leading to stress-related deformation of its topography, e.g. widening of structures. Surprisingly, the replication depth increases with increasing injection velocity up to 4 cm^3/s and decreases for higher injection velocities. The width of the holes was not found to vary with the injection velocity. We expected the replication depth to increase monotonously with increasing velocity, until reaching the full height of the mold structures, with the caveat that other micro- and macroscale defects like

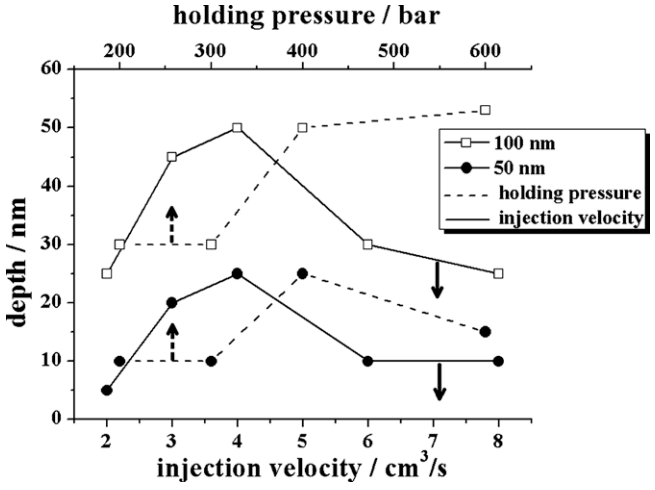

Fig. 3. Replication depth of 50 and 100 nm wide holes (mold: 58 nm high pillar structures) as a function of injection velocity (lower axis; holding pressure: 400 bars) or holding pressure (upper axis; injection speed: 4 cm^3/s) at a mold temperature of 125 °C and a melt temperature of 260 °C.

warpage and microcracks can appear at very high injection velocities. We currently explore the phenomenon of a maximum replication depth at intermediate velocities in more detail.

Variation in mold and melt temperature in the range explored showed no substantial influence on the replication fidelity. However, different research groups have shown that the replication depth can be improved by increasing melt and mold temperature, increasing injection velocity, as well as increasing the injection and holding pressure [5,7].

3.3. Bonding

Microfluidic chip parts and nanostructure chip parts, both injection molded in Topas 5013 were successfully thermally bonded. The bonding process caused a deformation of the whole area covering the microfluidic channel of about 2 μm in the channel center. The deformation of the nanostructures itself was analyzed by SEM after forced mechanical debonding. No measurable deformation was observed (Fig. 2d).

4. Conclusion

Injection molding is capable of mass producing arrays of nanoholes of 50 nm width and 35 nm in depth as well as 100 nm wide holes replicated to the full depth of 105 nm (Fig. 2c). The application of a fluorocarbon based antistiction coating improves the replication fidelity of shape and depth substantially. The coating did not cause any observable reduction in replication depth. Optimized process parameters, i.e. injection velocity and holding pressure, allow the fabrication of highly ordered nanostructures of controlled size with an aspect ratio of at least unity for structures 100 nm in width. Nanoscale features can be integrated in a polymer microfluidic system without substantial deformation of the structures though the overall surface may bend slightly during thermal bonding. We believe that further optimization of injection molding and bonding parameters and application of antistiction coatings may permit for smaller nanostructures with even higher aspect ratios and their registry to a microfluidic system.

Acknowledgements

This work was supported by The Danish Research Council for Technology and Production Sciences Grant No. 26-04-0074. We would like to thank J. Pedersen and A. Møller, DVD Norden A/S, for preparing the electroplated nickel replicas, as well as P. Shi for many useful discussions and continuous support with the electron beam lithography.

References

[1] G. Xie et al., Nanotechnology 19 (2008) 095605.
[2] C.-J. Ting et al., Journal of Micromechanics and Microengineering 18 (2008) 075001.
[3] H.-K. Koponen et al., Applied Surface Science 253 (2007) 5208–5213.
[4] M.J. Dalby et al., Nature Materials 6 (2007) 997–1003.
[5] C.K. Huang, Journal of Micromechanics and Microengineering 17 (2007) 1518.
[6] D. Macintyre, S. Thom, Microelectronic Engineering 41/42 (1998) 211.
[7] K. Mönkkönen et al., Polymer Engineering Science 42 (2002) 1600.
[8] H. Schift et al., Microelectronics and Engineering 53 (2000) 171–174.
[9] H. Pranov et al., Polymer Engineering Science (2006) 160.
[10] H. Schift, A. Kristensen, Nanoimprint lithography, in: B. Bhushan (Ed.), Springer Handbook of Nanotechnology, second ed., Springer, Berlin, 2007, pp. 239–278.
[11] Y. Guo, Microsystem Technology 13 (2007) 411–415.
[12] N. Lee et al., Applied Physics Letter 88 (2006) 073101.
[13] H. Pranov, Ph.D. Thesis, Technical University of Denmark, 2006.

Appendix III

Paper published in Journal of Micromechanic and Microengineering (2010)

Injection molded chips with integrated conducting polymer electrodes for electroporation of cells

K. Ø. Andresen, M. Hansen, M. Matschuk, S. T. Jepsen, H. S. Sørensen, P. Utko,T. S. Hansen, N. B. Larsen, N. Rozlosnik, R. Taboryski

IOP Publishing Journal of Micromechanics and Microengineering

J. Micromech. Microeng. **20** (2010) 055010 (9pp) doi:10.1088/0960-1317/20/5/055010

Injection molded chips with integrated conducting polymer electrodes for electroporation of cells

Kristian Ødegaard Andresen[1], Morten Hansen[1], Maria Matschuk[1], Søren Terpager Jepsen[2], Henrik Schiøtt Sørensen[2], Pawel Utko[1], Dávid Selmeczi[1], Thomas S Hansen[1], Niels B Larsen[1], Noemi Rozlosnik[1] and Rafael Taboryski[1,3]

[1] Department of Micro- and Nanotechnology, Technical University of Denmark, DTU Nanotech, Frederiksborgvej 399, DK-4000 Roskilde, Denmark
[2] Department of Photonics Engineering, Technical University of Denmark, DTU Fotonik, Frederiksborgvej 399, DK-4000 Roskilde, Denmark

E-mail: rata@nanotech.dtu.dk

Received 9 December 2009, in final form 7 March 2010
Published 7 April 2010
Online at stacks.iop.org/JMM/20/055010

Abstract
We present the design-concept for an all polymer injection molded single use microfluidic device. The fabricated devices comprise integrated conducting polymer electrodes and Luer fitting ports to allow for liquid and electrical access. A case study of low voltage electroporation of biological cells in suspension is presented. The working principle of the electroporation device is based on a focusing of the electric field by means of a constriction in the flow channel for the cells. We demonstrate the use of AC voltage for electroporation by applying a 1 kHz, ±50 V square pulse train to the electrodes and show delivery of polynucleotide fluorescent dye in 46% of human acute monocytic leukemia cells passing the constriction.

1. Introduction

When an electric field is applied to a cell, a nonuniform transmembrane potential is induced on the exposed cell. If the induced potential difference is large enough, the membrane may become permeabilized in a reversible process called electropermeabilization, allowing easier transport of ions and entrance of molecules that otherwise cannot easily cross the cell membrane. When focusing on approaches involving micro devices for electroporation, several methods of achieving transient high electric fields have been reported. For a recent review on microfluidic devices for electroporation, see e.g. Fox *et al* [1]. Electroporation is a mature and widely employed tool allowing for both the transfection of impermeant exogenous material through the cell membrane and for the release of intracellular content. The areas of realized and potential application include genetic manipulation, cloning cell fusion, antibody production, drug screening and cancer immunotherapy [2–5]. These applications often require disposal or cleaning of cuvettes and chips due to contamination by gene modified biological material or toxic compounds, and the need for cheap all polymer disposable chips is obvious for these applications.

A case study is presented concerning the use of a new prototyping concept to produce injection molded microfluidic devices for electroporation of biological cells (figure 1). In the presented all polymer device for electroporation, the cell medium itself partly constitutes the electrodes. A channel with a constriction serves to enhance the electrical field in the narrow section such that the field here is high enough for electroporation, and the field in the rest of the channel is too weak to have an adverse effect on the viability of cells [6, 7]. This technique avoids the high voltages associated with pulse generators, and avoids the difficulties associated with microfabricated electrodes, namely highly inhomogeneous field strengths at the electrode edges, as well as electrode deterioration. In addition, the presented flow-through system allows for a fast transfer of heat away from

[3] Author to whom any correspondence should be addressed.

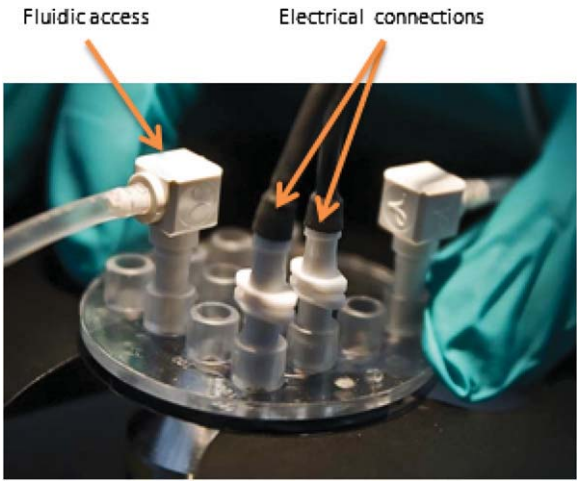

Figure 1. Photograph of injection molded chip for electroporation of biological cells, comprising electrical and fluidic access ports.

the channel constriction. A microfluidic chip for flow-through electroporation of cells requires practical inlet/outlet ports in order to allow for continuous operation not dependent on large cell reservoirs for electroporation of massive amounts of cells. Here, this has been achieved through integration of inlet/outlet ports designed according to the Luer fitting standard [8]. In addition to the novel features associated with the fabrication of the devices, we also demonstrate how an ac electric field is applied in order to avoid wearing of electrodes and bubble formation caused by electrochemical reactions.

Ideally, microfluidic research prototypes targeting life science applications with industrial potential should possess the following features; (1) low technology barrier roadmap to mass production, (2) low material costs, (3) high flexibility and (4) practical liquid input/output ports. The microfluidic chip concept, presented here, addresses all of these challenges. In particular, the novel features of this work are integrated conducting polymer electrodes to make an all polymer chip, for ease of fabrication and cost reduction; integrated inlet/outlet ports designed according to the Luer fitting standard for practical fluidic interconnect and flexibility; and the use of plasma assisted thermal bonding for improved assembly of the chips [9]. The low technology barrier to mass production is ensured by injection molding of the parts.

2. Experimental details

2.1. Fabrication of devices

Microfluidic devices addressing various biological applications presented in research papers are most often manufactured by means of rapid prototyping methods such as polydimethylsiloxane (PDMS) casting, laser milling or micromachining of polymeric materials [10–12] or adoption of clean room based micro-electro-mechanical-systems (MEMS) processes for microengineering of Si and glass wafers [13, 14]. Although these methods are quite mature, they suffer from serious drawbacks when it comes to industrial production feasibility and cost efficiency [15–18]. Hence, for single use devices, the Si/glass materials platform only applies to high value analysis, and is often combined with polymeric packaging that enables fluidic access [19–21]. The only material platform that can compete on fabrication and materials costs with the very mature silicon technology is the polymer injection molding platform [22–24]. However, polymer mass replication methods, such as injection molding and hot embossing, are poorly compatible with the requirements for flexibility and fast turn around times in modern research. Traditional injection molding tools are expensive to fabricate and lack flexibility. It often takes weeks of machining time to make the tools, and traditional machining is indeed very challenging for features below approximately 100 μm. The MEMS fabrication methods allow the fabrication of even nanometer sized features, and provide a feasible platform for fabrication of masters for polymer replication technologies such as imprinting and injection molding [25–27].

Injection molded lab on chip devices produced with clean room microfabricated mold inserts have been reported by several groups, but far less frequently than devices produced by the aforementioned rapid prototyping methods. The use of highly collimated synchrotron x-ray radiation and UV lithography was initially demonstrated as a method for producing high aspect ratio structures in the so-called LIGA[4] process [28, 29]. Moreover, injection molding has the appealing property that even nanometer-sized features can be replicated [30, 31]. McCormick *et al* reported on electrophoretic separation of DNA in the first injection molded biochip [32]. More recently Gadegaard *et al* reported on the replication of biomimetic nanostructures by injection molding [33]. Mair *et al* [34] reported on the use of TOPAS cyclic olefin copolymer for injection molding of microfluidic chips with integrated interconnects. Chien [35] reported on microinjection molding and hot embossing of a microfluidic platform used for DNA/RNA testing. Zou *et al* [36] reported on an injection molded polymer microfluidic chip with interdigitated Au electrode arrays for simultaneous dielectrophoretic manipulation and impedimetric detection of microparticles.

In this work, fabrication of devices started by fabrication of a master wafer by photolithography in the clean room. A chrome mask was used to define the flow channel pattern in SU-8 2075 photoresist, from MicroChem. Processing parameters provided by the supplier were used and resulted in 80 μm high channel structures protruding from the base of the substrate, a 100 mm diameter Si wafer. This Si master negative is thus characterized by a ridge feature corresponding to the microfluidic channels. The Si master was electroplated with Ni at DVD Norden A/S (www.dvdnorden.dk), a company which uses nickel masters to injection-mold DVDs. In order to comply with the DVD production process the Si master wafer was glued to a ∅180 mm glass plate by Norland Optical Adhesive 68 UV curing purchased from THORLABS. For the galvanization to proceed, the surface being deposited on must be electrically conductive. Therefore, a thin (the exact thickness is not a critical parameter) activation layer is sputtered onto the substrate. This layer consists of a

[4] German acronym for **Li**thographie, **G**alvanoformung, **A**bformung.

nickel–vanadium composite (7% vanadium by weight). The vanadium serves to inhibit oxidation of the nickel, which would otherwise interfere with the galvanic process. Finally the masters were electroplated with 300 μm Ni, to produce a Ni 'father'. The Ni 'father' electroform had the wrong polarity for injection molding and was subsequently converted by an additional galvanization process to form a 'mother' shim. In order to be able to separate the 'mother' shim from the 'father' after galvanization, the 'father' was immersed in an electrochemical passivation bath to form a non-reactive film on the surface of the shim. The advantage of using this double galvanization procedure is to exploit the flatness of the Si wafer to define the flatness of the resulting polymer parts. The double galvanization procedure can be avoided by inverting the polarity of the Si master; however, here one has to rely on the homogeneity of the SU-8 layer thickness, which is not better than $\pm 10\%$. The 300 μm thick Ni electroforms were punched into 85 mm diameter Ni shims by a customized punching tool. The shims had two flats, as found on Si wafers, to define the orientation of the pattern. The shims, produced this way, can withstand several thousands of cycles, which given the possibility to make several 'mother' shims from a single 'father' provides a reasonable roadmap for industrial production.

Parts were injection molded from Cyclic Olefin Copolymer (COC) TOPAS grade 8007 from TOPAS Advanced Polymers GmbH. An Engel Victory 80/45 Tech hydraulic injection molding machine equipped with an Engel pick up robot ERC 13/1-F was used for the injection molding. The macro part of the mold tool was made of Ampco tool material. TOPAS 8007 has a glass transition temperature (T_g) of 78 °C. Injection molding was done with a mold temperature slightly below T_g at 75 °C. The quality of the parts had a strong dependence on mold temperature, which was optimized to achieve the best quality. The parts were produced using a clamp tonnage of 50 kN. The fully automated pulsed heating cycle opened the water-cooled cavity at 40 °C to release the molded parts. Channel heights were defined by the thickness of the SU-8 layer on the master Si wafer, i.e. 80 μm. The channel layout consisted of pairwise fluidic channel connections between the Luer fluidic interconnect ports with each connection comprising a constriction in the channel width. The constrictions varied from 50 μm to 200 μm. Only the 50 μm constrictions appeared suitable for electroporation. Several hundred parts were injection molded and about one-tenth of the parts were further processed to integrate conducting polymer electrodes and assembled by thermal bonding[5].

Electrodes were made from conducting polymer poly(3,4-ethylenedioxythiophene) (PEDOT). PEDOT was applied by spin coating and *in situ* polymerization as described by Hansen *et al* [37] giving excellent adhesion to the TOPAS substrates. Pattern definition was obtained by a photolithographic process by masking with positive Microposit S1813 photoresist on the flat part (see figure 2). After exposure and development of the photoresist, the samples were etched in a reactive ion etch (RIE) system in an oxygen plasma for 2 min. The RIE etching to some extent destroys the TOPAS polymer chains, and care should be taken not to etch longer than necessary to remove the thin PEDOT layer. To remove the residual resist, the samples were flood exposed and rinsed in ethanol for 5 min followed by a wash in water. This procedure resulted in 100–200 nm PEDOT thin film electrodes with a sheet resistivity of order 100–1000 Ω/square. The electrode layout consisted of four fairly wide (5.3 mm) electrodes, such that each constriction channel was connected to a pair of electrodes. As shown in figure 2 the electrodes were deposited on the flat injection

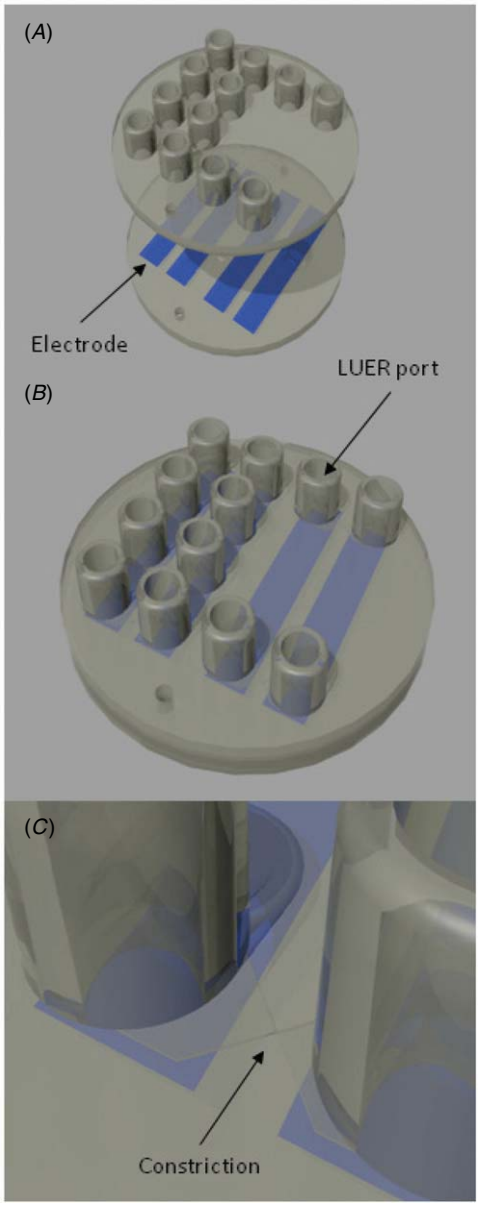

Figure 2. Ray-traced 3D model of the injection molded chip. The diameter of the chip is 50 mm. Two 2.1 mm location holes at the periphery are used to align the parts before bonding. (*A*) The two parts before bonding. The top part comprises the Luer fitting interconnect ports and the microfluidic channels. The flat bottom part comprises the conducting polymer electrodes (blue). (*B*) The bonded chip. (*C*) Details showing the microfluidic channel with the constriction for 'flow through electroporation'.

[5] More parts could have been assembled, but one-tenth was enough for the present project.

molded part, while the microfluidic channels were defined in the part with Luer fitting inlet/outlet ports. The two parts were bonded together by plasma-assisted thermal bonding [38] in a home built press. The bonding process takes 20 min for each device, the speed being limited by the heating and cooling cycles. However, the process is suitable for massive parallelization. The timing and choice of pressure are fairly critical as the polymer will begin to deform plastically as it approaches the glass transition temperature. It proves useful to place a piece of rubber in the press between the chip and the piston (we have used a transparent silicone rubber) to help disperse the pressure across the device and to compensate for tiny deviations from co-planarity of the two pistons. A special piston with holes to accommodate the Luer fittings was designed and used. Bonding conditions were the following: bonding force 50 kg distributed over the 16 cm^2 interface area of the bonded parts, bonding temperature 72 °C for 300 s, release temperature 40 °C. Prior to the bonding, the glass transition temperature of the surfaces of adjacent parts was lowered by plasma treatment [39]. The plasma treatment was done at 0.6 mbar of atmospheric air pressure for 15 s with a power of 50 W at 13.56 MHz. After bonding no further processing was done. A ray traced three-dimensional model of the final device is shown in figure 2.

2.2. Cells

To demonstrate electroporation, we have chosen THP-1 cells, an immortalized human monocytic cell line which is easy to handle and resembles primary monocytes from peripheral blood. THP-1 cells are suspension cells and are therefore less prone to cell adhesion on surfaces compared with other cell types including primary monocytes [40]. THP-1 cells were purchased from the American Tissue Culture Collection (ATCC; Rockville, MD) and handled as recommended by the manufacturer. Prior to electroporation experiments, the cells were starved in L-glutamine containing RPMI 1640 growth medium added 1% penicillin streptomycin, in a 5% CO_2 atmosphere at 37 °C and fresh medium was added so that cell concentration was always 5×10^4–8×10^5 cells mL^{-1}. Prior to electroporation, cells were centrifuged at 425 g and resuspended in diluted phosphate buffered saline (PBS) buffer containing 5 μM SYTOX Green (Invitrogen) to a final cell concentration equal to the one in the growth media. SYTOX Green is a dye which is membrane impermeable for live cells, and becomes fluorescent upon binding with polynucleotides. This dye should be excited by a 450–490 nm source in order to fluoresce. After electroporation and within maximally 20 min after the cell medium exchange, cells were counted in a Zeiss Axiovert 100S fluorescence microscope. For a single captured microscope image, up to 1000 cells were inspected in order to achieve reasonable statistics. The total number of cells was counted along with the number of cells which were fluorescent. Cells were counted by IQmaterials software from MediaCybernetics. The software identifies particles based on their color, using a threshold. For both phase contrast and fluorescence microscopy, the lighting from the lamp will not in general be entirely uniform and variations in illumination may cause a cell in one part of the image to be the same color as the background elsewhere. In order to avoid this, the background was equalized before cell counting. The captured images contain a certain amount of noise which may register as single pixel particles during counting. These can be removed by setting a minimum particle size, but due to the high resolution of images, significant slow-down may still occur. This was resolved simply by applying a slight blur at a 3 pixel width.

2.3. Experimental setup

For flow control we employed two single syringe pumps (New Era Pump Systems Inc., model NE-1000) providing a constant flow of 0.2 mL h^{-1}. Other flow speeds were investigated, but 0.2 mL h^{-1} was chosen as the best compromise to allow enough time for the cells to be permeated, while ensuring that cells did not sediment too much during operation. One of the pumps was used for the control experiment, where cells were driven through an identical chip, but with no electrical field applied. The other syringe pump was used to drive cells through the device with applied square pulses at 1 kHz frequency. The circuit comprised a function generator (USB oscilloscope, TiePie Handyscope HS3), which featured a single output channel ranging up to 12 V, and two input channels capable of measuring up to 80 V with 12 bit accuracy and 5 MHz sampling rate. The function generator was used to apply pulses and monitor the potential over the channel. In order to increase the applied voltage, a homebuilt power amplifier with voltage amplification by a factor of 6 was inserted between the function generator and the device, enabling pulse levels up to ±72 V. The two input channels were used to record the voltage across a 100 kΩ resistor connected in series with the channel and over the entire circuit (channel and resistor in series) respectively. This allowed extraction of the current through the device and the voltage across the channel by simple arithmetic applied to the recorded voltage data on the two input channels. The entire circuit was implemented using co-axial cables to avoid picking up noise. The PEDOT electrodes were connected by leads comprising spring loaded test pins mounted in male Luer connectors (Value Plastics Inc.) and inserted into Luer wells of the device. A Zeiss Axiovert 100 inverted microscope equipped with a digital camera was used to monitor the flow of cells through the channel.

3. Results

The cross-membrane potential that is required for the electrical breakdown of the lipid membrane can be measured experimentally using intracellular electrodes [41]. It varies with temperature, from about 1000 mV at 4 °C, to about 640 mV at 30 °C, relating to a factor of 2 decrease of the elastic modulus of the membrane as the temperature rises. The potential at different locations on phospholipid bilayer spheres during exposure in a homogeneous electric field of duration t can be calculated from [42]

$$U = 1.5 r E \cos(\theta) \left(1 - \exp\left(\frac{t}{\tau}\right)\right) \quad (1)$$

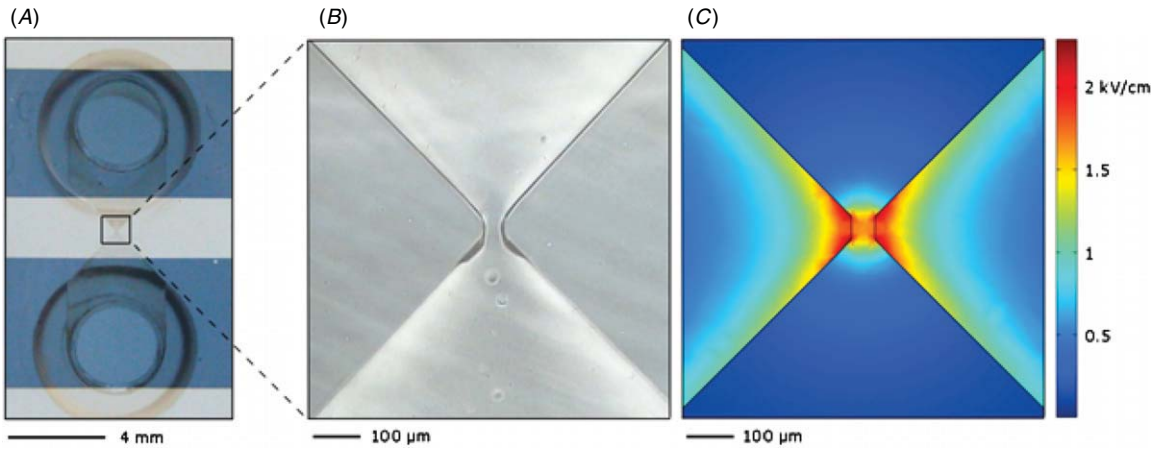

Figure 3. (*A*) Micrograph of a flow channel with electroporation unit comprising Luer fittings inlet/outlet ports, electrodes (blue) and a flow channel with constriction. (*B*) Details showing the 50 μm constriction with cells passing. (*C*) Numerical simulation of electric field strength through the constriction. The simulation was made with a 50 V applied voltage difference.

where E is the electric field strength, r is the cell radius, θ is the angle in relation to the direction of the electric field and τ is the capacitive–resistive time constant, which is usually estimated to be of order 1 ms [43]. It is widely observed that the choices for pulse amplitude and length are interchangeable to some extent; the amplitude can be reduced if one increases the pulse length, and vice versa. As an example, successful transfection with pulses of only 60 ns duration and 15 kV cm^{-1} amplitude has been reported [44]. High electric field strengths can be accomplished either by employing very high voltages, as in the case of commercially available devices for electroporation in vials and cuvettes, or by exploiting the high field strengths obtained with microstructured electrodes [45]. Both approaches have some drawbacks. High voltages of order kV are in general not desirable for safety reasons, while the use of microstructured electrodes gives rise to very inhomogeneous field strengths, and it is often a challenge to obtain a uniform treatment of all cells [46]. An alternative approach, particularly suitable for electroporation of suspension cells, was pioneered by Wang and Lu [7]. The 'flow through' approach of Wang and Lu relies on the focusing of the electric field in a constriction of a flow channel, while the cells are guided through the same constriction. The field is only strong enough inside the constriction to permeabilize the cells. The duration of the high field exposure can be controlled by the volumetric flow rate through the system. Using this approach we demonstrate electroporation of biological cells by applying voltage levels beneath the so-called extra low voltage level (ELV) of 50 V RMS [47]. Here we employ an AC version of the Wang and Lu electroporation method. The principle of operation is illustrated in figure 3. The two panels A and B show micrographs of subsections of the microchip including Luer inlet/outlet ports, electrodes and the fluidic channel with the constriction, while figure 3(*C*) shows a numerical model simulation of the electric field strength distribution in the microchannel. The simulation was performed using a finite element method with roughly 60 000 elements using the software package 'COMSOL'. The focusing of the field in the microchannel of the device is clearly demonstrated by this simulation. All cells passing the constriction will temporarily be exposed to an electric field strength of order 1 kV cm^{-1} with 50 V potential difference across the electrodes.[6]

The conductivity of a cell membrane is usually just below 1 mS cm^{-2} [48]. When the threshold voltage is applied, the conductivity increases rapidly, within about 1 μs reaching 1 S cm^{-2}, and within about 1 ms reaching 10 S cm^{-2}. Pore sizes are on the nanometer scale. If the electroporation is reversible, after pulsing there is a phased resealing of the membrane taking on the order of 10 s [49]. The required pulse lengths for successful electroporation are thus typically in the range of μs to ms; however, for pulse lengths below τ, higher field strengths are required in order to compensate the charge transfer during the membrane charging sequence. In the 'flow through' device, the pulse length is related to the flow velocity in the constriction. For a constriction volume (VOL) given by the dimensions length $\times$ width $\times$ height $=$ 50 $\times$ 50 $\times$ 80 μm^3, a rough estimation of the transition time based on the volumetric flow rate $Q = 0.2$ mL h^{-1} is given by $\Delta t = \mathrm{VOL}/Q = 3.6$ ms. A numerical finite element simulation in COMSOL for the velocity field in the flow channel of the device is shown in figure 4(*A*). The maximum velocity in the constriction is 2 cm s^{-1}. Due to the parabolic velocity profile in the laminar flow regime, the cells will not pass the constriction with exactly the same velocity; however, since the constriction cross-section dimensions are comparable to the cell dimensions (diameter $\approx$ 20 μm), it is likely that the distribution of passage times for the cells will be rather narrow. In order to check this, we sampled the voltage and current values during cell passage for some of the electroporation experiments. This allowed a compilation of the relative resistance change in the device during cell passage. Examples of this are seen in panels B and C of figure 4 for 0.8 mL h^{-1} and 0.2 mL h^{-1} flow rates respectively.

[6] This value is somewhat smaller than expected from a back of the envelope calculation with 50 V over 50 μm due to parasitic capacitance across the polymer and channel series resistance, and results from numerical simulation data.

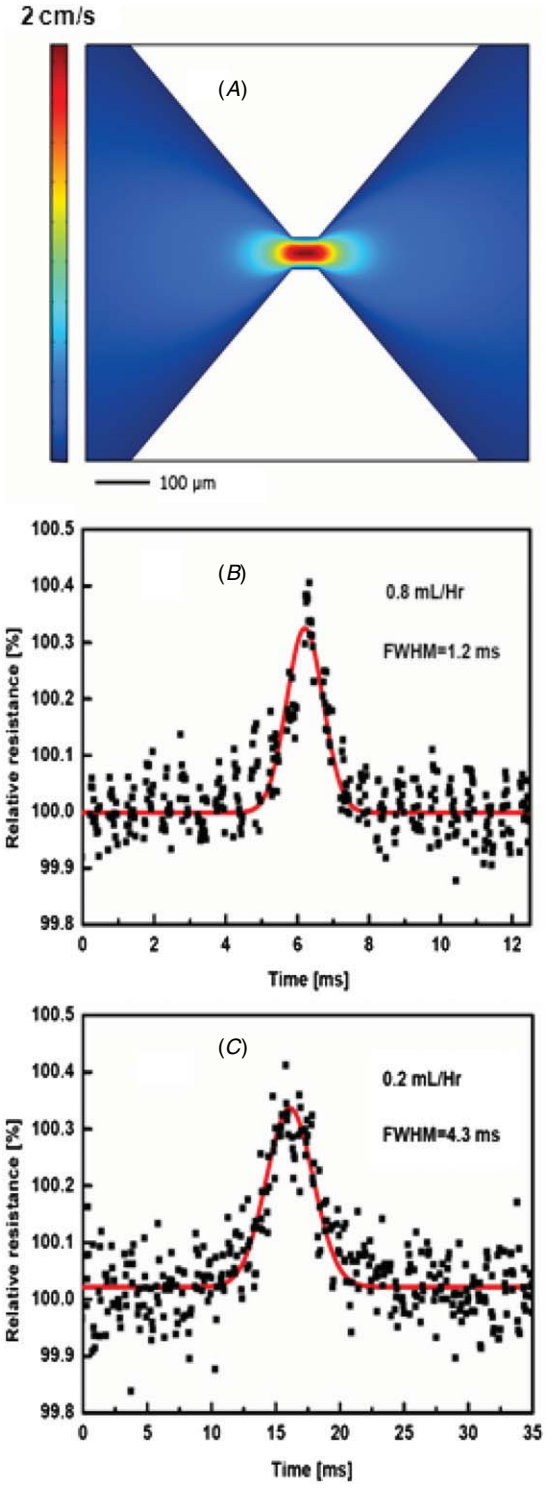

Figure 4. (*A*) Numerical simulation of the velocity field through the constriction. (*B*) Relative resistance change of the microfluidic channel as a function of time recorded as a cell passes the constriction (black data points). The volumetric flow rate was 0.8 mL h^{-1}. The full red curve is a Gaussian function fitted to the data with FWHM 1.2 ms. (*C*) Same as B but with 0.2 mL h^{-1} flow rate and Gaussian function with FWHM = 4.3 ms.

The data can be understood qualitatively by assuming that cells displace conducting buffer from the constriction when they pass. Hence, a transient rise in the resistance will result when a cell passes the constriction, in much the same way as in a Coulter particle counter [50]. The resistance of the constriction is about 1/3 of the overall resistance of the device, and an estimate of the transient amplitude for passage of a cell is given by the ratio of cell volume and constriction volume $\Delta R/R = (1/3) \cdot \mathrm{Vol_{cell}}/\mathrm{Vol_{constr.}}$, which for the signal amplitudes in figure 4 corresponds to realistic cell radii of approximately 8 μm. In order to evaluate the transit times, we observed that the measured resistance peaks empirically could be fitted to Gaussian functions, allowing an estimation of the transit times from the resulting full width half maximum (FWHM) of the Gaussians. The data did not allow a determination of the distribution of transit times, but gave a fairly good estimate of typical transit times. The transit times scaled well with the flow rate through the device. Hence, the transit time for cells passing with a flow rate of 0.8 mL h^{-1} was roughly four times shorter than for 0.2 mL h^{-1} flow rate as expected. Considering these measurements the question that naturally arises is whether cells that were permeabilized could be distinguished from nonpermeabilized cells due to the imposed difference in membrane conductance of the two species. This was, however, not possible with the present data, probably because the induced membrane conductance change was too small.

The next consideration relates to the frequency of operation for application of the electric field. Clearly, even 50 V is a very high voltage, and electrode reactions would readily cause serious deterioration of the PEDOT electrodes if operated in DC mode. However, here one can rely on the massive capacitances usually formed between electrodes and electrolytes due to the very thin Helmholtz double layers [51]. The large capacitances ensure a capacitive coupling to the electrolyte at even moderate frequencies. To this end, we characterized the devices by impedance spectroscopy with a standard PBS buffer as the electrolyte and a solution diluted with sugar. This was done using a potentiostat (from Princeton Applied Research, model: Versastat 3). The results for the PBS buffer are shown in figure 5(*A*), where the magnitude and phase of the impedance is plotted as a function of frequency. The layout of the device comprising electrodes and channel is shown in (*B*). A lumped element model, shown in (*C*), was constructed to fit the impedance spectroscopy data. The model comprised electrode resistors R_e, interface resistors R_i, interface capacitors C_i, channel resistor R_c and channel capacitor C_c. R_e was obtained independently, simply by measuring the electrode resistance without PBS buffer with an ohmmeter between the relevant ports for electrical connection and fluid access (see figure 5). R_e amounted to roughly 2 kΩ. R_i (3 kΩ) represents the undesirable connection between electrode and buffer involving electrode redox reactions, while C_i represents the huge electrode capacitance of 20 μF. R_c is the channel resistance fitted to 35 kΩ, while C_c is a small (10 pF) parasitic channel capacitance originating from electric field lines spreading into the polymer wall material around the constriction, as can be observed in the numerical simulation in the figure. C_c is responsible for the high frequency (>10 kHz) low pass filter behavior observed as a decay of impedance magnitude at high frequencies. The huge interface

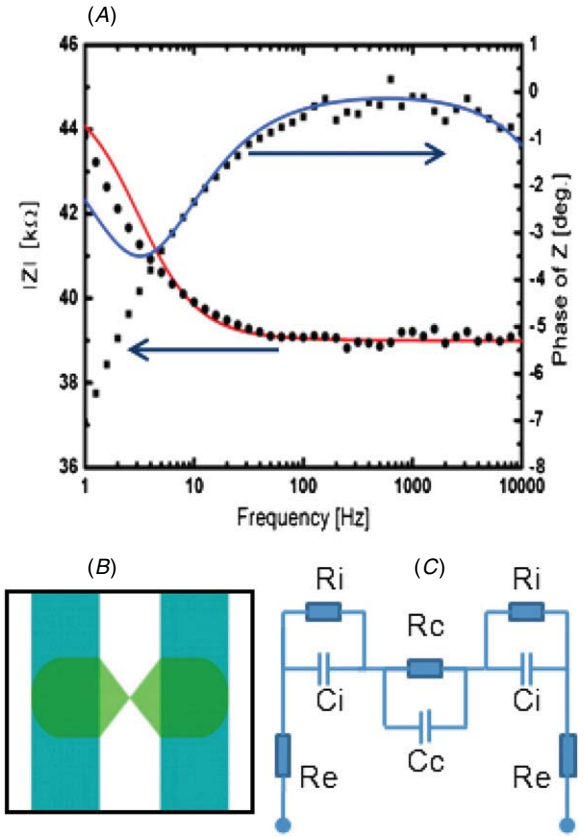

Figure 5. (*A*) Magnitude (•) and phase (■) of complex impedance recorded as a function of frequency. Full red and blue curves are fits to a lumped element model. (*B*) Layout of channel section constituting the model. The light green feature is the channel layout, while the dark green feature is the electrode layout. (*C*) The lumped element model constructed to make the fit in (*A*). The model comprised electrode resistors R_e (2 kΩ), interface resistors R_i (3 kΩ), interface capacitors C_i (20 μF), channel resistor R_c (35 kΩ) and channel capacitor C_c (10 pF).

capacitance is caused by the very thin Helmholtz double layer of the order of the Debye length $L_D = \sqrt{\epsilon k_B T/2e^2 c} \approx 1$ nm. Here ϵ is the dielectric constant of water, k_B is Boltzmann's constant, T is the absolute temperature, e is the elementary charge, and c is the ion concentration. For fitting the impedance data, C_i was replaced by a so-called constant phase element (CPE) with complex admittance $Y_{\mathrm{CPE}} = (\mathrm{i}\omega/2\pi \cdot \mathrm{Hz})^{\alpha} 2\pi \cdot \mathrm{Hz} \cdot C_i$.[7] In the fitting $\alpha = 0.9$ was used. The CPE concept is usually ascribed to the roughness of electrodes [52]. For $\alpha = 1$, CPE reduces to the normal admittance for a capacitor. As can be seen in figure 5, the lumped element model breaks down at frequencies below approximately 7 Hz, where the electrode reactions dominate, and this phenomenon cannot simply be represented by a resistor model. Also it can easily be seen that R_i becomes entirely shunted approximately at 1 kHz by the current running through C_i. For even higher frequencies, the parasitic channel capacitor begins to play a role, and shunts the electric field in the constriction. The behavior was qualitatively similar for the diluted buffer; only the fitted values for the channel and interface resistances changed. Consequently it was chosen to operate the devices at 1 kHz, square ±50 V pulses, although some decrease in field strength across the cell membranes was expected at the cross-over from positive to negative potential due to the charging of cell membranes, which are expected to charge with a capacitive–resistive time constant [43] of order 1 ms.[8]

For the electroporation experiments, a diluted buffer solution was used. This was done to decrease the buffer conductivity to avoid formation of gas bubbles in the constriction due to electrolysis of water molecules. The PBS buffer solution is widely used in biological research, is isotonic and serves to help maintain a constant pH of about 7.4, but has a rather high conductivity of 1.7 S m^{-1} at 300 K. The composition is 138 mM NaCl, 10 mM phosphate and 2.7 mM KCl. For our purpose, the NaCl concentration was reduced to 20 mM by the following procedure: for 100 mL of final solution, 14.6 mL PBS buffer was mixed with 4.6 g of glucose ($C_6H_6O_6$), and water was added until the solution reached 100 mL. This reduced the conductivity of the buffer by roughly a factor of 6.5 while maintaining the osmolarity.

Successful electroporation experiments on THP-1 cells were performed at 30 V and 50 V applied voltage, using a flow rate of 0.2 mL h^{-1} corresponding to an exposure time of 3.6 ms. For a 50 V applied voltage, the numerical simulations predict an electric field peak strength of order 1.7 kV cm^{-1} and a potential difference across the cell of order 2 V according to equation (1) and assuming cell radii of order 8 μm. The results of the electroporation experiments are seen in figure 6 for 30 V and 50 V square pulses respectively. For 50 V pulses SYTOX Green fluorescent dye was delivered to 46 ± 3% of the cells, while for 30 V pulses the dye was delivered to 14 ± 3% of the cells. The uncertainties for successful dye delivery fractions were obtained by averaging over several microscope images. The control experiments, where the cells were subjected to the same treatment except for application of the electric fields, showed delivery levels of order 8 ± 3% in both the 50 V and the 30 V experiments. A higher delivery fraction could likely be obtained by slightly higher voltage levels. However, this caused runaway heating phenomena in the constriction even with the sugar substituted buffer solution and would not allow compliance with the ELV standard [47]. In order to increase the delivery rate, the constriction could easily be redesigned to become shallower, less wide or comprising parallel constrictions. The only negative effect of this design change would be the requirement to decrease the flow rate in order not to decrease the exposure time to the field. Such a design change would cause more sedimentation of cells, but a natural counter measure would be to increase the length of the channel accordingly.

In the present work, we focus on demonstrating permeation of the cell membrane on real biological cells in our all-polymer device rather than assuring a high viability of cells after electroporation. The SYTOX Green dye will stain cells with a compromised cell membrane, hence, both dead and transfected cells. For a study with focus on real applications

[7] The non-elegant inclusion of the Hz frequency unit in the CPE formula is required for using the formula with SI units.

[8] Assuming a membrane capacitance $C_M \approx \frac{1\mu\mathrm{F}}{\mathrm{cm}^2}$ and a membrane resistance $R_{\mathrm{M}} \approx 1\ \mathrm{k\Omega\ cm}^2$.

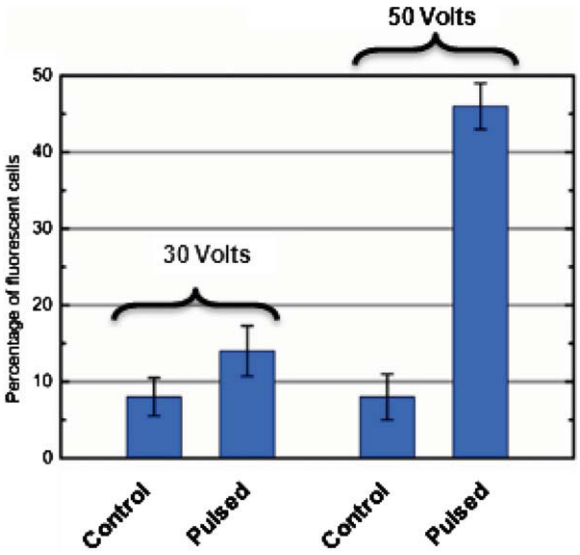

Figure 6. Histogram showing fractions of fluorescent cells after electroporation with ±30 V and ±50 V square pulses at 1 kHz. The control fractions refer to the data taken with cells from the same culture exposed to exactly the same treatment as the electroporated ones, except for the exposure to the electric field.

of the method, systematic experiments would be needed to document cell viability after electroporation, by e.g. applying a second vital stain such as Trypan blue. However, we did perform time-lapse microscopy for some of the electroporated cells, and found a significant part of the transfected cells viable, but a systematic study providing statistics was considered outside the scope of this work and was not carried out.

4. Conclusion

An all polymer single use electroporation chip was fabricated by means of a rapid prototyping method comprising microinjection molding[9]. Several hundred parts were fabricated by lithographic definition of father electroforms and subsequent replication by injection molding. Injection molded parts were further processed to integrate conducting polymer (PEDOT) electrodes and assembled by thermal bonding. The feasibility of having a fixed macroscopic basic form with Luer fitting input/output ports for both fluidic and electrical access combined with a flexible rapid prototyping fluidic channel layout system was demonstrated. The devices were characterized by numerical simulations and experiments to identify the parameter space for successful operation, in particular the parameters relating to voltage and frequency ranges of applied voltage pulses, and to the fluidic properties. In particular it was demonstrated that thin film PEDOT electrodes could withstand application of high voltages if operated at frequencies where the electrode redox reactions are shunted by capacitive coupling to the electrolyte. 'Flow through' electroporation with feasible exposure times was demonstrated in experiments carried out on human acute monocytic leukemia THP-1 cells. Delivery fractions of roughly half of the cell population were demonstrated by delivering a polynucleotide dye into the cells.

[9] Microinjection molding in this context refer to injection molding using microstructured mold inserts, and not injection molding using a so-called micro injection molding machine.

Acknowledgments

We would like to thank Dr Gertrud M Hjortø, DTU-Nanotech, for assistance with the cell handling, and Dr Eugen Stamate, RISØ-DTU, for assistance with the amplifier set-up.

References

[1] Fox M B, Esveld D C, Valero A, Luttge R, Mastwijk H C, Bartels P V, Van Den Berg A and Boom R M 2006 *Anal. Bioanal. Chem.* **385** 474–85
[2] Huang Y and Rubinsky B 2003 *Sensors Actuators* A **104** 205–12
[3] Tjelle T E, Corthay A, Lunde E, Sandlie I, Michaelsen T E, Mathiesen I and Bogen B 2004 *Mol. Ther.* **9** 328–36
[4] Shizuya H, Birren B, Kim U-J, Mancino V, Slepak T, Tachiiri Y and Simon M 1992 *Proc. Natl Acad. Sci. USA* **89** 8794–7
[5] Tsong T Y 1991 *Biophys. J.* **60** 297–306
[6] Huang Y and Rubinsky B 2001 *Sensors Actuators* A **89** 242–9
[7] Wang H-Y and Lu C 2006 *Anal. Chem.* **78** 5158–64
Wang H-Y and Lu C 2008 *Biotech. Bioeng.* **100** 579
[8] International Standard ISO 594-1 1st edn 1986
[9] Wu Z, Xanthopoulos N, Reymond F, Rossier J S and Girault H H 2002 *Electrophoresis* **23** 782–90
[10] Becker H and Locascio L E 2002 *Talanta* **56** 267–87
[11] Duffy D C, Cooper McDonald J, Schueller O J A and Whitesides G M 1998 *Anal. Chem.* **70** 4974–84
[12] Klank H, Kutter J P and Geschke O 2002 *Lab Chip* **2** 242–6
[13] Harrison D J, Fluri K, Seiler K, Fan Z, Effenhauser C S and Manz A 1993 *Science* **261** 895–7
[14] Andersson H and Van Den Berg A 2003 *Sensors Actuators* B **92** 315–25
[15] de Mello A 2002 *Lab Chip* **2** 31N–6N
[16] Figeys D and Pinto D 2000 *Anal. Chem.* **72** 330A
[17] Curtis A and Wilkinson C 2001 *Trends Biotechnol.* **19** 97
[18] Clayton J 2005 *Nat. Methods* **2** 621
[19] Spégel C, Heiskanen A, Pedersen S, Emnéus J, Ruzgasd T and Taboryski R 2008 *Lab Chip* **8** 323–9
[20] Asmild M *et al* 2003 *Receptors Channels* **9** 49–58
[21] Sigworth F J and Klemic K G 2005 *IEEE Trans. Nanobiosci.* **4** 121
[22] Heckele M and Schomburg W K 2004 *J. Micromech. Microeng.* **14** R1–R14
[23] Giboz J, Copponnex T and Mélé P 2007 *J. Micromech. Microeng* **17** R96–R109
[24] Becker H and Gärtner C 2008 *Anal. Bioanal. Chem.* **390** 89–111
[25] Ekstrand G, Holmquist C, Orlefors A E, Hellman B, Larson A and Andersson P 2000 *Micro Total Analysis Systems 2000* ed A van den Berg, W Olthius and P Bergveld (Dordrecht: Kluwer) pp 249–52
[26] Dang F, Tabata O, Kurokawa M, Ewis A A, Zhang L, Yamaoka Y, Shinohara S, Shinohara Y, Ishikawa M and Baba Y 2005 *Anal. Chem.* **77** 2140–6
[27] Romankiv L T 1997 *Electrochem. Acta* **42** 2985–3005
[28] Becker E W, Ehrfeld W, Miinchmeyer D, Betz H, Heuberger A, Pongratz S, Glashauser W, Michel H J and Siemens R v 1982 *Naturwissenschaften* **69** 520–3
[29] Piotter V, Hanemann T, Ruprecht R and Haußelt J 1997 *Microsyst. Technol.* **3** 129–33

[30] Mönkkönen K, Hietala J, Pääkönen P, Pääkönen E J, Kaikuranta T, Pakkanen T T and Jääskeläinen T 2002 *Pol. Eng. Sci.* **42** 1600
[31] Pranov H, Koblitz Rasmussen H, Larsen N B and Gadegaard N 2006 *Pol. Eng. Sci.* **46** 160–71
[32] McCormick R M, Nelson R J, AlonsoAmigo M G, Benvegnu J and Hooper H H 1997 *Anal. Chem.* **69** 2626–30
[33] Gadegaard N, Mosler S and Larsen N B 2003 *Macromol. Mater. Eng.* **288** 76–83
[34] Mair D A, Geiger E, Pisano A P, Fréchet J M J and Svec F 2006 *Lab Chip* **6** 1346–54
[35] Chien R-D 2006 *Sensors Actuators* A **128** 238–47
[36] Zou Z, Lee S and Ahn C H 2008 *IEEE Sens. J.* **8** 527
[37] Hansen T S, West K, Hassager O and Larsen N B 2007 *J. Micromech. Microeng.* **17** 860–6
[38] Tsao C-W and DeVoe D L 2009 *Microfluid Nanofluid* **6** 1–16
[39] Hyun J, Aspnes D E and Cuomo J J 2001 *Macromolecules* **34** 2395–7
[40] Martinet W, Schrijvers D M and Kockx M M 2003 *Biotech. Lett.* **25** 1025–9
[41] Coster H G L and Zimmermann U 1975 *J. Membr. Biol.* **22** 73–90
[42] Lundqvist J A, Sahlin F, Åberg M A I, Strömberg A, Eriksson P S and Orwar O 1998 *Proc. Natl Acad. Sci.* **95** 10356–60
[43] Malmivuo J and Plonsey R 1995 *Bioelectromagnetism* (New York: Oxford University Press) chapter 3
[44] White J A, Blackmore P F, Schoenbach K H and Beebe Stephen J 2004 *J. Biol. Chem.* **279** 22964–72
[45] Sedgwick H, Caron F, Monaghan P B, Kolch W and Cooper J M 2008 *J.R. Soc. Interface* **5** 123-S130
[46] MacQueen L A, Buschmann M D and Wertheimer M R 2008 *Bioelectrochemistry* **72** 141–8
[47] International Electrotechnical Commission standard: IEC 60364-4-41 Ed. 5.0 b:2005
[48] Jeuken L J C 2008 *Biophys. J.* **94** 4711–7
[49] Pucihar G, Kotnik T, Miklavc D and Teissie J 2008 *Biophys. J.* **95** 2837–48
[50] Gawad S, Schild L and Renaud Ph 2001 *Lab Chip* **1** 76–82
[51] Kötz R and Carlen M 2000 *Electrochim. Acta* **45** 2483–98
[52] Pajkossy T 1994 *J. Electroanal. Chem.* **364** 111–25

Bibliography

[Andresen 2010] K.Ø. Andresen, M. Hansen, M. Matschuk, S.T. Jepsen, H.S. Sørensen, P. Utko, T.S. Hansen, N.B. Larsen, N. Rozlosnik, and R. Taboryski, "Injection molded chips with integrated conducting polymer electrodes for electroporation of cells", *Journal of Micromechanic and Microengineering*, vol. 20, 2010, p. 1

[Ardenne 1938] M. von Ardenne, "Das Elektronen-Rastermikroskop: Theoretische Grundlagen", *Zeitschrift für Physik*, vol. 108, 1938, p. 553

[Arkles 1977] B. Arkles, "Tailoring Surfaces with Silanes", CHEMTECH, vol. **7**, 1977, p. 766

[Arnold 2004] M. Arnold, E.A. Cavalcanti-Adam, R. Glass, J. Blümmel, W. Eck, M. Kantlehner, H. Kessler, and J.P. Spatz, "Activation of integrin function by nanopatterned adhesive interfaces", *Chemphyschem : a European journal of chemical physics and physical chemistry*, vol. 5, 2004, p. 383

[Arnold 2008] M. Arnold, V.C. Hirschfeld-Warneken, T. Lohmüller, P. Heil, J. Blümmel, E. a Cavalcanti-Adam, M. López-García, P. Walther, H. Kessler, B. Geiger, and J.P. Spatz, "Induction of cell polarization and migration by a gradient of nanoscale variations in adhesive ligand spacing", *Nano letters*, vol. 8, 2008, p. 2063

[Bailey 1985] J. Bailey and D. Gingell, "Contacts of chick fibroblasts on glass : results and limitations of quantitative interfere) metry", *Journal of Cell Science*, 1985, p. 215

[Becker 1999] H. Becker, U. Heim, and O. Röttingen, "The fabrication of polymer high aspect ratio structures with hot embossing for microfluidic applications", *SPIE Conference on Microfluidic Devices and Systems*, Santa Clara, Califonia: 1999

[Bennett 1989] V. Bennett, "The spectrin-actin junction of erythrocyte membrane skeletons", *Biochimica et Biophysica Acta (BBA) - Reviews on Biomembranes*, vol. 988, 1989, p. 107

[Besser 2006] A. Besser and S. Safran, "Force-induced adsorption and anisotropic growth of focal adhesions", *Biophysical journal*, vol. 90, 2006, p. 3469

[Biancardo 2008] S.B.N. Biancardo, H. Pranov, and N.B. Larsen, "Protein In-Mold Patterning", *Advanced Materials*, vol. 20, 2008, p. 1825

[Biggs 2007] M.J.P. Biggs, R.G. Richards, N. Gadegaard, C.D.W. Wilkinson, and M.J. Dalby, "The effects of nanoscale pits on primary human osteoblast adhesion formation and cellular spreading", *Materials Science*, vol. 18, 2007, p. 399

[Carrell 1985] N. a Carrell, L. a Fitzgerald, B. Steiner, H.P. Erickson, and D.R. Phillips, "Structure of human platelet membrane glycoproteins IIb and IIIa as determined by electron microscopy", *The Journal of biological chemistry*, vol. 260, 1985, p. 1743

[Cavalcanti-Adam 2007] E.A. Cavalcanti-Adam, T. Volberg, A. Micoulet, H. Kessler, B. Geiger, and J.P. Spatz, “Cell spreading and focal adhesion dynamics are regulated by spacing of integrin ligands”, *Biophysical journal*, vol. 92, 2007, p. 2964

[Choi 2007] C.-hwan Choi, S.H. Hagvall, B.M. Wu, J.C.Y. Dunn, R.E. Beygui, and C.-jin C.J. Kim, “Cell interaction with three-dimensional sharp-tip nanotopography”, *Biomaterials*, vol. 28, 2007, p. 1672

[Chou 1997] S.Y. Chou, P.R. Krauss, W. Zhang, L. Guo, and L. Zhuang, “Sub-10 nm imprint lithography and applications”, *Journal of Vacuum Science Technology*, vol. B 15, 1997, p. 2897

[Cretel 2008] E. Cretel, A. Pierres, A.-M. Benoliel, and P. Bongrand, “How Cells Feel Their Environment : A Focus on Early Dynamic Events”, *Cell and Molecular Bioengineering*, vol. 1, 2008, p. 5

[Curtis 1997] A. Curtis and C.D.W. Wilkinson, “Topographical control of cells”, *Biomaterials*, vol. 18, 1997, p. 1573

[Curtis 2001a] A. Curtis and C.D.W. Wilkinson, “Nantotechniques and approaches in biotechnology”, *Trends in biotechnology*, vol. 19, 2001, p. 97

[Curtis 2001b] A. Curtis, B. Casey, J.O. Gallagher, D. Pasqui, M.A. Wood, and C.D.W. Wilkinson, “Substratum nanotopography and the adhesion of biological cells . Are symmetry or regularity of nanotopography important ?”, *Biophysical Chemistry*, vol. 94, 2001, p. 275

[Dalby 2004] M.J. Dalby, D. Giannaras, M.O. Riehle, N. Gadegaard, S. Affrossman, and A. Curtis, “Rapid fibroblast adhesion to 27 nm high polymer demixed”, *Biomaterials*, vol. 25, 2004, p. 77

[Dalby 2007] M.J. Dalby, N. Gadegaard, R. Tare, A. Andar, M.O. Riehle, P. Herzyk, C.D.W. Wilkinson, and R.O.C. Oreffo, “The control of human mesenchymal cell differentiation using nanoscale symmetry and disorder”, *Nature Materials*, vol. 6, 2007, p. 997

[Danilov 1989] Y. N. Danilov and R. L. Juliano, “(Arg-Gly-Asp), albumin conjugates as a model substratum for integrin-mediated cell adhesion”, *Experimental Cell Research*, vol. 182, 1989, p. 186

[Devaprakasam 2004] D. Devaprakasam, S. Sampath, and S.K. Biswas, “Thermal Stability of Perfluoroalkyl Silane Self-Assembled on a Polycrystalline Aluminum Surface”, *Langmuir*, vol. 20, 2004, p. 1329

[Evans 1983] E. a Evans and V. a Parsegian, “Energetics of membrane deformation and adhesion in cell and vesicle aggregation”, *Annals of the New York Academy of Sciences*, vol. 416, 1983, p. 13

[Fritz 2002] T. Fritz, H.S. Cho, K.J. Hemker, W. Mokwa, and U. Schnakenberg, “Characterization of electroplated nickel”, *Microsystem Technologies*, vol. 9, 2002, p. 87

[Gadegaard 2003] N. Gadegaard, S. Mosler, and N.B. Larsen, “Biomimetic Polymer Nanostructures by Injection Molding”, *Macromolecular Materials and Engineering*, vol. 288, 2003, p. 76

[Gadegaard 2006] N. Gadegaard, M.J. Dalby, E. Martines, K. Seunarine, M.O. Riehle, A. Curtis, and C.D.W. Wilkinson, "Nanopatterned surfaces for biomaterial applications.pdf", *Advances in Science and Technology*, vol. 53, 2006, p. 107

[Gallagher 2002] J.O. Gallagher, K.F. Mcghee, C.D.W. Wilkinson, and M.O. Riehle, "Interaction of Animal Cells with Ordered Nanotopography", *IEEE Transactions on Nanobioscience*, 2002, p. 24

[Ghibaudo 2009] M. Ghibaudo, L. Trichet, J. Le Digabel, A. Richert, P. Hersen, and B. Ladoux, "Substrate topography induces a crossover from 2D to 3D behavior in fibroblast migration", *Biophysical journal*, vol. 97, 2009, p. 357

[Grampel 2002] R. D. van de Grampel, "Surfaces of Fluorinated Polymer Systems", *Ph.D. thesis*, Technische Universität Eindhoven, 2002

[Guo 1994] L.-H. Guo, J.S. Facci, G. McLendon and R. Moshert, "Effect of Gold Topography and Surface Pretreatment on the Self-Assembly of Alkanethiol Monolayers" *Langmuir,* vol. 10, 1994, p. 4588

[Guo 2007] Y. Guo, G. Liu, X. Zhu, and Y. Tian, "Analysis of the demolding forces during hot embossing", *Microsystem Technologies*, vol. 13, 2007, p. 411

[Heyderman 2000] L.J. Heyderman, H. Schift, C. David, J. Gobrecht, and T. Schweizer, "Flow behaviour of thin polymer films used for hot embossing lithography", *Microelectronic Engineering*, vol. 54, 2000, p. 229

[Heyderman 2001] L.J. Heyderman, H. Schift, C. David, B. Ketterer, M.A.D. Maur, and J. Gobrecht, "Nanofabrication using hot embossing lithography and electroforming", *Microelectronic Engineering*, vol. 57-58, 2001, p. 375

[Hofmann 1997] U.G. Hofmann, C. Rotsch, W.J. Parak, and M. Radmacher, "Investigating the cytoskeleton of chicken cardiocytes with the atomic force microscope", *Journal of Structural Biology*, vol. 119, 1997, p.84

[Hong 2004] G. Hong, A.S. Holmes, and M.E. Heaton, "SU8 resist plasma etching and its optimisation", *Microsystem Technologies*, vol. 10, 2004, p. 357

[Huang 2007] C.K. Huang, "Polymeric nanofeatures of 100 nm using injection molding for replication", *Micromechanics and Microengineering*, vol. 17, 2007, p. 1518

[Hughes 1979] R.C Hughes, S.D.J. Pena, J. Clark, and R.R. Dourmashkin, "Molecular requirements for the adhesion and spreading of hamster fibroblasts", *Experimental Cell Research*, vol. 121, 1979, p.307

[Humphries 1986] M.J. Humphries, S.K. Akiyama, A. Komoriya, K. Olden, and K.M. Yamada, "Identification of an alternatively spliced site in human plasma fibronectin that mediates cell type-specific adhesion", *The Journal of Cell Biology*, vol. 103, 1986, p. 2637

[Hutt 1996] D.A. Hutt and G.J. Leggett, "Influence of Adsorbate Ordering on Rates of UV Photooxidation of Self-Assembled Monolayers", *Journal of Physical Chemistry*, vol. 100, 1996, p. 6657

[Jaszewski 1999] R.W. Jaszewski, H. Schift, B. Schnyder, A. Schneuwly, and P. Groning, "The deposition of anti-adhesive ultra-thin Teflon-like films and their interaction with polymers during hot embossing", *Journal of Applied Surface Science*, vol. 143, 1999, p. 301

[Johansson 2002] B.-L. Johansson, A. Larsson, A. Ocklind, and Ke Hrlund, “Characterization of air plasma-treated polymer surfaces by ESCA and contact angle measurements for optimization of surface stability and cell growth”, *Journal of Applied Polymer Science*, vol. 86, 2002, p. 2618

[Kanchanawong 2010] P. Kanchanawong, G. Shtengel, A.M. Pasapera, E.B. Ramko, M.W. Davidson, H.F. Hess, and C.M. Waterman, “Nanoscale architecture of integrin-based cell adhesions”, *Nature*, vol. 468, 2010, p. 580

[Kang 1998] J.F. Kang, R. Jordan, and A. Ulman, ” Wetting and Fourier Transform Infrared Spectroscopy Studies of Mixed Self-Assembled Monolayers of 4‘-Methyl-4-mercaptobiphenyl and 4‘-Hydroxy-4-mercaptobiphenyl”, *Langmuir*, vol. 14, 1998, p. 3983

[Khanarian 2001] G. Khanarian and H. Celanese, “Optical properties of cyclic olefin copolymers”, *Optical Engineering*, vol. 40, 2001, p. 1024

[Kim 2006] S.-jin Kim, H. Yang, K. Kim, Y.T. Lim, and H.-bong Pyo, “Study of SU-8 to make a Ni master-mold : Adhesion, sidewall profile, and removal”, *Electrophoresis*, vol. 27, 2006, p. 3284

[Kim 2008] D.J. Kim, R. Pitchimani, D.E. Snow, and L.J. Hope-Weeks, “A simple method for the removal of thiols on gold surfaces using an NH4OH-H2O2-H2O solution”, *Scanning*, vol. 30, 2008, p. 118

[Klompen 2005] E. T.J. Klompen, “Mechanical properties of solid polymers”, *Ph.D. thesis*, Technische Universität Eindhoven, 2005

[Kong 2008] D. Kong, B. Ji, and L. Dai, “Nonlinear mechanical modeling of cell adhesion”, *Journal of theoretical biology*, vol. 250, 2008, p. 75

[Koponen 2007] H.-kaisa Koponen, I. Saarikoski, T. Korhonen, M. Pa, R. Kuisma, T.T. Pakkanen, M. Suvanto, and T.A. Pakkanen, “Modification of cycloolefin copolymer and poly (vinyl chloride) surfaces by superimposition of nano- and microstructures”, *Applied Surface Science*, vol. 253, 2007, p. 5208

[LaBianca 1995] N. LaBianca and J. Gelorme, “High aspect ratio resist for thick film applications”, *Proceedings of SPIE,* vol. 2438, 1995, p. 846

[Larsen 2008] A.V. Larsen, L. Poulsen, H. Birgens, M. Dufva, and A. Kristensen,” Pinched flow fractionation devices for detection of single nucleotide polymorphisms”, *Lab on a Chip*, vol. 8, 2008, p. 818

[Lee 2006] N. Lee, S. Choi, and S. Kang, “Self-assembled monolayer as an antiadhesion layer on a nickel nanostamper in the nanoreplication process for optoelectronic applications”, *Applied Physics Letters*, vol. 88, 2006, p. 1

[Lehnert 2004] D. Lehnert, B. Wehrle-haller, C. David, U. Weiland, C. Ballestrem, B.A. Imhof, and M. Bastmeyer, “Cell behaviour on micropatterned substrata : limits of extracellular matrix geometry for spreading and adhesion”, *Journal of Cell Science*, vol. 117, 2004, p. 41

[Liou 2006] A.C. Liou and R.H. Chen, “Injection molding of polymer micro- and sub-micron structures with high-aspect ratios”, *International Journal of Advanced Manufacturing Technology*, vol. 28, 2006, p. 1097

[Macintyre 1998] D. Macintyre and S. Thoms, “Fabrication of high resolution features by Injection Molding”, *Microelectronic Engineering*, vol. 41/42, 1998, p. 211

[Maluf 2004] N. Maluf and K. Williams, “An Introduction to Microelectromechanical System Engineering” (chapter 3: “Processes for Micromechaning”), *Artech House* , 2004, p. 33

[Martinez 2008] E. Martinez, E. Engel, J.A. Planell, and J. Samitier, “Effects of artificial micro- and nano-structured surfaces on cell behaviour”, *Annals of Anatomy*, vol. 191, 2008, p. 126

[Massia 1991] S.P. Massia and J. a Hubbell, “An RGD spacing of 440 nm is sufficient for integrin alpha V beta 3-mediated fibroblast spreading and 140 nm for focal contact and stress fiber formation”, *The Journal of cell biology*, vol. 114, 1991, p. 1089

[Mitchell 2005] S. a Mitchell, M.R. Davidson, and R.H. Bradley, “Improved cellular adhesion to acetone plasma modified polystyrene surfaces”, *Journal of colloid and interface science*, vol. 281, 2005, p. 122

[Mönkkönen 2002] K. Mönkkönen, J. Hietala, P. Pääkkönen, E.J. Pääkönen, T. Kaikuranta, T.T. Pakkanen, and T. Jääskeläinen, “Replication of Sub-Micron Features Using Amorphous Thermoplastics”, *Polymer Engineering and Science*, vol. 42, 2002, p. 1600

[Nicolas 2006] A. Nicolas and S. Safran, “Limitation of cell adhesion by the elasticity of the extracellular matrix”, *Biophysical journal*, vol. 91, 2006, p. 61

[Nikolova 2004] D. Nikolova, E. Dayss, G. Leps, and A. Wutzler, “Surface modification of cycloolefinic copolymers for optimization of the adhesion to metals”, *Surface and Interface Analysis*, vol. 36, 2004, p. 689

[Nunes 2010] P.S. Nunes, P.D. Ohlsson, O. Ordeig, and J.P. Kutter, “Cyclic olefin polymers: emerging materials for lab-on-a-chip applications”, *Microfluidics and Nanofluidics*, vol. 9, 2010, p. 145

[Ohashi 2002] T. Ohashi, Y. Ishii, Y. Ishikawa, T. Matsumoto, and M. Sato, “Experimental and numerical analyses of local mechanical properties measured by atomic force microscopy for sheared endothelial cells”, *Bio-Medical Materials and Engineering*, vol. 12, 2002, p. 319

[Owen 2005] G.R. Owen, D.O. Meredith, I. Gwynn, and R.G. Richards, “Focal adhesion quantification - a new assay of material biocompatibility? Review”, *European cells & materials*, vol. 9, 2005, p. 85

[Palsson 2008] E. Palsson, “A 3-D model used to explore how cell adhesion and stiffness affect cell sorting and movement in multicellular systems”, *Journal of theoretical biology*, vol. 254, 2008, p. 1

[Park 2003] S. Park, C. Padeste, H. Schift, and J. Gobrecht, “Nanostructuring of anti-adhesive layers by hot embossing lithography”, *Microelectronic Engineering*, vol. 67-68, 2003, p. 252

[Park 2004] S. Park, H. Schift, C. Padeste, and B. Schnyder, “Anti-adhesive layers on nickel stamps for nanoimprint lithography”, *Microelectronic Engineering*, vol. 74, 2004, p. 196

[Patla 2010] I. Patla, T. Volberg, N. Elad, V. Hiershfeld-Warneken, C. Grashoff, R. Fässler, J.P. Spatz, B. Geiger, and O. Medalia, “Dissecting the molecular architecture of integrin adhesion sites by cryo-electron tomography”, *Nature cell biology*, vol. 12, 2010, p. 909

[Pesen 2005] D. Pesen and J.H. Hoh, “Micromechanical architecture of the endothelial cell cortex”, *Biophysical Journal*, vol. 88, 2005, p. 670

[Pranov 2006] H. Pranov, H.K. Rasmussen, N.B. Larsen, and N. Gadegaard, “On the Injection Molding of Nanostructured Polymer Surfaces”, *Polymer Engineering and Science*, vol. 46, 2006, p. 160

[Pries 2000] A.R. Pries, T.W. Secomb, and P. Gaehtgens, “The endothelial surface layer”, *Pflgers Archiv European Journal of Physiology*, vol. 440, 2000, p. 653

[Raiber 2005] K. Raiber, a Terfort, C. Benndorf, N. Krings, and H. Strehblow, “Removal of self-assembled monolayers of alkanethiolates on gold by plasma cleaning”, *Surface Science*, vol. 595, 2005, p. 56

[Reitsma 2007] S. Reitsma, D.W. Slaaf, H. Vink, M. a M.J. van Zandvoort, and M.G. a oude Egbrink, “The endothelial glycocalyx: composition, functions, and visualization”, *Pflügers Archiv : European journal of physiology*, vol. 454, 2007, p. 345

[Rivas 1991] G. a Rivas, J. a Aznárez, P. Usobiaga, J.L. Saiz, and J. González-Rodríguez, “Molecular characterization of the human platelet integrin GPIIb/IIIa and its constituent glycoproteins”, *European biophysics journal*, vol. 19, 1991, p. 335

[Rotsch 1999] C. Rotsch, K. Jacobson, and R. Radmacher, “Dimensional and mechanical dynamics of active and stable edges in motile fibroblasts investigated by using atomic force microscopy”, *Proceedings of the National Academy of Sciences of the United States of America*, vol. 96, 1999, p. 921

[Safran 2005] S. Safran, N. Gov, A. Nicolas, U. Schwarz, and T. Tlusty, “Physics of cell elasticity, shape and adhesion”, *Physica A: Statistical Mechanics and its Applications*, vol. 352, 2005, p. 171

[Sato 2004] H. Sato, N. Kataoka, F. Kajiya, M. Katano, T. Takigawa, and T. Masuda, “Kinetic study on the elastic change of vascular endothelial cells on collagen matrices by atomic force microscopy”, *Colloids and Surfaces B: Biointerfaces*, vol. 34, 2004, p. 141

[Savitskiy 1961] Y.M. Savitskiy and U.A. Duysemalieyev, “Mechanical Properties of Vanadium-alloyed Copper and Nickel-Vanadium Alloys at elevated Temperatures”, *Metal Science and Heat Treatment*, vol. 3, 1961, p. 126

[Schift 2000] H. Schift, C. David, M. Gabriel, J. Gobrecht, L.J. Heyderman, W. Kaiser, S. Koppel, and L. Scandella, “Nanoreplication in polymers using hot embossing and injection molding”, *Microelectronic Engineering*, vol. 53, 2000, p. 171

[Schift 2005] H. Schift, S. Saxer, and S. Park, “Controlled co-evaporation of silanes for nanoimprint stamps”, *Nanotechnology*, vol. 16, 2005, p. 171

[Schift 2007] H. Schift and A. Kristensen, “Handbook of Nanotechnology” (chapter 8: “Nanoimprint Lithography”), *Springer*, 2007, p. 239

[Schift 2008] H. Schift, “Nanoimprint lithography : An old story in modern times ? A review”, *Vacuum Science Technology*, vol. 26, 2008, p. 458

[Schmitz 2008] J. Schmitz, M. Benoit, and K.-E. Gottschalk, “The viscoelasticity of membrane tethers and its importance for cell adhesion”, *Biophysical journal*, vol. 95, 2008, p. 1448

[Selhuber-Unkel 2010] C. Selhuber-Unkel, T. Erdmann, M. López-García, H. Kessler, U.S. Schwarz, and J.P. Spatz, “Cell adhesion strength is controlled by intermolecular spacing of adhesion receptors”, *Biophysical journal*, vol. 98, 2010, p. 543

[Ikeurasekiguchi 2005] H. Ikeurasekiguchi, T. Sekiguchi, and M. Koike, “Characterization and degradation of ZEP520 resist film by TOF-PSID and NEXAFS”, *Journal of Electron Spectroscopy and Related Phenomena*, vol. 144-147, 2005, p. 453

[Shattil 2010] S.J. Shattil, C. Kim, and M.H. Ginsberg, “The final steps of integrin activation: the end game”, *Nature reviews. Molecular cell biology*, vol. 11, 2010, p. 288

[Shim 2010] J.S. Shim, A.W. Browne, and C. Ahn, “An on-chip whole blood/plasma separator with bead-packed microchannel on COC polymer”, *Biomedical Microdevices*, vol. 12, 2010, p. 949

[Shin 2005] J.Y. Shin, J.Y. Park, C. Liu, J. He, and S.C. Kim, “Chemical structure and physical properties of cyclic olefin copolymers (IUPAC Technical Report)”, *Pure and Applied Chemistry*, vol. 77, 2005, p. 801

[Shtengel 2009] G. Shtengel, “Interferometric fluorescent super-resolution microscopy resolves 3D cellular ultrastructure”, *Proceedings of the National Academy of Sciences of the United States of America*, vol. 106, 2009, p. 3125

[Simon 2003] A. Simon, T. Cohen-Bouhacina, V.C. Porte, J.P. Aime, J. Amedee, R. Bareille, and C. Baquey, “Characterization of dynamic cellular adhesion of osteoblasts using atomic force microscopy”, *Cytometry A*, vol. 54, 2003, p. 36

[Singer 1987] I.I. Singer, D.W. Kawka, S. Scott, R.A. Mumford, and M.W. Lark, “The fibronectin cell attachment sequence Arg-Gly-Asp-Ser promotes focal contact formation during early fibroblast attachment and spreading”, *Journal of Cell Biology*, vol. 104, 1987, p. 573

[Sniadecki 2006] N.J. Sniadecki, R.A. Desai, S.A. Ruiz, and C.S. Chen, “Nanotechnology for Cell – Substrate Interactions”, *Annals of Biomedical Engineering*, vol. 34, 2006, p. 59

[Song 2007] I.-H. Song, Y. Jin, and P.K. Ajmera, “Fabrication of a polymeric tapered HARMs array utilizing a low-cost nickel electroplated mold insert”, *Microsystem Technologies*, vol. 13, 2007, p. 287

[Tate 2000] J. Tate, J.A. Rogers, C.D.W. Jones, B. Vyas, D.W. Murphy, W. Li, Z. Bao, R.E. Slusher, A. Dodabalapur and H.E. Katz, “Anodization and Microcontact Printing on Electroless Silver: Solution-Based Fabrication Procedures for Low-Voltage Electronic Systems with Organic Active Components”, *Langmuir*, vol. 16, 2000, p. 6054

[Theilade 2007] U.A. Theilade and H.N. Hansen, “Surface microstructure replication in injection molding”, *International Journal of Advanced Manufacturing Technology*, vol. 33, 2007, p. 157

[Ting 2008] C.-jen Ting, F.-yu Chang, C.-feng Chen, and C.P. Chou, “Fabrication of an antireflective polymer optical film with subwavelength structures using a roll-to-roll micro-replication process”, *Micromechanics and Microengineering*, vol. 18, 2008, p. 9

[Titushkin 2007] I. Titushkin and M. Cho, “Modulation of cellular mechanics during osteogenic differentiation of human mesenchymal stem cells”, *Biophysical Journal*, vol. 93, 2007, p. 3693

[Vogel 2006] V. Vogel and M. Sheetz, “Local force and geometry sensing regulate cell functions”, *Nature reviews:Molecular Cell Biology*, vol. 7, 2006, p. 265

[Wehrle-Haller 2002] B. Wehrle-Haller and B. Imhof, “The inner lives of focal adhesions”, *Trends in Cell Biology*, vol. 12, 2002, p. 382

[Wilkinson 2002] C.D.W. Wilkinson, M.O. Riehle, M. Wood, J.O. Gallagher, and A. Curtis, “The use of materials patterned on a nano- and micro-metric scale in cellular engineering”, *Materials Science and Engineering*, vol. 19, 2002, p. 263

[Winter 2009] S. Winter, S. Wilson, and M. Guttmann, “Partielle Resistmetallisierung für hohe Aspektverhältnisse”, *Mikroproduktion*, vol. 3, 2009, p.46

[Wiseman 2004] P.W. Wiseman, C.M. Brown, D.J. Webb, B. Hebert, N.L. Johnson, J. a Squier, M.H. Ellisman, and a F. Horwitz, “Spatial mapping of integrin interactions and dynamics during cell migration by image correlation microscopy”, *Journal of Cell Science*, vol. 117, 2004, p. 5521

[Xie 2008] G. Xie, G. Zhang, F. Lin, J. Zhang, Z. Liu, and S. Mu, “The fabrication of subwavelength anti-reflective nanostructures using a bio-template”, *Nanotechnology*, vol. 19, 2008, p. 5

[Yamane 2000] Y. Yamane, H. Shiga, H. Haga, K. Kawabata, K. Abe, and E. Ito, “Quantitative analyses of topography and elasticity of living and fixed astrocytes”, *Journal of Electron Microscopy*, vol. 49, 2000, p. 463

[Yoo 2009] Y.-eun Yoo, T.H. Kim, D.-sun Choi, H.-joo Lee, S.J. Choi, and S.K. Kim, “Study on Molding of a Nanostructured Plastic Plate and Its Surface Properties”, *Japanese Journal of Applied Physics*, vol. 48, 2009, p. 1

[Zhou 2005] Z. Zhou, “Handbook of Microscopy for Nanotechnology” (chapter 10: “Electron beam Lithography”), *Kluwer Academic Publishers*, 2005, p. 287

INTERNET LINKS

[Attension2011] *accessed on 23/02/2011*
Attension, BiolinScientific, Sweden, “Contact Angle”, *http://www.attension.com/contact-angle.aspx*

[CML2011] *accessed on 25/02/2011*
Cell Migration lab, University of Reading, England, “Cell Adhesion”, *http://www.reading.ac.uk/cellmigration/adhesion.htm*

[Conway2005] *accessed on 01/04/2011*
J. W. Coway, E-beam Process for ZEP520A to be used for Metal Liftoff and RIE, Standford University, *http://snf.stanford.edu/Process/Lithography/EBResist/ZEP520-Anisole.pdf*

[CPN2011] *accessed on 10/02/2011*
CustomPartNet, USA, *http://www.custompartnet.com/wu/InjectionMolding*

[GEA2011-SEM] *accessed on 20/02/2011*
“Scanning Electron Microscopy (SEM)”, *http://serc.carleton.edu/research_education/geochemsheets/techniques/SEM.html*

[Gelest2011] *accessed on 11/03/2011*
Gelest Inc., “Hydrophobicity, Hydrophilicity and Silane Surface Modification” (brochure) *http://www.gelest.com/literature.asp*

[Henderson2011] *accessed on 23/02/2011*
C. Henderson, Georgia Tech School for Chemical & Biomolecular Enginieering, USA, “Fundamentals of Electron Beam Lithography”, *http://henderson.chbe.gatech.edu/Introductions/intro%20to%20e-beam%20lithography.htm*

[HIMT2011] *accessed 26/02/2011*
Heidelberg Instruments GmbH, Germany, *http://www.himt.de/img/writing_strategy.jpg*

[Howland2011] *accessed on 13/03/2011*
Rebecca Howland and Lisa Benatar, “A Practical Guide to Scanning Probe Microscopy”, chapter 4.1. “Tip Convolution”, *http://www.mechmat.caltech.edu/~kaushik/park/contents.htm*

[Kopeliovich2011] *accessed on 23/02/2011*
D. Kopeliovich, SubsTech, Israel, “Nickel Electroplating”, *http://www.substech.com/dokuwiki/doku.php?id=nickel_electroplating*

[Leapfrog2011] *accessed on 13/03/2011*
LEAPFROG IP, Europe,“Automatic Interliner Assembly”, *http://www.leapfrogeu.org/LeapfrogIP/main.asp?pg=rma_results#Automatic%20interliner%20assembly*

[NIST2011] *accessed 10/03/2011*
NIST, USA, “X-ray Photoelectron Spectroscopy Database”, *http://srdata.nist.gov/xps/*

[Ramehart2011] *accessed on 23/02/2011*
Ramé-Hart Instrument Co, Netcong, USA, “Information on Contact Angle”, *http://www.ramehart.com/contactangle.htm*

[UT2011] *accessed on 26/02/2011*
L.V. Llona, Nickel Electroplating, University of Twente, *http://www.utwente.nl/ewi/tst/research/microfabrication/mmflowcontrollers*

[WIKI2011-DRIE] *accessed on 20/02/2011*
Wikipedia – The free Encyclopedia, “Deep reactive-ion etching”, *http://en.wikipedia.org/wiki/Deep_reactive-ion_etching* (english) and *http://de.wikipedia.org/wiki/Reaktives_Ionentiefen%C3%A4tzen* (german)

[WIKI2011-IM] *accessed on 27/03/2011* Wikipedia – The free Encyclopedia, “Injection Molding”, *http://en.wikipedia.org/wiki/Injection_molding*

[WIKI2011-RIE] *accessed on 20/02/2011* Wikipedia – The free Encyclopedia, “Deep reactive-ion etching”, *http://en.wikipedia.org/wiki/Reactive-ion_etching*

[WIKI2011-SEM] *accessed on 20/02/2011* Wikipedia – The free Encyclopedia, “Scanning Electron Microscopy”, *http://en.wikipedia.org/wiki/Scanning_electron_microscope*

[WIKI2011-XPS] *accessed on 10/03/2011* Wikipedia – The free Encyclopedia, “X-ray photoelectron spectroscopy”, *http://en.wikipedia.org/wiki/X-ray_photoelectron_spectroscopy*

[Zemlyanov2007] *accessed on 10/02/2011* Dmitry Zemlyanov, "Introduction to X-ray Photoelectron Spectroscopy and to XPS Applications," 2007 *http://nanohub.org/resources/2668*